Theoretical and Numerical Investigation of Radiative Extinction of Diffusion Flames

By

Anjan Ray

A DISSERTATION

Submitted to
Michigan State University
in partial fulfillment of the requirements
for the degree of

DOCTOR OF PHILOSOPHY

Department of Mechanical Engineering

1996

ABSTRACT

Theoretical and Numerical Investigation of Radiative Extinction of Diffusion Flames

By

Anjan Ray

The influence of soot radiation on diffusion flames was investigated using both analytical and numerical techniques. Soot generated in diffusion flames dominate the flame radiation over gaseous combustion products and can significantly lower the temperature of the flame. In low gravity situations there can be significant accumulation of soot and combustion products in the vicinity of the primary reaction zone owing to the absence of any convective buoyant flow. Such situations may result in substantial suppression of chemical activities in a flame and the possibility of a radiative extinction may also be anticipated. The purpose of this work was to not only investigate the possibility of radiative extinction of a diffusion flame but also to qualitatively and quantitatively analyze the influence of soot radiation on a diffusion flame.

In this study, first a hypothetical radiative loss profile of the form of a $sech^2$ was assumed to influence a pure diffusion flame. It was observed that the reaction zone can, under certain circumstances, move through the radiative loss zone and locate

itself on the fuel side of the loss zone, contrary to our initial postulate. On increasing the intensity and/or width of the loss zone it was possible to extinguish the flame and extinction plots were generated. In the presence of a convective flow, however, the movement of the temperature and reaction rate peaks indicated that the flame behavior is more complicated compared to a pure diffusion flame.

A comprehensive model of soot formation, oxidation and radiation was used in a more involved analysis. The soot model of Syed, Stewart and Moss [1] was used for soot nucleation and growth and the model of Nagle and Strickland-Constable [2] was used for soot oxidation. The soot radiation was considered in the optically thin limit. An analysis of the flame structure revealed that the radiative loss term is countered both by the reaction term and the diffusion term. The essential balance for the soot volume fraction was found to be between the processes of soot convection and soot growth. Such a balance yielded to analytical treatment and the soot volume fraction could be expressed in the form of an integral. The integral was evaluated using two approximate methods and the results agreed very well with the numerical solutions for all cases examined.

In loving memory of my mother

ACKNOWLEDGMENTS

I wish to express my very sincere gratitude to Dr. I. S. Wichman for his guidance. He took active interest in my work and participated in all stages of problem solving. It was a great privilege to work with him.

I would also like to thank Dr. J. V. Beck, Dr. M. Miklavcic and Dr. M. Zhuang for serving on my thesis committee and for offering important suggestions for improvement.

This work was supported by the microgravity combustion research program of the NASA Lewis Research Center. In Spring, 1996 this work was supported by a generous fellowship award from the Michigan State University Graduate School.

I am grateful to my colleagues Zori Pavlova, Nandu Lakkaraju and Bukky Oladipo for creating and sustaining a friendly atmosphere at work. I would like to thank my friend Umashankar for his elaborate help on formatting my thesis using LaTeX. Bipasha helped me with some of the drawings in this thesis.

My friends have been extremely supportive throughout. I would fondly remember the long telephone conversations with Mayukh and Debabrata. We exchanged ideas, shared good humor and infused inspiration into one another. The team of friends at East Lansing created an atmosphere of bonhomie which has been of paramount importance to me. Rabi, Ajit, Nidhan, Ashim and Kuntal have been great friends and have always been there for me.

The greatest inspiration for my Doctoral work came from my parents. I have learned a lot from the courage and fortitude of my father through difficult times and

a great personal loss. He taught me the value of exploring new avenues and to remain undaunted in the worst of times. Even in the midst of great pain and suffering, my mother lent her unrelenting support for me in the early stages of my Doctoral work. Her ecstasy would have known no bounds today. Her invisible presence continues to nourish my inner self and this work is a tribute to how much she has always meant to me.

TABLE OF CONTENTS

LIST OF TABLES

LIST OF FIGURES

CHAPTER 1

Introduction

The influence of soot radiation on flames has received significant attention in recent years [3],[4],[5],[6],[7],[8],[9]. Thermal radiation from combustion products and soot lower the temperature of the flame and decelerate chemical activities. The purpose of this study is to critically assess the effect of soot radiation on diffusion flames and investigate whether under certain circumstances radiative energy losses can result in an extinction of a diffusion flame.

Soot radiation has considerable influence on flames established in low gravity situations. In normal gravity the combustion products and the flame-generated soot get convected away from the primary reaction zone due to buoyancy induced flows. However, in microgravity, there is no buoyant flow and the combustion products and soot reside in the vicinity of the primary reaction zone. In addition, the absence of convective flow results in longer residence time and more soot is produced in a low gravity situation. Thus, the formation of greater amount of soot and its vicinity to the primary reaction zone suggest stronger soot radiation effects in microgravity. There is thus a possibility that the drainage of energy from the flame by means of soot radiation may be so great in microgravity that the flame may no longer be able

to sustain itself. Thus a radiative extinction of the flame is anticipated under such situations [10].

Thermal radiation from a flame can be due to (1) radiation from the combustion gases at high temperature and (2) radiation from combustion generated particulates, i.e., soot. According to the calculations of Grosshandler and Modak [11] for soot volume fractions $> 10^{-7}$ soot radiation is dominant. In the present work, gas radiation has been neglected and soot radiation was modeled assuming the optically thin limit. Kennedy *et al.* [12] have observed that for small flames and for moderate soot loadings the optically thin limit is appropriate for soot radiation. The purpose of our investigation was to qualitatively and quantitatively study the effect of soot radiation on flames. In particular, the possibility of a radiative extinction was examined thoroughly.

The soot radiation from a flame depends on the soot volume fraction distribution in the flame, which is difficult to predict. There are considerable uncertainties in determining the soot formation and oxidation rates. In particular, the soot distribution in a flame depends on the fuel structure, the temperature distribution, the influence of inerts, the pressure of the system, etc. Since soot radiation is intimately coupled with the soot volume fraction distribution, it becomes difficult to predict the radiation from a flame.

A review of the existing literature in the research area is presented in chapter 2. The primary focus is on soot evolution, soot modeling and soot radiation.

In chapter 3 the influence of a hypothetical heat loss term of the form of a $sech^2$ on a pure diffusion flame established between two diffusing walls of fuel and oxidizer was investigated. The thickness of the loss zone and its separation distance from the ideal, infinite reaction rate flame location were parametrically varied. The influence of increasing the intensity of the loss zone was also investigated.

The effect of a similar heat loss profile on a diffusion flame with convective fuel

blowing from the wall was also examined. Chapter 4 elucidates interesting results of the effect of fuel blowing on the flame in the presence of radiative losses.

An analytical model was developed for the soot layer profile and thickness on the assumption of infinite reaction rate profiles for temperature and species mass fractions. Chapter 5 outlines the basic assumptions of the model, its derivation and comparison with numerical results. Then, a prescribed soot volume fraction profile was used to formulate a radiative loss term and its influence on the flame structure was examined.

In chapter 6 the comprehensive problem of soot radiation for a diffusion flame established between an oxidizer and a fuel wall was examined. Similar to chapter 4, a convective fuel flow from the fuel wall was assumed. A heat loss profile was *not* assumed in this case. Instead, the soot model of Moss and co-workers [1] was used and a soot volume fraction equation was solved in conjunction with the coupled energy and species mass fraction equations. Results indicate extremely interesting flame behavior due to radiative losses.

Chapter 7 briefly states the conclusions of the current work. Recommendations for future work are also outlined.

CHAPTER 2

Literature Review

2.1 Introduction

In this chapter a review of the existing literature pertaining to the research problem is presented. As discussed in chapter 1, the influence of soot radiation on a diffusion flame depends strongly on the soot formation and oxidation chemistry. In the following sections the soot evolution and burnout processes are reviewed, the soot radiation effect is discussed and the effect of various parameters on soot radiation is analyzed in the light of the existing literature.

2.2 Background

Most practical combustion systems burn in the diffusion flame mode. In a diffusion flame the process of physical mixing of the reactants is generally intended to be much slower than the chemical reaction between the fuel and the oxidizer. Consequently, the flame is (generally) kinetically controlled. By contrast, the constituents are already mixed before they enter the combustor in a premixed flame. In our research problem we shall focus on diffusion flames only; hence the following review pertains to diffusion flames.

2.3 Soot

Carbonaceous particles generated during gas phase combustion reactions are called soot. Soot is formed because of incomplete combustion of fossil fuels and other organic matter. Principal sources of soot emissions are coal burning furnaces, refuse burning, coke production processes, wood burning in home fireplaces, the open burning of waste, and gasoline and diesel powered engines.

Under ideal conditions the combustion of hydrocarbons leads to mainly carbon dioxide and water. Ideal conditions may be specified by stoichiometric composition of the combustible mixture, i.e., the oxygen content of the mixture everywhere is sufficient to convert the fuel completely according to the formal chemical equation $C_xH_y + (x + y/4)O_2 \rightarrow xCO_2 + (y/2)H_2O$. Under these conditions a maximum of heat is released and a maximum of chemical energy is available for mechanical work.

In practical combustion devices such as industrial furnaces, gas turbines, or combustion engines conditions locally deviate from ideality. When the locally available oxygen is not sufficient to convert the fuel according to the formal chemical equation mentioned above, other products of incomplete combustion such as carbon monoxide, hydrogen, hydrocarbons and soot are produced in addition to carbon dioxide and water.

2.3.1 How Does Soot Affect Us?

Emission of soot to the atmosphere from various industrial combustion processes is undesirable for various reasons. Soot particles contribute to reduced atmospheric visibility and increased particulate fallout. Also, emission of soot is often associated with carcinogenic polycyclic aromatic hydrocarbons. Consequently, the adverse health effect is an important issue regarding soot particle emission: the emission of soot in the atmosphere is unquestionably hazardous and undesirable. However, the

next question is, should soot formation be avoided altogether? This question has various answers depending on the combustion process being considered. Soot emission from a practical combustion appliance such as an internal combustion engine reflects poor combustion conditions and a loss of efficiency. It has deleterious consequences for the maintenance of the device. For such devices, the designer would like to avoid soot formation altogether. The same objective also applies in case of fires, whose mechanism of propagation often involves radiant transfer from hot soot particles.

However, for flames in furnaces and boilers the generation of soot is necessary as a radiation source for efficient heat transfer. For such flames, the principle is to generate as much soot as necessary in such a way that it can be burnt up again in the available time. The carbon black industry is in sharp contrast to the above and the objective is to produce as much soot as possible by fuel pyrolysis.

2.3.2 Appearance

Soot generated in combustion processes is not a uniquely defined substance [13],[14]. It is normally black. The first soot particles result from condensation reactions in the gas phase. These particles, as well as the individual primary particles that compose soot aggregates can be reasonably approximated as spherical [15]. The elementary particles adhere to each other to form straight or branched chains. These chains agglomerate and form the visible soot flocculates, generally as a fluffy substance.

2.3.3 Morphology and Chemical Structure

Research has been conducted in laminar and turbulent, (rich and lean) premixed and nonpremixed flames, momentum and buoyancy driven flames, stirred reactors, spray flames, shock tubes, and common combustor devices such as engines and furnaces. There are many similarities in the morphological characteristics [16] for the soot

produced from such different configurations. The similarities in soot morphology suggest that a common developmental history governs the formation process, even in very different combustion configurations [15]. Besides carbon, soot particles also contain hydrogen (10 to 25%), oxygen ($O(1\%)$) and nitrogen atoms ($O(0.1\%)$) [15].

Electron diffraction indicates the presence of C-C bonds in soot [17].

2.3.4 Characterization of the Soot Distribution

Characterization of the soot distribution is done using three important parameters. The soot volume fraction, f_v, is the volume of soot present in a unit volume of gas and is expressed in units of $m^3{}_{soot}/m^3{}_{gas}$. The soot particle size is characterized by a length scale d which equals the diameter for a spherical particle. The particle number density is denoted by n and is defined as the number of soot particles per unit volume of gas. The three parameters f_v, d and n are related and for spherical monodisperse soot particles $f_v = n\pi d^3/6$. In general, soot particulates are neither spherical nor monodisperse. The preceding relation, therefore, may be considered as yet another generic measure of soot.

2.3.5 Soot Evolution

There are two important stages of soot particle formation, viz., particle inception and particle growth. The following discussion provides a brief description of the two stages. However, it has to be kept in mind that the above classification is somewhat mechanistic and in an actual combustion process such distinctions are not very clear [15].

(1) Particle Inception The first condensed phase material is generated from the fuel molecules via their oxidation and/or pyrolysis products [14]. Such products include acetylene and its higher analogues and polycyclic aromatic hydrocarbons. These two

types of unsaturated hydrocarbons are often considered the most likely precursors of soot in flames [14]. Because soot is formed in the intermediate stages of chemical decomposition the oxidation and pyrolysis products alluded to are reaction intermediates like aldehydes, various radical compounds, alcohols and other such trace materials.

The condensation reactions of such species often lead to the first recognizable soot particles known as nuclei. The first particles are very small ($d < 2$ nm); for this reason, even a large number density results in negligible soot loading in the region of their formation, which is generally confined to the vicinity of the primary reaction zone (i.e., where most of the heat release occurs).

(2) Particle Growth Particle growth takes place by means of both surface growth and coagulation. Surface growth means gas species become attached to the soot particle surface and incorporated in the particulate phase. Haynes and Wagner [14] have remarked that for soot formation to occur the species with the correct hydrogen content have to condense followed by subsequent dehydrogenation. Surface growth reactions lead to an increase in the amount of soot but the number density remains the same. In the process of coagulation particles grow by colliding and coalescing, thereby decreasing the number density. Here the volume fraction remains the same. Particle growth is therefore generally considered to be the result of simultaneous surface growth and coagulation.

Almost all of the soot mass is provided by surface growth reactions. However, the inception process is calculated to be the rate limiting step in the formation of soot. This has been explained from different perspectives in the literature. Fuel pyrolysis leads to particle inception; some researchers believe that this may be the most important factor [18], [19], [20], [21]. Also important is the formation of initial surface area delivered from the inception region and available for growth [22], [23].

However there is at least one exception to the widely held belief that particle

inception controls soot production. Based upon modeling considerations, Kennedy *et al.* [12] disagree that particle inception controls soot production. Instead, they propose that surface growth is the most important factor. The relative importance of surface growth and particle inception is a key issue in quantitative models of soot formation.

2.3.6 Soot Oxidation

The link between soot production within the flame and the smoke yield from the flame is the oxidation of soot particles. Soot is oxidized in the high temperature combustion zone leading to decreased soot mass. As observed by [15] a great many experimental measurements have been conducted in the last twenty years on the soot formation process in different flame configurations. Yet, only a handful of studies have been performed on soot oxidation processes, and most of these only quite recently.

The particle destruction rate depends on the flame structure, the temperature field and the concentration distribution of oxidizing species, principally OH, O_2 and O atoms. Nagle and Strickland-Constable [2] derived a semi-empirical formula for pyrolytic graphite oxidation by O_2 for a temperature range $1300 - 2300\ K$. In their analysis they assumed that oxidation by other species was negligible.

In many combustion conditions it is clear that OH is also an important oxidizer of soot particles [24]. For soot to escape from a nonpremixed flame, it must pass through a relatively hot reaction zone where the concentration of OH is relatively large.

Puri and Santoro [24] have examined the question of how much CO is produced from the oxidation of soot by OH and O_2 in laminar hydrocarbon flames. They derived an expression for the soot oxidation rate (or the CO production rate) by applying a fundamental kinetic theory approach.

2.3.7 The Influence of Fuel Structure

It has been observed that smaller the hydrocarbon molecule, the greater the resistance to smoke emission.

An increase of the fuel flow rate increases the height of a diffusion flame, say a Bunsen-type flame for definiteness. The character of the flame also changes. Initially the flame is almost completely blue. As the flow rate increases the flame height grows and the flame tip becomes yellow. Further increases in fuel flow rate result in the appearance of an orange zone. A subsequent increase in fuel flow rate leads to a critical value when soot escapes the luminous zone. The sooting tendency is typically quantified by measuring this critical smoke point height.

The measurement of smoke points of various fuels has been utilized to rank different fuels in order of increasing sooting tendencies; thus polyaromatics > aromatics > alkynes > alkenes > alkanes > alcohols [15]. Fuels with a greater tendency to soot emit smoke at lower fuel mass flow rates.

2.3.8 Effect of Pressure

The effect of pressure on soot formation in diffusion flames has been investigated over a wide range of conditions. Generally speaking, low pressures reduce carbon formation while high pressures promote it [14].

2.3.9 Influence of Additives

Dilution of fuel flow by addition of inert gases such as Ar, He and N_2 generally decreases the tendency to sooting [25]. If sufficient diluent is added, carbon luminosity can be suppressed altogether [26]. The possible reason for this is the substantial temperature reductions in flames in such situations.

When CO_2 or H_2O is added to the fuel, there is a considerable reduction in

soot-forming tendency [25] and a concentration of 45% CO_2 completely suppresses luminosity in methane/air diffusion flames [26]. McLintock [25] has suggested that the influence of CO_2 and H_2O is exerted primarily in the soot oxidation zone where these species presumably promote soot burnout.

Some additives promote soot formation. Foremost among these are the halogens, particularly bromine [18], [27]. It has been suggested that these species act by catalyzing radical recombination, thus neutralizing excess OH radicals which could otherwise oxidize soot or soot precursors [14].

2.3.10 Influence of Oxygen Addition

The effect of oxygen addition to the fuel is complex [14]. In ethylene flames, small additions result in pronounced increased soot emissions [18], [28]. The effect of the increasing yield is not purely thermal as it is far greater than that obtained at the same maximum flame temperature produced by oxygen enrichment of the air [14].

In the case of other fuels, both soot promotion and inhibition have been observed as the result of oxygen addition. Jones and Rosenfeld [29] concluded that ethylene is the exception and that, for fuels such as propane, butane, and even propylene, oxygen suppresses soot emissions.

2.4 Soot Models

A large number of experimental studies of soot formation and burnout in diffusion flames have been carried out in the last two decades or so. However the effort at developing suitable models for describing the soot processes in a flame has been relatively less [15]. In what follows we take a look at some of the important modeling efforts that have been undertaken.

Kennedy and coworkers [12] have proposed a soot formation model for laminar

diffusion flames based on a correlation between soot surface growth rates and the mixture fraction. Detailed chemistry was not used, instead the mixture fraction was calculated. The temperature, density and the gas composition were determined as functions of the mixture fraction. Axisymmetric, boundary layer forms of the momentum equation were numerically integrated along with the soot volume fraction equation. An energy equation was *not* solved. Oxidation by both molecular oxygen and OH were included in the model. The thermochemistry of the flame was determined from the results of a detailed laminar counterflow diffusion flame code. A constant soot number density was assumed. The calculations were carried out for the axisymmetric, laminar ethylene diffusion flame of [30]. Good agreement was obtained with the measurements for two different experimental conditions. However it was found that the decrease in temperature that occurs with radiative energy loss has a significant impact on the soot loadings in these flames. Therefore, a more thorough approach to the problem of accounting for radiation in a diffusion flame was deemed necessary.

In a subsequent work [31] the energy equation was solved along with the continuity, momentum and mixture fraction equations. A radiative loss term was included in the energy equation based on the assumption of the optically thin limit. Calculations were carried out for the axisymmetric laminar jet diffusion flame [30] and a Wolfhard-Parker two-dimensional flame [32]. The temperature, density, and viscosity were determined as functions of the mixture fraction and the enthalpy by using a type of constrained equilibrium chemistry model. Further work includes the prediction of sooting heights of laminar diffusion flames of Santoro *et al.* [30]. The agreement was good in all cases. Their results indicated that OH was the dominant oxidizer of soot low in the co-flow axisymmetric flames but as the flame tip was approached the oxidation by O_2 became more important.

Moss and coworkers have developed a two-equation model for soot processes in

laminar diffusion flames [1], [33]. They used a Wolfhard-Parker burner in both two- and three-slot configurations producing a substantially two-dimensional thin flame suitable for laser extinction measurements of soot volume fraction. The model parameters controlling the proposed rate processes for nucleation, surface growth and agglomeration were determined by a comparison between detailed model prediction and experimental measurement. Both prediction and experiment indicated that soot formation is restricted to a comparatively narrow range of mixture fractions (between 0.06 and 0.2). The model parameters incorporated in their analysis must be adjusted for each fuel. Predictions of the soot field were compared to experimental data obtained for laminar ethylene/air and methane/air diffusion flames. For methane/air diffusion flames it was observed that in contrast with ethylene/air diffusion flames the growth of soot volume fraction with height (and hence residence time) is non-linear.

Leung *et al.* [34] outlined a simplified reaction mechanism for the formation, growth and combustion of soot particles in laminar nonpremixed flames. The model was combined with detailed gas phase chemistry. The soot nucleation and growth reactions were linked to the gas phase by presuming that pyrolysis products, acetylene in their case, and not the fuel itself, are of primary importance in the soot formation process. The model involves the solution of two additional conservation equations for soot mass fraction and soot number density. They assumed that the number of active sites present locally in the flame is proportional to the square root of the total surface area available locally in the flame. The radiative heat loss is modeled in a simple manner by adjusting the adiabatic flame temperature by means of a heat loss factor. Model predictions were compared with the experimental data of Vandsburger *et al.* [35] for counterflow diffusion flames. The agreement was quite good.

2.5 Soot Radiation

Soot emits in a continuous spectrum in the visible and infrared regions and can often double or triple the heat radiated by the gaseous products alone [36]. For soot radiation scattering can be neglected compared to absorption [36]. Since soot particles are very small, they are generally at the same temperature as the flame [37]. An analysis of transient radiative cooling of a strongly radiating turbulent diffusion flame was carried out by Gore and Jang [8]. They mention that for strongly radiating flames, where up to 60 percent of the heat of reaction may be lost by radiation, a detailed treatment of the radiation heat transfer is needed. The radiative source term was expressed as the energy absorbed minus the energy emitted by a small local participating volume. The energy absorbed was calculated from the large-scale radiation field by integrating the flux over the surface of the small volume. The energy emitted depends on the temperature and absorption coefficient of the material in the small volume. Gas phase radiation was neglected and soot radiation was included using the Rayleigh approximation for soot particles. Two representative distributions of soot volume fractions were used. A unique flame structure involving an inflection point in the temperature profile near the soot layer was observed for strongly radiating flames. This is caused by the transfer of energy to the soot layer by diffusion from both sides balancing the high radiative loss.

In a later study Gore *et al.* [38] studied the structure of turbulent, non-premixed, strongly radiating acetylene/air flames. The analysis extended the laminar flamelet concept to include the effects of local radiative heat loss/gain. Measurements of mean and fluctuating emission temperatures and radiation intensities and data concerning flame structure were used to evaluate the predictions. Results showed good agreement between measurements and predictions of flame structure. In a related study [39] specific absorption coefficients of soot particles were reported in the infrared region

for three different fuels with varying C/H ratios.

A coupled radiation and soot kinetics calculation was carried out by Sivathanu and Gore [9] for laminar acetylene/air and acetylene-methane/air diffusion flames. The simplified soot model of Fairweather *et al.* [40] was used for the soot kinetics. The predicted soot volume fractions were found to be in reasonable agreement with measurements. It was found that the use of a constant radiative fraction in strongly radiating flames is not effective for predicting the observed trends in axial and radial distributions of soot volume fractions. The predicted temperature profiles support the structure of strongly radiating flames discovered earlier [8].

2.6 Diffusion Flames in Microgravity

In low gravity, or microgravity (μg), many combustion phenomena can be studied to yield more insight into the fundamental processes. Combustion in normal gravity creates buoyancy-induced flows through the production of hot gases, which are less dense than air. Suppressing such flows in microgravity helps researchers in several ways. First, the microgravity environment makes experiments easier to model, thus making it a better environment for testing theories. Second, the virtual elimination of buoyant flows permits the study of phenomena which are obscured by gravity.

An interesting case of microgravity diffusion flames pertains to the investigation of candle flames [41]. The ignition and behavior of candle flames was observed photographically in free-fall (drop tower) tests under $19\% - 25\%$ O_2 concentrations in a nitrogen-diluted, 1-atm environment. In normal gravity a candle flame assumes a tear-drop shape. However, in microgravity there is no "up" or "down" and the flame tends toward sphericity. In normal gravity, the buoyant flow removes combustion products from the primary reaction zone and supplies fresh oxidizer. For a microgravity candle flame this transport does not take place and consequently the supply of

fuel and oxidizer are diminished. Hence the flame temperature is lowered and the candle in microgravity produces a flame of much lower power. Due to diminished flame temperature, little or no soot forms. The soot in microgravity is confined within the fuel-rich region defined by the blue zone. In normal gravity, soot convects across the blue reactive zone which produces a much larger visible flame. It was also observed that the main reaction zone, as indicated by the visible blue region, is much farther away from the wick. This distance, referred to here as the flame standoff distance, gives an indication of the magnitude of the heat flux from the flame to the liquid fuel in the wick. In normal gravity, this distance is about 1 mm at the base of the flame; in microgravity it is about 5 mm.

However it will be presumptuous to conclude from these experiments that microgravity flames are in general less sooty than their normal gravity counterparts. As noted in [42] the observed microgravity diffusion flames are longer, wider and often sootier than their normal gravity counterparts. They are dimmer and more reddish, which indicates a lower flame temperature. It was also remarked in [42] that the thermal radiation from a microgravity flame and its surroundings can be an order of magnitude greater in microgravity than in normal gravity. However, at low oxygen concentrations, blue, soot-free flames appear in microgravity, whereas the identical normal gravity flames do not show any significant reduction in soot formation at low oxygen concentrations.

An excellent review of microgravity combustion research has been published recently [43]. It has been pointed out in the review that under atmospheric conditions, diffusion flames are buoyant and an increase in velocity is observed on moving away from the burner exit. However, for a weakly buoyant condition the velocity rapidly decays near the burner exit. The streamwise velocities are roughly inversely proportional to the distance from the burner exit for nonbuoyant flames. This tends to increase the effectiveness of soot oxidation processes relative to soot growth processes

for nonbuoyant flames in comparison with buoyant flames. Also, residence times in nonbuoyant flames are significantly higher than for buoyant flames of comparable size, providing longer absolute times for soot nucleation, growth and oxidation. Thus, it is remarked in [43] that "any resemblance between soot processes within nonbuoyant and buoyant laminar diffusion flames clearly is fortuitous".

The differences in soot processes of microgravity and normal gravity diffusion flames have been found to be very important in a recent work [44]. Experiments were conducted to investigate the behavior of soot particles in diffusion flames under microgravity conditions using a 490 m drop shaft (10 second microgravity duration) in Hokkaido, Japan. Butane jet diffusion flames and flames arising from the combustion of paper were observed in microgravity. The oxygen concentration of the surroundings, the butane flow rate, and the burner diameter were varied as experimental parameters. From the observation of transmission electron microscope (TEM) images it was found that a large number of luminous spots appear in diffusion flames in microgravity. The diameters of the agglomerated particles are approximately 0.1 mm, 200 to 500 times as large as those generated under normal gravity. These particles are the resultant agglomeration of a large number of primary particles. Local flow velocity, residence time of generated particles in the generation region, and oxygen concentration of the surrounding ambient dominate the agglomeration and growth of the soot particles. Therefore, these particles are formed in the limited areas of diffusion flames where the aforementioned conditions are satisfied. The investigation of [44] also verifies that microgravity diffusion flames have a much larger volume than those under normal gravity.

Interesting recent work on methane and ethylene flames has been done by Atreya *et al.* [45]. A small porous sphere made from a low density and a low heat capacity insulating material was used to uniformly supply fuel at a constant rate to the expanding diffusion flame. A theoretical model was formulated on the assumption

of infinite reaction rate and unity Lewis number. Both experimental and theoretical results show that as the flame radius increases, the flame expansion process becomes diffusion controlled and the flame radius grows as the square root of time.

In a related work Pickett *et al.* [46] studied the characteristics of methane, ethylene and acetylene flames. For the same flow rate of fuel the ethylene and acetylene flames were found to be much sootier and smaller. For all the fuels the flame is initially blue (non-sooty) but becomes bright yellow (sooty) under μg conditions. Later, as the μg time progresses, the flame grows in size and becomes orange and less luminous and the soot seems to disappear. An explanation of the above phenomenon was offered on the basis of some theoretical calculations. The soot volume fraction first quickly increases and later decreases as the local concentration of combustion products increases. Essentially, further soot formation is inhibited by the increase in the local concentration of the combustion products and soot oxidation is enhanced. Thus, at the onset of μg conditions, initially a lot of soot is formed in the vicinity of the flame front (the outer faint blue envelope) resulting in bright yellow emission. As the flame grows, several events reduce the flame luminosity: (i) the soot is pushed toward cooler regions by thermophoresis. In fact, for sootier fuels this leads to the formation of a soot shell, (ii) the high concentration of combustion products left behind by the flame front inhibits soot formation and promotes soot oxidation, (iii) the dilution and radiative heat losses caused by the increase in the concentration of combustion products reduces the flame temperature which in turn reduces the soot formation rate and flame luminosity.

CHAPTER 3

Influence of a Simple Heat Loss Profile on a Pure Diffusion Flame

3.1 Introduction

The interaction between the structure of a diffusion flame (DF) and the flame radiation is quite complex. As discussed in chapter 2, soot is formed and oxidized in a diffusion flame as a consequence of a variety of physical and chemical processes. There are considerable uncertainties in the description of soot processes in a flame and the soot evolution mechanisms are not completely understood. Hence, the solution of the complex problem of diffusion flame - soot radiation interaction is very involved. The energy, species and soot volume fraction equations are all coupled and contain nonlinear source terms. We chose not to solve the complex problem at the very outset. Instead, we investigated the effect of a simple and contrived heat loss profile on a pure diffusion flame established between two diffusing walls of fuel and oxidizer. This chapter is essentially the next logical step in the generalization of the model outlined in Appendix A.

A review of pure diffusion flames without heat losses is presented first. In the following sections we define the problem geometry, describe the particular form of

the heat loss profile used, formulate the conservation equations, briefly indicate the numerical method used and discuss the results.

3.2 Review of Pure Diffusion Flame Results

In a diffusion flame the characteristic flow time is much greater than the characteristic chemical reaction time. This implies that the chemical reaction is much faster than the transport of species to the flame unless the flame is near or approaching the extinction stage. A pure diffusion flame is established when both oxidizer and fuel are transported to the flame by means of diffusion only. No convective flow is present. Some important characteristics of pure diffusion flames have been discussed in [47]. Using the activation energy asymptotic (AEA) method [47] provides an analysis of the detailed nature of the temperature and reaction rate profiles. It was observed that the maximum of the reaction rate profile usually will not coincide with the temperature profile maximum. They may be close, and the maximum of the temperature will be in the vicinity of the maximum of reaction rate, but they will almost never coincide. The only exception is the symmetric flame for which the overall stoichiometric coefficient, $o(=\nu Y_{FF}/Y_{OO})$, equals unity. This study also shows for a fuel-rich flame that $Z_f \leq Z_r \leq Z_\tau$, i.e., the peak of the reaction rate profile (Z_r) lies between the Burke-Schumann flame location (Z_f) and the peak of the temperature profile (Z_τ) for fuel rich conditions. For oxidizer-rich conditions $Z_\tau \leq Z_r \leq Z_f$. It may be argued that in the thin-flame limit all diffusion flames are "pure" diffusion flames because the mixture fraction transformation discussed in Williams [48] produces an equation resembling $T_{ZZ} \propto |\nabla Z|^{-2} w$, where $|\nabla Z|$ is the magnitude of the mixture fraction gradient perpendicular to the flame. However, $|\nabla Z|$ depends strongly on the heat flow conditions and in effect introduces a new parameter that must be accounted for in a complete analysis. Hence, though the value of $|\nabla Z_f|$ (i.e., $|\nabla Z|$ evaluated at the

flame sheet) may be "buried" into a suitably redefined Damköhler number it must of course be "resurrected" when later conducting a full examination of the problem.

3.3 Problem Geometry

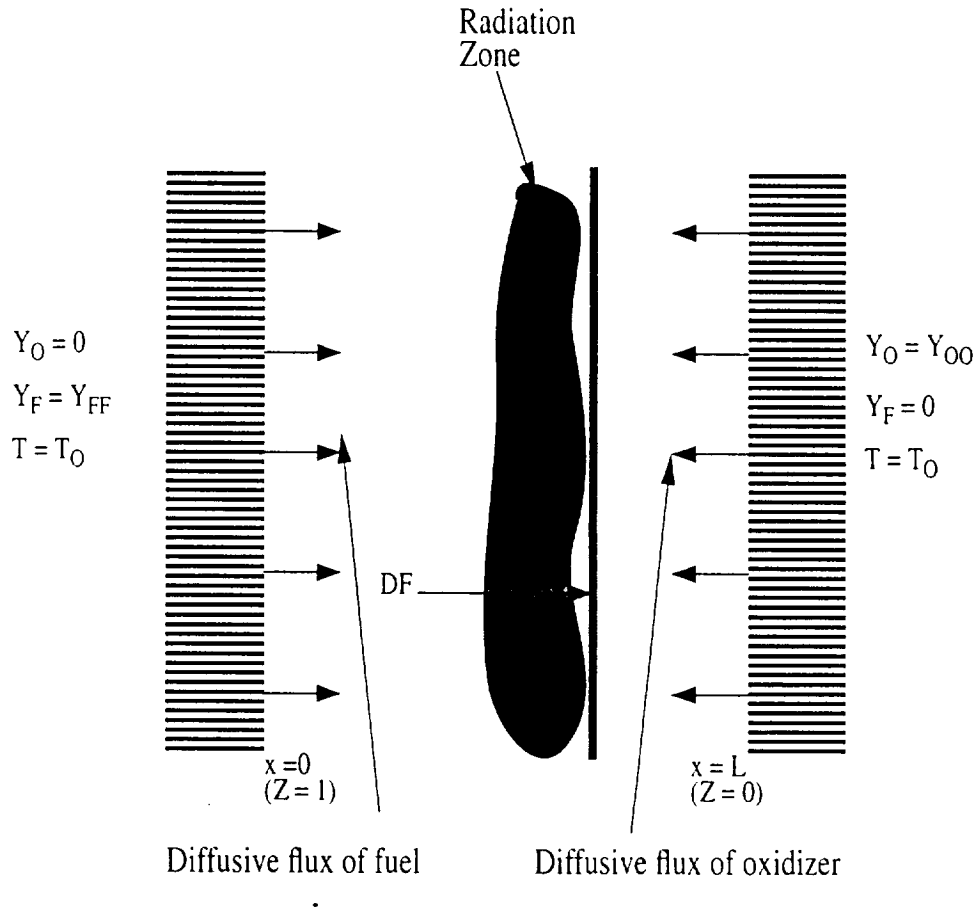

Figure 3.1. The problem geometry.

Figure 3.1 schematically depicts the problem geometry. The physical coordinate for our one dimensional problem is designated by x. The fuel wall and the oxidizer wall are located at $x = 0$ and $x = L$ respectively. Both the walls issue diffusive fluxes of the respective constituents. A diffusion flame is established between the two walls. A

soot layer is assumed to exist on the fuel-side of the DF, consistent with experimental observations [30]. The walls have the ambient temperature T_0. There is no fuel on the oxidizer wall and no oxidizer on the fuel wall. The fuel and oxidizer mass fractions at the respective walls are specified to have values Y_{FF} and Y_{OO} as shown in Figure 3.1.

3.4 Choice of Parameter values

The combustion reaction under consideration is assumed to be a global, one-step chemical reaction of the form $F + \nu O \rightarrow (1 + \nu)P$, where F denotes the fuel and O denotes the oxidizer. Methane is nominally the fuel under consideration and oxygen is the oxidizing specie, although we must recall that real methane-oxygen reactions require of the order of 100 reaction steps and individual property choices for the separate species. The fuel-oxidizer mass ratio, ν, is four for the methane-oxygen combustion reaction. The combustion products are denoted by P. A suitable set of parameter values must be used to generate a reasonable range of Damköhler number and flame temperature values. The adiabatic flame temperature is given by $T_f = T_0 + Q_F Y_{FF}/[C_p(1 + \phi)]$, where Q_F is the heat release per unit mass of fuel from the combustion reaction and C_p is the specific heat of the mixture. The overall stoichiometric coefficient is denoted by ϕ and is given by $\nu Y_{FF}/Y_{OO}$. However, the use of the above formula produces unrealistically high adiabatic flame temperature values. Thus, the above equation for T_f was modified to produce a practical range of adiabatic flame temperatures.

A set of realistic hydrocarbon combustion flame temperatures was used from the work of Wichman [49] for the analysis of flame spread over thermoplastics. The idea there was that the fuel mass fraction can not reasonably be determined at the surface but a more-or-less generic flame temperature can still be evaluated. This flame temperature varies only with the free-stream oxidizer mass fraction Y_{OO}. The

value of Y_{FF}, i.e., the fuel mass fraction in the hypothetical fuel stream for our present calculations was assumed to be 0.85. The oxidizer mass fractions (Y_{OO}) and the flame temperatures (T_f) are tabulated in Table 3.1.

Table 3.1. Flame Temperature versus Y_{OO} data

Y_{OO}	0.211	0.233	0.247	0.276	0.329	0.432	0.533	0.727	1.0
T_f	2137	2230	2295	2385	2515	2684	2789	2919	3026

A fourth order polynomial was fitted to the above data to obtain

$$T_f = 486.66 + 12230.85Y_{OO} - 25728.64{Y_{OO}}^2 + 25360.02{Y_{OO}}^3 - 9323.0{Y_{OO}}^4 \quad (3.1)$$

Using the above expression, we generate more points for a (Y_{OO},T_f) plot.

We calculate Q_F by using the relation $Q_F = (T_f - T_0)C_p(1 + o)/Y_{FF}$ for T_f = 2137 K, Y_{OO} = 0.211, Y_{FF} = 0.85 and T_0 = 298 K. The calculated value of Q_F is 11959.43 KJ/kgK. We now introduce a modified formula for calculation of the flame temperature and write

$$T_f = T_0 + \frac{Q_F Y_{FF} f(Y_{OO})}{C_p(1 + o)} \quad (3.2)$$

Next we calculate the values of the modification factor, $f(Y_{OO})$, by using the above expression. The calculated value of Q_F and the (Y_{OO}, T_f) data obtained using equation 3.1 were utilized for this purpose. On obtaining $f(Y_{OO})$ data, we use an exponential fit of the following form to arrive at a functional relationship between f and Y_{OO}:

$$f = 1.25\exp(-2.99Y_{OO}) + 0.33 \quad (3.3)$$

Finally, we use the above expression for $f(Y_{OO})$ to calculate T_f for any set of Y_{OO} and Y_{FF} values in equation 3.2. A plot of T_f versus Y_{OO} is shown in Figure 3.2. The

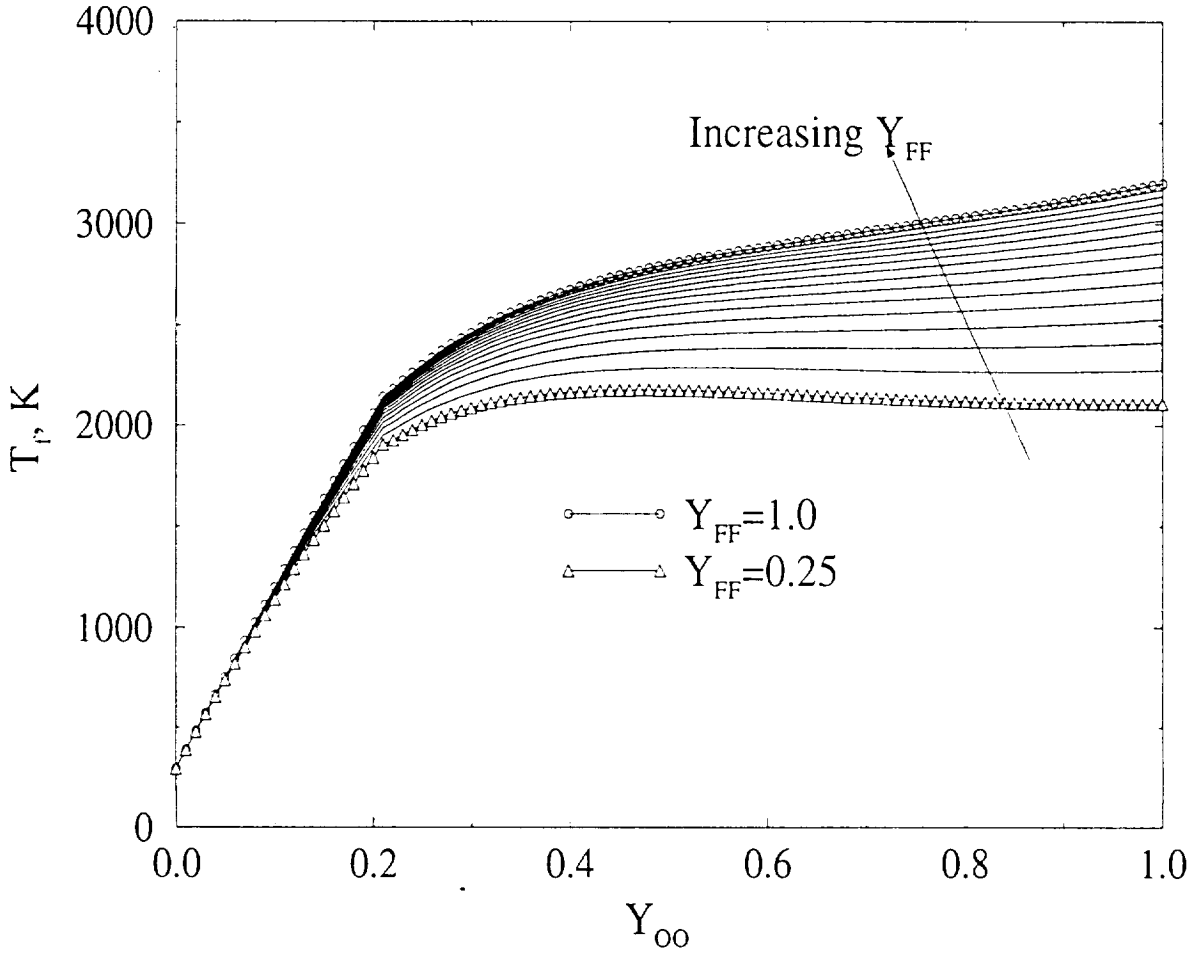

Figure 3.2. Flame Temperature as a function of Y_{OO} for different values of Y_{FF}.

Y_{FF} values corresponding to the different curves in the plot range from 0.25 to 1.0. The lowest curve is for $Y_{FF} = 0.25$. The curves above are for $Y_{FF} = 0.30, 0.35, 0.40$ etc. It has to be noted that for $Y_{FF} = 0.25$ and 0.30 the peak flame temperature does not occur at $Y_{OO} = 1$ because of the slight local maximum in the range $0 < Y_{OO} < 1$. For this reason we shall not use these curves. However, for higher values of Y_{FF} we do obtain temperature profiles whose maxima occur at $Y_{OO} = 1$. These profiles will be used. Also, we note that since we are interested in the effect of soot radiation on diffusion flames, we are not concerned with low values of Y_{FF} which do not produce significant amounts of soot. Hence, in our analysis, Y_{FF} values of 0.30 and lower are not used.

The parameter values in the work of Tzeng *et al.* [50] were used in this dissertation. The important values are shown in Table 3.2. These values were used in all

Table 3.2. Parameter values

Specific heat	C_p	1.35	J/kgK
Thermal diffusivity	α_0	1.24×10^{-4}	m^2/s
Fuel-oxidant mass ratio	ν	4.0	
Pre-exponential factor	A	5×10^7	$1/s$
Activation energy	E	121, 841.7	$KJ/kmol$
Heat release	Q_F	11959.43	KJ/KgK

the chapters of this dissertation except for the pre-exponential factor in chapter 6, as noted in section 6.2.

3.5 Formulation

Here we write the equations and boundary conditions for conservation of energy and species. The energy conservation equation is

$$\rho C_p[T_t + uT_x] = (\lambda T_x)_x + Q_F \dot{w}_F - \frac{dq_R}{dx}. \tag{3.4}$$

with boundary conditions $T(x = 0) = T_0$ and $T(x = L) = T_0$, where T_0 is the temperature at the fuel and oxidizer walls, assumed to be 298 K. Here T is the temperature, ρ is the density, C_p is the specific heat of the mixture, λ is the thermal conductivity and u is the velocity. The volumetric radiative heat loss term is $-dq_R/dx$ with units W/m^3. The heat release due to combustion is Q_F and $\dot{w}_F$ is the reaction rate term. An Arrhenius type expression was assumed for the one-step irreversible reaction, so the reaction rate is $\dot{w}_F = \rho A Y_O Y_F \exp -E/RT$. The quantity A denotes the pre-exponential factor. The thermal conductivity is λ. The oxidizer mass fraction equation is

$$\rho[Y_{O_t} + uY_{O_x}] = (\rho D_O Y_{O_x})_x - \nu \dot{w}_F. \tag{3.5}$$

with boundary conditions $Y_O(x = 0) = 0$ and $Y_O(x = L) = Y_{OO}$. Here D_O is the mass diffusivity of the oxidizer. Similarly the fuel mass fraction equation is

$$\rho[Y_{F_t} + uY_{F_x}] = (\rho D_F Y_{F_x})_x - \dot{w}_F, \tag{3.6}$$

with boundary conditions $Y_F(x = 0) = Y_{FF}$ and $Y_F(x = L) = 0$; D_F is the mass diffusivity of the fuel.

The above equations are now transformed to a mass coordinate system. The transformed coordinate is $Z = 1 - s/s_0$ where $s = \int_0^x \rho dx$ and $s_0 = \int_0^L \rho dx$. We note that $Z = 1$ when $x = 0$ and $Z = 0$ when $x = 1$. The coordinate Z happens to be

identical to the mixture fraction coordinate for our simple problem. The following expressions hold for the above transformation:

$$\frac{\partial}{\partial t}|_x = [-\frac{1}{s_0}((\rho u)_0 - (\rho u)_x) + \frac{s}{s_0^2}((\rho u)_0 - (\rho u)_L)]\frac{\partial}{\partial Z}|_t + \frac{\partial}{\partial t}|_Z \tag{3.7}$$

and

$$\frac{\partial}{\partial x}|_t = -\frac{\rho}{s_0}\frac{\partial}{\partial z}|_t \tag{3.8}$$

Since we are considering a pure diffusion flame, $(\rho u)_{x=0} = (\rho u)_{x=L} = 0$, i.e., there are no convective flows from the walls. Application of these operators to the energy and species equations gives

$$T_t = \frac{\rho\lambda}{C_p s_0^2}T_{ZZ} + \frac{Q_F}{\rho C_p}\dot{w}_F + \frac{1}{C_p s_0}\frac{dq_R}{dZ}, \tag{3.9}$$

assuming $\rho\lambda$ to be a constant.

$$Y_{Ot} = \frac{\rho_0{}^2 D_{O0}}{s_0{}^2}Y_{OZZ} - \frac{\nu\dot{w}_F}{\rho}. \tag{3.10}$$

assuming $\rho^2 D_O$ to be a constant, and

$$Y_{Ft} = \frac{\rho_0{}^2 D_{F0}}{s_0{}^2}Y_{FZZ} - \frac{\dot{w}_F}{\rho}, \tag{3.11}$$

assuming $\rho^2 D_F$ to be a constant. In equations (3.9)-(3.11), we have also assumed the Lewis number to be unity and we have considered equal species diffusivities. The quantities with subscript 0 correspond to the reference condition.

We now introduce the nondimensional variables $\tau = (T - T_0)/(T_f - T_0)$, $y_O = Y_O/Y_{OO}$, $y_F = Y_F/Y_{FF}$, $\bar{s} = s/(\rho_0 L)$. Consequently, $\bar{s}_0 = s_0/(\rho_0 L) = \int_0^1 \bar{\rho} d\bar{x}$ where $\bar{\rho} = \rho/\rho_0$ and $\bar{x} = x/L$. After some rearrangement, our nondimensional equations

simplify to

$$\tau_{\bar{t}} = \frac{1}{\bar{s}_0^2}\tau_{ZZ} + \bar{Q}_F \mathcal{D} r + \frac{N_R}{\bar{s}_0}\frac{d\bar{q}_R}{dZ}, \tag{3.12}$$

$$y_{O\bar{t}} = \frac{1}{\bar{s}_0^2} y_{OZZ} - \phi \mathcal{D} r, \tag{3.13}$$

$$y_{F\bar{t}} = \frac{1}{\bar{s}_0^2} y_{FZZ} - \mathcal{D} r, \tag{3.14}$$

where r is the nondimensional reaction rate and N_R is a radiation number evaluated as the ratio of the reference radiative and conductive fluxes, given by $N_R = q_{R,ref}/(\lambda_0(T_f - T_0)/L)$. The thermal conductivity at the reference condition is denoted by λ_0. The quantity $\mathcal{D}$ is the Damköhler number given by t_{ref}/t_{chem}, where the reference diffusion time $t_{ref} = L^2/\alpha_0$ and the characteristic chemical time $t_{chem} = 1/[AY_{OO}\exp(-E/RT_f)]$. The nondimensional quantity $\bar{q}_R$ is given by $q_R/q_{R,ref}$, where $q_{R,ref}$ is a reference radiative heat flux. The nondimensional heat release, $\bar{Q}_F$, is given by $Q_F Y_{FF}/[C_p(T_f - T_0)]$ and equals $(1 + \phi)$ since the adiabatic flame temperature is defined as $T_f = T_0 + Q_F Y_{FF}/[C_p(1 + \phi)]$. We note that in the prefactor multiplying the reaction term of equation 3.12 we do not utilize the temperature correction discussed in section 3.4. In addition, we have defined $\bar{t} = t/t_{ref}$. The nondimensional reaction term, r, is written in the form $r = y_O y_F \exp[-\beta(1-\tau)/(1-\alpha(1-\tau))]$, where $\alpha = 1 - T_0/T_f$ and $\beta = E\alpha/(R_u T_f)$; E is the activation energy and R_u is the universal gas constant. The quantity β is known as the Zeldovich number.

3.5.1 Infinite Reaction Rate (IRR) Solutions as Initial Conditions

Equations 3.12-3.14 are the governing conservation equations for τ, y_O and y_F for the case of finite rate chemistry. The equations become much simpler when the reaction rate is infinite. In this case, all fuel reaching the flame surface is consumed instantaneously, and similarly for the oxidizer. Thus no fuel exists on the oxidizer

side and no oxidizer exists on the fuel side, i.e., $y_O y_F = 0$ on both sides of the flame. The energy equation can now be solved in two adjacent domains, the oxidizer side ($0 \leq Z \leq Z_f$) and the fuel side ($Z_f \leq Z \leq 1$) of the flame. The flame location is designated by Z_f. For our simple problem the mass coordinate Z coincides with the mixture fraction, a conserved scalar. In the absence of radiative losses the steady state energy equation becomes $\tau_{ZZ} = 0$. Since at the flame $\tau = 1$, the solution of the steady state energy equation ($\tau_{ZZ} = 0$, since $N_R = 0$ and the reaction term can be excluded) for the infinite reaction rate (IRR) situation gives $\tau = Z/Z_f$ for $0 \leq Z \leq Z_f$ and $\tau = (1 - Z)/(1 - Z_f)$ for $Z_f \leq Z \leq 1$. Similarly, y_O and y_F can be solved for the infinite reaction rate situation and we get $y_O = (1 - Z) - (1 - Z_f)\tau$ for $0 \leq Z \leq Z_f$ and $y_F = Z - Z_f \tau$ for $Z_f \leq Z \leq 1$.

Next, we must evaluate Z_f, the coordinate location of the (IRR) flame. As mentioned, Z is the mixture fraction coordinate, defined as $Z = (\phi y_F + 1 - y_O)/(\phi + 1)$. At the flame, y_O and y_F are both zero so that $Z_f = 1/(\phi + 1)$. With the knowledge of Z_f the nondimensional temperature and species equations can all be determined exactly. The profiles so obtained are used as initial profiles for the numerical solution of the transient conservation equations (3.12)-(3.14).

3.5.2 Simple Heat Loss Profile

As shown in Appendix A the-simplest model heat loss profile is the "top hat" profile used therein. Because of the discontinuous derivatives at the edges of the top hat profile, it is not as convenient for numerical reasons as a smooth and continuous heat loss profile. For primarily this reason, the profile that we shall use here is of the form of a $sech^2$ in mixture fraction space, viz.,

$$-\frac{d\bar{q}_R}{dZ} = sech^2(B(Z - Z_R)). \tag{3.15}$$

The location where the maximum of $-d\bar{q}_R/dZ$ occurs is denoted by Z_R.

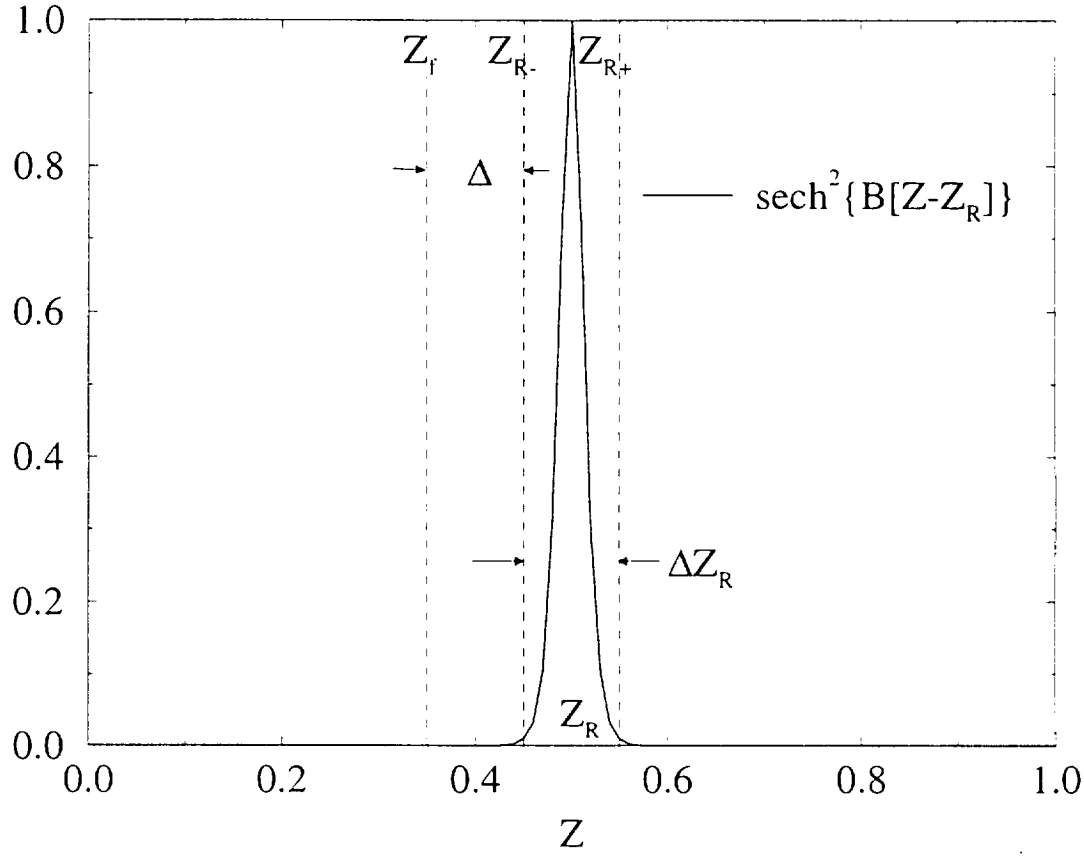

Figure 3.3. The chosen heat loss profile of the form of a $sech^2$.

Figure 3.3 illustrates the nature of variation of the heat loss profile in the mixture fraction space. We note that the maximum value of the profile is unity. We define the Z locations where the value of the function is 1% of its peak value as the two tails of the function, located respectively at Z_{R-} and at Z_{R+}, with $Z_{R-} < Z_{R+}$. The maximum of the $-d\bar{q}_R/dZ$ profile occurs at $Z_R = (Z_{R-} + Z_{R+})/2$. The width of the loss zone is defined to be $\Delta Z_R = Z_{R+} - Z_{R-}$. The separation distance of the loss zone from the location of the ideal Burke-Schumann flame Z_f is given by $\Delta = Z_{R-} - Z_f$. In the subsequent analysis, we shall vary the thickness ΔZ_R, as well as the separation

distance Δ in order to study the influence of the loss zone on the flame structure. The thickness of the loss zone can be chosen by selecting different values of the parameter B in equation 3.15.

From equation 3.12 we note that the radiative loss term is given by $(N_R/\bar{s}_0)d\bar{q}_R/dZ$, and hence, another important way to modify the loss term is to experiment with the value of its amplitude, $N_R/\bar{s}_0$. We can choose different values of N_R, the radiation number. The quantity $\bar{s}_0$, being given by $s_0/(\rho_0 L)$ is a consequence of the solution obtained and for this reason is evaluated at each time step.

We recall that for the top hat profile the integrated heat loss is $\int_0^1 (N_R/\bar{s}_0)(U(Z_{R-}) - U(Z_{R+}))dZ = N_R \Delta Z_R$. In this case the integrated heat loss is given by $\int_0^1 N_R sech^2[B(Z - Z_R)]dZ = N_R/(B\bar{s}_0)[tanhB(1 - Z_R) + tanhBZ_R]$. For large B this simplifies to $2N_R/B + O(B^{-2})$ showing that the top-hat loss zone thickness ΔZ_R corresponds to $2/B$, or $B = 2/\Delta Z_R$. Consequently, in analytical formulæ for the top-hat profile (see Appendix A, equation A.40) we can substitute for ΔZ_R the value $2/B$ in order to test their correspondence to the $sech^2$ profile.

3.6 Numerical Solution

Equations 3.12, 3.13 and 3.14 were numerically solved using the finite difference method. The nonlinear source terms were linearized using Newton's method. For each time step iterations were used until the sum of normalized residuals became smaller than 1×10^{-6}. The transient conservation equations were integrated to steady state.

3.7 Relation Between Temperature and Density

We utilize the ideal gas law to derive a relation between the temperature and density of the system. We can write $pV = (m/\bar{W})R_uT$ where p is the pressure, V is the volume, R_u is the universal gas constant and $\bar{W}$ is the average molecular weight of the mixture. The quantity m is the mass of the mixture. Hence the pressure can be expressed as $p = \rho RT$ where ρ is the density and R is the *characteristic* gas constant for the mixture, given by $R = R_u/\bar{W}$. If we assume $\rho_0 RT_0$ to be the constant pressure of the system then introduction of $\alpha = 1 - T_0/T_f$ and $\tau = (T - T_0)/(T_f - T_0)$ results in the following important relation:

$$\bar{\rho} = \frac{(1-\alpha)}{(1-\alpha(1-\tau))} \tag{3.16}$$

We observe that when the temperature is that of the ambient, i.e., $T = T_0 = 298\ K$ then $\tau = 0$, $\bar{\rho} = 1$, i.e., $\rho = \rho_0$. At the flame temperature (T_f) the nondimensional density $\bar{\rho} = (1-\alpha)$ and consequently $\rho = (1-\alpha)\rho_0$. Equation 3.16 is used extensively in all the chapters of this dissertation.

3.8 Evaluation of $\bar{s}_0$

Equations 3.12-3.14 indicate that in order to solve the τ, y_O and y_F equations in time, we need to evaluate $\bar{s}_0$ at every time step. We recall that $\bar{s}_0$ is given by the expression $\int_0^1 \bar{\rho} d\bar{x}$. The quantity $\bar{s}_0$ enters the analysis by virtue of the coordinate transformation $Z = 1 - \bar{s}/\bar{s}_0$. By differentiating both sides of this transformation relation, we obtain $dZ/d\bar{x} = -\bar{\rho}/\bar{s}_0$, since $\bar{s} = \int_0^{\bar{x}} \bar{\rho} d\bar{x}$ and $\bar{x} = x/L$. We recall that $Z = 1$ when $\bar{x} = 0$ and $Z = 0$ when $\bar{x} = 1$, as noted previously in section 3.5. Using the transformation relation between Z and $\bar{x}$ subject to the above mentioned boundary conditions, we

get

$$\bar{s}_0 = \frac{1}{\int_0^1 \frac{1}{\bar{\rho}} dZ}. \tag{3.17}$$

and the relation between the $\bar{x}$ and Z coordinates can be written as

$$\bar{x} = \frac{\int_Z^1 (1/\bar{\rho}) dZ}{\int_0^1 (1/\bar{\rho}) dZ} \tag{3.18}$$

On obtaining the solutions for τ, y_O and y_F equation 3.18 is used to transform the solutions back to the physical coordinate $\bar{x}$. Thus, $\bar{s}_0$ can be evaluated once the $\bar{\rho}$ distribution is known. The normalized density $\bar{\rho}$ can be related to the τ distribution by virtue of equation 3.16. Hence, the expression for $\bar{s}_0$ can alternatively be written as

$$\bar{s}_0 = \frac{1}{\int_0^1 dZ + (\alpha/(1-\alpha)) \int_0^1 \tau dZ} \tag{3.19}$$

Hence on obtaining the τ profile we can determine the quantity $\bar{s}_0$. When the temperature throughout the domain is the same as the ambient temperature T_0, then $\tau = 0$ everywhere and using equation 3.19, we obtain $\bar{s}_0 = 1$. If we next assume that the temperature everywhere in the domain is the same as the adiabatic flame temperature T_f then $\tau = 1$ and $\bar{s}_0 = (1 - \alpha)$. Since the minimum and maximum values of temperature are T_0 and T_f respectively, the quantity $\bar{s}_0$ must obey the limits $(1 - \alpha) \leq \bar{s}_0 \leq 1$.

3.9 Results and Discussion

Figure 3.4 depicts the nondimensional temperature, τ, plotted as a function of the mixture fraction coordinate, Z, for different values of the radiation number, N_R, for particular parameter values shown in the title of the figure. The oxidizer and fuel mass fractions at the respective walls are $Y_{OO} = 0.6$ and $Y_{FF} = 0.8$. In our

subsequent analysis we keep the same set of (Y_{OO}, Y_{FF}) and vary the location, width and intensity of the radiative loss zone. It has to be mentioned here that the above set of (Y_{OO}, Y_{FF}) represents a typical case and is employed extensively in the following chapters. The qualitative trends for other Y_{OO} and Y_{FF} values are similar. The

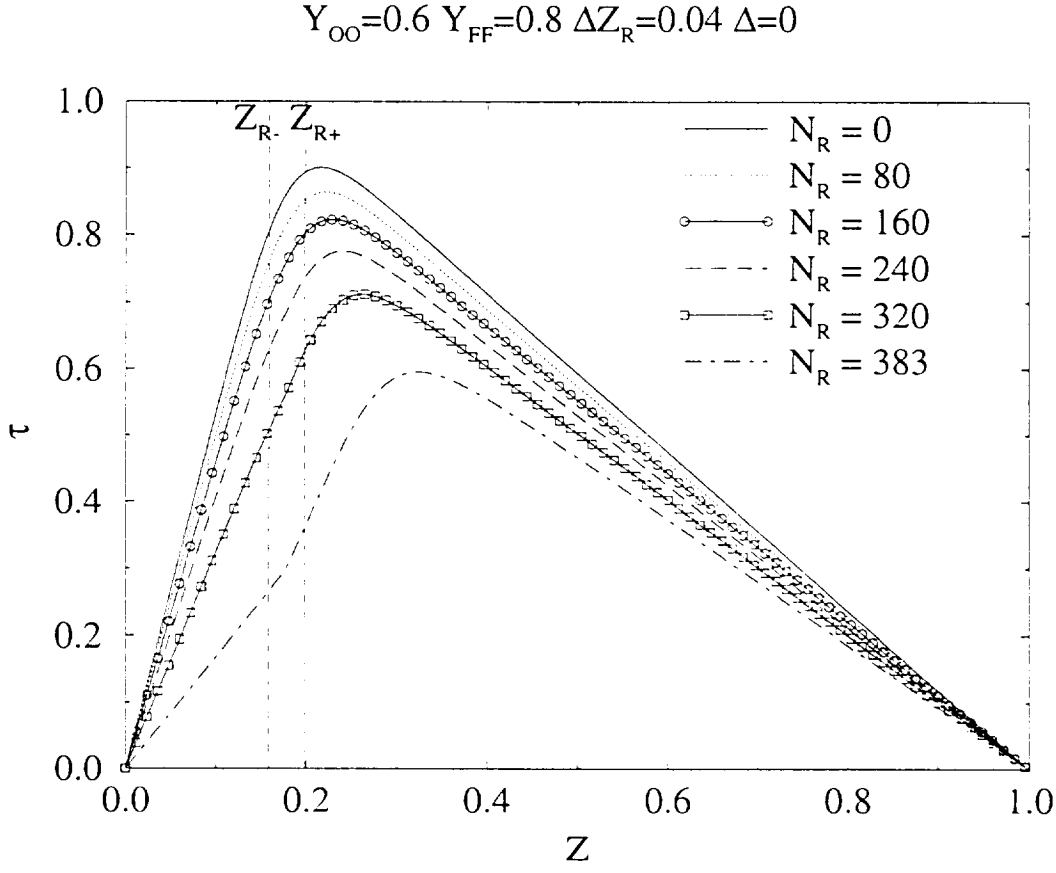

Figure 3.4. Effect of Radiation Number N_R on Temperature Profile.

thickness of the radiative loss zone is 0.04 for all values of N_R and the separation distance of the loss zone from the stoichiometric flame location is zero. We observe that the flame temperature profile is uniformly lowered as the value of N_R increases. Also, the flame temperature peak keeps moving toward the fuel wall as the value of N_R is increased. The drop in flame temperature, as well as the shift of the peak,

become more prominent for higher values of N_R. For a value of N_R greater than 383, we do not obtain a steady state temperature profile, indicating the occurrence of a radiative extinction. This maximum or upper bound for N_R is then defined as $N_{R,extinction}$, i.e., $N_{R,extinction} = 383$ for this case. We also note from Figure 3.4 that there is a change of slope of the temperature profile in the radiative loss zone for higher values of N_R, i.e., between Z_{R-} and Z_{R+}.

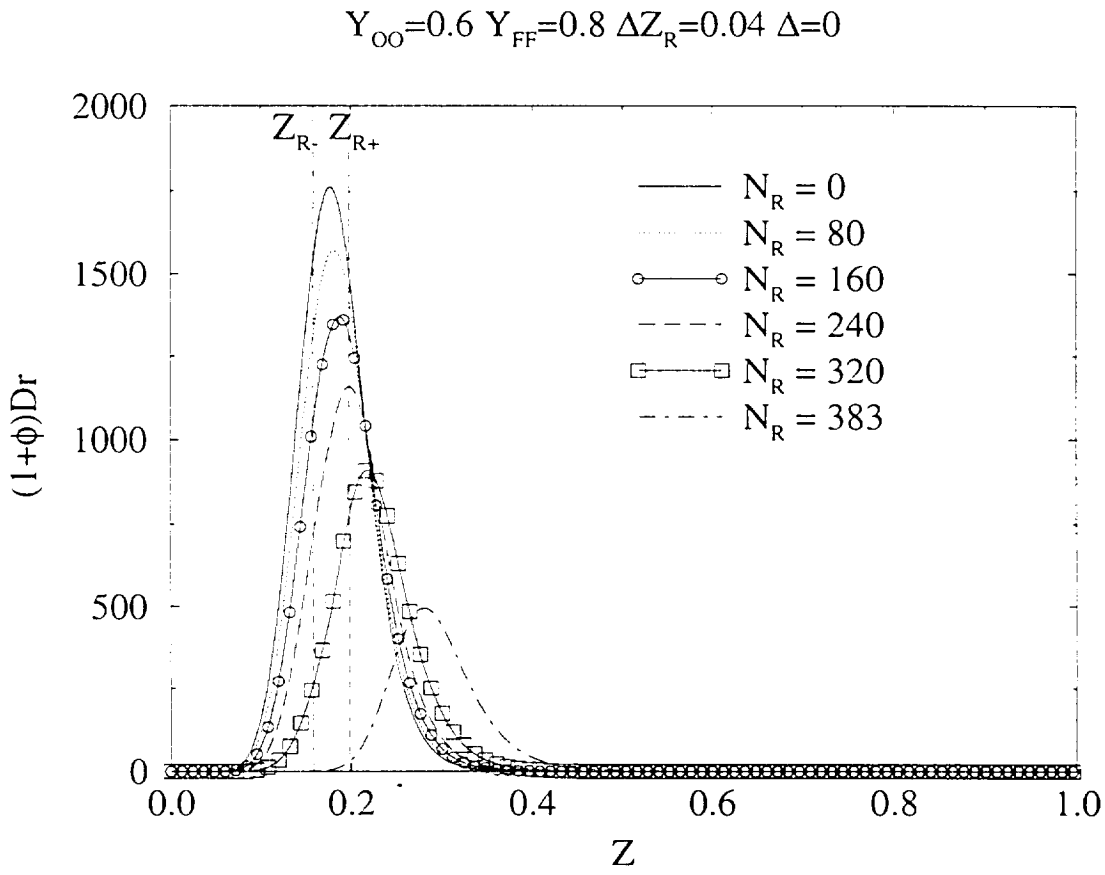

Figure 3.5. Effect of Radiation Number N_R on Reaction Rate.

Figure 3.5 shows the nondimensional reaction rate term $((1+\phi)\mathcal{D}r)$ for the same situation. We observe that the reaction rate profile collapses for increasing N_R values.

The reaction rate peak also moves towards the fuel side; this movement becomes more conspicuous for higher values of N_R. We notice that the reaction rate profile has managed to almost move beyond the rightmost side of the radiation loss zone (indicated by the dashed lines at Z_{R-} and Z_{R+}) for the highest value of N_R.

We now focus on the temperature and species profiles for the situation when $N_R = 383$ for the above case, i.e., at the brink of extinction. Figure 3.6 also shows

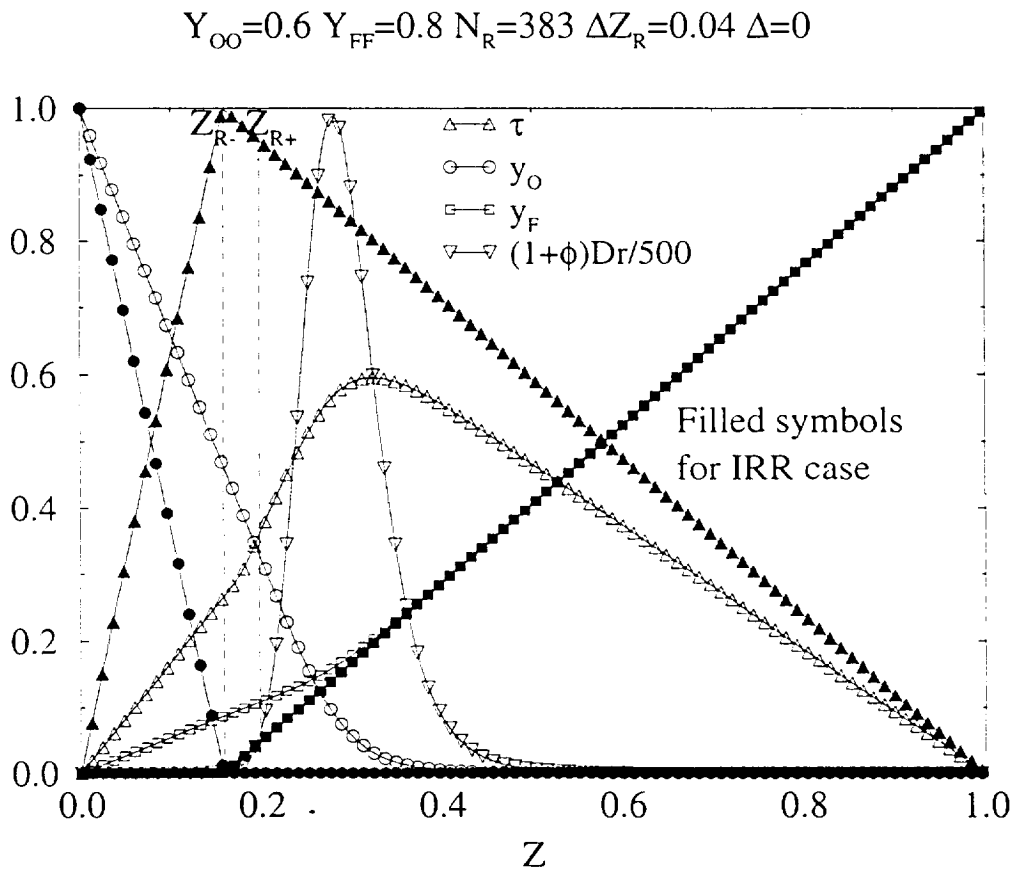

Figure 3.6. τ, y_O, y_F profiles for finite and infinite reaction rates. Also shown is the reaction rate profile.

the temperature and species profiles for the same flame ($Y_{OO} = 0.6$, $Y_{FF} = 0.8$, $N_R = 0$) for the infinite reaction rate (IRR). We notice that when $N_R = 383$ the

slope of the y_O profile is quite different from its IRR counterpart. On the other hand, the slope of the y_F profile follows the IRR y_F profile closely until a Z-value of about 0.3, when its slope starts decreasing. This plot therefore demonstrates explicitly the contrast between the IRR situation and the finite chemistry situation with appreciable radiative losses. The migration of the peaks of temperature and reactivity profiles is particularly striking. Also, an abrupt change of the temperature profile seems to take place in the zone of radiative losses, i.e., between Z_{R-} and Z_{R+}. We add for emphasis that from the strictly physical viewpoint the finite-rate solution has attained a rather extreme form, since the reaction zone has almost completely propagated through the loss zone. In Figure 3.6 we see that the loss zone is now on the oxidizer side of the reaction rate profile. As we shall see, extreme cases like this are not the norm. They are also physically unrealistic but mathematically permissible in our simplified model with a prescribed heat loss function.

We illustrate the details of the flame structure in Figure 3.7, where we plot the contributions of the different terms in the energy equation when the steady state solution has been achieved. The loss term is given by $(N_R/\bar{s}_0)sech^2(B(Z-Z_R))$ and the diffusion term, as in equation 3.12, is $(1/\bar{s}_0^2)\tau_{ZZ}$. We have already noted from figure 3.5 that for $N_R = 383$ the reaction rate profile has penetrated through the radiative loss zone. Figure 3.7 indicates that the diffusion term recovers the radiative losses almost entirely and the reaction term doesn't contribute to the diffusion term in such a recovery process. This represents a completely different physical problem, when the radiative loss term exists on the oxidizer side of the primary reaction zone (flame). This result is, as already mentioned, clearly in conflict with our hypothesis that the heat losses take place on the fuel side of the flame due to flame-generated particulates. This occurs because our hypothetical radiative loss profile is simply a prescribed function in Z, and as such, it does not contain any mechanism for loss-

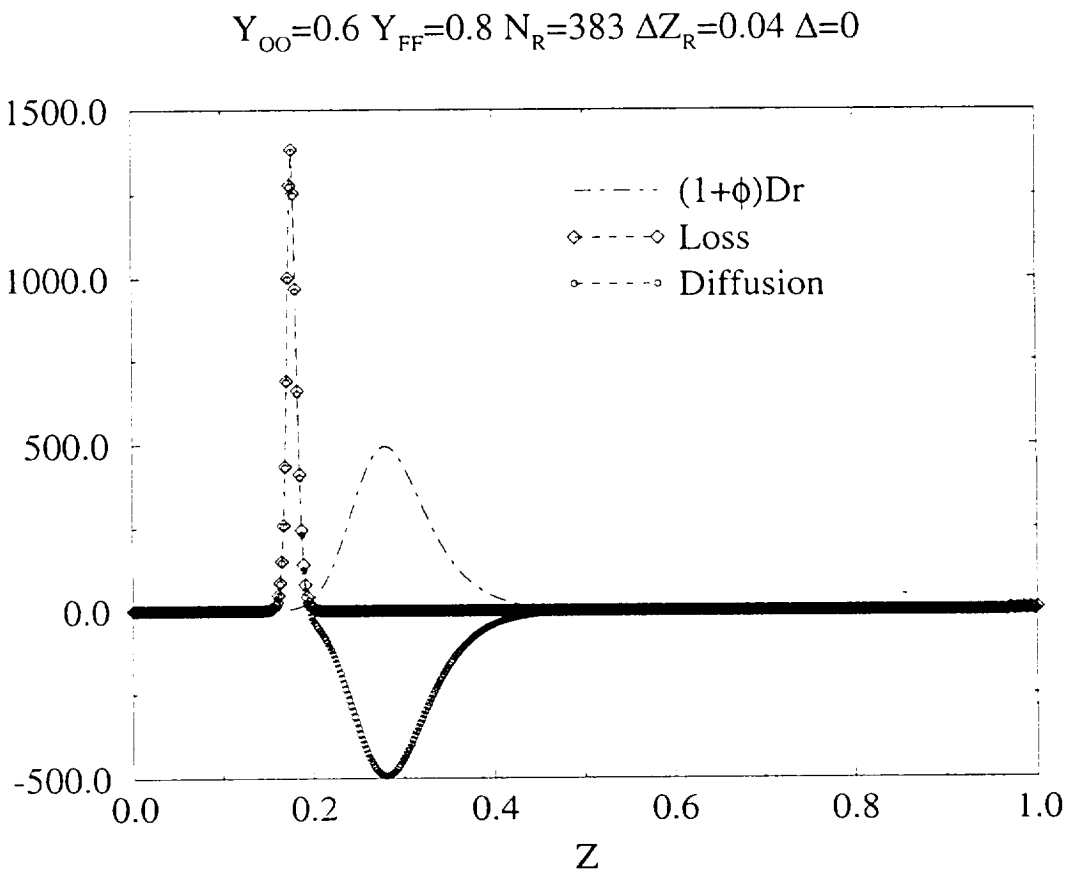

Figure 3.7. The flame structure when $N_R = 383$.

zone movement as the temperature and species profiles change, as a real soot zone invariably must.

In order to observe the effect of a thicker loss zone, we now increase ΔZ_R to a value of 0.1. We notice that the drop in the temperature profile is more significant

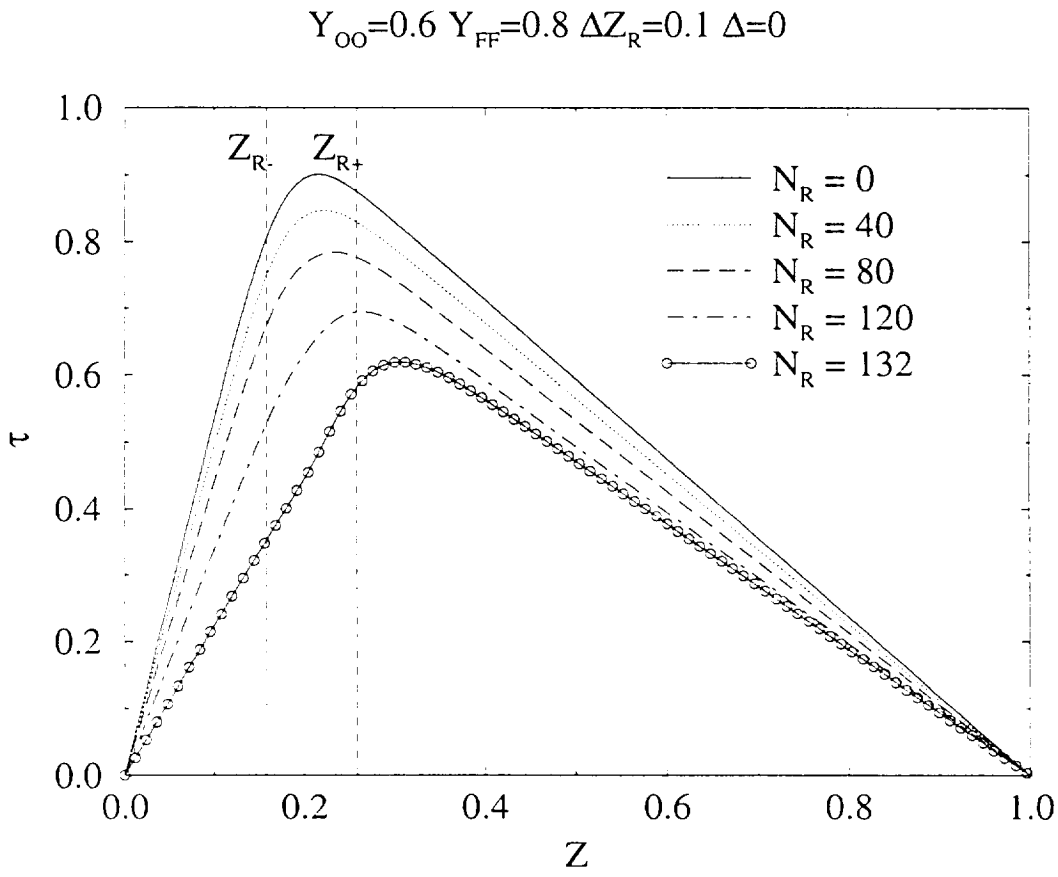

Figure 3.8. Effect of N_R on τ profile for thicker loss zone.

in this case and the flame extinguishes at a lower value of the radiation number, viz., for $N_R = 132$.

Next we consider the situation when the leftmost side of the loss zone is sufficiently removed from Z_f for a flame with $Y_{OO} = 0.6$ and $Y_{FF} = 0.8$. The thickness of the loss zone is $\Delta Z_R = 0.06$ and the separation distance, Δ, is 0.1 in this case. Figure 3.9

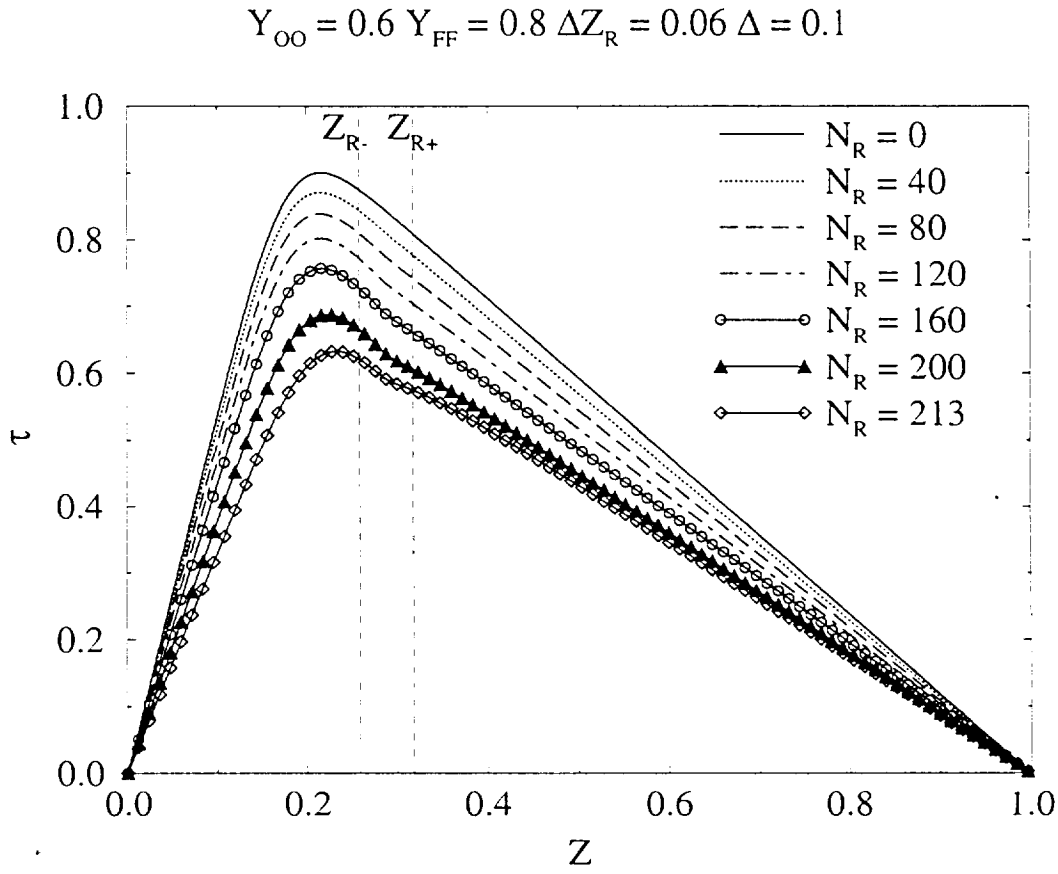

Figure 3.9. Effect of N_R on τ profile for $\Delta = 0.1$.

indicates that the flame temperature decreases with increasing value of N_R. In this case, however, the movement of the peak nondimensional flame temperature doesn't seem very pronounced, though it *does* move towards the fuel side. Correspondingly, Figure 3.10 shows the variation of the reaction term, $(1+\phi)\mathcal{D}r$ for increasing values of N_R. As mentioned for the preceding cases, therefore, the reaction zone does not always propagate through the loss zone. A sufficient separation and magnitude of the loss term appear sufficient to prevent the through-transit.

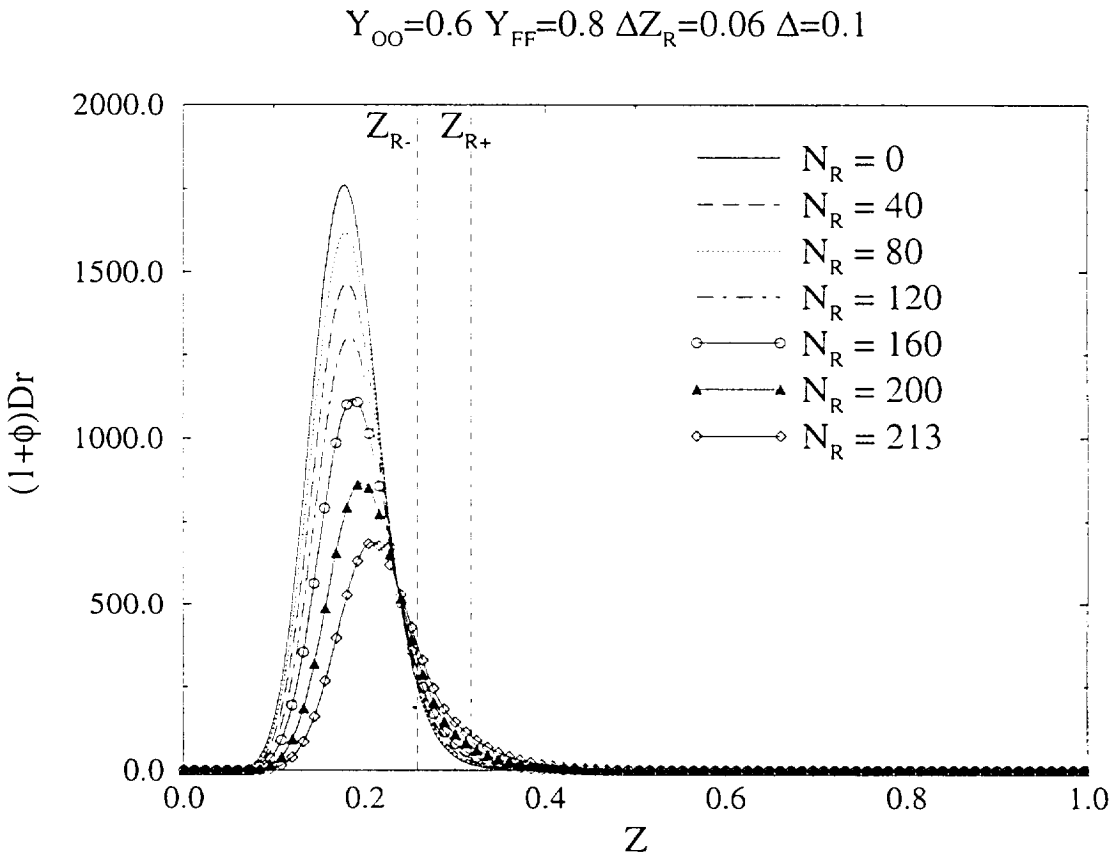

Figure 3.10. Effect of N_R on $(1+\phi)\mathcal{D}r$ profile for $\Delta = 0.1$.

We see that the movement of the reaction rate profile is not very pronounced

either. We note that the reaction rate peak is always to the left of the temperature peak, i.e., $Z_f < Z_r < Z_\tau$. This is in accordance with the results obtained for pure diffusion flames without radiative losses [47], as discussed before.

Figure 3.11 is an extinction plot for the case when $\Delta Z_R = 0.06$ and $\Lambda = 0$. Extinction values of N_R are plotted as a function of Z_f, the theoretical flame location in the mixture fraction coordinate. We recall here that Z_f is related to the overall

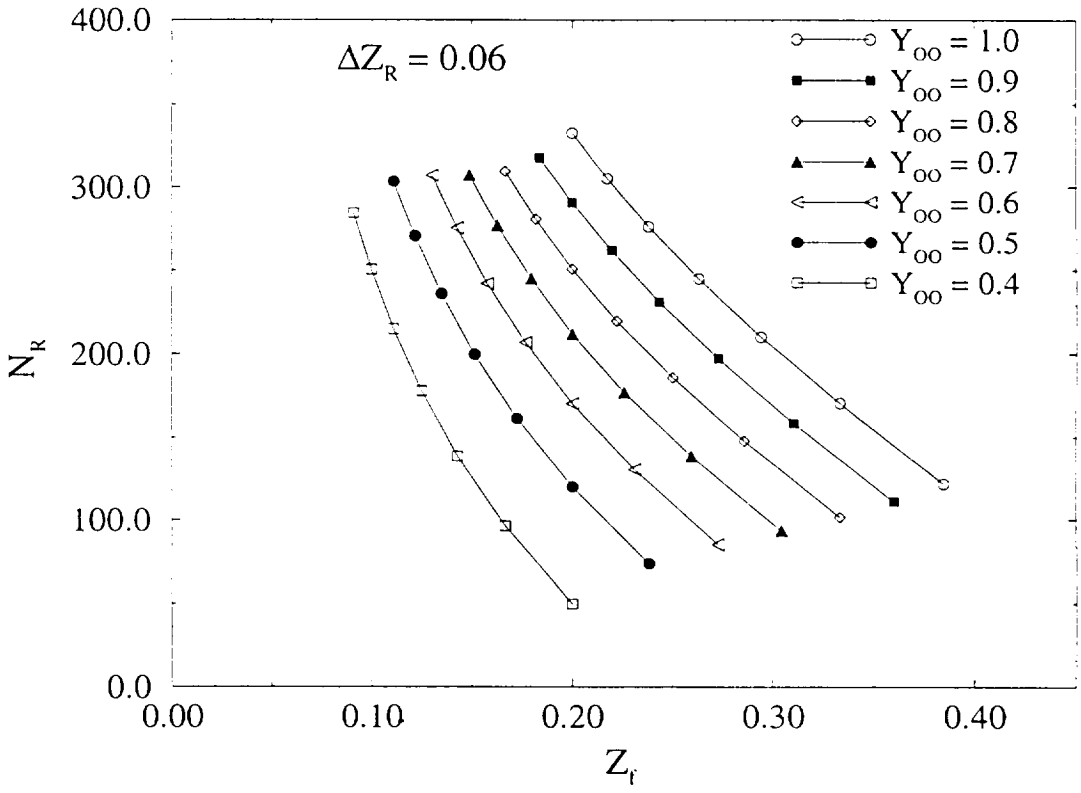

Figure 3.11. Extinction Plot for $\Delta Z_R = 0.06$ and $\Lambda = 0$.

stoichiometric coefficient o $(= \nu Y_{FF}/Y_{OO})$ by the expression $Z_f = 1/(1 + o)$. We notice that for a given value of the oxidizer mass fraction at the wall, $(N_R)_{extinction}$

increases as Z_f is decreased. A decrease in Z_f implies an increase in o, which, for a given Y_{OO}, indicates an increase in Y_{FF}. As Y_{FF} increases, the reaction rate becomes more vigorous and it becomes more difficult to extinguish the flame through the application of radiative losses. This explains the nature of the curves that we obtain on the extinction plot. Also, for the same value of Z_f, i.e., for the same value of o, a lower value of Y_{OO} indicates a correspondingly smaller value of Y_{FF}, and hence, the reaction rate also becomes smaller in magnitude. It then becomes easier to extinguish the flame. This explains why the curves in Figure 3.11 all shift towards the left for decreasing values of Y_{OO}.

Our focus is next shifted to some quantities of practical interest. We evaluate the heat transfer to the wall from flames with the same stoichiometry ($Y_{OO} = 0.6$ and $Y_{FF} = 0.8$) but with different thicknesses of the radiative loss zones and for different separation distances (Δ) from Z_f. Let $Q_{W;O}$ denote the heat transferred to the oxidizer wall by the flame per unit surface area of the wall. We reckon that the oxidizer wall will have a stronger effect on the flame than the fuel wall owing to the proximity of the flame to the oxidizer wall. The flame transfers heat to the oxidizer wall by means of both conduction and radiation, and hence, $Q_{W;O} = Q_{W;O,cond} + Q_{W;O,rad}$, where the conduction flux is $Q_{W;O,cond} = -\lambda(dT/dx)|_{x=L}$ and the radiative flux is $Q_{W;O,rad} = 0.5\times\int_0^L(dq_R/dx)dx$. We assume that half of the radiative losses travel to each wall: this assumption is reasonable in the thermally-thin limit we consider here. We can transform the expressions for $Q_{W;O,cond}$ and $Q_{W;O,rad}$ to the Z coordinate and normalize $Q_{W;O}$ by the reference conductive flux $\lambda_0(T_f - T_0)/L$. The normalised $\bar{Q}_{W;O} = (1/\bar{s}_0)(d\tau/dZ)|_{Z=0} + 0.5\times(1/\bar{s}_0).N_R\int_0^1(1/\bar{s}_0)(d\bar{q}_R/dZ)dZ$. The quantity $\bar{Q}_{W;O}\bar{s}_0$ is plotted in Figure 3.12.

From Figure 3.12 it is apparent that the heat transfer characteristics do not depend strongly on the separation distance Δ, and consequently, we see four reasonably

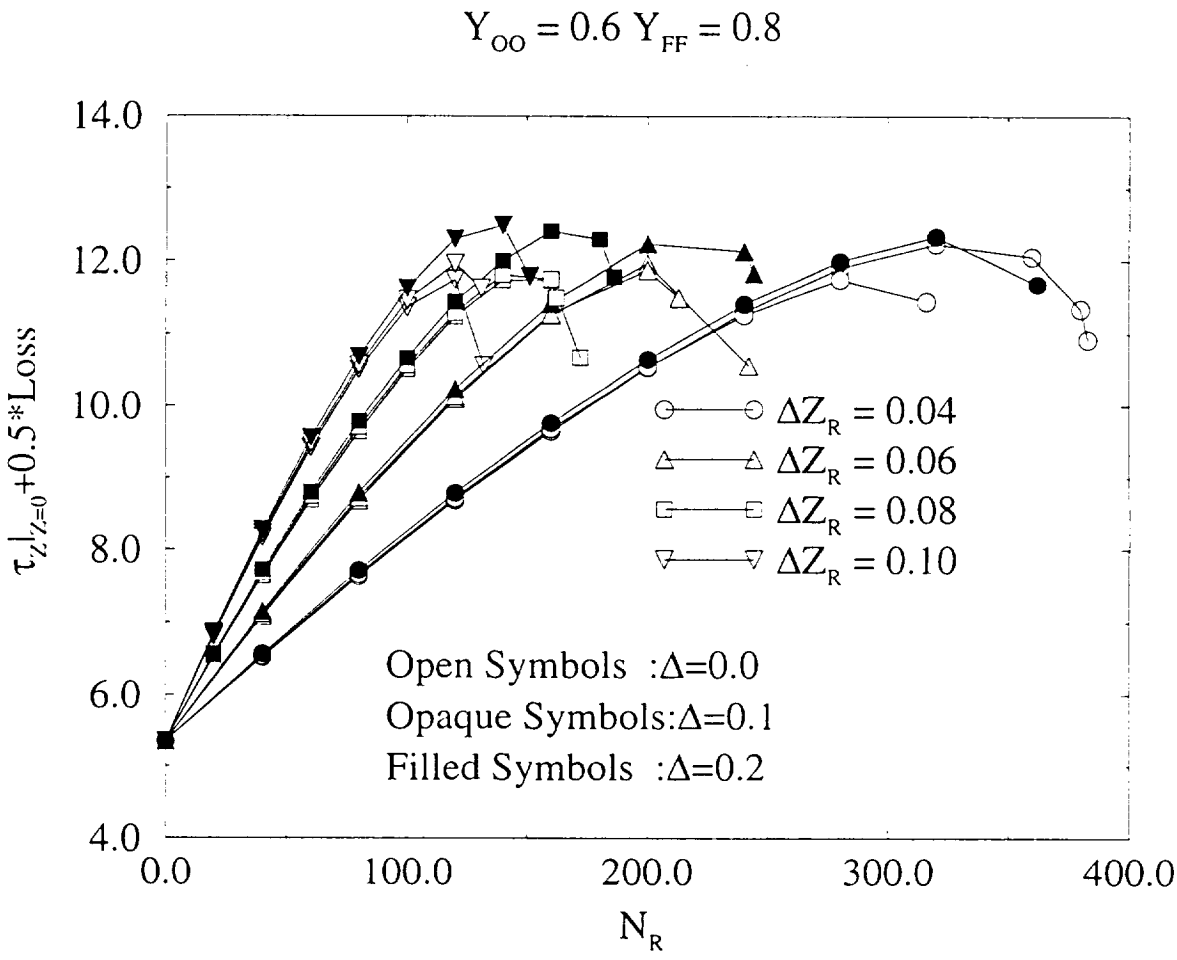

Figure 3.12. Heat Transfer to the oxidizer wall as a Function of N_R.

distinct groups of curves corresponding to loss zones of four different thicknesses. However, as is evident from the plot, the separation distance Δ does become important for higher values of N_R, close to extinction. We will notice that nearing extinction, the flame attempts to reduce the heat losses to the wall as much as possible. Also, the value of N_R required for extinction is higher when the heat loss zone is very thin, as intuitively obvious.

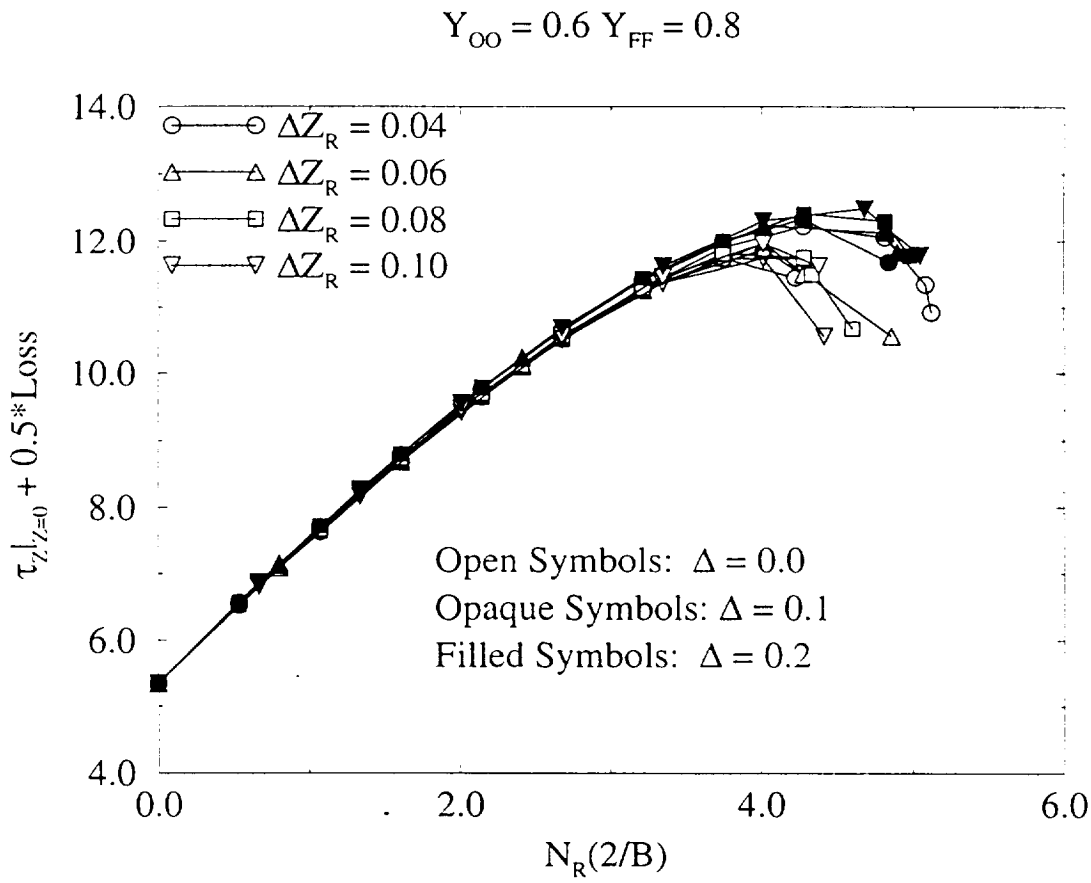

Figure 3.13. Heat Transfer to the oxidizer wall as a Function of $N_R(2/B)$.

We also plotted $\bar{Q}_{W;O\bar{s}_0}$ as a function of the quantity $N_R(2/B)$. Figure 3.13 clearly shows that the quantity $N_R(2/B)$, which is approximately the value of the integral

$\int_0^1 N_R sech^2[B(Z - Z_R)]dZ$, is able to collapse the wall heat transfer data except very near extinction. Thus, when plotted against $N_R(2/B)$, $\bar{Q}_{W,O}\bar{s}_0$ does not reveal any appreciable dependance on either the separation distance Δ or even the thickness of the loss zone ΔZ_R.

Another quantity of practical interest is the radiative fraction χ, given by the ratio q_{Rad}/q_{Total}. The quantity q_{Rad} is the integral of the radiative loss term ($\int_0^1 N_R sech^2[B(Z - Z_R)]dZ$) and q_{Total} is the integrated value of the reaction rate in mixture fraction space, i.e., $\int_0^1 (1+\phi)\mathcal{D}rdZ$. From Figure 3.14 we notice that q_{Total} decreases with increasing values of N_R. This happens because with increased intensity of the radiative loss zone, reaction rate values decrease, as observed in Figures 3.5 and 3.10. For thicker loss zones, the drop in q_{Total} with increasing values of N_R is more rapid.

We have already noted in section 3.5.2 that the integral of the radiative loss term profile is approximately $(N_R/\bar{s}_0)(2/B)$. Hence, it is of interest to plot the total heat release q_{Total} as a function of the quantity $N_R(2/B)$. The result is shown in the Figure 3.15. Figure 3.15 indicates that the quantity $N_R(2/B)$ characterizes the total heat release rate very well and the curves for different loss zone thicknesses virtually collapse on one another except for large values of N_R close to extinction.

Figure 3.16 illustrates the variation of χ as a function of N_R for different thicknesses of the loss zones and for $\Delta = 0$. We observe that χ increases with increasing N_R for a flame with a given loss zone thickness. The integrated quantity q_{Rad} increases with N_R and, since correspondingly the q_{Total} values decrease, χ, which is a ratio of the above quantities, increases. In order to produce a given value of χ, a higher value of N_R is required for a flame with a thinner loss zone. Similar to the study of q_{Total} we plot χ as a function of $N_R(2/B)$ in Figure 3.17. It is clear from the figure that the use of $N_R(2/B)$ collapses the data very well except close to extinction. So, the quantity

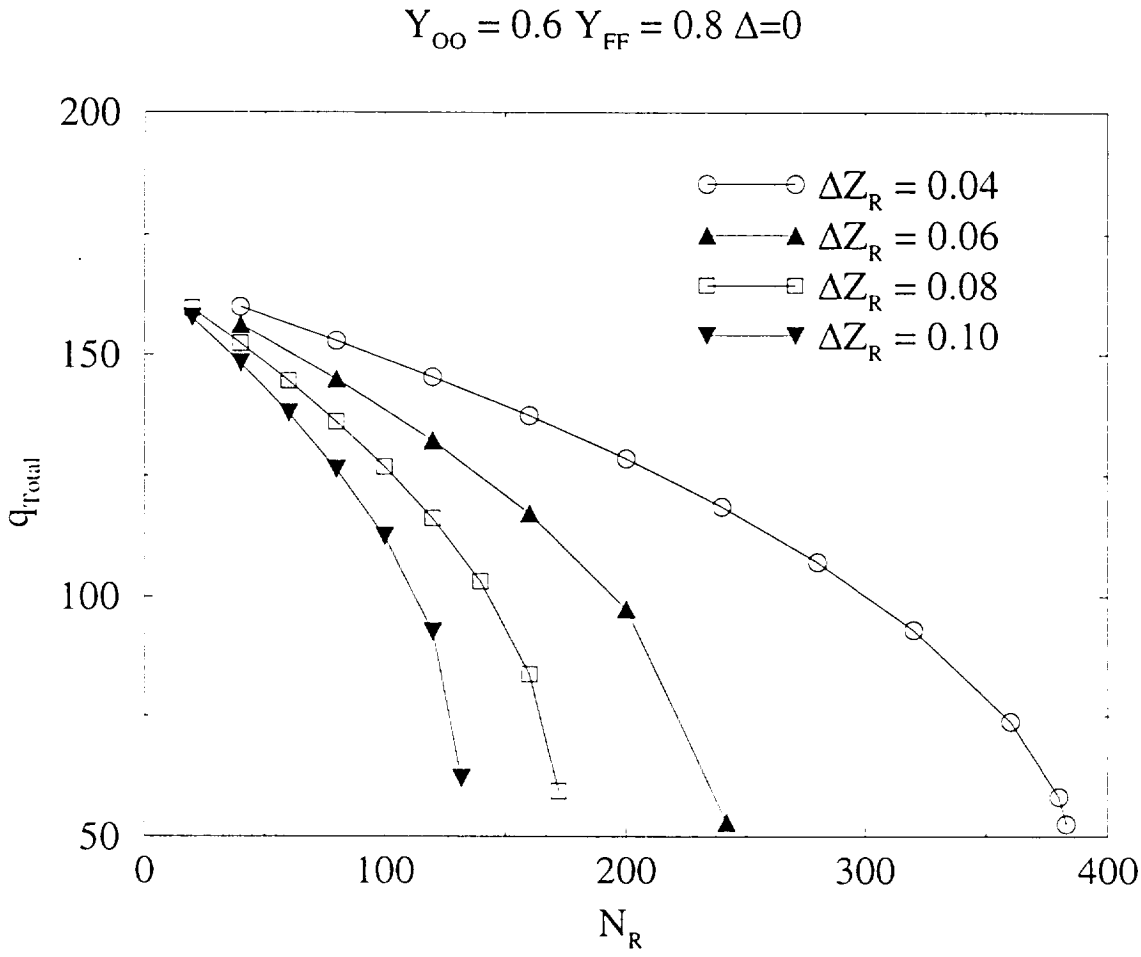

Figure 3.14. q_{Total} as a function of N_R.

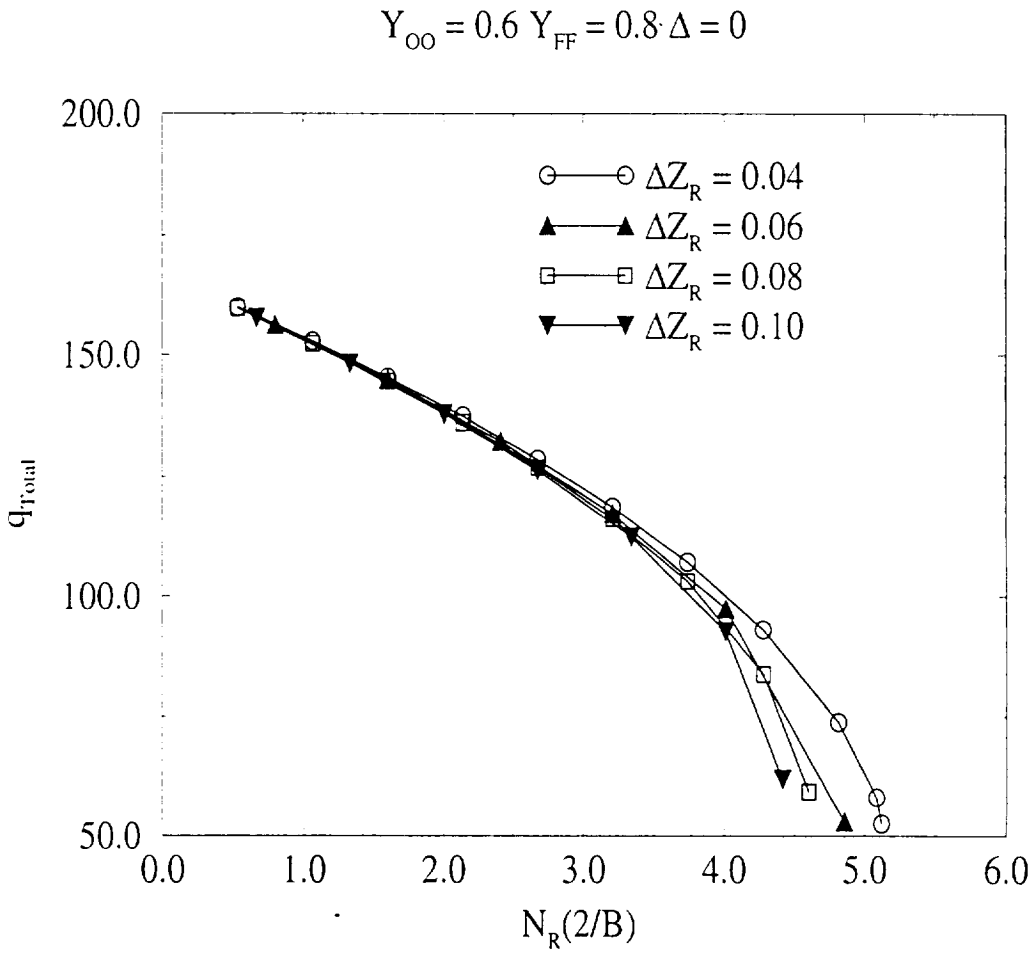

Figure 3.15. q_{Total} as a function of $N_R(2/B)$.

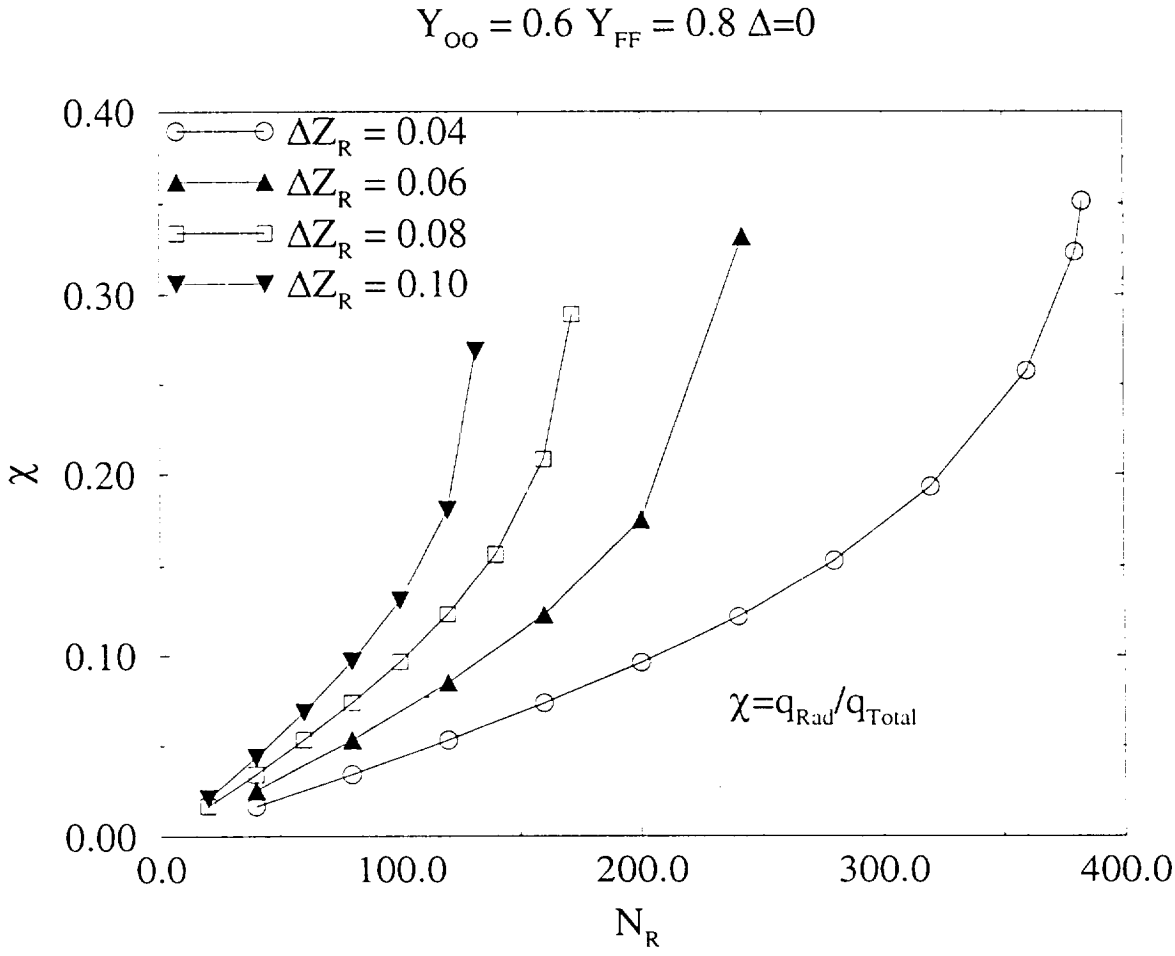

Figure 3.16. χ as a function of N_R

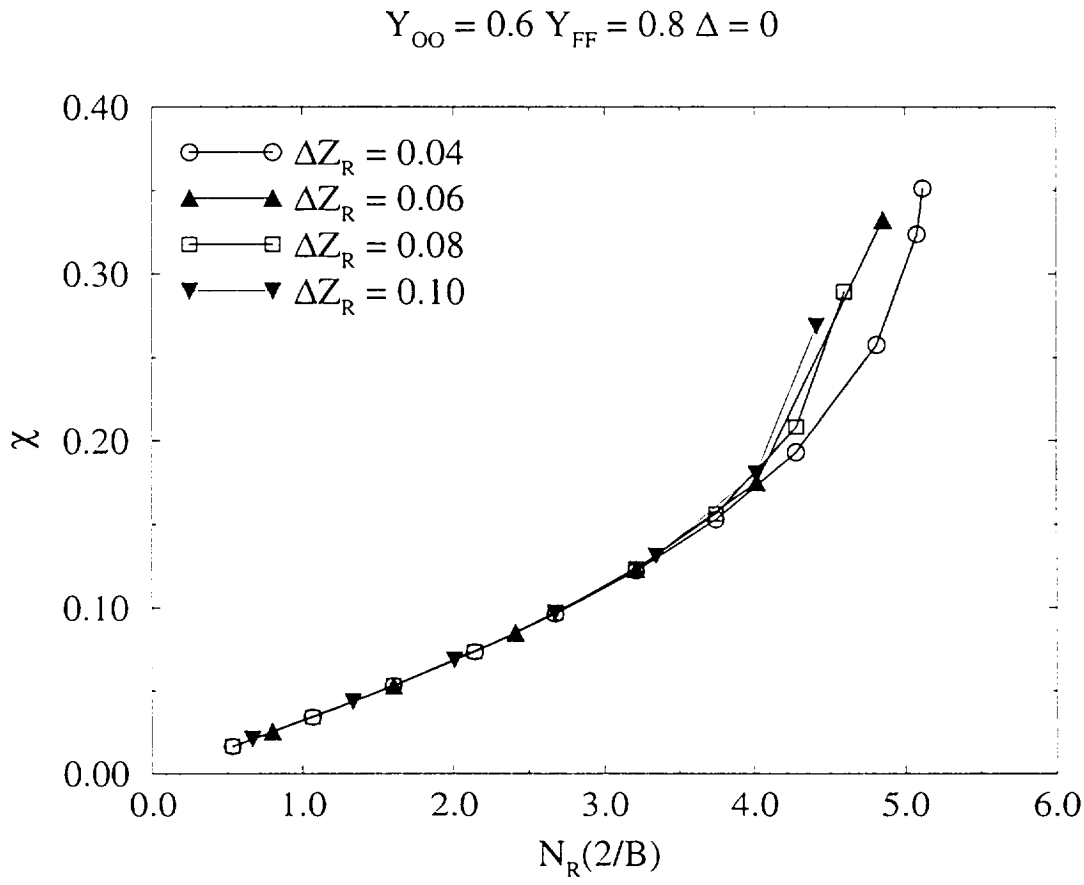

Figure 3.17. χ as a function of $N_R(2/B)$

$N_R(2/B)$ can be used to correlate the radiative fraction quite effectively. Figure 3.18

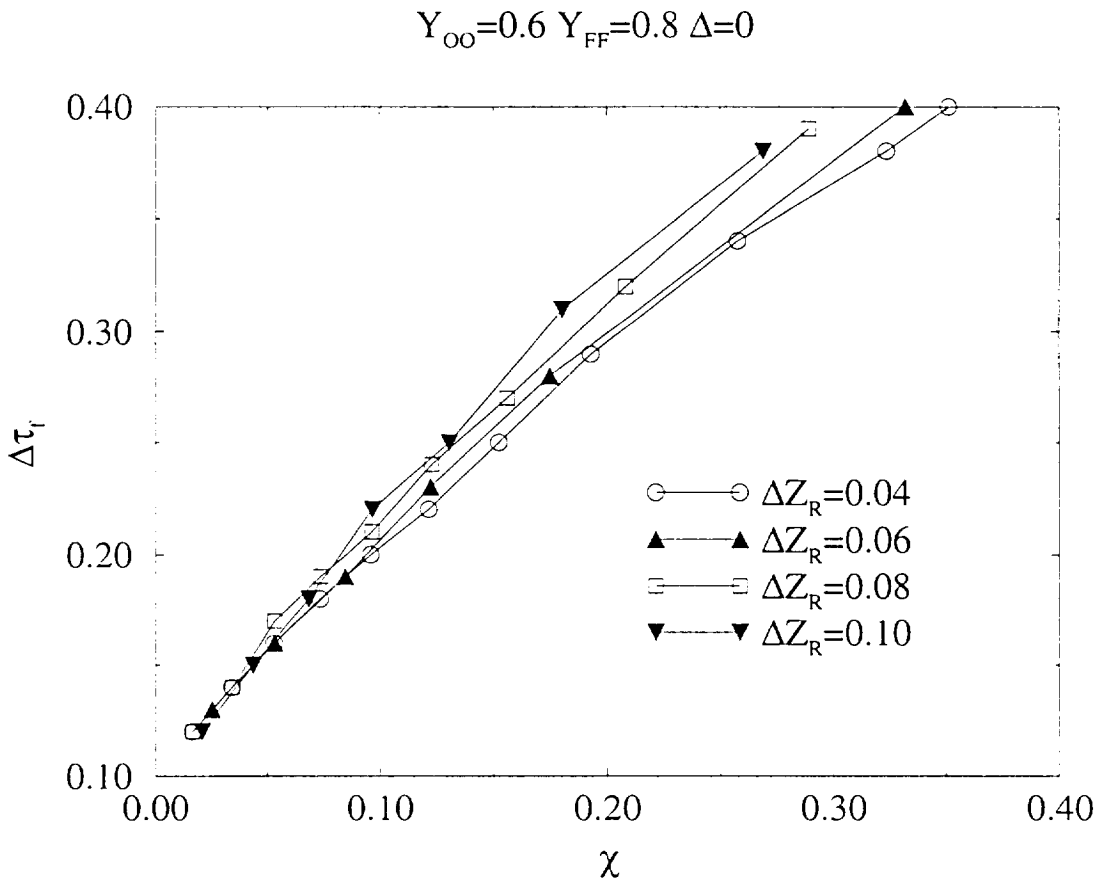

Figure 3.18. $\Delta\tau_f$ as a function of the radiative fraction

shows the variation of the drop in flame peak temperature, $\Delta\tau_f$, as a function of the radiative fraction χ. If we denote the maximum temperature by τ_f, then $\Delta\tau_f$ is defined as $1 - \tau_f$. We recall that the temperature has been normalized in such a way that the peak nondimensional temperature, τ, for the infinite reaction rate situation always has the value of unity, regardless of the oxidizer and fuel mass fractions. Thus, $\Delta\tau_f$ represents the drop in peak temperature for finite rate chemistry and radiative loss situation, in comparison to the IRR situation. The increase in $\Delta\tau_f$ with χ was

almost linear for smaller values of χ. However the curves for the different loss zone thicknesses diverged from one another for higher values of the radiative loss fraction χ.

3.9.1 Comparison with the top-hat profile

It has been previously mentioned (section 3.5.2) that the results for the $sech^2$ heat loss profile can be compared with the results in Appendix A for the top-hat profile. However, the thickness ΔZ_R of the top-hat profile must be chosen to be $2/B$, where the value of B is determined from the choice of the thickness of the $sech^2$ profile. For example, when $(\Delta Z_R)_{sech^2}$ is chosen to be 0.06, the constant $B = 99.7$ and consequently $(\Delta Z_R)_{top-hat} = 2/99.7 \simeq 0.02$. As illustrated in Appendix A both analytical and numerical methods were used to determine the extinction value of N_R for the top-hat profile. Here, we compare analytical and numerical results for the top-hat profile with the numerical solutions for the $sech^2$ profile. Figure 3.19 depicts the extinction N_R values plotted as a function of Z_f when $Y_{OO} = 0.7$, $(\Delta Z_R)_{sech^2} = 0.06$, $(\Delta Z_R)_{top-hat} = 0.02$ and $\Delta = 0.1$. The direction of increasing Y_{FF} has also been indicated on the plot. The numerical solutions reveal that the $sech^2$ and the top-hat profiles produce very similar $N_{R,extinction}$ values. This indicates that the integrated value of the radiative loss term is the quantity which determines the extinction N_R value. The extinction N_R values obtained by analytical method are quite different from the numerical solution. However, on close inspection of the curves depicted in Figure 3.19 we notice that the ratio of the analytically obtained values to the numerical solution is about 4 for all the Z_f values plotted in Figure 3.19. This indicates that a modification of the analytical formula based on the inclusion of a correction factor should yield close correspondence between the analytical and numerical results.

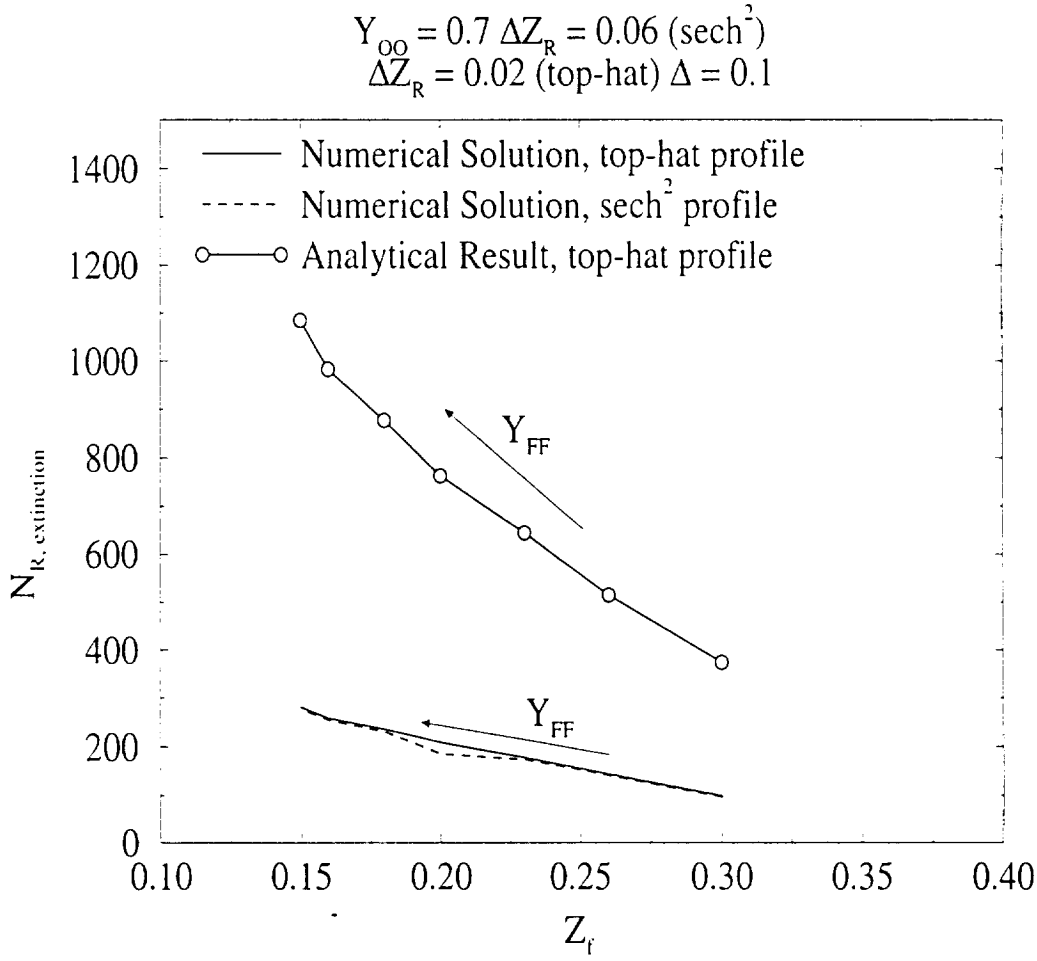

Figure 3.19. Comparison of $N_{R,extinction}$ values for $sech^2$ and top-hat profiles.

3.10 Conclusions

The influence of a simple and hypothetical heat loss zone on a pure diffusion flame was investigated in detail in this chapter. The loss profile was of the form of a $sech^2$ and we varied the intensity and the width of the loss zone to study the behavior of a pure diffusion flame. The loss zone was always postulated to lie on the fuel side of the ideal Burke-Schumann flame. The location of the loss zone on the fuel side relative to the ideal flame location Z_f was also varied. In all situations the increase of the radiation number N_R resulted in a movement of the flame toward the fuel side. We found that for thin loss zones located close to Z_f the reaction zone may even migrate to the fuel side of loss zone for significantly high values of N_R. In such a situation the loss zone exists on the oxidizer side of the flame, contrary to our initial postulate. This happens because our hypothetical loss zone is static and does not contain any mechanism for movement. The reaction rate profile, on the other hand, is free to move and hence locates itself on the fuel side of the loss zone in certain cases.

Extinction plots were generated for different flames for given loss zone thicknesses (ΔZ_R) and given separation distances (Δ). The plots indicated that for a given Y_{OO}, an increase in Y_{FF} results in higher values of extinction radiation number (N_R).

Nondimensional heat transfer rates to the oxidizer wall were also investigated. The results indicated that the separation distance Δ did not have a significant influence on the wall heat transfer characteristics.

The total heat release in the combustion process, q_{Total}, was found to decrease with increasing values of N_R and the rate of decrease was quite rapid for thicker loss zones. It was found that the quantity $N_R(2/B)$ characterizes q_{Total} very well and the curves for the different loss zone thicknesses and separation distances all collapse onto one another except near extinction.

Investigation of the radiative fraction (χ) showed that χ increases with increasing

values of N_R and the rate of increase is steeper for thicker loss zones. The flame, however, extinguishes at a larger value of χ for loss zones which are relatively thin. The quantity $N_R(2/B)$ collapses the q_{Total} and radiative fraction values very well except near flame extinction.

CHAPTER 4

Influence of a Simple Heat Loss Profile on a Diffusion Flame with Fuel Blowing

4.1 Introduction

In this chapter the influence of a simple $sech^2$ heat loss profile on a diffusion flame is investigated when there is a convective fuel flow through the fuel wall. Thus, the problem treated in this chapter differs from the one in chapter 3 only in the fuel wall boundary condition.

In the following section, we present the problem definition. The formulation of the conservation equations is quite similar to that in the previous chapter and is discussed only briefly. A discussion of the important results follows.

4.2 Problem Definition

Figure 4.1 shows the geometry of the problem under consideration. A diffusion flame is established between the oxidizer and fuel walls. A diffusive flux of oxidizer is

supplied by the oxidizer wall. Fuel is released from the fuel wall through the combined influences of diffusion and convection. A mass flux $\dot{m} = (\rho u)|_{x=0}$ issues from the fuel wall. The oxidizer wall allows the mass flux flowing from the fuel side to pass through the oxidizer wall, thereby preventing the transient accumulation of matter in the region between $x = 0$ and $x = L$. Both walls are maintained at temperature T_0. The species boundary conditions have been illustrated in Figure 4.1.

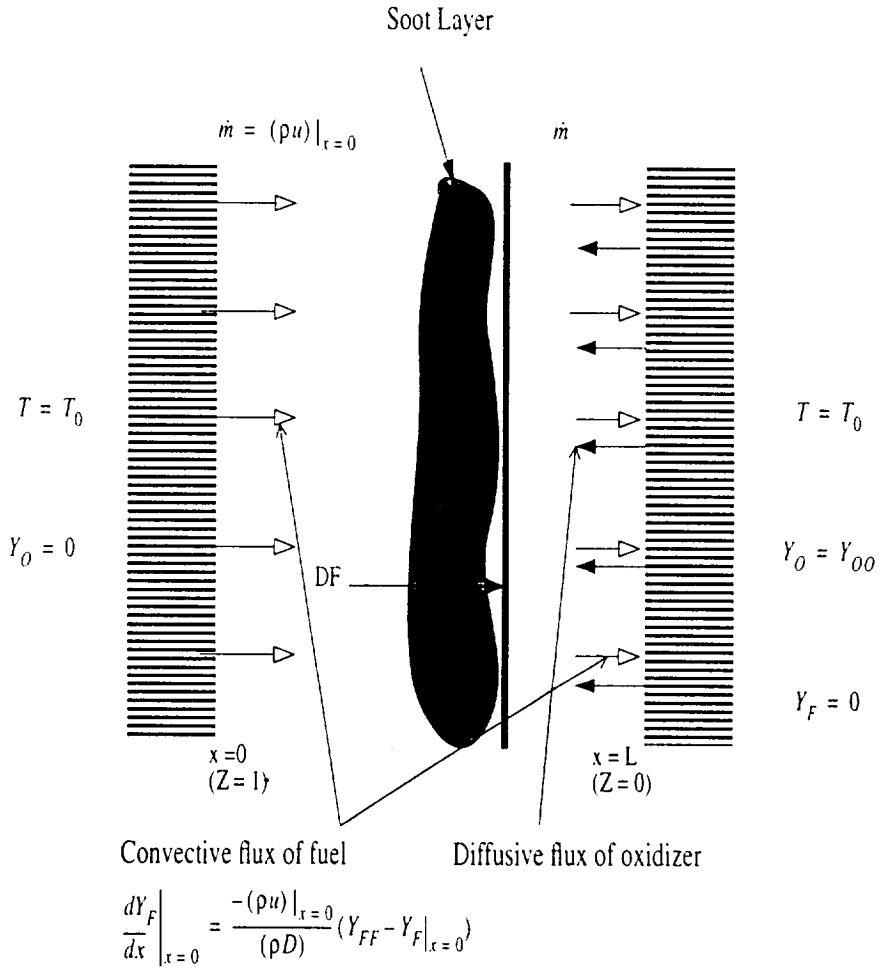

Figure 4.1. The problem geometry and definition.

4.3 Formulation

The equations we shall solve are the energy and species equations for oxidizer and fuel. The energy equation is given by

$$\rho C_p[T_t + uT_x] = (\lambda T_x)_x + Q_F \dot{w}_F - \frac{dq_R}{dx}. \tag{4.1}$$

with boundary conditions $T(x = 0) = T_0$ and $T(x = L) = T_0$, where T_0 is the ambient temperature, assumed to be 298 K. The oxidizer equation is

$$\rho[Y_{O_t} + uY_{O_x}] = (\rho D_O Y_{O_x})_x - \nu \dot{w}_F, \tag{4.2}$$

with boundary conditions $Y_O(x = 0) = 0$ and $Y_O(x = L) = Y_{OO}$. As in the previous chapter, a one-step, irreversible chemical reaction of the form $F + \nu O \rightarrow (1 + \nu)P$ is assumed. Finally, the fuel equation is given by

$$\rho[Y_{F_t} + uY_{F_x}] = (\rho D_F Y_{F_x})_x - \dot{w}_F, \tag{4.3}$$

with boundary conditions $dY_F/dx|_{x=0} = -(\dot{m}/\rho D_F)(Y_{FF} - Y_F|_{x=0})$ and $Y_F(x = L) = 0$. The quantity $\dot{m}$ is the mass flux from the fuel wall, equal to ρu.

Using the coordinate transformation $Z = 1 - s/s_0$ where $s = \int_0^x \rho dx$ and $s_0 = \int_0^L \rho dx$ and proper normalizations (as outlined in the previous chapter), the above equations transform to

$$\tau_{\bar{t}} = \frac{1}{\bar{s}_0}\tau_Z + \frac{\alpha_0}{u_0 L \bar{s}_0^2}\tau_{ZZ} + \bar{Q}_F \mathcal{D}r + \frac{N_R}{\bar{s}_0}\frac{d\bar{q}_R}{dZ}. \tag{4.4}$$

$$y_{O\bar{t}} = \frac{1}{\bar{s}_0} y_{OZ} + \frac{\alpha_0}{u_0 L \bar{s}_0^2} y_{OZZ} - \phi \mathcal{D}r. \tag{4.5}$$

$$y_{F\bar{t}} = \frac{1}{\bar{s}_0} y_{FZ} + \frac{\alpha_0}{u_0 L \bar{s}_0^2} y_{FZZ} - \mathcal{D}r \tag{4.6}$$

where $\mathcal{D}$ is the Damköhler number, given by $\mathcal{D} = t_{ref}/t_{chem}$ and r is the nondimensional reaction term given by $r = y_{OY_F}\exp(-\beta(1-\tau)/(1-\alpha(1-\tau)))$ where $\alpha = 1-T_0/T_f$ and $\beta = E\alpha/RT_f$ is the Zeldovich number. The reference time scale is $t_{ref} = L/u_0$ and the characteristic chemical time scale is $t_{chem} = 1/[AY_{OO}\exp(-E/RT_f)]$. The nondimensional quantity $\bar{Q}_F$ is given by $\bar{Q}_F = Q_F Y_{FF}/C_p(T_f - T_0)$ and $\bar{s}_0 = s_0/s_{0,ref}$ where $s_{0,ref} = \rho_0 L$. The velocity u_0 is the magnitude of u at $x = 0$, i.e., at $Z = 1$. Note that the first terms on the right hand side of each of the above equations originate due to the convective fuel flow and were not present in the governing equations for a pure diffusion flame, as illustrated in section 3.5 of chapter 3.

The above equations are solved numerically to obtain nondimensional temperature and species mass fraction profiles for different radiation loss profiles. The radiation number N_R in the above is a ratio of the reference radiative and convective fluxes, given by $N_R = q_{R,ref}/(\rho_0 u_0 C_p \Delta T)$. This is in contrast to the definition of N_R for a pure diffusion flame, where N_R was defined to be a ratio of reference radiative and conductive fluxes.

4.4 Boundary Condition for the Fuel Equation

In contrast to chapter 3, the fuel mass fraction at the fuel wall is not prescribed in this case. Instead, it is assumed that fuel issues from the fuel wall by both diffusion and convection. A balance between the rate of depletion of the fuel in the reservoir and the rate of fuel issue gives the necessary equation for the boundary condition. In fact, the fuel mass fraction in the reservoir is held constant.

The amount of reservoir fluid lost through a unit surface area per unit time is $\rho_0 u_0$, where ρ_0 is the density at the reservoir wall temperature, i.e., T_0, and u_0 is the velocity at the fuel wall. Correspondingly, the reservoir is deprived of $\rho_0 u_0 Y_{FF}$ amount of the fuel species. The fuel leaving the reservoir surface and entering the

free stream does so under the combined influence of diffusion and convection. The diffusion rate, by virtue of Fick's law, is $-\rho D_F(dY_F/dx)|_{x=0}$, where D_F is the diffusion coefficient of fuel in fuel/air mixture. The convective fuel flow rate is $(\rho_0 u_0)Y_F|_{Z=1}$. Writing the balance equation yields

$$\frac{dY_F}{dx}|_{x=0} = \frac{-(\rho_0 u_0)}{\rho D_F}(Y_{FF} - Y_F|_{x=0}). \tag{4.7}$$

In the Z coordinate the fuel wall boundary condition assumes the following form:

$$\frac{dy_F}{dZ}|_{Z=1} = \frac{u_0 L \bar{s}_0}{D_{F0}}(1 - y_F|_{x=0}). \tag{4.8}$$

where $y_F = Y_F/Y_{FF}$, as before, and D_{F0} is the value of the diffusion coefficient of the fuel at the reference condition.

4.5 Solution for Infinite Reaction Rate

The temperature and species profiles for the infinite reaction rate (IRR) situation are used as initial profiles. Hence, our first task is to obtain such solutions. In the limit of infinite reaction rate the flame sheet is infinitesimally thin. Fuel and oxidizer are depleted in the flame in the stoichiometric proportion. No fuel exists on the oxidizer side of the flame and no oxidizer exists on the fuel side, i.e., there is no leakage through this diffusion flame.

Under such conditions, we can solve for the τ, y_O and y_F profiles in two adjacent domains *without* requiring the reaction term. We solve the following energy equation in the oxidizer side of the interval subject to the boundary conditions $\tau(Z = 0) = 0$ and $\tau(Z = Z_f) = 1$, where Z_f is the flame location:

$$\frac{1}{\bar{s}_0}\tau_Z + \frac{\alpha_0}{u_0 L \bar{s}_0^2}\tau_{ZZ} = 0. \tag{4.9}$$

The above equation must also be solved in the adjacent fuel-side domain, i.e., between $Z = Z_f$ and $Z = 1$, with $\tau(Z = 1) = 0$. A similar procedure must be followed for the species equations, although $y_O = 0$ on the fuel side and $y_F = 0$ on the oxidizer side account for the zero leakage parts of the y_O, y_F solutions. However, Z_f is yet to be determined. For that purpose, a mixture fraction variable is first defined as follows:

$$\zeta = \frac{\phi y_F + 1 - y_O}{\phi + 1} \tag{4.10}$$

We note here that unlike chapter 4 the variable Z does not correspond to the mixture fraction. We observe that ζ satisfies an equation of the same form as the τ and species profiles for the IRR situation, i.e.,

$$\frac{1}{\bar{s}_0}\zeta_Z + \frac{\alpha_0}{u_0 L \bar{s}_0^2}\zeta_{ZZ} = 0 \tag{4.11}$$

The solution for ζ is

$$\zeta = [1 - \exp(-Z/c)] \tag{4.12}$$

where $c = \alpha_0/(u_0 L \bar{s}_0)$. At the flame, y_O and y_F are both zero, which, by virtue of equation 4.10 indicates that $\zeta_f = 1/(\phi + 1)$. Correspondingly, Z has the value $Z_f = c\ln((1 + \phi)/\phi)$. The equations for τ, y_O and y_F profiles can now be solved for. The solutions for τ are

$$\tau = \begin{cases} \frac{1-e^{-Z/c}}{1-e^{-Z_f/c}} & 0 \le Z \le Z_f, \\ \frac{e^{-1/c}-e^{-Z/c}}{e^{-1/c}-e^{-Z_f/c}} & Z_f \le Z \le 1. \end{cases} \tag{4.13}$$

The solutions for y_O are

$$y_O = \begin{cases} \frac{e^{-Z/c}-e^{-Z_f/c}}{1-e^{-Z_f/c}} & 0 \le Z \le Z_f, \\ 0 & Z_f \le Z \le 1. \end{cases} \tag{4.14}$$

Finally, the solutions for y_F are

$$y_F = \begin{cases} 0 & 0 \leq Z \leq Z_f, \\ 1 - e^{-(Z-Z_f)/c} & Z_f \leq Z \leq 1. \end{cases} \tag{4.15}$$

A plot of the temperature and species profiles is shown in Figure 4.2 for $L = 0.01$

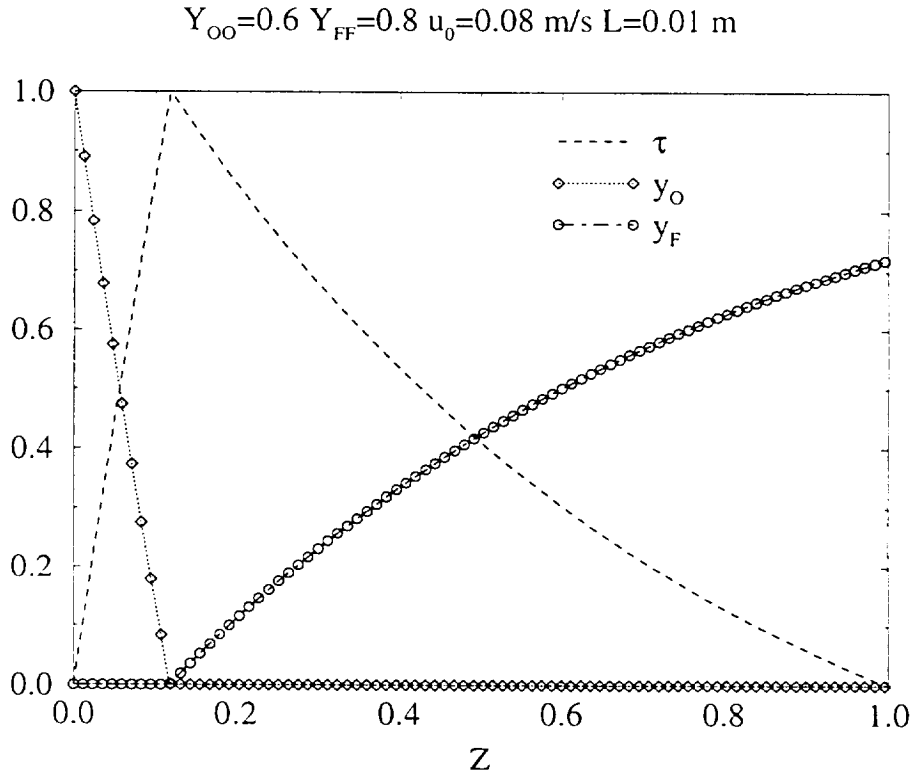

Figure 4.2. IRR profiles for τ, y_O and y_F

m, $u_0 = 0.08\ m/s$, $Y_{OO} = 0.6$ and $Y_{FF} = 0.8$. We note here that equations 4.13, 4.14 and 4.15 have to be solved iteratively because the quantity c depends on $\bar{s}_0$, which depends on the solution and can not be ascertained apriori. The procedure is to guess a value for c, i.e., for $\bar{s}_0$ and then use equations 4.13-4.15 to determine τ, y_O and y_F profiles. On obtaining the τ profile the density ($\bar{\rho}$) profile can also be determined

using the relation $\bar{\rho} = (1-\alpha)/(1-\alpha(1-\tau))$, where $\alpha = 1 - T_0/T_f$. Then, $\bar{s}_0$ can be evaluated using the procedure outlined in section 3.8. Using this fresh value of $\bar{s}_0$ the quantity c can be calculated again. The new value of c is then used to determine τ, y_O and y_F profiles. The new τ profile is then used to calculate the value of c again. This procedure is repeated until convergence is obtained and we find the τ, y_O and y_F profiles for the infinite reaction rate case.

4.6 Parameter Values

The parameter values used in this chapter are the same as those used in chapter 3. The length of the domain is $L = 1.05\ cm$ unless otherwise mentioned. The velocity of fuel flow at the wall, i.e., u_0 is a new parameter in this chapter. The value of u_0 was varied from 0.02 m/s through 0.14 m/s.

4.7 Results and Discussion

The method of analysis in this case is the same as in chapter 3. However, the additional variable u_0 must be taken into account in the examination.

Figure 4.3 illustrates the variation of the temperature profile for different values of u_0 for a given flame in the absence of radiative losses ($N_R = 0$). The values of u_0 range from 0.06 m/s to 0.14 m/s. We define a nondimensional parameter $u_0 L/\alpha_0$ for characterising the fuel blowing rate and tabulate is in Table 4.1.

Table 4.1. $u_0 L/\alpha_0$ for different values of u_0.

$u_0\ m/s$	0.06	0.08	0.10	0.12	0.14
$u_0 L/\alpha_0$	5.08	6.77	8.46	10.15	11.84

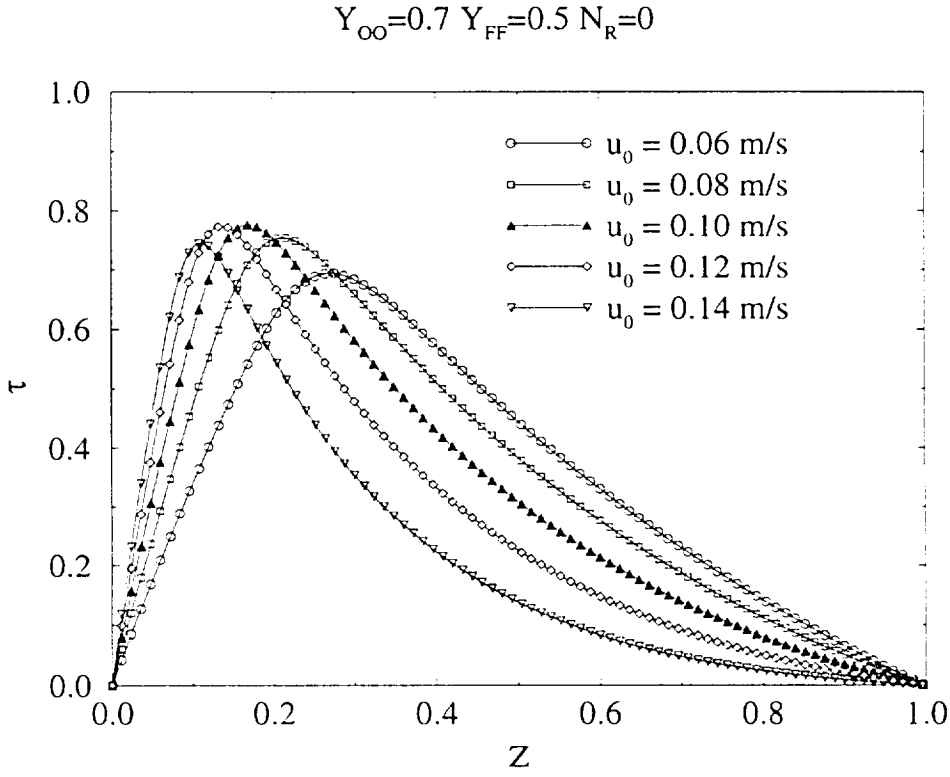

Figure 4.3. Effect u_0 on τ profile for a given flame.

As u_0 is increased, the flame moves closer to the oxidizer wall. We recall that the rate of depletion of fuel from the fuel wall is given by $(\rho_0 u_0) Y_{FF}$. For higher values of u_0, more fuel issues from the reservoir. The oxidizer mass fraction at the oxidizer wall being unchanged, the flame has to move toward the oxidizer wall since the rate of supply of fuel is now greater. As u_0 is increased from 0.06 m/s to 0.10 m/s through 0.08 m/s, the peak temperature also increases, as evidenced by Figure 4.3. However, on further increase of u_0, the peak temperature decreases. The reasonable explanation for this is the proximity of the oxidizer wall. For $u_0 = 0.14$ m/s, the flame is quite close to the oxidizer wall and loses much heat to the wall. On closer scrutiny of Figure 4.3, it can be observed that for higher values of u_0, a fixed increment in the value of u_0 results in a smaller shift of the temperature profile toward the oxidizer wall. The flame seems to "feel" the presence of the wall as u_0 is increased and resists the attempt of the convective flow to force it against the wall.

The slope of the temperature profile at the wall is a measure of the extent of the heat transfer to the wall. Figure 4.4 shows the slope, τ_Z, at the walls, $Z = 0$ and $Z = 1$, plotted as a function of u_0 for the flame under consideration ($Y_{OO} = 0.7$, $Y_{FF} = 0.5$, $N_R = 0$). The plot clearly exhibits that the heat transfer to the oxidizer wall (at $Z = 0$) is much higher than that to the fuel wall. Because it is closer to the flame, the oxidizer wall exercises a significant influence on it. The influence of wall heat transfer is an important issue for deciding the location and strength of the flame.

The reaction rate term, $(1 + \phi)\mathcal{D}r$, is plotted as a function of Z in Figure 4.5. The increase in u_0 clearly results in the movement of the reaction rate profile toward the oxidizer wall. The value of the peak reaction rate also increases as u_0 increases. However, as observed for the τ profile, the proximity of the wall results in a drop in the peak value of $(1 + \phi)\mathcal{D}r$ for higher values of u_0. We also notice that for $u_0 = 0.06$ m/s the reaction rate profile is quite broad. However, as u_0 is increased, the reaction

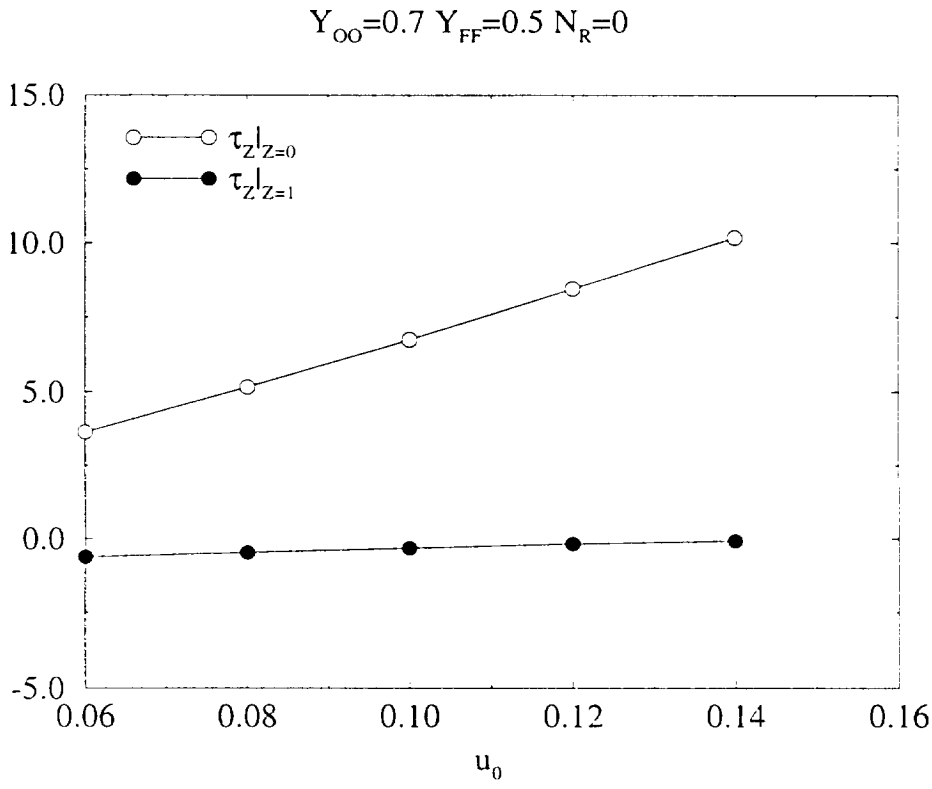

Figure 4.4. Effect u_0 on τ_Z for a given flame.

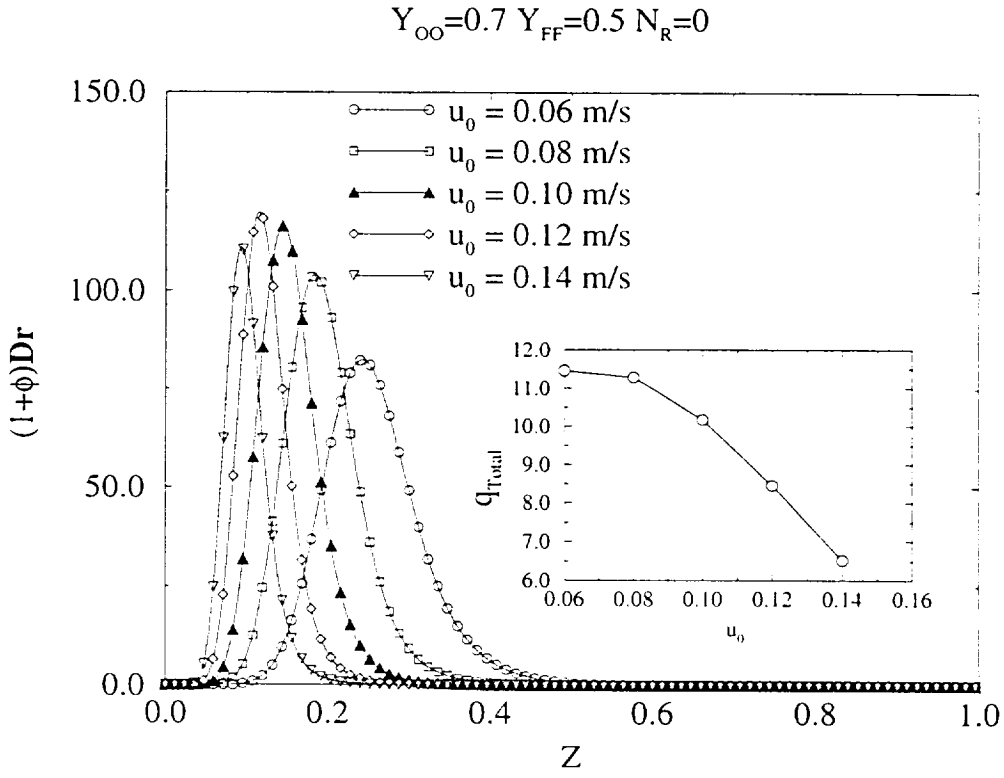

Figure 4.5. Effect of u_0 on $(1 + \phi)\mathcal{D}r$ for a given flame.

rate profile becomes narrower. Since the peak of the reaction rate profile increases as u_0 increases (for sufficiently large distance from the wall) and it simultaneously becomes narrower, the total heat release in the process of combustion, q_{Total}, which is the integrated value of $(1 + \sigma)\mathcal{D}r$, is also calculated. Figure 4.5 shows as inset a plot of q_{Total} as a function of u_0. It is clear that q_{Total} decreases as u_0 is increased for this flame. The rate of decrease is significantly enhanced for higher values of u_0, i.e., when the flame is in the close proximity of the oxidizer wall.

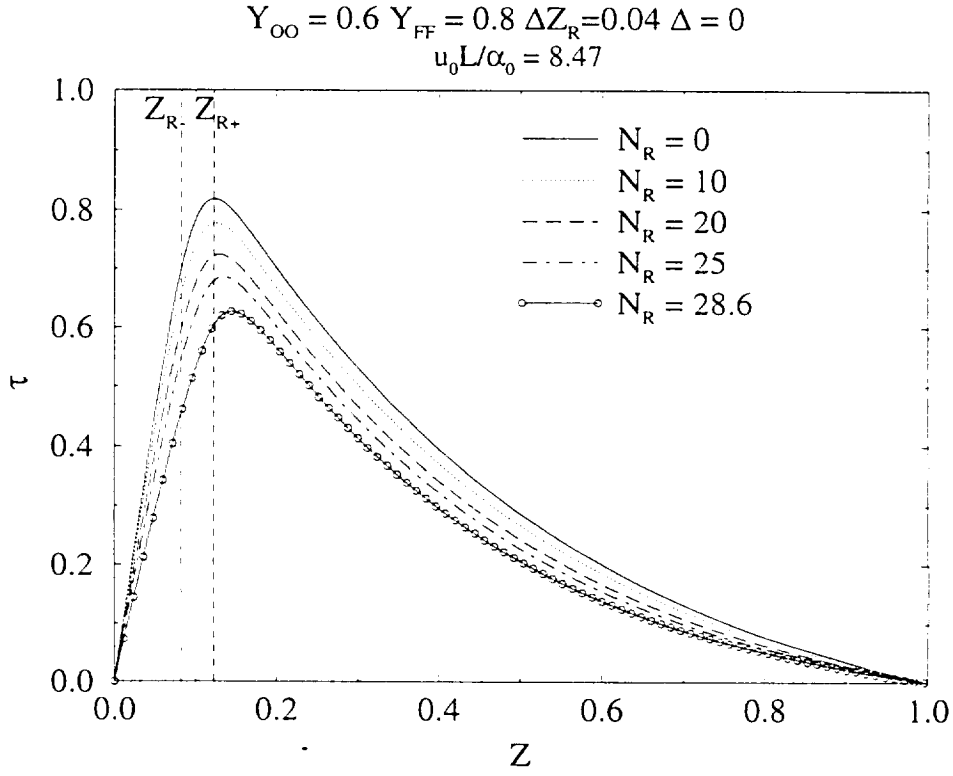

Figure 4.6. Effect of N_R on the temperature profile.

Next, the effect of increasing the intensity of the radiative loss zone, N_R, on a diffusion flame with prescribed fuel and oxidizer mass fractions in the respective reservoirs and a given u_0 through the fuel wall is investigated. The thickness of the loss

zone, ΔZ_R, is assumed to be 0.04 and the separation distance Δ is zero. As is evident from Figure 4.6, the temperature profile is uniformly and monotonically lowered as N_R is increased. The peak of the temperature profile moves toward the fuel wall with increased radiative losses. For N_R values greater than 28.6, the temperature profile crashes to zero; here we can not obtain a steady state profile. We also observe that for higher values of N_R, a given incremental increase in N_R results in a relatively greater degree of collapse of the temperature profile, i.e., the collapse of the temperature profile is accelerated. Simultaneously, the rate of movement of the temperature peak toward the fuel wall is also enhanced for higher values of N_R.

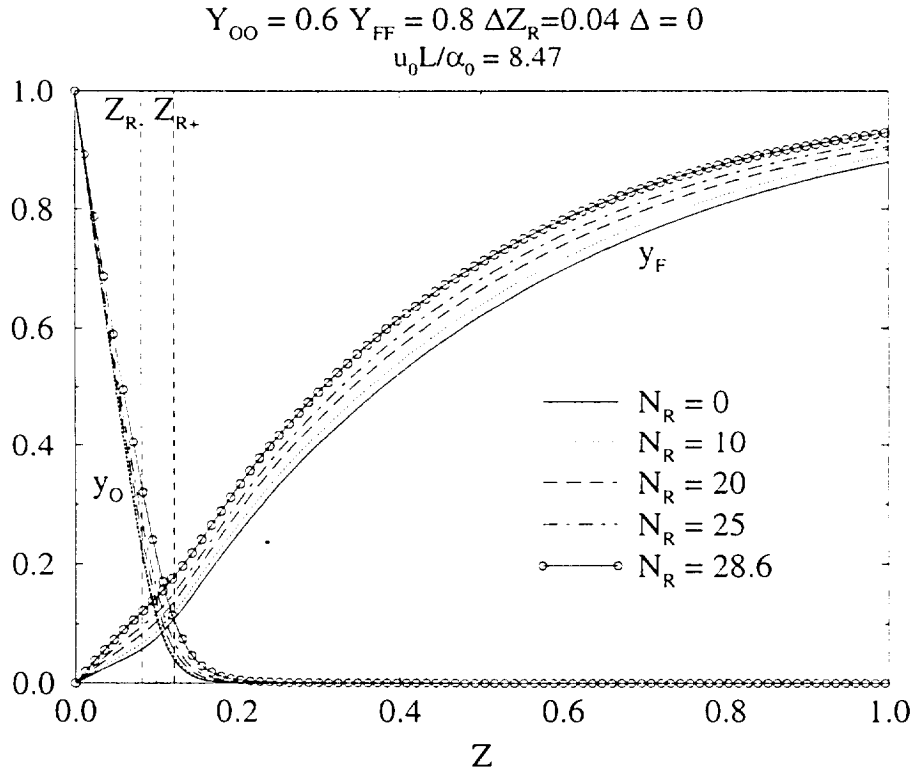

Figure 4.7. Effect of N_R on y_O and y_F profiles.

Figure 4.7 shows the species profiles, y_O and y_F, as a function of the Z coordinate. We recall once again that Z is not the mixture fraction, see equation 4.12. The change in the oxidizer profile is not very pronounced. However, the y_F profile significantly changes for increasing values of N_R. For $N_R = 28.6$, y_F everywhere is conspicuously greater than for the no-loss case. The reaction rate decreases with increasing N_R and, consequently, the flame consumes less fuel and oxidizer. Hence, both the oxidizer and fuel mass fractions are greater everywhere for higher values of N_R.

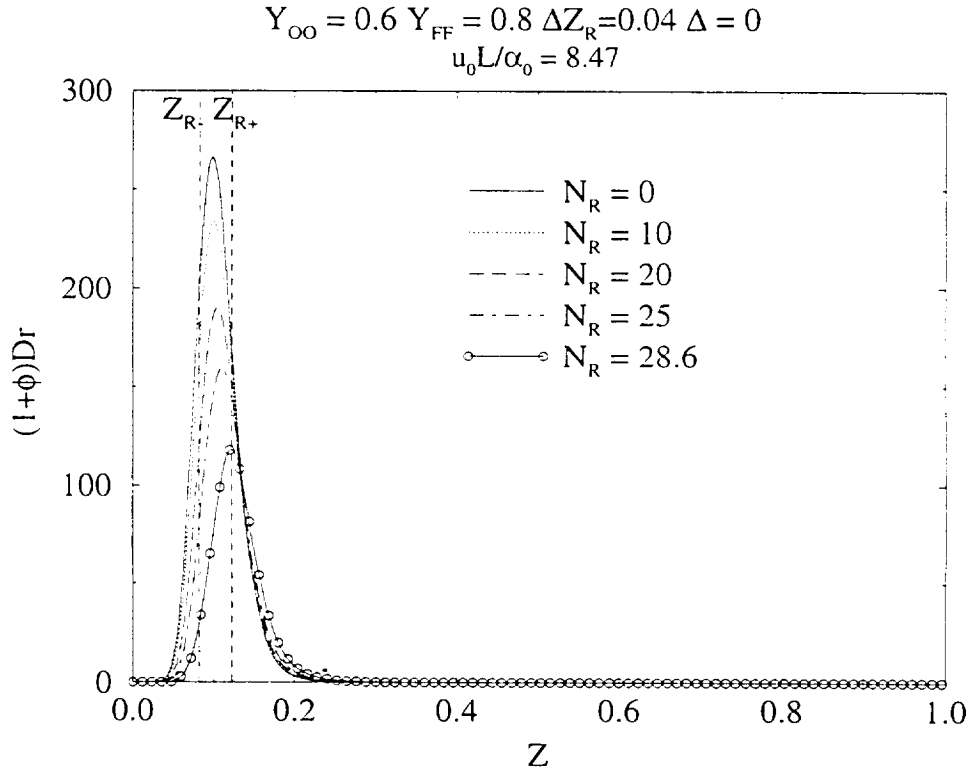

Figure 4.8. Effect of N_R on reaction rate profiles.

The reaction rate profiles are illustrated in Figure 4.8. With increased radiative losses, the reaction rates decrease significantly. Also, consistent with the migration

of the temperature peak, the reaction rate peak also moves toward the fuel side. The rate of decrease in the reaction rate peak seems to increase for higher values of N_R. It is clear from a comparison of Figure 4.6 and Figure 4.8 that the temperature peak at Z_τ is further to the oxidizer side than the reactivity peak Z_r for each and every value of the radiation number N_R.

The influence of increasing the loss zone thickness is investigated next (Figure 4.9): ΔZ_R is now increased to 0.1. The peak of the temperature profile indicates a migra-

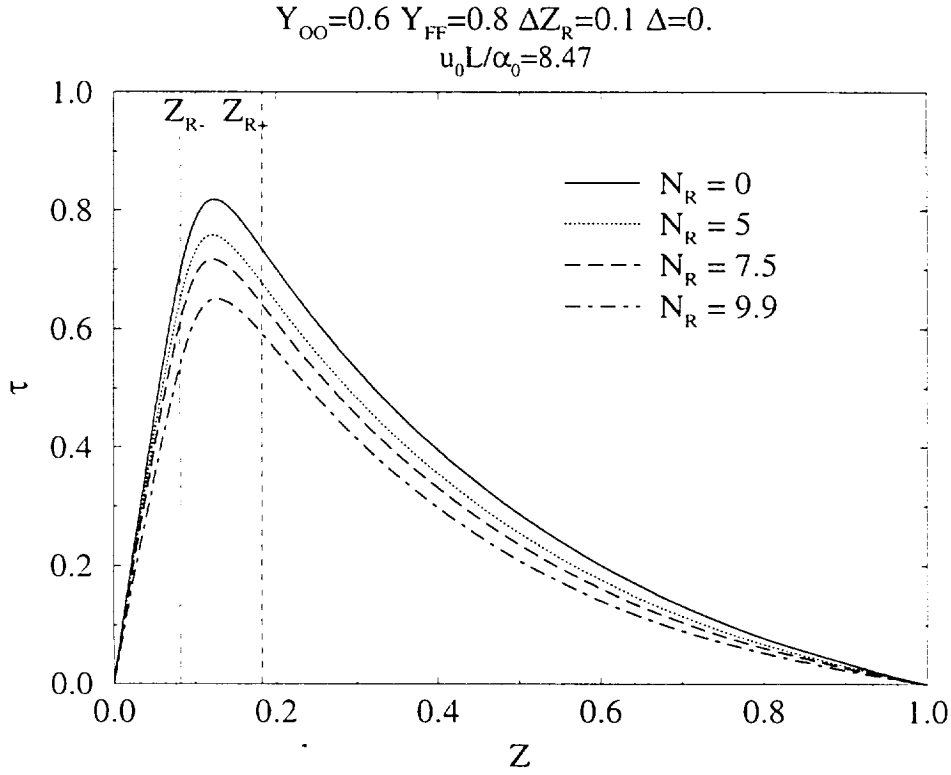

Figure 4.9. τ profiles when $\Delta Z_R = 0.1$ and $\Delta = 0$.

tion toward the fuel wall. The movement is not very conspicuous, though, possibly because for the entire flame history the reaction zone is squarely inside the loss zone. Substantial movement to either side seems to be completely restricted. Similarly, the

reaction rate profile, shown in Figure 4.10, also exhibits a corresponding movement of the peak toward the fuel wall, although this movement is also very insignificant. We now turn our attention to the structure of the flame when $N_R = 9.9$, $\Delta Z_R = 0.1$

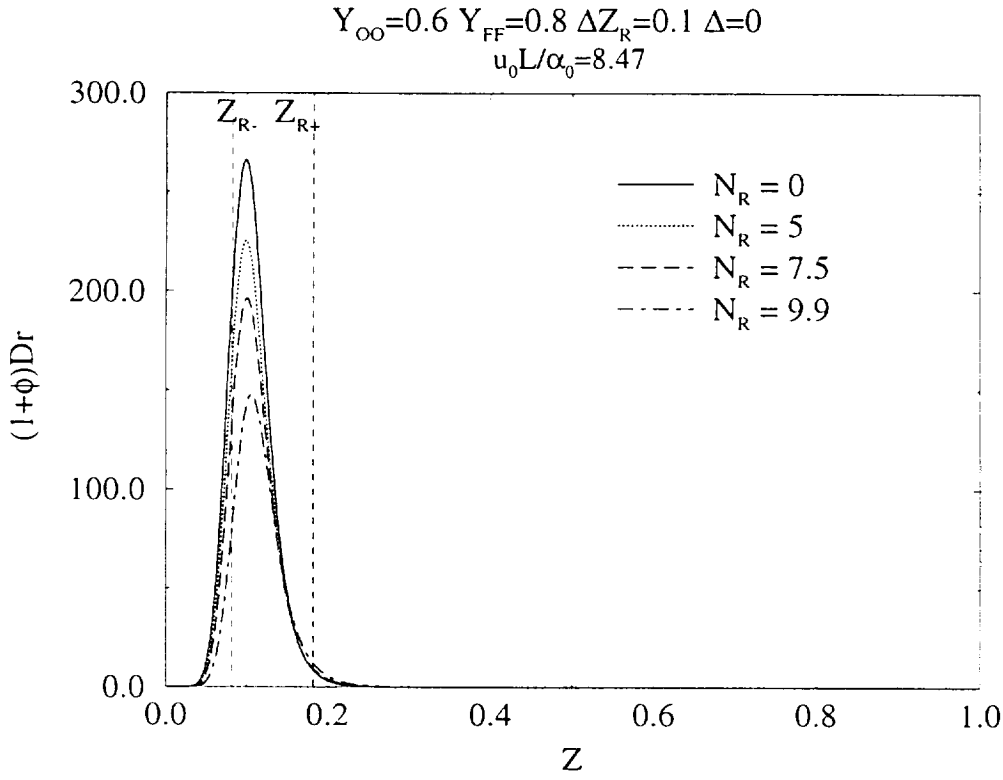

Figure 4.10. $(1 + \phi)\mathcal{D}r$ profiles when $\Delta Z_R = 0.1$ and $\Delta = 0$.

and $\Delta = 0$. For such a situation the flame is at the brink of extinction and any further increase of N_R results in the temperature profile crashing to zero everywhere. Figure 4.11 illustrates the profiles of the different terms in the energy equation. The convection $((1/\bar{s}_0)\tau_Z)$ and the diffusion $((\alpha_0/(u_0 L \bar{s}_0^2))\tau_{ZZ})$ terms balance one another very near the oxidizer wall and the reaction term is extremely small in that region. The primary balance in the vicinity of the flame, however, is between the reaction term and the diffusion term, i.e., the heat released by virtue of the combustion reac-

tion is diffused away from the primary reaction zone. The radiation loss is principally recovered by the reaction term.

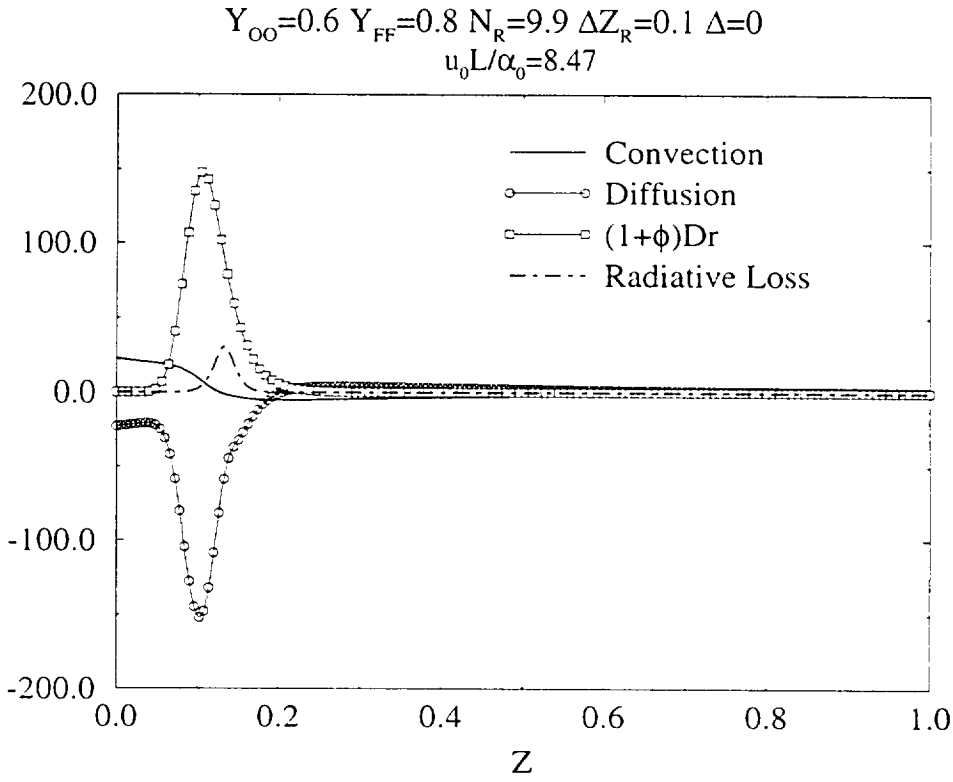

Figure 4.11. Flame structure when $N_R = 9.9$, $\Delta Z_R = 0.1$ and $\Delta = 0$.

We now investigate the effect of shifting the loss zone from the IRR flame location, Z_f. We consider the same flame as before, except we now introduce a separation distance of $\Delta = 0.1$. The nondimensional temperature profiles are plotted in Figure 4.12 for different values of N_R. Interestingly, in this case the maximum of the temperature profile shifts toward the oxidizer side. The reaction rate profiles also indicate a slight movement of the peak toward the oxidizer wall in Figure 4.13. This result is a rather

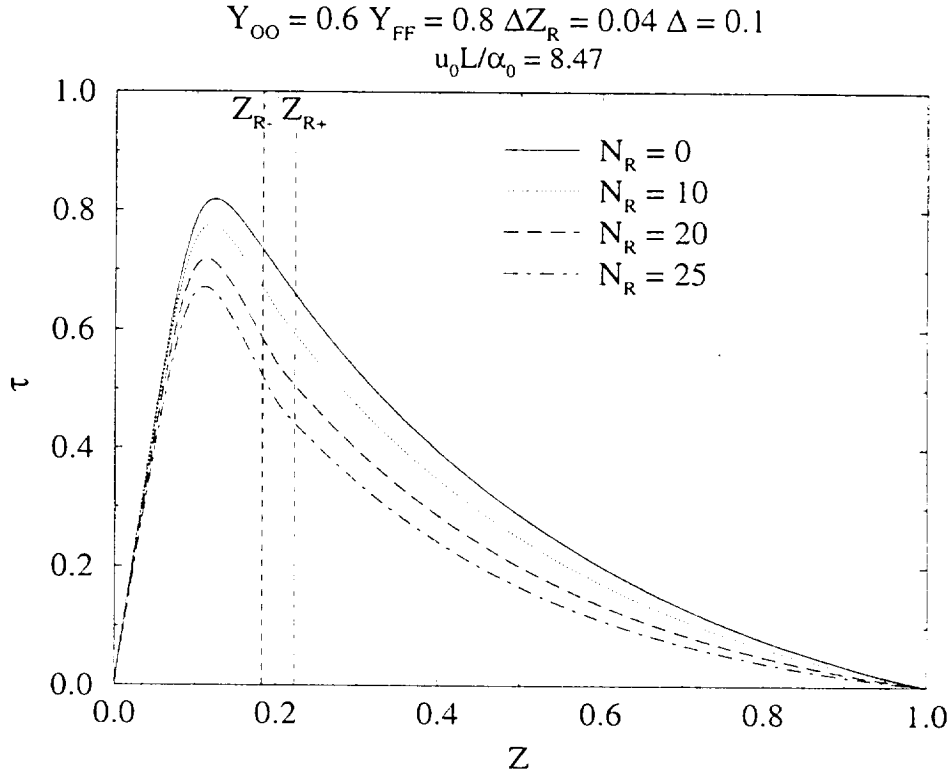

Figure 4.12. Loss zone is now separated from flame location. Observe the movement of the peak toward the oxidizer wall.

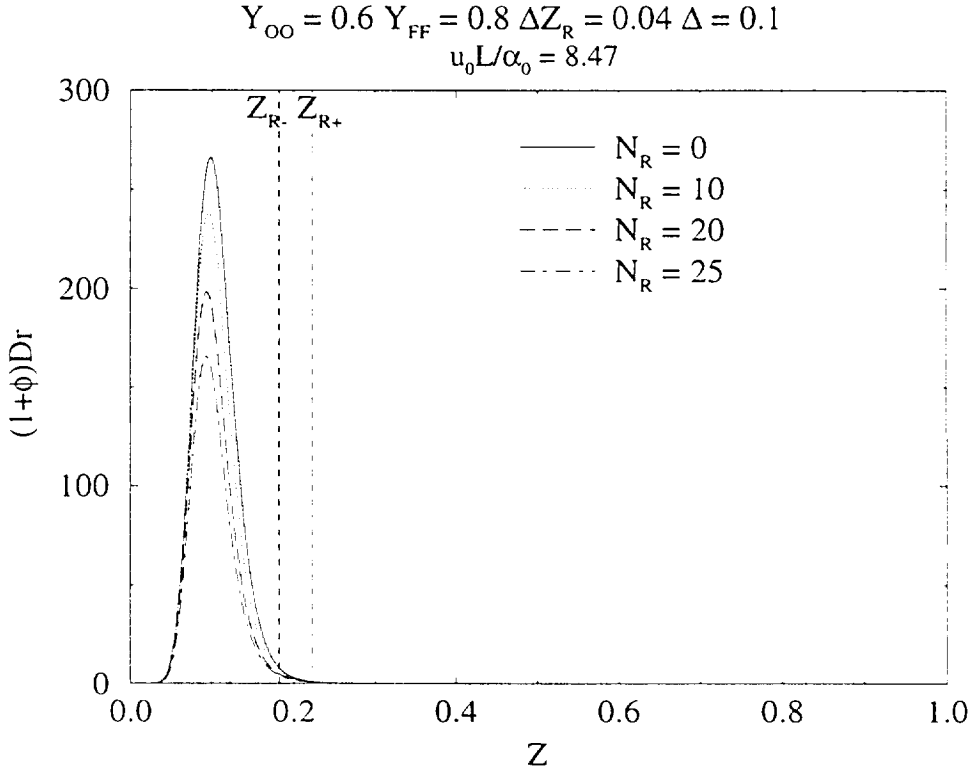

Figure 4.13. Reaction rate profiles when $\Delta = 0.1$.

interesting contrast to the case of the pure diffusion flame, where the reaction zone always moved toward the loss zone. Here we must observe that there are the three simultaneous influences of convection, diffusion and reaction: each can respond to the heat loss zone. In the pure diffusion flame we allowed only diffusion and reaction to counter the loss zone, and the response was predictable: the reaction zone always shifted toward the loss zone, even in those cases where it could never penetrate it (see Figures 3.9 and 3.10) of chapter 3. Here, convection from the fuel wall can force the reaction zone toward the oxidizer side, away from the loss zone.

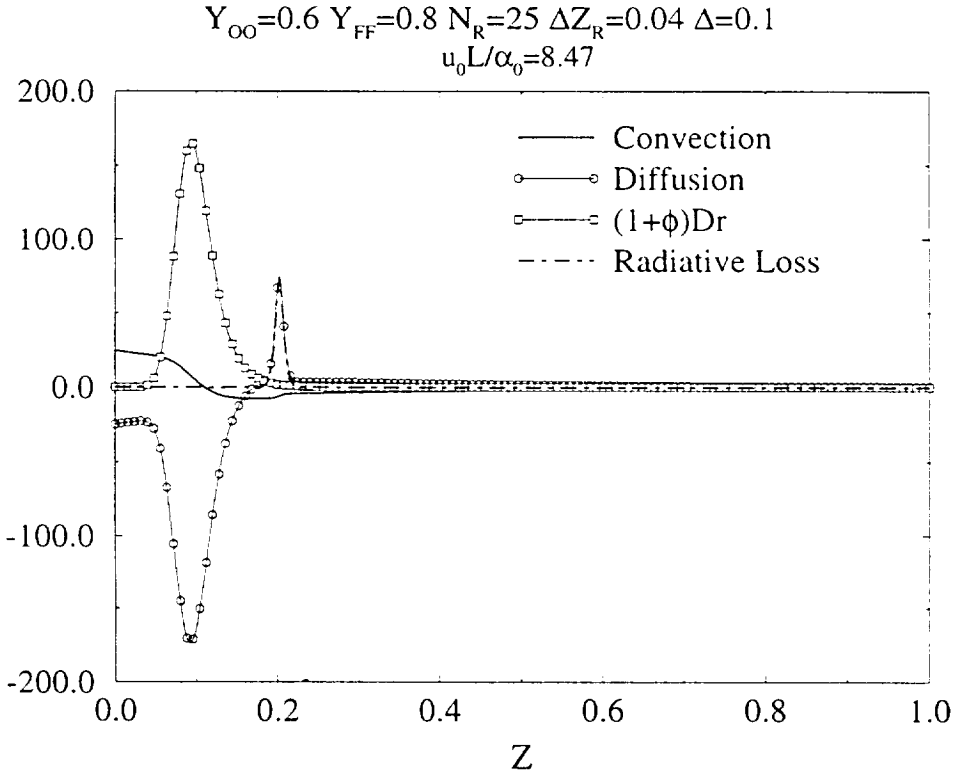

Figure 4.14. Flame structure when $N_R = 25$, $\Delta Z_R = 0.04$ and $\Delta = 0.1$.

Figure 4.14 shows the structure of the flame when $N_R = 25$, $\Delta Z_R = 0.04$ and $\Delta = 0$. For such a situation, the flame is at the brink of extinction. The convection,

diffusion, reaction and radiative loss terms of the energy equation are plotted to show the relative importance of each term. The primary balance is between the reaction and diffusion terms. It is also observed that the radiative loss term is recovered almost entirely by the diffusion term and that the two curves are virtually indistinguishable in the radiative loss zone. Interestingly, the reaction term does not contribute significantly toward recovering the radiative losses. This is because the heat loss zone is placed at a significant distance from the IRR flame location, Z_f, so the primary balance is between reaction and diffusion.

It is interesting to compare Figure 4.11 with Figure 4.14. In the former case the heat loss profile was placed right next to the ideal flame location Z_f. Hence, the reaction term had to battle the radiative loss term, unlike in the latter case when $\Delta = 0.1$ and the loss term was placed some distance away from the ideal flame location. Thus, the two flames have significantly different structures. So the separation distance Δ between Z_f and Z_{R-} plays an important role and decides how the loss term will be recovered. A significantly high value of Δ results in heat diffusion into the radiative loss zone by means of conduction. However when $\Delta = 0$ the reaction term has to counteract the effect of the imposed heat loss profile.

For the same separation distance of $\Delta = 0.1$ the loss zone thickness ΔZ_R is now increased to 0.08. As expected the flame extinguishes for a lower value of N_R (Figure 4.15). For $N_R > 13.1$ we do not obtain a steady flame. The location of the maximum flame temperature moves toward the oxidizer wall for increasing values of N_R. An investigation of the reaction rate profile also indicates similar behavior (Figure 4.16).

Let us investigate the effect of changing the velocity u_0 on the temperature and reaction rate profiles. The value of u_0 is decreased from 0.10 m/s to 0.05 m/s. The nondimensional parameter $u_0 L/\alpha_0$ decreases from 8.47 to 4.24. Interestingly, it is more difficult to extinguish the flame in this case. On decreasing the velocity u_0 the

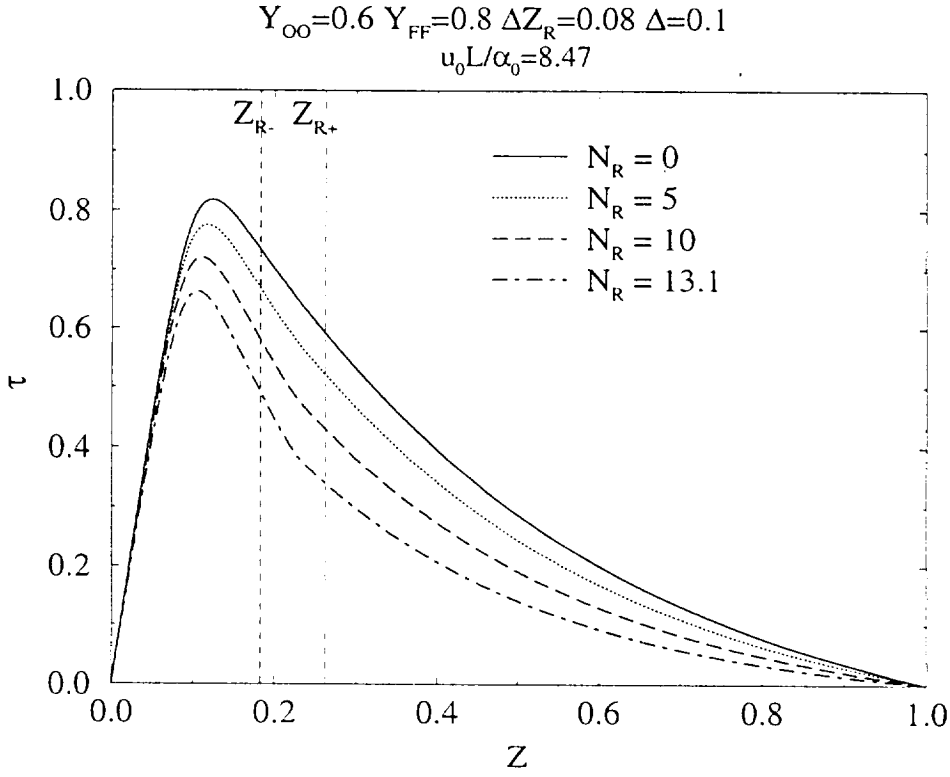

Figure 4.15. τ profiles when $\Delta Z_R = 0.08$ and $\Delta = 0.1$.

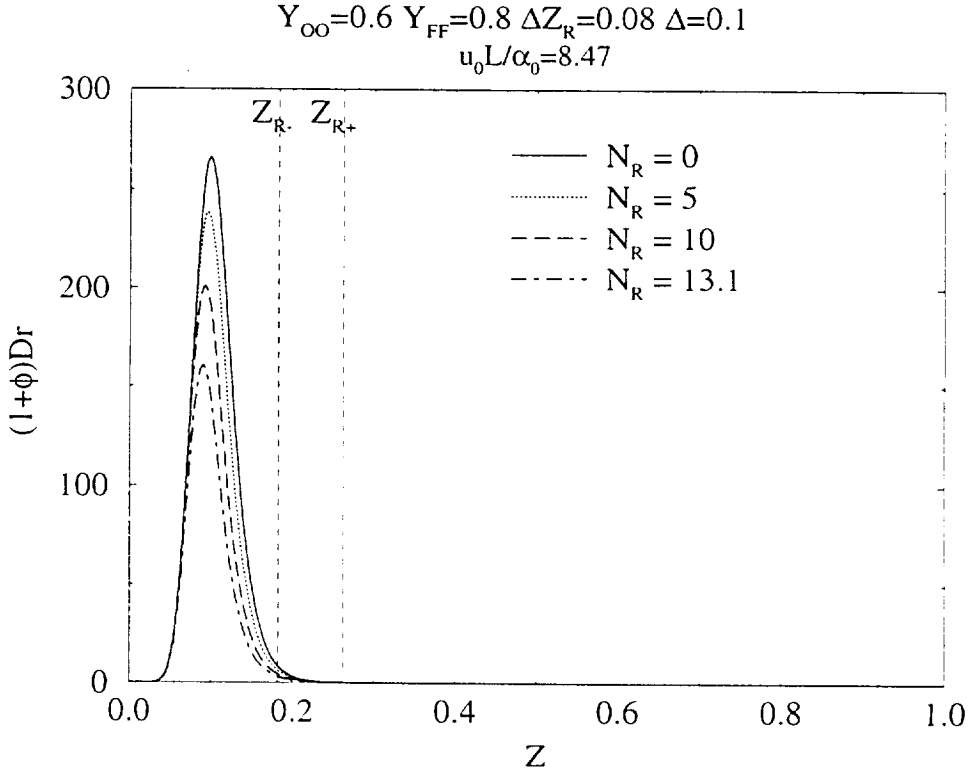

Figure 4.16. $(1 + \phi)\mathcal{D}r$ profiles when $\Delta Z_R = 0.08$ and $\Delta = 0.1$.

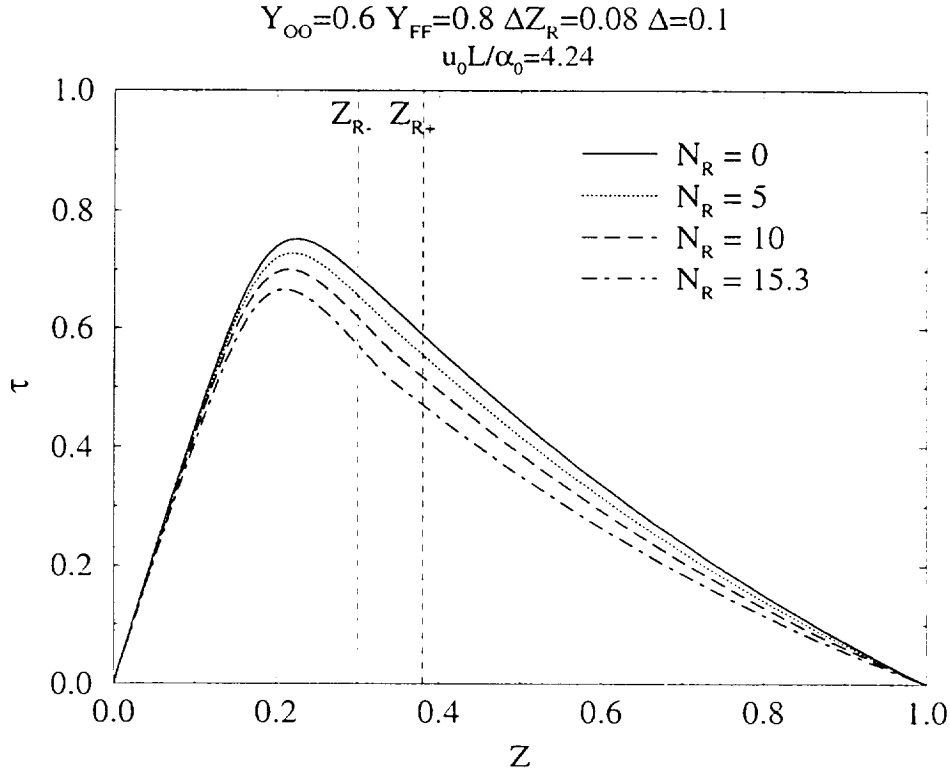

Figure 4.17. τ profiles when $u_0L/\alpha_0 = 4.24$.

flame moves away from the oxidizer wall and Z_f increases from 0.08 to 0.2. The flame loses less heat to the oxidizer wall when u_0 is smaller and consequently can survive for higher values of N_R. In this case also the location of the peak flame temperature, Z_τ, moves toward the oxidizer wall. Similar behavior was also observed for the reaction rate profile.

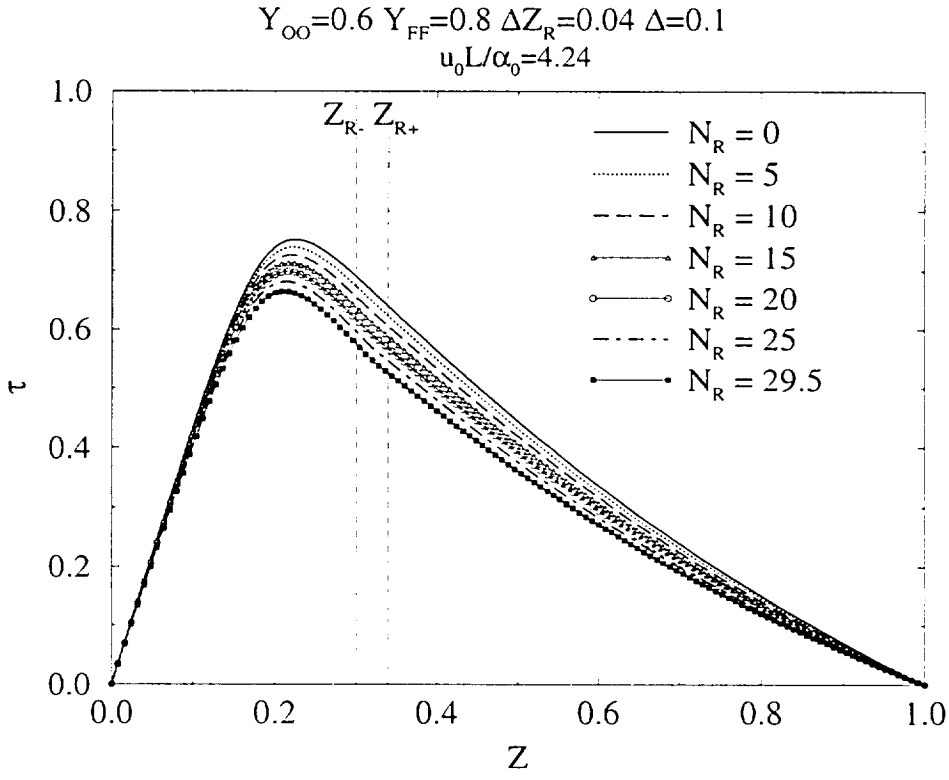

Figure 4.18. τ profiles when $u_0 L/\alpha_0 = 4.24$ and $\Delta Z_R = 0.04$.

The loss zone thickness ΔZ_R is then halved for the same value of $u_0 = 0.05$ m/s. Predictably, it becomes harder to extinguish the flame and the extinction value of N_R is 29.5, beyond which we do not obtain a steady state temperature profile. Consistent with previous observations we find that Z_τ moves toward the oxidizer wall with increasing values of N_R.

As explained in chapter 3 the heat transfer to the wall is important to examine. In the present situation, $Q_{W,O}$, i.e., the heat transfer to the oxidizer wall, is normalized with the reference convective heat flux, i.e., $\rho_0 u_0 C_p(T_f - T_0)$ to yield $\bar{Q}_{W,O} = (\alpha_0/(u_0 L \bar{s}_0))(d\tau/dZ)|_{Z=0} + 0.5\times(1/\bar{s}_0).N_R \int_0^1 (1/\bar{s}_0) d\bar{q}_R/dZ$. The quantity $\bar{Q}_{W,O}\bar{s}_0$ is plotted as a function of N_R in Figure 4.19.

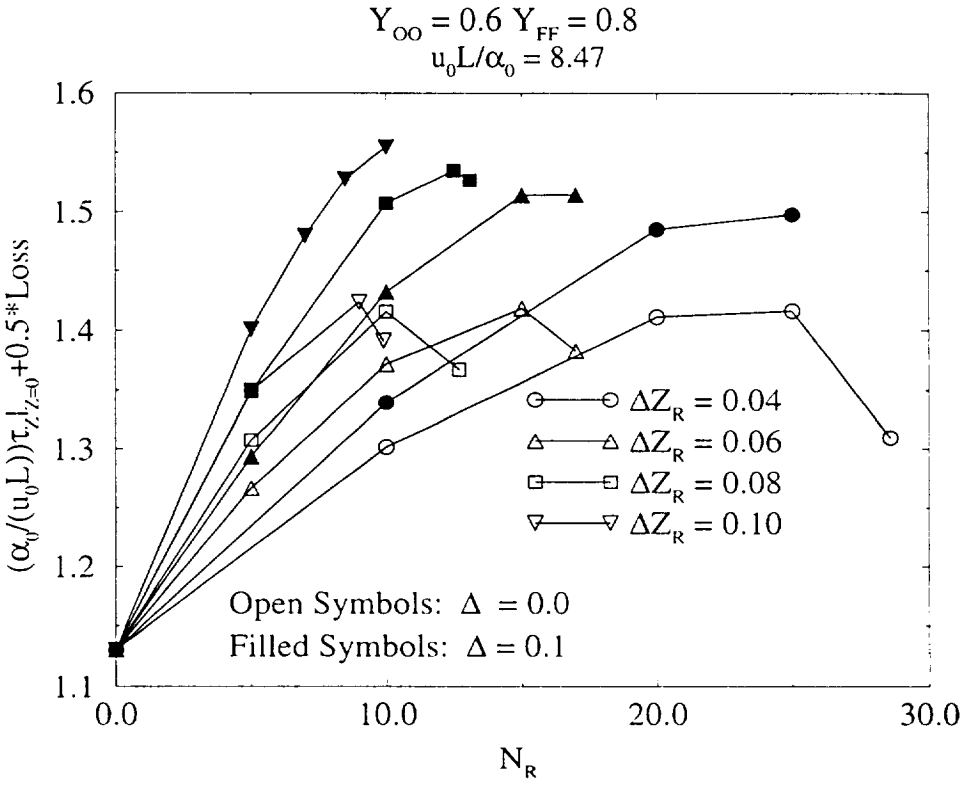

Figure 4.19. Heat transfer to the oxidizer wall as a function of N_R for the fuel blowing situation.

A comparison of Figure 4.19 with Figure 3.12 of chapter 3 reveals that unlike for a pure diffusion flame, the wall heat transfer characteristic curves are not grouped according to different loss zone thicknesses. The separation distance Δ seems to have significant impact in this case. In order to study this in greater detail we plot

$\bar{Q}_{W,O}\bar{s}_0$ as a function of the quantity $N_R(2/B)$ in Figure 4.20. We recall here that this quantity was very useful in collapsing the wall heat transfer, the total heat release and the radiative fraction data for a pure diffusion flame, as discussed in chapter 3. Figure 4.20 shows that for this situation we get two distinct sets of curves for the

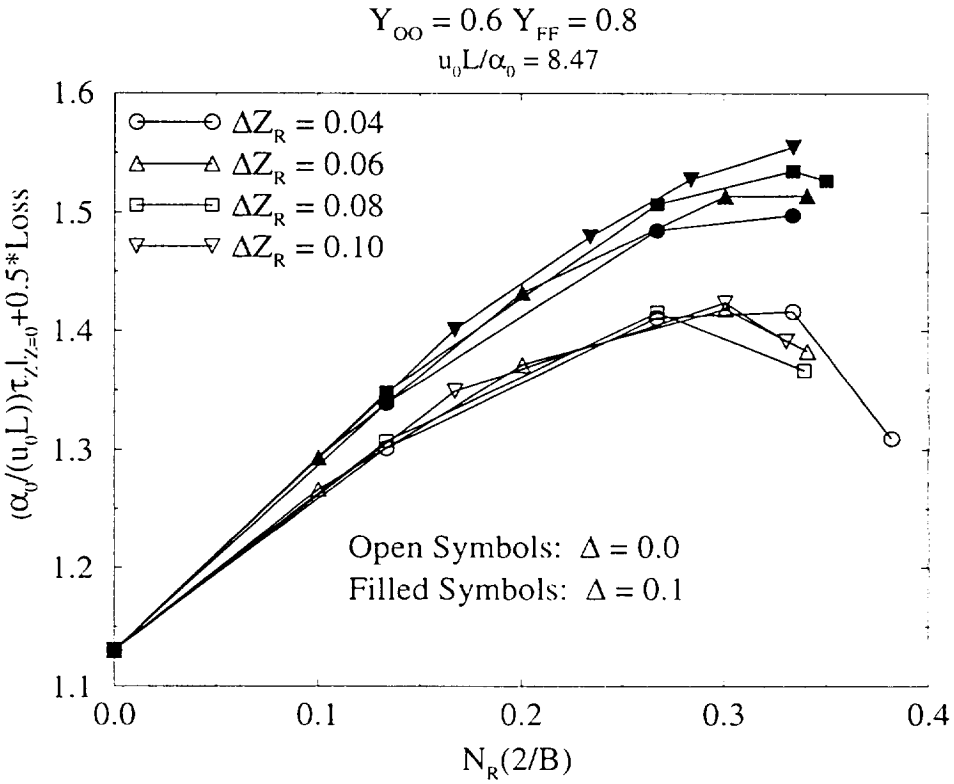

Figure 4.20. Heat transfer to the oxidizer wall as a function of $N_R(2/B)$ for the fuel blowing situation.

two different separation distances used. Hence, the separation distance of the loss zone from the flame turns out to be a very important parameter for a diffusion flame with fuel blowing. For a pure diffusion flame the separation distance Δ was not very important for the heat transfer to the wall since the data collapsed to one single curve.

We now focus on the radiative fraction, χ, given by the ratio q_{Rad}/q_{Total}. First,

the quantity q_{Total} is plotted as a function of the radiation number N_R in Figure 4.21. For thinner loss zones the rate of decrease of q_{Total} with N_R is less pronounced. For

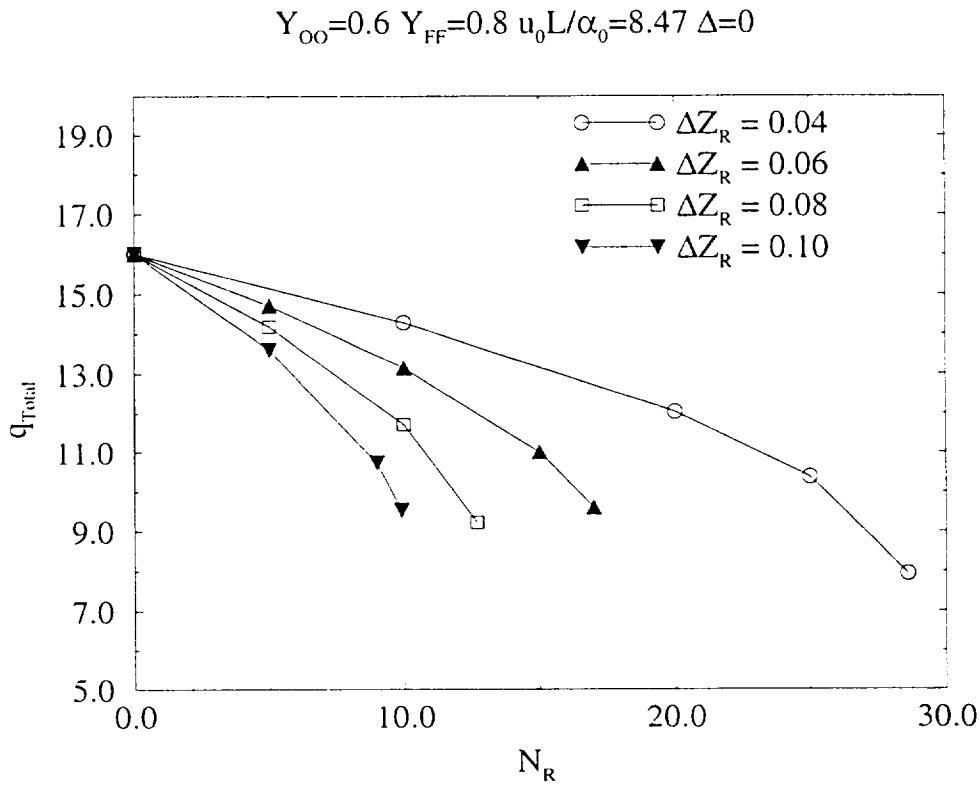

Figure 4.21. The total heat release in the combustion process plotted as a function of the radiation number N_R.

$\Delta Z_R = 0.10$, for example, q_{Total} steeply decreases with increasing values of N_R. In Figure 4.22 we plot q_{Total} values as a function of $N_R(2/B)$. As expected, the total heat release values correlate very well with $N_R(2/B)$ with a nearly straight-line dependence for $N_R(2/B)$ values less than approximately 0.25.

Figure 4.23 illustrates the variation of the radiative fraction χ with the radiation number N_R. The magnitude of χ increases with increasing N_R until extinction occurs. It is observed here that the values of χ are significantly lower than for a pure diffusion

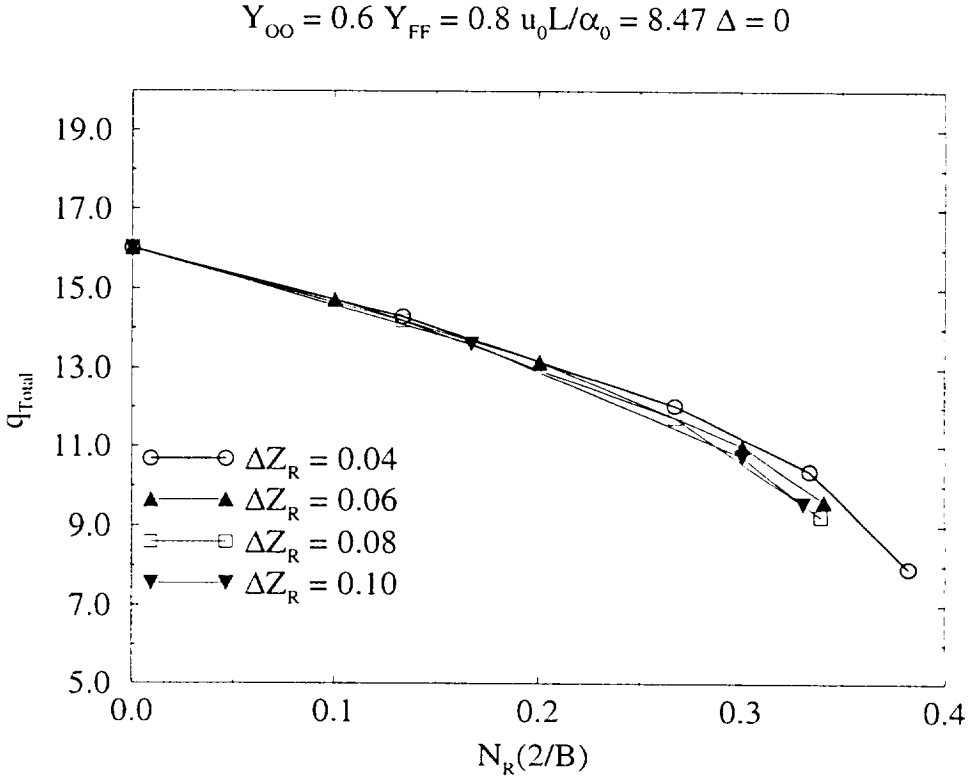

Figure 4.22. The total heat release in the combustion process plotted as a function of $N_R(2/B)$.

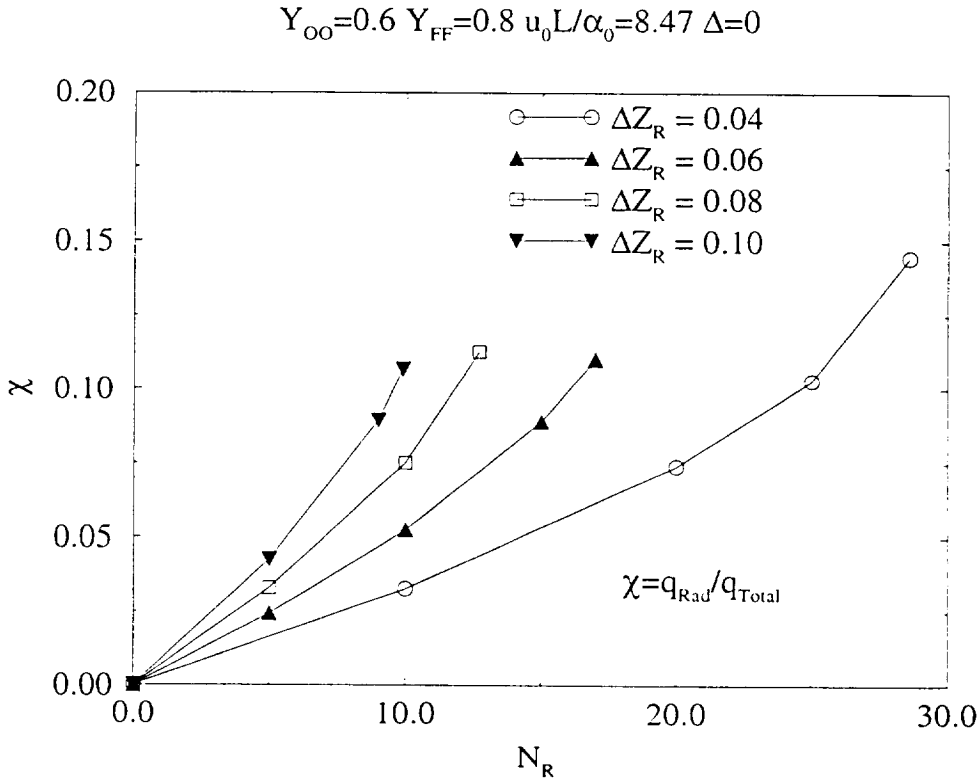

Figure 4.23. The total radiative fraction χ versus the radiation number N_R.

flame (see Figure 3.16).

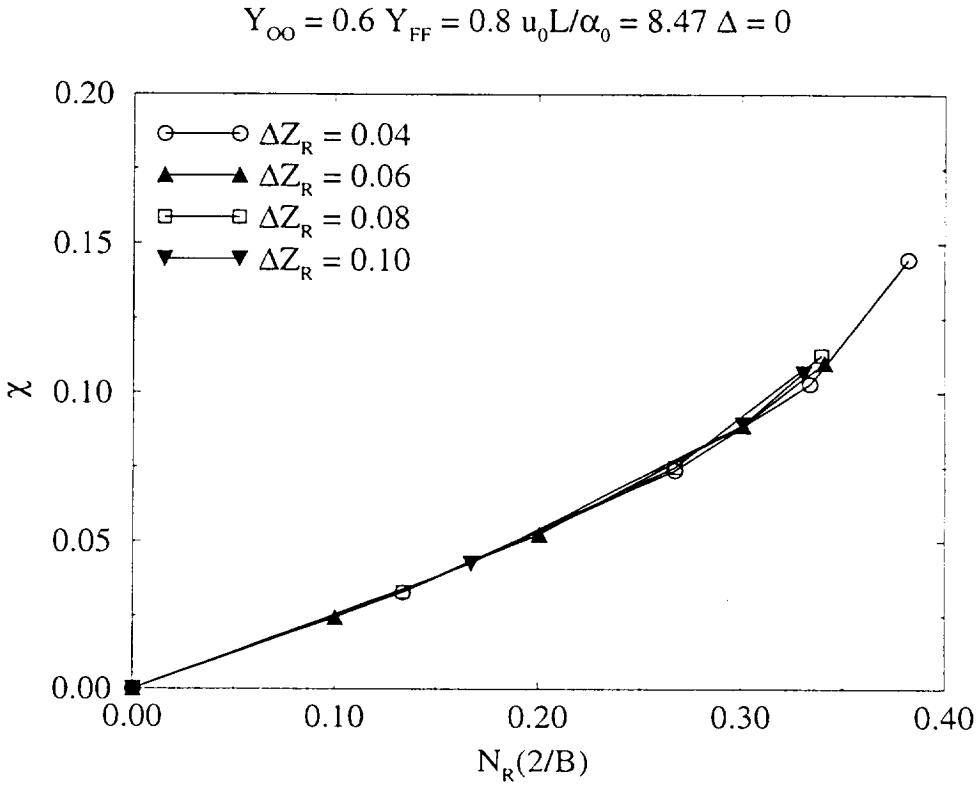

Figure 4.24. The total radiative fraction χ versus $N_R(2/B)$.

Next, in Figure 4.24 we plotted the radiative fraction χ as a function of $N_R(2/B)$, and, as expected, the curves for the different loss zone thicknesses collapsed onto one another. Thus, the quantity $N_R(2/B)$ is of great importance when analyzing important quantities of practical interest.

Figure 4.25 shows the variation of the drop in peak flame temperature as a function of the radiative fraction χ. As mentioned in chapter 3, $\Delta\tau_f$ is defined as $1 - \tau_f$. The quantity $\Delta\tau_f$ was found to increase almost linearly with the increase of the radiative fraction χ. It is also observed that the $\Delta\tau_f$ curves diverge from one another for high values of N_R for the different loss zone thicknesses shown in the figure.

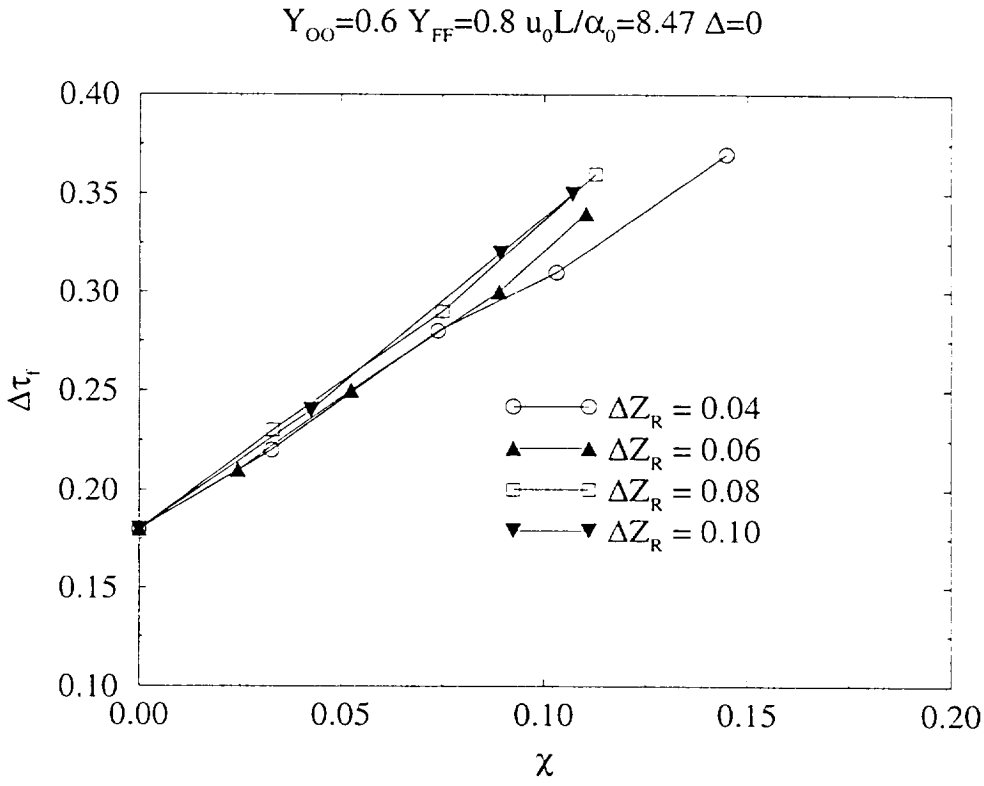

Figure 4.25. $\Delta\tau_f$ as a function of the radiative fraction χ.

4.8 Conclusions

In this chapter the influence of a $sech^2$ heat loss profile on a diffusion flame with fuel blowing from the fuel wall was investigated. The analysis in this chapter is quite similar to that in chapter 3. However, the influence of convection gives rise to more complexities in the flame behavior compared to a pure diffusion flame.

An important parameter in this chapter is the fuel blowing velocity at the fuel wall, i.e., u_0. An increase in u_0 resulted in a flame movement toward the oxidizer wall. The peak flame temperature also increased. The reaction rate profile became taller and narrower as the flame moved closer to the oxidizer wall. The integrated value of the reaction rate, q_{Total}, however, decreased with increasing u_0. The proximity of the oxidizer wall is the primary reason for such a decrease in q_{Total}. When the flame is close to the oxidizer wall it loses much heat to the wall and hence there is a resultant decrease in the q_{Total} values. It was also observed that the rate of movement of the flame toward the oxidizer wall slowed down at higher values of the fuel blowing rate.

Next, the intensity, the width and the location of the $sech^2$ heat loss zone were varied systematically to examine the influence of each of the variables on the flame. An increase in the width of the radiation loss zone resulted in a smaller value of extinction radiation number i.e., $N_{R,extinction}$. It was observed that for loss zones placed right next to the infinite reaction rate (IRR) flame location, Z_f, the reaction term recovers the radiation loss term and the diffusion term does not contribute significantly to such a recovery process. If, however, the loss term is placed at a significant distance from Z_f, the reaction term does not recover the loss term. Rather, the diffusion term has to counter the loss term and conduct heat to the region of loss. Thus, the flame structure depends significantly on where the loss zone is placed.

The migration of the temperature and reactivity peaks was also investigated for each situation. It was observed that for loss zones placed at a sufficient distance

from Z_f the flame may move slightly toward the oxidizer wall in certain cases. Such behavior is in sharp contrast with pure diffusion flames studied in chapter 3. For pure diffusion flames, the reaction zone always moved toward the fuel wall for increased heat losses. For diffusion flames with fuel blowing, however, the presence of convection complicates matters significantly, and the flame may move in the opposite direction.

For a loss zone of a given thickness and separation distance, it was observed that decreasing the fuel blowing velocity, u_0, resulted in a higher extinction radiation number. When u_0 is decreased the flame moves more toward the fuel wall and away from the oxidizer wall. Hence it loses less heat to the oxidizer wall and it then becomes more difficult to extinguish the flame.

An analysis of the heat transfer to the wall revealed that the separation distance Δ has significant influence on the characteristics of the curves. However, a similar examination of the heat transfer characteristics for pure diffusion flames in chapter 3 indicated that the separation distance Δ was not important at all. Hence, the analysis in the current chapter suggests that the introduction of fuel blowing can give rise to a variety of interesting behaviors. The quantity $N_R(2/B)$ was found to be quite useful, as in chapter 3 in correlating the wall heat transfer rate, the total heat release and the radiative fraction.

CHAPTER 5

Estimation of Soot Layer Profile and Thickness

5.1 Introduction

In this chapter approximate methods for estimating the soot layer profile and thickness are discussed. A soot volume fraction equation was developed based on the model of Syed, Stewart and Moss [1]. The equation was then numerically solved subject to the assumption of infinite reaction rate (IRR) profiles for temperature and species. A thorough analysis of the results revealed that the essential balance for the soot volume fraction equation is between the convection and the soot growth rate terms. Such a balance yielded to analytical treatment and resulted in an expression for the soot volume fraction profile in integral form. The integral was evaluated by two approximate methods. A comparison of the results using the analytical formulæ with the numerical solution indicated good agreement. A soot radiation term was then formulated using the soot volume fraction profile thus obtained. The effect of soot radiation on the temperature profile was investigated using the radiation term in the energy equation.

In the following sections, we discuss the Syed, Stewart and Moss [1] model, develop

the soot volume fraction equation, investigate the numerical solution, derive analytical expressions for the soot volume fraction profile and compare the analytical results with the numerical solution. The influence of a prescribed soot volume fraction profile on the radiation characteristics of a diffusion flame is also described.

5.2 Soot Model

The soot model used here is based on the work by Syed, Stewart and Moss [1]. Their two-equation model consists of a number density equation and a volume fraction equation

$$\frac{d}{dt}(\frac{n}{N_0}) = \hat{\alpha} - \hat{\beta}(\frac{n}{N_0})^2, \tag{5.1}$$

$$\rho_s \frac{df_V}{dt} = \hat{\gamma}(\rho_s f_V)^{\frac{2}{3}} n^{\frac{1}{3}} + \hat{\delta}. \tag{5.2}$$

The quantity n is the soot particle number density (number of particles per m^3) and f_V is the soot volume fraction in $m^3{}_{soot}/m^3{}_{gas}$. The density of soot, ρ_s, is assumed to be 1800 kg/m^3. The quantity N_0 is the Avogadro number, 6.0×10^{26}. In equation 5.1 the term $\hat{\alpha}$ corresponds to the process of soot nucleation. The second term on the right hand side accounts for the decrease in particle number density due to coagulation. Soot nucleation results in inception of new particles and hence, a corresponding increase in the number density. The process of coagulation results in a decrease in number density and hence the $-$ve sign before $\hat{\beta}$. As noted in [14], theoretically the decrease in particle number density can be expected to occur according to the Smoluchowski equation $dN/dt = -\mathcal{K}N^2$ where the rate constant $\mathcal{K}$ depends on the particle diameter. The coagulation term in equation 5.1 bears close resemblance to the Smoluchowski equation. The coefficients $\hat{\alpha}$, $\hat{\beta}$, $\hat{\gamma}$ and $\hat{\delta}$ are given by the following

expressions [1]:

$$\begin{aligned}
\hat{\alpha} &= C_{\hat{\alpha}}\rho^2 T^{\frac{1}{2}} X_F \exp(-T_{\hat{\alpha}}/T) && \text{(Nucleation)} \\
\hat{\beta} &= C_{\hat{\beta}} T^{\frac{1}{2}} && \text{(Coagulation)} \\
\hat{\gamma} &= C_{\hat{\gamma}}\rho T^{\frac{1}{2}} X_F \exp(-T_{\hat{\gamma}}/T) && \text{(Surface Growth)} \\
\hat{\delta} &= 144 \times \hat{\alpha} && \text{(Nucleation)}
\end{aligned} \tag{5.3}$$

In the above, X_F is the mole fraction of the parent fuel, i.e., methane in our case. It can be shown that $X_F = Y_F \bar{W}/W_F$, where Y_F is the fuel mass fraction, $\bar{W}$ is the average molecular weight of the mixture and W_F is the molecular weight of the fuel. The quantities $T_{\hat{\alpha}}$ and $T_{\hat{\gamma}}$ are activation temperatures and have the values 46.1×10^3 K and 12.6×10^3 K respectively. The quantities $\hat{\alpha}$ and $\hat{\delta}$ are related to soot particle nucleation and $\hat{\beta}$ and $\hat{\gamma}$ are related to the processes of coagulation and surface growth respectively. The values of the constants $C_{\hat{\alpha}}$, $C_{\hat{\beta}}$ and $C_{\hat{\gamma}}$ are [1]

$$\begin{aligned}
C_{\hat{\alpha}} &= 6.54 \times 10^4 && [m^3/kg^2 K^{1/2} s] \\
C_{\hat{\beta}} &= 1.3 \times 10^7 && [m^3/K^{1/2} s] \\
C_{\hat{\gamma}} &= 0.1 && [m^3/kg^{2/3} K^{\frac{1}{2}} s]
\end{aligned} \tag{5.4}$$

5.3 Examination of the Soot Model

In this section, an asymptotic mathematical examination of the Syed, Stewart and Moss [1] model is carried out to enhance our understanding of the model. Writing $\eta = n/N_0$, $\bar{\eta} = \eta/\eta_0$, $\bar{t} = t/t_0$, $\bar{T} = T/T_*$, $\bar{\rho} = \rho/\rho_*$ and using the expressions for $\hat{\alpha}$, $\hat{\beta}$, $\hat{\gamma}$ and $\hat{\delta}$ from 5.3 we can simplify equation 5.1 to get:

$$\frac{d\bar{\eta}}{d\bar{t}} = a\bar{\rho}^2 \bar{T}^{1/2} e^{-(\frac{T_{\hat{\alpha}}}{\bar{T}} - \bar{T}_{\hat{\alpha}})} - b\bar{T}^{\frac{1}{2}}\bar{\eta}^2 \tag{5.5}$$

where $a = (X_F N_0 t_0 C_{\hat{a}} \rho_*^2 T_0^{\frac{1}{2}} \epsilon^{-\bar{T}_{\hat{a}}})/n_0$ and $b = (C_3 T_*^{1/2} n_0 t_0)/N_0$. The quantities a and b are related to soot nucleation and particle coagulation, respectively. The quantity n_0 is a reference number density. Similarly, writing $\bar{f}_V = f_V/f_{V0}$, equation 5.2 can be recast in the following form:

$$\frac{d\bar{f}_V}{d\bar{t}} = c\bar{\rho}\bar{T}^{\frac{1}{2}} e^{-(\frac{\bar{T}_{\hat{s}}}{\bar{T}} - \bar{T}_{\hat{s}})} \bar{f}_V^{\frac{2}{3}} \bar{\eta}^{\frac{1}{3}} + d\bar{\rho}^2 \bar{T}^{\frac{1}{2}} e^{-(\frac{\bar{T}_{\hat{a}}}{\bar{T}} - \bar{T}_{\hat{a}})} \tag{5.6}$$

where $c = X_F n_0^{1/3} t_0 C_{\hat{s}} \rho_* T_*^{1/2} e^{-T_{\hat{s}}}/\rho_s f_{V0}^{1/3}$ and $d = 144 C_{\hat{a}} t_0 \rho_*^2 T_*^{1/2} X_F \epsilon^{-T_{\hat{a}}}/\rho_s f_{V0}$. The quantities c and d are respectively related to the processes of surface growth and nucleation. We now choose t_0 such that $c = 1$, which results in $t_0 = (\rho_s^{\frac{1}{3}} f_{V0}^{\frac{1}{3}} \epsilon^{T_{\hat{s}}})/(X_F n_0^{\frac{1}{3}} C_{\hat{s}} \rho_* T_*^{\frac{1}{2}})$. This is done because we expect that the increase of f_V is mostly through surface growth, and the balance (df_V/dt)~surface growth reflects the overall soot creation time scale. The quantities a, b and d are then evaluated using the above value of t_0. Next, the reference quantities ρ_* and T_* are chosen in such a way that $\bar{\rho}\bar{T} = 1$. Equations (5.5) and (5.6) can now be written (after dropping the bars on various quantities) as

$$\frac{d\eta}{dt} = aT^{-\frac{3}{2}} \epsilon^{-(\frac{T_{\hat{a}}}{T} - T_{\hat{a}})} - bT^{\frac{1}{2}} \eta^2 \tag{5.7}$$

subject to $\eta(0) = 0$ and

$$\frac{df_V}{dt} = T^{-\frac{1}{2}} \epsilon^{-(\frac{T_{\hat{s}}}{T} - T_{\hat{s}})} f_V^{\frac{2}{3}} \eta^{\frac{1}{3}} + dT^{-\frac{3}{2}} e^{-(\frac{T_{\hat{a}}}{T} - T_{\hat{a}})} \tag{5.8}$$

subject to $f_V(0) = 0$. Particle number density and volume fraction are both zero at the initial time ($t = 0$). Next, it is assumed that the system is isothermal, and the nondimensional $T = 1$, i.e., T_* is the constant temperature of the system. Two distinct cases are studied in the following subsection depending on the level of saturation of η.

5.3.1 Rapid equilibration of η

Let us assume that the particle concentration η rapidly equilibrates to its asymptotic value. This assumption is of practical relevance and is supported in the literature [1], [12]. In that limit, $d\eta/dt = 0$ and by virtue of equation 5.7, $\eta = \sqrt{(a/b)}$. If for convenience we define the maximum value of η as 1, then $a = b$. The equality of a and b can be exploited to yield an expression for the characteristic number density n_0,

$$\frac{n_0}{N_0} = \sqrt{\frac{C_\delta}{C_\beta}\rho_*^2 X_F e^{(-\frac{T_\delta}{T_*})}}.$$

With $T = 1$ equation 5.7 becomes

$$\frac{d\eta}{dt} = a(1 - \eta^2), \tag{5.9}$$

with $\eta(0) = 0$. The solution for equation 5.9 yields $\eta = (e^{2at}-1)/(e^{2at}+1)$. Examining the limit $\lim_{a\to\infty}\eta$, we conclude that a rapid equilibration of η to unity occurs when $a \gg O(1)$. The equilibration time is $t \simeq a^{-1}$. Similarly, equation 5.8 reduces to the following when $T = 1$:

$$\frac{df_V}{dt} = f_V{}^{\frac{2}{3}}\eta^{1/3} + d, \tag{5.10}$$

with the initial condition $f_V(0) = 0$. When η rapidly equilibrates to unity equation 5.10 becomes $df_V/dt = f_V{}^{\frac{2}{3}} + d$. In terms of new variables $\delta = f_V{}^{\frac{1}{3}}/\sqrt{d}$ and $\xi = t/3\sqrt{d}$, this equation becomes

$$\delta^2\frac{d\delta}{d\xi} = 1 + \delta^2, \tag{5.11}$$

subject to $\delta(0) = 0$. The substitution $\delta = \tan\theta$ gives $\tan^2\theta d\theta = d\xi$, with $\theta(0) = 0$. Consequently, $\xi = \tan\theta - \theta$ and, in terms of original variables, we have

$$t = 3\sqrt{d}[\frac{f_V{}^{\frac{1}{3}}}{\sqrt{d}} - tan^{-1}(\frac{f_V{}^{\frac{1}{3}}}{\sqrt{d}})]. \tag{5.12}$$

Solution of the above transcendental equation constitutes the first problem under consideration. We note that in the limit when $d \ll O(1)$ the second term in the above equation is negligible and we obtain the well-known result $f_V \sim (t/3)^3$. In the more general situation, a rapid equilibration of η is *not* assumed and equation 5.10 is solved using the result $\eta = (e^{2at} - 1)/(e^{2at} + 1)$. In the following, we carry out a discussion and comparison of the results for the two problems.

The numerical solution of equation 5.10 was obtained using the *NAG* fortran library routine *D02PCF*. This routine uses the Runge-Kutta method.

Figure 5.1 shows two sets of results for the soot volume fraction profiles. In the first case, d was set equal to 0.5, since d is the only parameter value which needs to be prescribed for the solution of equation 5.10. For $d = 0.5$ the saturated η assumption (equation 5.12) gives an f_V profile which is quite similar to the more general unsaturated case. For large times, however, the two curves tend to diverge, albeit at a rather slow rate.

When $d = 0.005$ the curves for saturated and unsaturated cases are virtually indistinguishable. It can be recalled at this point that d is the nucleation term in the soot volume fraction equation 5.10 and for a small value of d, the soot profile saturates fairly quickly. Hence, in this case, the assumption of η rapidly saturating to the value of unity is quite good. Also, when $d = 0.5$ the amount of soot generated is much more compared to the $d = 0.005$ case. This is because a much stronger nucleation term results in a higher soot volume fractions. Also plotted in both figures is the function $(t/3)^3$. As mentioned before, when $d \ll O(1)$, it is expected that $f_V \sim (t/3)^3$.

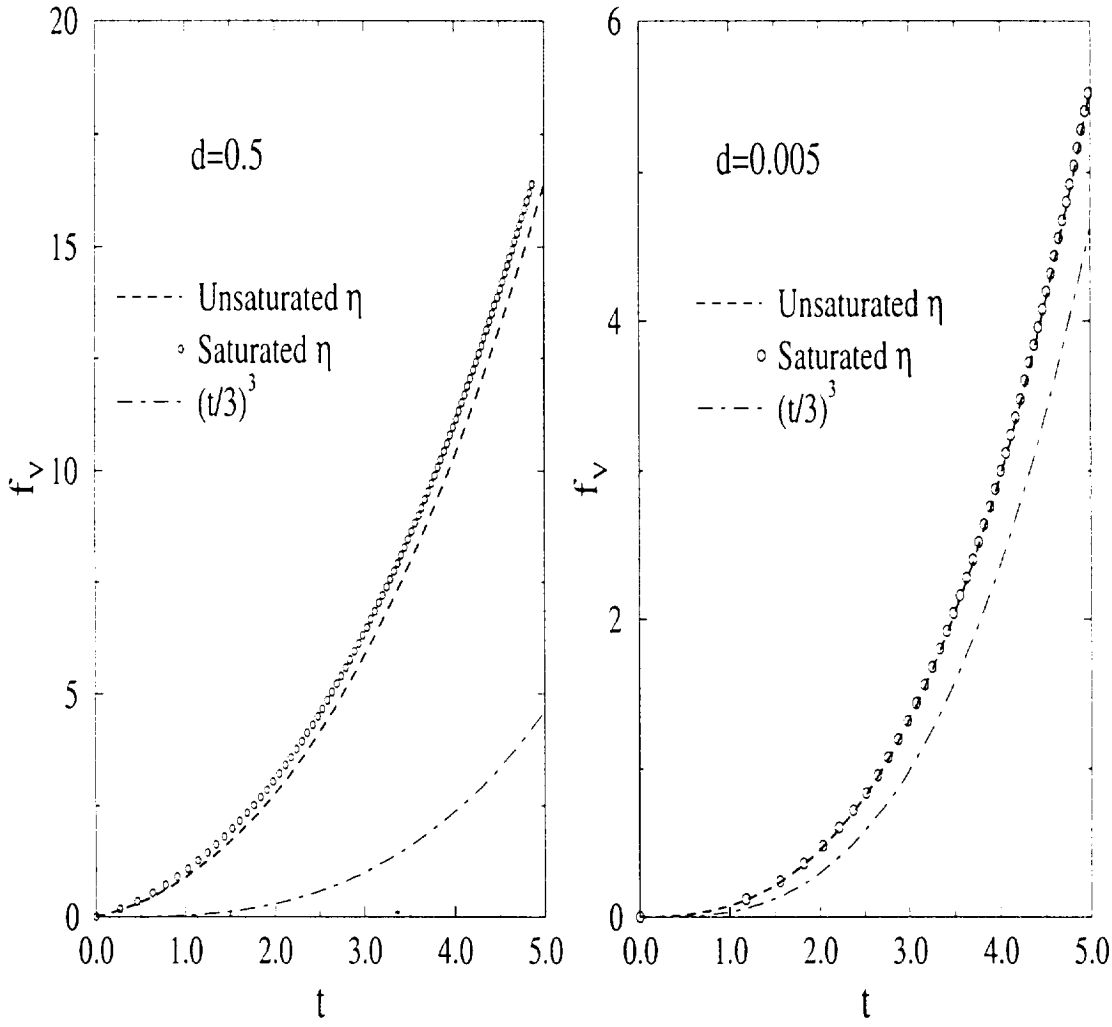

Figure 5.1. Comparison of f_V profiles for $d = 0.5$ and $d = 0.005$.

When $d = 0.005$ we see that the numerical solutions are indeed comparable to the $(t/3)^3$ curve. However, for $d = 0.5$, the $(t/3)^3$ curve is significantly different from the numerical solutions.

5.4 Formulation of the Full Problem

The problem geometry and boundary conditions are the same as described in Chapter 4 and illustrated in Figure 4.1. The soot volume fraction equation has the following form:

$$\rho(f_{V_t} + (u + u_T)f_{V_x}) = (\rho D_s f_{V_x})_x + \dot{w}_n + \dot{w}_g - \dot{w}_{ox}. \tag{5.13}$$

In equation 5.13 $\dot{w}_n$, $\dot{w}_g$ and $\dot{w}_{ox}$ are, respectively, the soot nucleation, growth and oxidation rates in units of kg/m^3s, u_T is a thermophoretic velocity term, which is neglected in the present analysis. Equation 5.13 contains a soot diffusivity, D_s, which is taken to be 1% of the gas diffusivity [12]. The physical coordinate of our problem is x with $0 \leq x \leq L$. The boundary conditions are $f_V(x = 0) = 0$ and $f_V(x = L) = 0$.

First we transform the equations to a (Z, t) system of coordinates, where $Z = 1 - s/s_0$ with $s = \int_0^x \rho dx$ and $s_0 = \int_0^L \rho dx$. As a result the soot volume fraction equation takes the following form:

$$f_{V_t} - \frac{(\rho_0 u_0 + \rho u_T)}{s_0} f_{VZ} = \frac{\rho^2 D_S}{{s_0}^2} f_{VZZ} + \frac{1}{\rho}(\dot{w}_n + \dot{w}_g - \dot{w}_{ox}). \tag{5.14}$$

Now, we define $\bar{t} = t/t_{ref}$ and $\bar{f}_V = f_V/f_{V_0}$, where f_{V_0} is a suitably chosen reference value. Consequently, the volume fraction equation becomes

$$\frac{\partial \bar{f}_V}{\partial \bar{t}} - \frac{(1 + \bar{m}_T)}{\bar{s}_0} \frac{\partial \bar{f}_V}{\partial Z} = \frac{D_{s0}}{u_0 L \bar{s}_0^2} \frac{\partial^2 \bar{f}_V}{\partial Z^2} + (\bar{A}\bar{r}_n + \bar{B}\bar{r}_g - \bar{C}\bar{r}_{ox}). \tag{5.15}$$

Here, $\bar{A} = Y_{FF} t_{ref}/f_{V_0} t_n$, $\bar{B} = Y_{FF} t_{ref}/f_{V_0} t_g$ and $\bar{C} = Y_{OO} t_{ref}/f_{V_0} t_{ox}$. The

quantities t_n, t_g and t_{ox} are characteristic time scales for the processes of soot nucleation, growth and oxidation respectively and are given by $t_n = \rho_0 Y_{FF}/\dot{w}_{n,ref}$, $t_g = \rho_0 Y_{FF}/\dot{w}_{g,ref}$ and $t_{ox} = \rho_0 Y_{OO}/\dot{w}_{ox,ref}$. The quantity t_{ref} is the characteristic flow time, given by $t_{ref} = L/u_0$, and $\dot{w}_{n,ref}$, $\dot{w}_{g,ref}$ and $\dot{w}_{ox,ref}$ are reference values for normalizing nucleation, growth and oxidation terms, respectively. We have also used $\bar{s}_0 = s_0/(\rho_0 L)$. The nondimensional thermophoretic term is denoted by $\bar{m}_T = \bar{\rho} u_T/u_0$. The soot diffusivity at the reference condition is D_{s0}. The rate terms $\bar{r}_n$, $\bar{r}_g$ and $\bar{r}_{ox}$ are respectively for soot nucleation, growth and oxidation and $\bar{r}_n = \dot{\bar{w}}_n/\bar{\rho}$, where $\dot{\bar{w}}_n = \dot{w}_n/\dot{w}_{n,ref}$. The growth rate term $\bar{r}_g$ and the oxidation rate term $\bar{r}_{ox}$ are defined similarly. Next, we assume that the temperature and species profiles are for the infinite reaction rate (IRR) case, which implies that no fuel exists on the oxidizer side and no oxidizer exists on the fuel side. In the absence of oxidizer on the fuel side, the source term for oxidation in the soot volume fraction equation can be discarded. Further, on neglecting the thermophoretic effect, the soot volume fraction equation reduces to

$$\frac{\partial \bar{f}_V}{\partial \bar{t}} - \frac{1}{\bar{s}_0}\frac{\partial \bar{f}_V}{\partial Z} = \frac{D_{s0}}{u_0 L \bar{s}_0^2}\frac{\partial^2 \bar{f}_V}{\partial Z^2} + (\bar{A}\bar{r}_n + \bar{B}\bar{r}_g) \tag{5.16}$$

At this stage, the expressions for $\bar{A}$ and $\bar{B}$ are still to be determined. The quantities $\bar{A}$ and $\bar{B}$ depend on the time scales t_n and t_g respectively, which, in turn, depend on the choices of $\dot{w}_{n,ref}$ and $\dot{w}_{g,ref}$. By comparing equation 5.13 with the volume fraction equation (equation 5.1) of the Syed, Stewart and Moss model [1], we can write $\dot{w}_n = \rho\hat{\delta}/\rho_s$ and $\dot{w}_g = (\rho/\rho_s)\hat{\gamma}(\rho_s f_V)^{2/3} n^{1/3}$. On substituting the expression for $\hat{\delta}$ using equation 5.3 we get $\dot{w}_n = 144 C_{\hat{\alpha}} \rho^3 T^{1/2} X_F e^{-T_{\hat{\alpha}}/T}$. Hence $\dot{w}_{n,ref} = 144 C_\alpha \rho_0^3 T_f^3 X_{F0} e^{-T_{\hat{\alpha}}/T_f}$ can be chosen as a reference for the soot nucleation term. A reference value of the soot growth rate term can now be written as $\dot{w}_{g,ref} = (\rho_0/\rho_s)\hat{\gamma}_0 n_0^{1/3}(\rho_s f_{V0})^{2/3}$, with $\hat{\gamma}_0 = C_{\hat{\gamma}} \rho_0 T_f^{1/2} X_{F0} e^{-\frac{T_{\hat{\gamma}}}{T_f}}$. The quantities with suffixes 0 are at the reference condition. On obtaining $\dot{w}_{n,ref}$ an expression can now

be written for t_n and consequently $\bar{A}$ can be expressed conveniently as

$$\bar{A} = (\frac{L}{u_0}) \frac{144 \rho_0{}^2 C_{\dot{\alpha}} T_f{}^{\frac{1}{2}} X_{F0} e^{-\frac{T_{\dot{\alpha}}}{T_f}}}{(\rho_s f_{V0})}. \tag{5.17}$$

Similarly, since we have obtained the expression for $\dot{w}_{g,ref}$, we can now write an expression for t_g and hence for $\bar{B}$.

$$\bar{B} = (\frac{L}{u_0}) \frac{C_{\dot{\gamma}} \rho_0 T_f{}^{\frac{1}{2}} X_{F0} e^{-\frac{T_{\dot{\gamma}}}{T_f}} n_0{}^{\frac{1}{3}}}{(\rho_s f_{V0})^{\frac{1}{3}}}. \tag{5.18}$$

We now focus our attention on the nondimensional rate terms in equation 5.16, viz., $\bar{r}_n$ and $\bar{r}_g$. As mentioned before, $\bar{r}_n = \dot{\bar{w}}_n / \bar{\rho}$ and $\dot{\bar{w}}_n = \dot{w}_n / \dot{w}_{n,ref}$. Using the expressions for $\dot{w}_n$ and $\dot{w}_{n,ref}$ we can obtain the following expression for $\bar{r}_n$:

$$\bar{r}_n = \frac{(1-\alpha)^2}{(1-\alpha(1-\tau))^{\frac{3}{2}}} y_F e^{\frac{-\bar{\beta}_{\dot{\alpha}}(1-\tau)}{(1-\alpha(1-\tau))}}. \tag{5.19}$$

The quantity $\bar{\beta}_{\dot{\alpha}} = T_{\dot{\alpha}}(T_f - T_0)/T_f{}^2$ and α, as before, is given by $\alpha = 1 - T_0/T_f$. In the above we have also utilized the relation between temperature and density, i.e., $\bar{\rho} = (1-\alpha)/(1-\alpha(1-\tau))$, by virtue of equation 3.16.

An expression can also be found for the rate quantity $\bar{r}_g$ using the expressions for $\dot{w}_g$ and $\dot{w}_{g,ref}$. The expression for $\bar{r}_g$ takes the following form:

$$\bar{r}_g = \frac{(1-\alpha)^{\frac{4}{3}} y_F{}^{\frac{1}{6}} \bar{f}_V{}^{\frac{2}{3}}}{(1-\alpha(1-\tau))^{\frac{5}{6}}} e^{-(\bar{\beta}_{\dot{\gamma}} + \frac{\bar{\beta}_{\dot{\alpha}}}{6})(\frac{1-\tau}{1-\alpha(1-\tau)})}. \tag{5.20}$$

At this stage we notice that the expression for $\bar{B}$ in equation 5.18 involves an unknown reference number density, n_0. In order to evaluate that, the soot particle number density equation has to be examined

$$\rho(\eta_t + (u + u_T)\eta_x) = (\rho D_s \eta_x)_x + \dot{\omega}_n - \dot{\omega}_c, \tag{5.21}$$

where $\eta = n/N_0$. The ω's in the above are the rates of production of particle number density in a cubic meter multiplied by the density ρ and hence have the units of $kg/(m^6 s)$. By writing $\bar{\eta} = \eta/\eta_0$, $\bar{t} = t/t_{ref}$ and transforming the equation to the mass-based Z coordinate, we can write the normalized number density equation in the following form:

$$\bar{\eta}_{\bar{t}} - \frac{(1+\bar{m}_T)}{\bar{s}_0}\bar{\eta}_Z = \frac{D_{s0}}{u_0 L \bar{s}_0^2}\bar{\eta}_{ZZ} + \frac{\dot{\bar{\omega}}_n}{\bar{\rho}}\frac{\dot{\omega}_{n,ref}}{\rho_0\eta_0}t_{ref} - \frac{\dot{\bar{\omega}}_c}{\bar{\rho}}\frac{\dot{\omega}_{c,ref}}{\rho_0\eta_0}t_{ref}. \qquad (5.22)$$

We notice that $\rho_0\eta_0/\dot{\omega}_{n,ref}$ has the unit of time and thus qualifies as a characteristic nucleation time scale. Hence $(\rho_0\eta_0/\dot{\omega}_{n,ref})/t_{ref}$ is a ratio of a characteristic nucleation time scale and the characteristic flow time. Let us call the above ratio $\bar{\epsilon}$. We then multiply equation 5.22 by $\bar{\epsilon}$ to obtain

$$\bar{\epsilon}(\bar{\eta}_{\bar{t}} - \frac{(1+\bar{m}_T)}{\bar{s}_0}\bar{\eta}_Z) = \bar{\epsilon}\frac{D_{s0}}{u_0 L \bar{s}_0^2}\bar{\eta}_{ZZ} + \frac{\dot{\bar{\omega}}_n}{\bar{\rho}} - \frac{\dot{\bar{\omega}}_c}{\bar{\rho}}\frac{\dot{\omega}_{c,ref}}{\dot{\omega}_{n,ref}} \qquad (5.23)$$

When nucleation is rapid $\bar{\epsilon}\rightarrow 0$ and the quantities multiplied by $\bar{\epsilon}$ become negligible and equation 5.23 essentially reduces to a balance of the nucleation and coagulation terms, and the number density reaches a steady or saturated value, exactly as the simplified model in section 5.3.1. We get $\dot{\bar{\omega}}_n/\bar{\rho} - \dot{\bar{\omega}}_c/\bar{\rho}\dot{\omega}_{c,ref}/\dot{\omega}_{n,ref}$ and hence $\dot{\omega}_n = \dot{\omega}_c$. At this stage we compare (5.21) with equation 5.2 of the Syed, Stewart and Moss model [1] and write $\dot{\omega}_n^{\cdot} = \rho\hat{\alpha} = C_{\hat{\alpha}}\rho^3 T^{1/2} X_F \epsilon^{-T_\alpha/T}$ and $\dot{\omega}_c = \rho\hat{\beta}(n/N_0)^2 = \rho C_{\hat{\beta}} T^{1/2}(n/N_0)^2$. The equality $\dot{\omega}_n = \dot{\omega}_c$ is then utilized to obtain an expression for the reference number density, $n_0 = \rho_0 N_0 (C_{\hat{\alpha}}/C_{\hat{\beta}})^{1/2} {X_{F0}}^{1/2} \epsilon^{-T_{\hat{\alpha}}/2T_f}$. The reference fuel mole fraction X_{F0} equals $Y_{FF}\bar{W}/W_F$. Using the above n_0, the quantity $\bar{B}$ can be readily determined.

5.5 Numerical Solution

Equation 5.16 is numerically solved for a range of parameter values to obtain a solution for the soot volume fraction. The equation is discretized by finite difference method and the source terms are linearized using Newton's method. The steady state solution is reached when the sum of normalized residuals between successive time steps becomes smaller than 1×10^{-6}. The initial soot volume fraction value was assumed to be zero everywhere in the domain. A typical solution is shown in Figure 5.2. In order to further investigate the importance of various terms in the soot

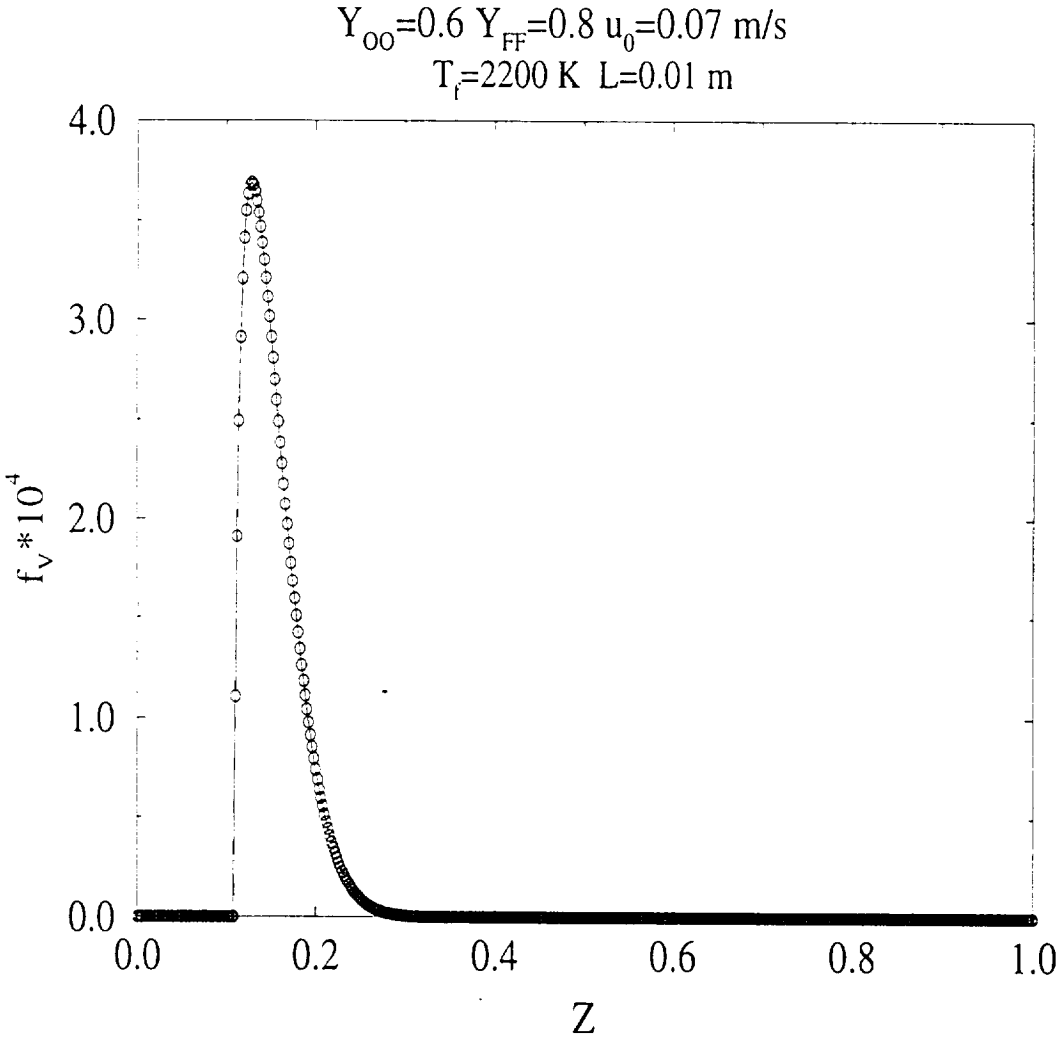

Figure 5.2. Soot Volume Fraction Profile

volume fraction equation, the convection, diffusion, soot nucleation and growth terms are all plotted in Figure 5.3. The abscissa of the plot is $(Z - Z_f)$, where Z_f is the

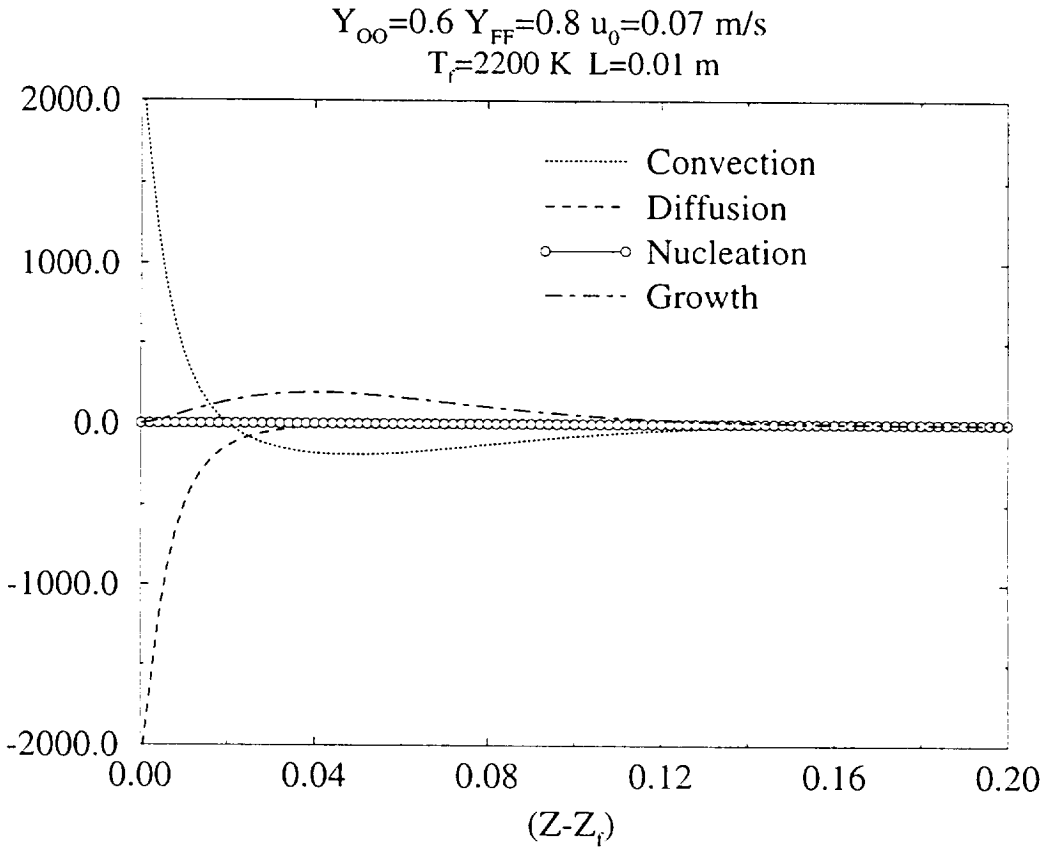

Figure 5.3. The structure of the soot volume fraction profile

location of the Burke-Schumann flame. We note that close to Z_f, there is a balance between the convection $((1/\bar{s}_0)d\bar{f}_v/dZ)$ and diffusion $((D_{s0}/u_0L\bar{s}_0^2)d^2\bar{f}_v/dZ^2)$ terms. However, the diffusion term is quite small at an incremental distance from Z_f, and for the most part of the soot layer, the essential balance is between the convection term and the growth $(\bar{B}\bar{r}_g)$ term. The nucleation term $(\bar{A}\bar{r}_n)$ is very small in comparison to the other terms.

The above insight about the fundamental structure of the soot layer is utilized in the development of an analytical expression for the soot volume fraction profile.

5.6 Analytical Approximation

As noted in the previous section, the primary balance for the soot volume fraction is between the convection and the growth terms, except very near Z_f. Hence, we assert that equation 5.16 can be further reduced to

$$-\frac{1}{\bar{s}_0}\frac{d\bar{f}_V}{dZ} = \bar{B}\bar{r}_g. \tag{5.24}$$

in the steady state limit. The quantity $\bar{B}$ is a constant, and $\bar{r}_g$ is the nondimensional soot growth term, derived from the Syed, Stewart and Moss model, is given by equation 5.20. Next, we relate dZ to $d\tau$ in order to determine a solution for $f_V(\tau)$. The fuel side ($Z_f \leq Z \leq 1$) Burke-Schumann temperature distribution is used for the above purpose

$$\tau = \frac{\epsilon^{-1/c} - \epsilon^{-Z/c}}{\epsilon^{-1/c} - \epsilon^{-Z_f/c}}, \tag{5.25}$$

where $c = \alpha_0/(u_0 L \bar{s}_0)$ and Z_f, the ideal flame location, is given by $Z_f = c\ln((1+o)/o)$. A detailed analysis of the infinite reaction rate situation is included in section 4.5 of chapter 4. The fuel mass fraction profile is

$$y_F = 1 - \epsilon^{-(Z-Z_f)/c}. \tag{5.26}$$

In terms of τ, y_F can be written as

$$y_F = a(1-\tau). \tag{5.27}$$

where $a = 1 - e^{-(1-Z_f)/c}$. After a little algebraic manipulation, dZ can be written in terms of $d\tau$ as $dZ = -[(ac)/(1 - a(1 - \tau))]d\tau$. By substituting the expression for y_F in terms of τ and dZ in terms of $d\tau$, equation 5.24 is transformed into

$$\frac{1}{\bar{f}_V^{2/3}} d\bar{f}_V = [\bar{B}\bar{s}_0(1-\alpha)^{4/3}a^{13/6}c]\frac{(1-\tau)^{7/6}e^{-(\bar{\beta}_{\bar{r}}+\frac{\bar{\beta}_{\bar{A}}}{6})(\frac{1-\tau}{1-\alpha(1-\tau)})}}{(1-\alpha(1-\tau))^{5/6}(1-a(1-\tau))}d\tau. \tag{5.28}$$

At this stage we observe that in order to integrate the soot volume fraction profile, we need to impose suitable boundary conditions. Before we made any approximations, the boundary conditions for the soot volume fraction were $\bar{f}_V = 0$ at $Z = 0$ and at $Z = 1$. However, the soot diffusion term has been dropped, which was the only second order term in equation 5.16. The resulting approximate equation is first order, and only one boundary condition can be used. We use the condition that the soot volume fraction is zero at the fuel wall, i.e., at $Z = 1$. We expect to obtain a soot volume fraction profile which is located preferentially on the fuel side of the diffusion flame. It has to be kept in mind also that in order to substitute for dZ in terms of $d\tau$, the temperature profile on the fuel side was used, and hence, any soot volume fraction which we may see on the oxidizer side is actually non-existent.

We now integrate equation 5.28 subject to the boundary condition that $\bar{f}_V = 0$ when $\tau = 0$. From equation 5.28 we find that the important integral to evaluate is

$$I_1 = \int_0^{\tau} \frac{(1-\tau)^{7/6}e^{-(\bar{\beta}_{\bar{r}}+\frac{\bar{\beta}_{\bar{A}}}{6})(\frac{1-\tau}{1-\alpha(1-\tau)})}}{(1-\alpha(1-\tau))^{5/6}(1-a(1-\tau))}d\tau \tag{5.29}$$

By substituting $u = 1 - \tau$ and writing $\beta_{r\alpha} = \bar{\beta}_{\bar{r}} + \frac{\bar{\beta}_{\bar{A}}}{6}$ we arrive at the following expression for I_1:

$$I_1 = \int_u^1 \frac{u^{7/6}e^{\frac{-\bar{\beta}_{r\alpha}u}{(1-\alpha u)}}}{(1-\alpha u)^{5/6}(1-au)}du \tag{5.30}$$

The integral in equation 5.30 could not be analytically evaluated. In order to simplify matters, the exponents 7/6 and 5/6 on u and $(1 - \alpha u)$ respectively were replaced by

1. Let the modified integral be called I_2. Then, I_2 happens to be integrable analytically. An analytical result was obtained using the commercial code *MAPLE*, and the result so obtained was verified using another commercial code, *MATHEMATICA*. The following expression is obtained for I_2:

$$I_2 = (A + B + C + D)/(a\alpha(\alpha - a)), \tag{5.31}$$

where

$$\begin{aligned} A &= -\alpha e^{\frac{\beta_{\gamma\alpha}}{\alpha - a}} Ei(1, \tfrac{\beta_{\gamma\alpha}(a-1)}{(\alpha-1)(\alpha-a)}) \\ B &= (\alpha - a)e^{\frac{\beta_{\gamma\alpha}}{\alpha}} Ei(1, \tfrac{-\beta_{\gamma\alpha}}{(\alpha-1)\alpha}) \\ C &= -(\alpha - a)e^{\frac{\beta_{\gamma\alpha}}{\alpha}} Ei(1, \tfrac{-\beta_{\gamma\alpha}}{(\alpha(1-\tau)-1)\alpha}) \\ D &= \alpha e^{\frac{\beta_{\gamma\alpha}}{\alpha - a}} Ei(1, \tfrac{-\beta_{\gamma\alpha}}{(\alpha(1-\tau)-1)\alpha}), \end{aligned} \tag{5.32}$$

where $Ei(1, x)$ is a notation for the exponential integral. The indexed family of exponential integrals, $Ei(n, x)$ where n is a non-negative integer, is defined as $Ei(n, x) = \int_1^\infty e^{-xt}/t^n dt$ for real, positive x.

Integral I_2, thus calculated, is compared with the numerical solution. Also, Laplace's method was used as an alternative method to approximately evaluate the integral I_1. The following section briefly describes the analysis.

5.7 Integral Evaluation Using Laplace's Method

The integral in equation 5.30 can be approximately evaluated using Laplace's method and can be written as $I_1 = \int_{1-\tau}^1 g(u)e^{f(u)}du$ where $g(u) = (1 - \alpha u)^{-5/6}(1 - au)^{-1}$ and $f(u) = -\beta_{\gamma\alpha}u/(1 - \alpha u) + \ln u^{7/6}$.

Let us next consider the integral $I(x) = \int_a^b e^{xh(t)}f(t)dt$, where $h(t)$ is real and x is positive and large. Assume that the integral exists, i.e., it has a finite value.

According to Laplace, only the immediate neighborhood of the point corresponding to the maximum value of $h(t)$ in $[a, b]$ contributes to the asymptotic expansion of $I(x)$. Similarly, for expansion of the integral I_1 the value of u for which $f(u)$ is a maximum is sought first. Let us denote the value as u^*. Equating df/du to 0 and evaluating d^2f/du^2 to ascertain that f attains a maximum at u^*, we find that $u^* = 7/(6\beta_{\gamma\alpha})$. Next the integral I_1 is expanded in the following form:

$$I_1 = \int_{1-\tau}^{1} [g(u^*) + (u-u^*)g'(u^*) + ...]e^{f(u^*)+(u-u^*)f'(u^*)+\frac{(u-u^*)^2}{2}f''(u^*)+\cdots}du \qquad (5.33)$$

By using the result $f'(u^*) = 0$ and evaluating the different derivatives of $f(u)$ and $g(u)$ at u^* and assuming a large $\beta_{\gamma\alpha}$ the above integral can be easily evaluated. After some algebraic manipulation and neglecting higher order terms in the expansion of the integral, we obtain the following simplified result for the integral I_1:

$$I_1 = \frac{0.7136}{\beta_{\gamma\alpha}^{\frac{13}{6}}} erfc[\sqrt{\frac{3}{7}}\beta_{\gamma\alpha}(\tau^* - \tau)], \qquad (5.34)$$

where τ^* is the value of nondimensional temperature corresponding to the value u^*, i.e., $\tau^* = 1 - u^*$. Hence, using equation 5.28 and equation 5.34 we can write the following expression for the soot volume fraction:

$$\bar{f}_v^{\frac{1}{3}} = [\bar{B}\bar{s}_0(1-\alpha)^{4/3}a^{13/6}c]\frac{0.2379}{\beta_{\gamma\alpha}^{\frac{13}{6}}} erfc[\sqrt{\frac{3}{7}}\beta_{\gamma\alpha}(\tau^* - \tau)]. \qquad (5.35)$$

5.8 Comparison of Results

Figure 5.4 shows a comparison of the numerical solution and the analytical solutions for the soot volume fraction profiles. In Figure 5.4 "Method 1" refers to the solution using exponential integrals and "Method 2" refers to the solution using Laplace's method. It is seen that both the methods result in soot profiles which have substan-

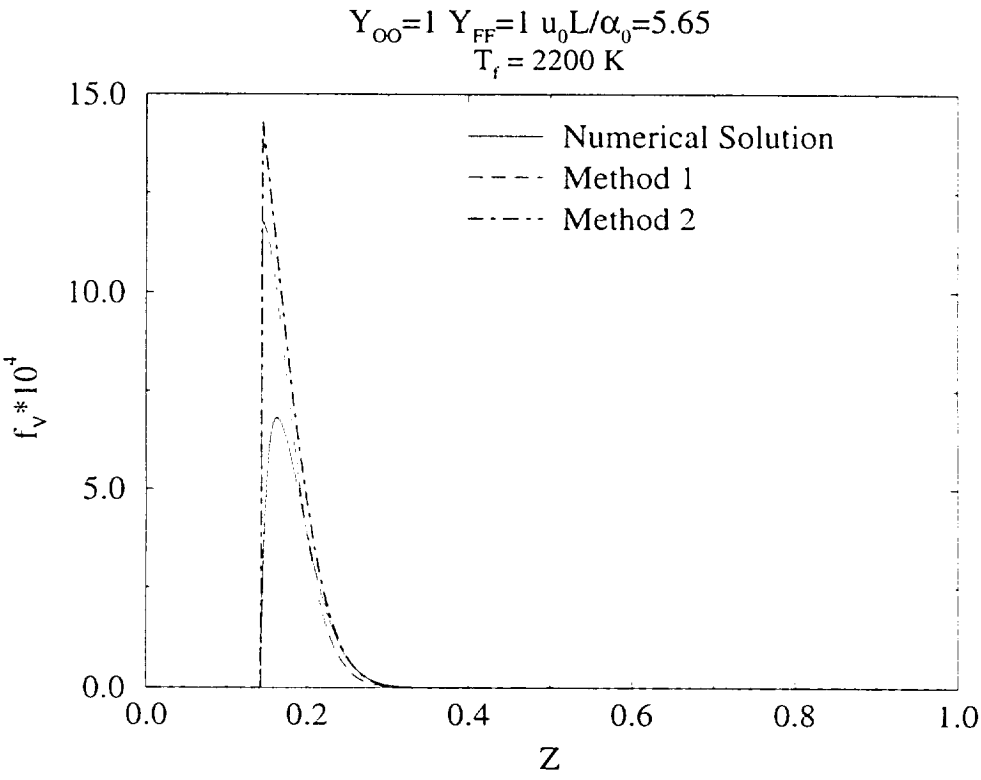

Figure 5.4. The analytical solutions plotted along with the numerical solution.

tially different maximum values compared to the numerical solution. This happens because the soot profile maximum is close to the flame location, Z_f, where the effect of soot diffusion is prominent, as observed in the section 5.5. Since the diffusion term was neglected for the analytical solution, the disagreement between the numerical and analytical solutions is quite conspicuous near Z_f. However, consistent with the discussion in the previous section, a much better agreement is obtained near the trailing edge of the soot layer, i.e., further from Z_f. The agreement between the analytical and numerical solutions is excellent in that region. Consequently, the thickness of the soot layer can now be analytically predicted fairly accurately.

5.9 Influence of soot radiation

In this section, we shift our attention to the effect of radiation on a diffusion flame established between a fuel and an oxidizer wall, with a convective fuel flow from the fuel wall. This configuration is the same as in Chapter 4. However, the radiation term used here is different. A soot volume fraction profile, generated using the method described in section 5.5 was used to formulate a radiative loss term.

5.9.1 Background

Understanding of soot radiation and its proper incorporation in the model are extremely important for the current research. The radiation from a flame depends on the soot profile, which depends on the particular fuel used, the temperature profile and the species profiles. In this section we will assume a soot volume fraction based on the numerical solution of the soot volume fraction equation described in section 5.5. A radiation term is formulated based on the "optically thin" assumption for the soot radiation. A review of the existing literature pertaining to soot radiation is included in section 2.5 of chapter 2.

5.9.2 Formulation of the Radiation term

For a sooty flame the major part of the radiation is a continuum radiation that is simpler to model than the radiation due to water and carbon dioxide. For soot volume fractions $> 10^{-7}$, soot radiation should be dominant judging by the calculations of Grosshandler and Modak [11]. For small flames and moderate soot loadings with which we are dealing, the optically thin limit is appropriate. In this limit

$$\frac{dq_R}{dx} = 4a_p\sigma(T^4 - T_0{}^4), \tag{5.36}$$

where, a_p is the Planck Mean absorption coefficient and σ is the Stefan-Boltzmann constant which has a value of $5.6696\times10^{-8}\ W/m^2K^4$. The quantity a_p is given by

$$a_p = \frac{\int_0^\infty \kappa(\lambda, f_V)e_b(\lambda)d\lambda}{\int_0^\infty e_b(\lambda)d\lambda}. \tag{5.37}$$

Kennedy *et al.* [31] used $\kappa = 7f_V/\lambda$, where κ is the absorption coefficient and λ is the wavelength of radiation. For a blackbody the spectral distribution of hemispherical emissive power in a vacuum is given as a function of absolute temperature and wavelength by the following expression:

$$e_b(\lambda) = \frac{2\pi C_1}{\lambda^5[e^{\frac{C_2}{\lambda T}} - 1]}. \tag{5.38}$$

This is known as *Planck's spectral distribution of emissive power*. The constant C_1 has the value $0.59544\times10^{-16}\ Wm^2$ and $C_2 = 1.4388\times10^{-2}\ mK$. Using the expression for e_b in equation 5.37 and substituting $y = C_2/(\lambda T)$, the following expression is obtained for a_p:

$$a_p = \frac{14\pi f_V C_1 T}{\sigma C_2{}^5}\int_0^\infty \frac{y^4 dy}{e^y - 1}. \tag{5.39}$$

The integral $\int_0^\infty y^4 dy/(e^y - 1)$ is the fourth order Riemann zeta function and whose value is 24.8862. Hence, $a_p = 1864.32 f_V T$.

By transforming equation 5.36 to the Z coordinate and using $\bar{q}_R = q_R/\rho_0 u_0 C_p(T_f - T_0)$, $\tau = (T - T_0)/(T_f - T_0)$, $\bar{\rho} = \rho/\rho_0$ and $\bar{s}_0 = s_0/(\rho_0 L)$ we obtain

$$\frac{1}{\bar{s}_0}\frac{d\bar{q}_R}{dZ} = -\frac{4a_p\sigma L T_f^4}{\rho C_p(T_f - T_0)u_0}[(1 - \alpha(1 - \tau))^4 - (1 - \alpha)^4]. \tag{5.40}$$

By using equation 3.16 for the relationship between temperature and density we can further reduce the expression for $(1/\bar{s}_0)(d\bar{q}_R/dZ)$ and write

$$\frac{1}{\bar{s}_0}\frac{d\bar{q}_R}{dZ} = -\Gamma_R \bar{f}_V(1 - \alpha(1 - \tau))^2((1 - \alpha(1 - \tau))^4 - (1 - \alpha)^2). \tag{5.41}$$

where Γ_R is given by

$$\Gamma_R = \frac{4378.21 C_1 L f_{V_0} T_f^6}{\rho_0 C_p T_0 (T_f - T_0) u_0 C_2^5}. \tag{5.42}$$

The energy equation for this situation is the same as equation 4.1 of chapter 4. In the Z coordinate the energy equation becomes

$$\tau_t = \frac{1}{\bar{s}_0}\tau_Z + \frac{\alpha_0}{u_0 L \bar{s}_0^2}\tau_{ZZ} + \bar{Q}_F \mathcal{D}_F r + \frac{1}{\bar{s}_0}\frac{d\bar{q}_R}{dZ}. \tag{5.43}$$

where we have used $\bar{q}_R = q_R/q_{R,ref}$ and $\bar{Q}_F = Q_F Y_{FF}/C_p(T_f - T_0) = (1 + \phi)$. The reference quantity $q_{R,ref}$ was chosen to be $\rho_0 u_0 C_p(T_f - T_0)$. Hence, the radiative loss term is given by $1/\bar{s}_0(d\bar{q}_R/dZ)$. We note that we have already derived an expression for the loss term in equation 5.41. The energy equation can now be solved numerically using a prescribed soot volume fraction profile in conjunction with the coupled oxidizer and fuel mass fraction equations. The species equations are the same as equations 4.5 and 4.6 of chapter 4.

5.9.3 Results

Figure 5.5 shows a plot of the temperature and species profiles of a flame with a radiative energy loss modeled as in the previous section. The prescribed soot volume fraction profile is also shown on the same plot. Next, the structure of the flame is

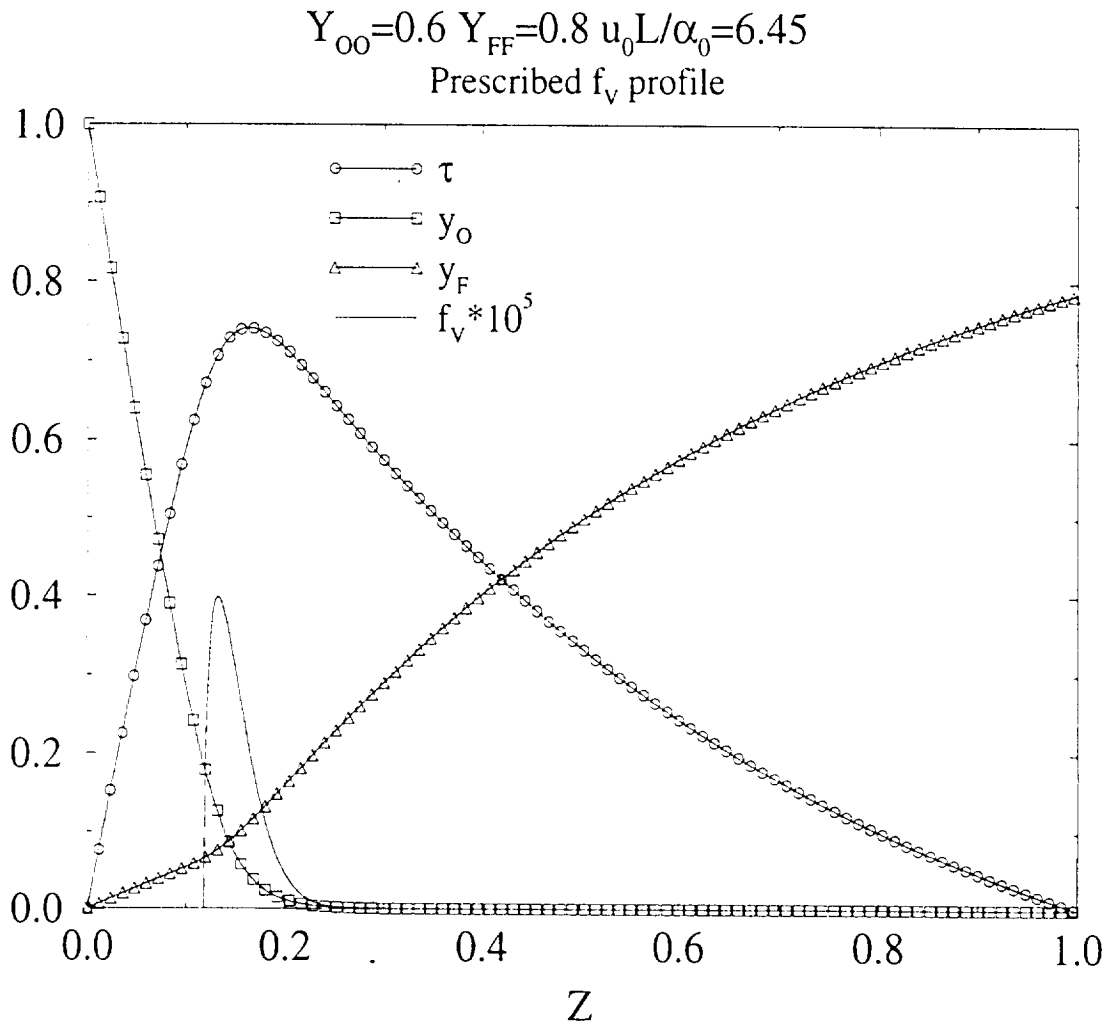

Figure 5.5. τ, y_O and y_F profiles for prescribed soot volume fraction.

shown in Figure 5.6. The convection, diffusion and reaction terms of the nondimensional energy equation are plotted along with the radiative loss term. This figure can be compared with the structure of a similar flame with a $sech^2$ type radiative loss

term, as illustrated in Figure 4.11 of Chapter 4. The similarity in the structure of the two flames is quite striking and suggests that the simple $sech^2$ type radiative loss profile is a fairly good approximation which is capable of revealing interesting aspects of the diffusion flame behavior when subject to radiative heat loss.

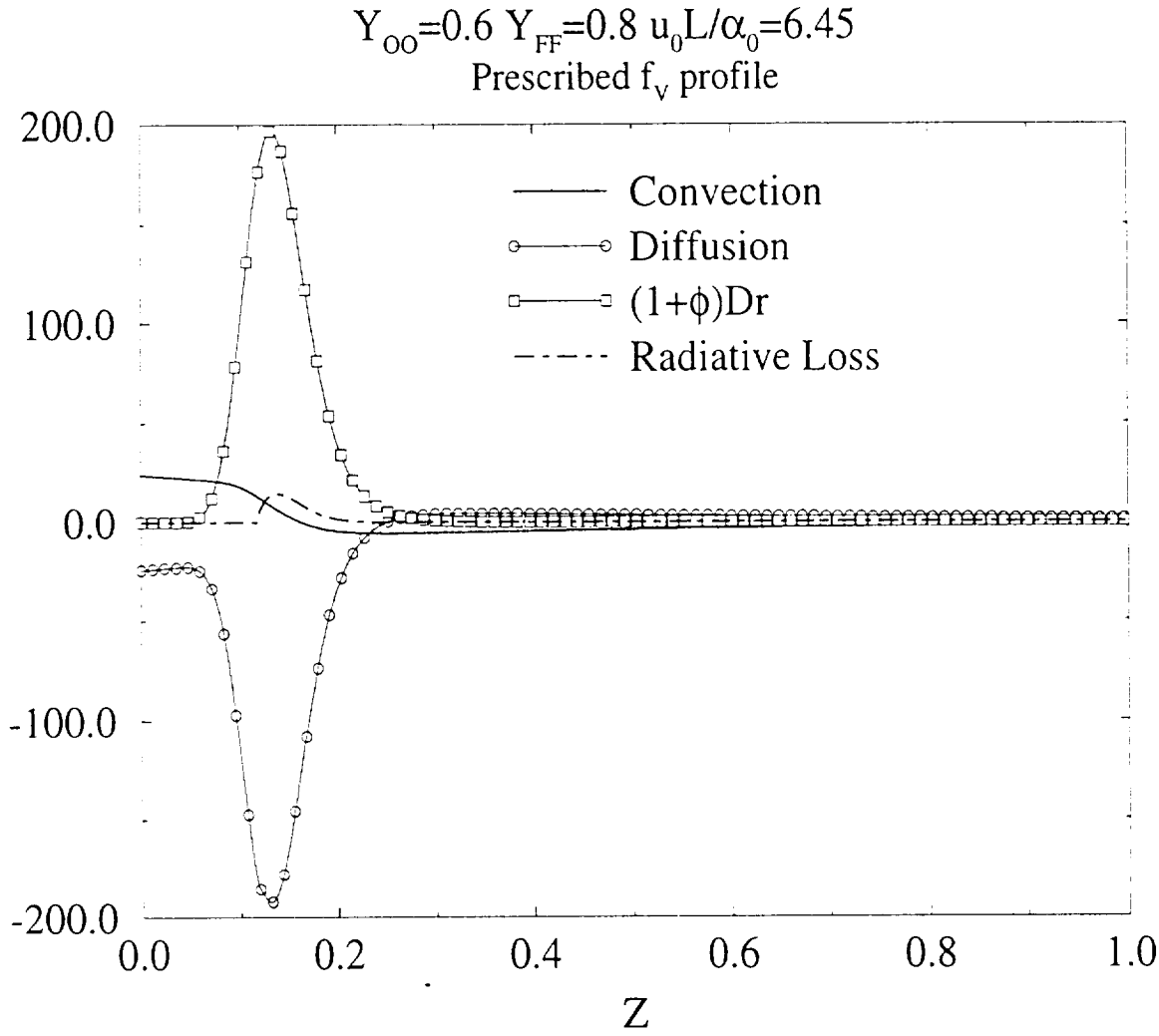

Figure 5.6. Structure of the flame. Note the radiative loss term.

5.10 Conclusions

A simplified analysis of the soot profile was carried out in this chapter using the Syed, Stewart and Moss [1] model. Burke-Schumann temperature and species profiles were assumed and the soot volume fraction equation was solved numerically for a diffusion flame established between an oxidizer and a fuel wall. Oxygen diffused out of the oxidizer wall and fuel was released from the fuel wall by means of both diffusion and convection. It was observed that for the soot volume fraction equation the primary balance was between the processes of soot convection and soot growth. Equating the expressions for these two quantities resulted in an analytical expression for the soot volume fraction in integral form. The integral was evaluated using two methods: the first one involving exponential integrals and the other using Laplace's method. The analytical profiles matched well with the numerical solution except very near the flame location Z_f. Close to the Burke-Schumann flame location, the soot diffusion term is strong and there the essential balance is between the soot convection and the soot diffusion, the soot growth term being relatively much smaller. However, the thin zone may be an artifice of the IRR approximation itself. The analytical expressions, which were derived on the basis of the *soot convection* $\sim$ *soot growth* balance, do not predict the soot volume fraction values accurately near the infinite reaction rate (IRR) flame location. However, for most part of the soot layer the soot volume fraction profile is predicted well by the analytical formulæ. Consequently, the soot layer thickness can also be accurately predicted using analytical methods.

A soot radiation term was also developed on the assumption of the optically thin limit for the radiation. A soot volume fraction profile obtained from the numerical solution was used in the expression for the soot radiation term. The radiation term was then included in an energy equation as a sink term and the equation was solved simultaneously with the coupled fuel and oxidizer species equations. The results

revealed that the flame structure closely resembles the structure of the flames studied in chapter 4 for $sech^2$ heat loss profiles. Such a resemblance indicates that the simple $sech^2$ heat loss profile examined in chapters 3 and 4 is capable of revealing interesting details of the flame structure.

CHAPTER 6

Investigation of the Comprehensive Soot Radiation Problem

In the previous chapters we have analyzed with simplified models of soot profile and radiation loss effects. In the current chapter we deal with the complex problem of soot radiation and diffusion flame interaction using a soot model chosen from the available literature. Here we use the two equation model of Syed, Stewart and Moss [1] for the soot volume fraction and the soot number density. Their model has been developed based on experiments with different fuels and for a range of flow conditions; we have examined this model analytically in chapter 5. A two-dimensional Wolfhard-Parker burner was used for their experiments in order to fix various undetermined constants. This model has been used by Syed *et al.* [1] for both laminar and turbulent flame predictions. Recently, Ku *et al.* [51] have used this model for the simulation of microgravity turbulent diffusion flames and the agreement of the model with experiments was very good. In the following sections, we first describe the conservation equations and then formulate the final, non-dimensional equations including the Syed, Stewart and Moss [1] soot model. Then, we discuss some interesting results obtained from the numerical solutions of the conservation equations. Although our results indicate a variety of interesting behaviors, a radiative

extinction was not observed, suggesting to us that a steady state extinction is unlikely.

6.1 Formulation

There are six conservation equations of importance in our problem, viz., the mass, the energy, the oxidizer and fuel species, the soot volume fraction and the soot number density equations. At this stage we also note that on an overall basis, we can account for three principal chemical reactions, as noted below

$$\begin{aligned} fuel + air &\rightarrow products \\ fuel &\rightarrow soot \\ soot + oxygen &\rightarrow products \end{aligned}$$

It has to be kept in mind, however, that each of the above overall reactions is very complex in reality and consists of hundreds, and may be even thousands of steps and intermediate products.

The continuity equation is

$$\frac{\partial \rho}{\partial t} + \frac{\partial \rho u}{\partial x} = 0 \tag{6.1}$$

At steady state, $\partial \rho u / \partial x = 0$ and hence, $\rho u = \rho_0 u_0$, since the mass flow rate is $\dot{m} = \rho_0 u_0$. Hence,

$$u = u_0 / \bar{\rho} \tag{6.2}$$

The energy equation has three source terms accounting for the heat generation due to the primary chemical reaction, the radiative heat loss and the heat generation due to soot oxidation. The energy equation is

$$\rho C_p (T_t + u T_x) = (\lambda T_x)_x + Q_F \dot{w}_F - \frac{dq_R}{dx} + Q_{ox} \dot{w}_{ox}. \tag{6.3}$$

We assume that the reaction $C + \frac{1}{2}O_2 = CO + Q_{ox}$ takes place for soot oxidation, with Q_{ox} being the heat release. The heat release in the above oxidation process is 53 $kCal$/mole of O_2 [52], [53]. Hence, $Q_{ox} = 9246.29$ kJ/kg of C.

The oxidizer equation has a depletion term due to the primary reaction and another one accounting for soot oxidation, viz.,

$$\rho(Y_{Ot} + uY_{Ox}) = (\rho D_O Y_{Ox})_x - \nu\dot{w}_F - \frac{4}{3}\dot{w}_{ox}. \tag{6.4}$$

We also note that for every kg of C 4/3 kg of O_2 is required due to the oxidation reaction for soot particles, hence the coefficient 4/3 for the oxidation rate $\dot{w}_{ox}$ in the above equation.

The fuel mass fraction equation includes depletion terms due to the primary chemical reaction as well as the conversion to soot particles,

$$\rho C_p(Y_{Ft} + uY_{Fx}) = (\rho D_F Y_{Fx})_x - \dot{w}_F - \frac{4}{3}\dot{w}_g. \tag{6.5}$$

For the conversion of fuel to soot, we assume a very simple overall reaction of the form $CH_4 \rightarrow C + 2H_2$. If the soot growth rate is $\dot{w}_g$ kg of C/m^3s, then the depletion rate of the fuel due to soot growth is $(4/3)\dot{w}_g$ kg of fuel/m^3s, since 1 kg of C is produced from 4/3 kg of fuel, according to the above chemical reaction.

Finally, we have two conservation equations for the soot volume fraction and the soot particle number density, viz.,

$$\rho(f_{Vt} + (u + u_T)f_{Vx}) = (\rho D_s f_{Vx})_x + \dot{w}_n + \dot{w}_g - \dot{w}_{ox}. \tag{6.6}$$

and

$$\rho(\eta_t + (u + u_T)\eta_x) = (\rho D_s \eta_x)_x + \dot{\omega}_n - \dot{\omega}_c. \tag{6.7}$$

In the above, $\dot{w}_n$, $\dot{w}_g$ and $\dot{w}_{ox}$ are respectively the soot nucleation, growth and oxidation rates in units of kg/m^3s. The quantities $\dot{\omega}_n$ and $\dot{\omega}_c$ are the nucleation and coagulation rates in units of $(kg/m^3)(number/m^3s)$. The soot volume fraction in units of $m^3{}_{soot}/m^3{}_{gas}$ is f_V and η is the number density of soot particles normalized by Avogadro's number ($N_0 = 6.0\times10^{26}$), i.e., $\eta = n/N_0$. The thermophoretic velocity term is denoted by u_T. A discussion of thermophoresis is included in section 6.1.1. The soot diffusivity, D_s, is usually quite small and was assumed to be 1% of the gas diffusivity [12].

As in the preceding chapters we transform the equations to a (Z,t) system of coordinates, where $Z = 1 - s/s_0$ with $s = \int_0^x \rho dx$ and $s_0 = \int_0^L \rho dx$. As a result, our conservation equations take the following form:

energy:

$$T_t - \frac{\rho_0 u_0}{s_0} T_Z = \frac{(\rho\lambda)}{C_p {s_0}^2} T_{ZZ} + \frac{1}{\rho C_p}(Q_F \dot{w}_F + \frac{\rho}{s_0}\frac{dq_R}{dZ} + Q_{ox}\dot{w}_{ox}), \tag{6.8}$$

Oxidizer mass fraction:

$$Y_{Ot} - \frac{\rho_0 u_0}{s_0} Y_{OZ} = \frac{\rho^2 D_O}{{s_0}^2} Y_{OZZ} - \frac{1}{\rho}(\nu\dot{w}_F + \frac{4}{3}\dot{w}_{ox}). \tag{6.9}$$

Fuel mass fraction:

$$Y_{Ft} - \frac{\rho_0 u_0}{s_0} Y_{FZ} = \frac{\rho^2 D_F}{{s_0}^2} Y_{FZZ} - \frac{1}{\rho}(\dot{w}_F + \frac{4}{3}\dot{w}_g). \tag{6.10}$$

Soot volume fraction:

$$f_{Vt} - \frac{(\rho_0 u_0 + \rho u_T)}{s_0} f_{VZ} = \frac{\rho^2 D_S}{{s_0}^2} f_{VZZ} + \frac{1}{\rho}(\dot{w}_n + \dot{w}_g - \dot{w}_{ox}). \tag{6.11}$$

Soot number density:

$$\eta_t - \frac{(\rho_0 u_0 + \rho u_T)}{s_0}\eta_Z = \frac{\rho^2 D_S}{{s_0}^2}\eta_{ZZ} + \frac{1}{\rho}(\dot{\omega}_n - \dot{\omega}_c). \tag{6.12}$$

In the above, we have assumed the quantities $\rho\lambda$, $\rho^2 D_O$, $\rho^2 D_F$ and $\rho^2 D_s$ to be constant. Next, we nondimensionalize the above equations. We use $\tau = (T - T_0)/(T_f - T_0)$, $y_O = Y_O/Y_{OO}$, $y_F = Y_F/Y_{FF}$ and $\bar{f}_V = f_V/f_{V_0}$, where f_{V_0} is a suitably chosen reference value. Also, we define a set of characteristic times for the different chemical processes. The characteristic chemical time for the primary reaction is denoted by $t_{chem} = \rho_0 Y_{FF}/\dot{w}_{F,ref}$. The quantities $t_n = \rho_0 Y_{FF}/\dot{w}_{n,ref}$ and $t_g = \rho_0 Y_{FF}/\dot{w}_{g,ref}$ are, respectively, the characteristic times for the processes of soot nucleation and soot growth. The characteristic time scale for soot oxidation is $t_{ox} = \rho_0 Y_{OO}/\dot{w}_{ox,ref}$. The quantity $\bar{\rho}$ is the nondimensional density and the following terms are also used: $\bar{r}_F = \dot{\bar{w}}_F/\bar{\rho}$, $\bar{r}_n = \dot{\bar{w}}_n/\bar{\rho}$, $\bar{r}_g = \dot{\bar{w}}_g/\bar{\rho}$ and $\bar{r}_{ox} = \dot{w}_{ox}/\bar{\rho}$. Consequently, the energy equation becomes

$$\frac{\partial \tau}{\partial \bar{t}} - \frac{1}{\bar{s}_0}\frac{\partial \tau}{\partial Z} = \frac{\alpha_0}{u_0 L {s_0}^2}\frac{\partial^2 \tau}{\partial Z^2} + \bar{Q}_F \mathcal{D}_F \bar{r}_F + \frac{1}{\bar{s}_0}\frac{d\bar{q}_R}{dZ} + \bar{Q}_{ox}\mathcal{D}_{ox}\bar{r}_{ox}. \tag{6.13}$$

where $\bar{q}_R$ is given by $q_R/\rho_0 u_0 C_p \Delta T$. The radiation term $(1/\bar{s}_0)(d\bar{q}_R/dZ)$ is modeled exactly as in section 5.9.2 of chapter 5 and is given by equation 5.41. The quantity $\bar{s}_0$ equals $s/(\rho_0 L)$ and $\mathcal{D}_{ox}$ is a ratio of the characteristic flow time and the characteristic oxidation time, i.e., t_{ref}/t_{ox}, where $t_{ref} = L/u_0$. The oxidizer mass fraction equation becomes

$$\frac{\partial y_O}{\partial \bar{t}} - \frac{1}{\bar{s}_0}\frac{\partial y_O}{\partial Z} = \frac{\alpha_0}{u_0 L \bar{s}_0^2}\frac{\partial^2 y_O}{\partial Z^2} - (o\mathcal{D}_F \bar{r}_F + \frac{4}{3}\mathcal{D}_{ox}\bar{r}_{ox}) \tag{6.14}$$

Correspondingly the fuel equation takes the following shape:

$$\frac{\partial y_F}{\partial \bar{t}} - \frac{1}{\bar{s}_0}\frac{\partial y_F}{\partial Z} = \frac{\alpha_0}{u_0 L \bar{s}_0^2}\frac{\partial^2 y_F}{\partial Z^2} - \left(\mathcal{D}_F \bar{r}_F + \frac{4}{3}\left(\frac{\bar{B} f_{V_0}}{Y_{FF}}\right)\bar{r}_g\right) \tag{6.15}$$

The volume fraction equation looks like the following:

$$\frac{\partial \bar{f}_V}{\partial \bar{t}} - \frac{(1+\bar{m}_T)}{\bar{s}_0}\frac{\partial \bar{f}_V}{\partial Z} = \frac{D_{s0}}{u_0 L \bar{s}_0^2}\frac{\partial^2 \bar{f}_V}{\partial Z^2} + (\bar{A}\bar{r}_n + \bar{B}\bar{r}_g - \bar{C}\bar{r}_{ox}) \qquad (6.16)$$

In the above, we have assumed $\alpha_0 = D_{O0} = D_{F0}$ and $\bar{A} = Y_{FF}t_{ref}/f_{V0}t_n$, $\bar{B} = Y_{FF}t_{ref}/f_{V0}t_g$ and $\bar{C} = Y_{OO}t_{ref}/f_{V0}t_{ox}$. The quantity $\bar{m}_T$ is given by $\bar{\rho}u_T/u_0$. For the soot number density, following the analysis in section 5.4 of chapter 5 we can write $\dot{\omega}_n = \dot{\omega}_c$, i.e., the soot number density equation rapidly saturates and at steady state the soot nucleation and coagulation rates are equal.

We will now focus our attention on the different rate expressions. The quantity $\dot{w}_F$ is the rate of primary chemical reaction, and has the form $\rho A Y_O Y_F \exp(-E/RT)$, where A is the pre-exponential exponent and E is the activation energy.

As mentioned before, for the processes of soot nucleation, growth and coagulation we have used the Syed, Stewart and Moss [1] model. A detailed description of the model can be found in section 5.2 of chapter 5 and the expressions for $\bar{r}_n$, $\bar{r}_g$ are as formulated in section 5.4 and are respectively given by equations 5.19 and 5.20. The soot oxidation rate term, $\bar{r}_{ox}$ was modeled using the semi-empirical formula of Nagle and Strickland-Constable [2].

6.1.1 The Influence of Thermophoresis

Thermophoresis is the phenomenon wherein small particles, when suspended in a gas in which there exists a temperature gradient ∇T, experience a force in the direction opposite to that of ∇T [54]. A common example of thermophoresis is the blackening of the glass globe of a kerosene lantern; the temperature gradient established between the flame and the globe drives the carbon particles produced in the combustion process towards the globe, where they deposit. Thermophoresis is of practical importance in many industrial applications, such as thermal precipitators.

The temperature gradients in our flames are quite steep and hence, an examination of the effect of thermophoresis is duly warranted. Santoro *et al.* [30] observes that soot particles can usually be treated as being in the free molecular limit for flame conditions, i. e., the particle diameter is much smaller than the mean free path of the gas. Under such conditions, the thermophoretic velocity, u_T can be written as $u_T = -(3/[4(1 + \pi A/8)])(\nu/T)\nabla T$, where ν is the kinematic viscosity of the gas and A is the accommodation coefficient which usually is taken to be 0.9 or 1.0 [30]. Assuming $A = 0.9$ we obtain the following expression for the thermophoretic velocity of the gas:

$$u_T = -0.55\frac{\nu}{T}\nabla T \tag{6.17}$$

The $-$ ve sign in the above indicates that the thermophoretic velocity is in the direction of decreasing temperature. The thermophoretic velocity component is simply added to the convective flow velocity, as in equations 6.6 and 6.7.

Next, we carry out the necessary coordinate transformation and express the quantity $\bar{m}_T = \bar{\rho}u_T/u_0$ as in equation 6.16.

$$\bar{m}_T = \frac{0.55\nu(1-\alpha)^2}{[1-\alpha(1-\tau)]^3(u_0 L\bar{s}_0)}\frac{d\tau}{dZ} \tag{6.18}$$

A discussion of the influence of thermophoresis pertaining to this research problem is included in section 6.4.

6.2 Parameter Values

The parameter values assumed here are the same as in chapters 3 and 4. However, the value of the pre-exponential factor, A, was taken from the work of Chen *et al.* [55]. For the quantity A/ρ they used a value of $5.2\times10^{13}\ cm^3/gm - s$. We assumed a reference value of $\rho = 0.0012\ gm/cm^3$ and hence our $A = 1.95\times10^9\ 1/s$. The adiabatic

flame temperature correlation used in chapter 3 was also used in this chapter. The length of the domain, $L = 0.02\ m$ and as before, the thermal diffusivity at the reference condition, $\alpha_0 = 1.24 \times 10^{-4}\ m^2/s$ [50]. The kinematic viscosity of the gas phase is assumed to be $\nu = 8.68 \times 10^{-5}\ m^2/s$.

6.3 Numerical Solution

The nondimensional temperature, species and soot volume fraction equations were numerically integrated using the finite difference method. The non linear source terms were linearized using Newton's method. The Burke-Schumann profiles for temperature and species were used as initial profiles. The soot volume fraction was assumed to be zero everywhere at the initial time. The transient conservation equations were integrated to steady state.

6.4 Results and Discussion

Figure 6.1 illustrates the temperature, species and soot volume fraction profiles in the Z coordinate when $Y_{OO} = 0.6$, $Y_{FF} = 0.7$ and $u_0 L/\alpha_0 = 3.23$, which corresponds to $u_0 = 0.02\ m/s$. The nondimensional temperature profile indicates a substantial effect of radiative losses. An examination of the species profiles reveals that there is no significant diffusion of oxidizer and fuel to the opposite sides of the flame. The soot volume fraction profile resides primarily on the fuel side of the flame, in accordance with experimental observations [30]. Note that there is a slight change of slope of the temperature profile in the radiative loss zone.

The nondimensional temperature profile indicates a significant effect of radiative losses. The species profiles indicate that there is no significant diffusion of oxidizer and fuel to the opposite sides of the flame. The soot volume fraction profile resides

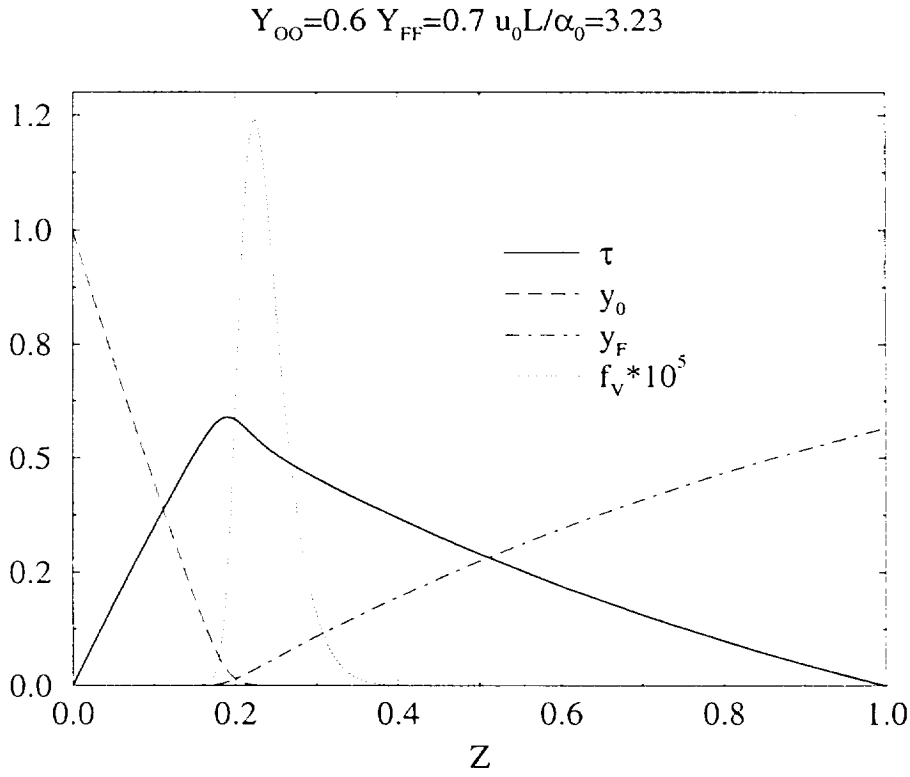

Figure 6.1. Temperature, species and soot volume fraction profiles.

primarily on the fuel side of the flame, in accordance with experimental observations [30].

The profiles are depicted again in the physical coordinate in Figure 6.2 in order to provide an idea of the magnitudes of various quantities. The fuel wall is at $x = 0\ mm$ and the oxidizer wall is at $x = 20\ mm$. The maximum temperature is about 1745 K which occurs at $x = 15.55\ mm$. The soot volume fraction peak is at 14.31 mm. We also observe that soot exists between approximately $x = 10\ mm$ and $x = 16\ mm$.

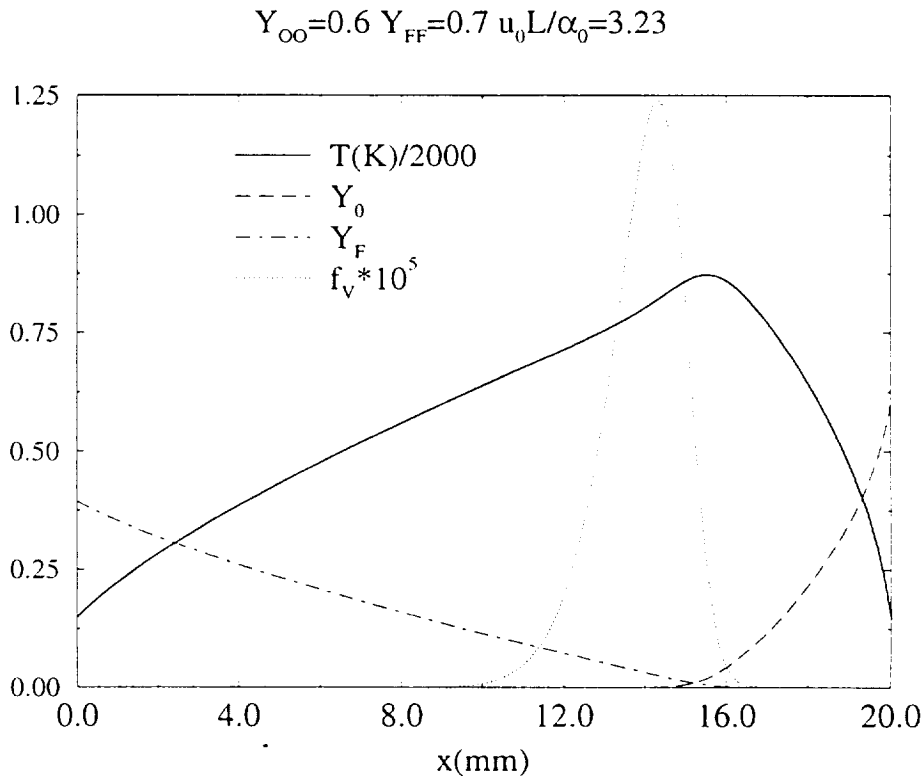

Figure 6.2. Temperature, species and soot volume fraction profiles in the physical coordinate, x.

We examine the temperature profile more closely in Figure 6.3. The temperature profiles for the infinite reaction rate (IRR) situation and the profile for finite rate chemistry in the absence of radiation are also plotted in the same figure. It is clear

that the effect of radiative loss is quite pronounced and the peak nondimensional temperature drops from about 0.8 to 0.59. The decrease is approximately 510 K. Another interesting aspect to be noticed is the slope of the oxidizer side temperature profile is nearly the same for all the three cases. The fuel side slope decreases considerably on the inclusion of radiative losses.

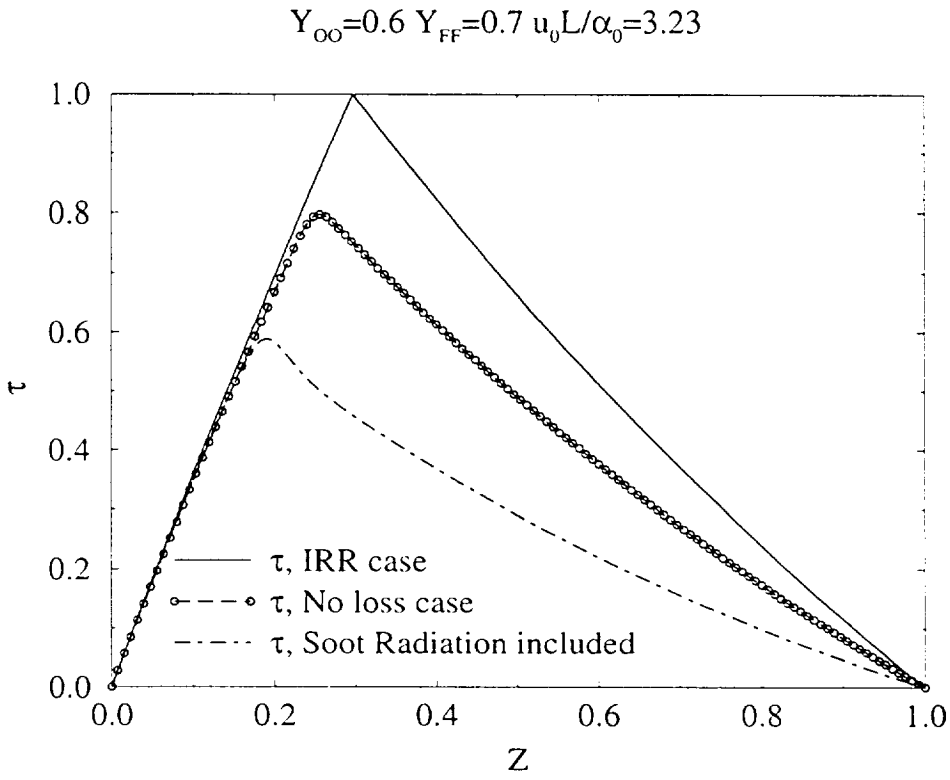

Figure 6.3. τ profiles for three different situations.

The profiles of the different terms in the energy equation are plotted in Figure 6.4. On close inspection of Figure 6.4 we note that the oxidation term, $Q_{ox}\mathcal{D}_{ox}r_{ox}$ is very small everywhere compared to the other terms. The convection and diffusion terms roughly balance one another near the oxidizer wall ($Z = 0$). The reaction term $((1+o)\mathcal{D}r)$ is balanced for the most part by the diffusion term, $\alpha_0/(u_0L\bar{s}_0^2)\tau_{ZZ}$. The

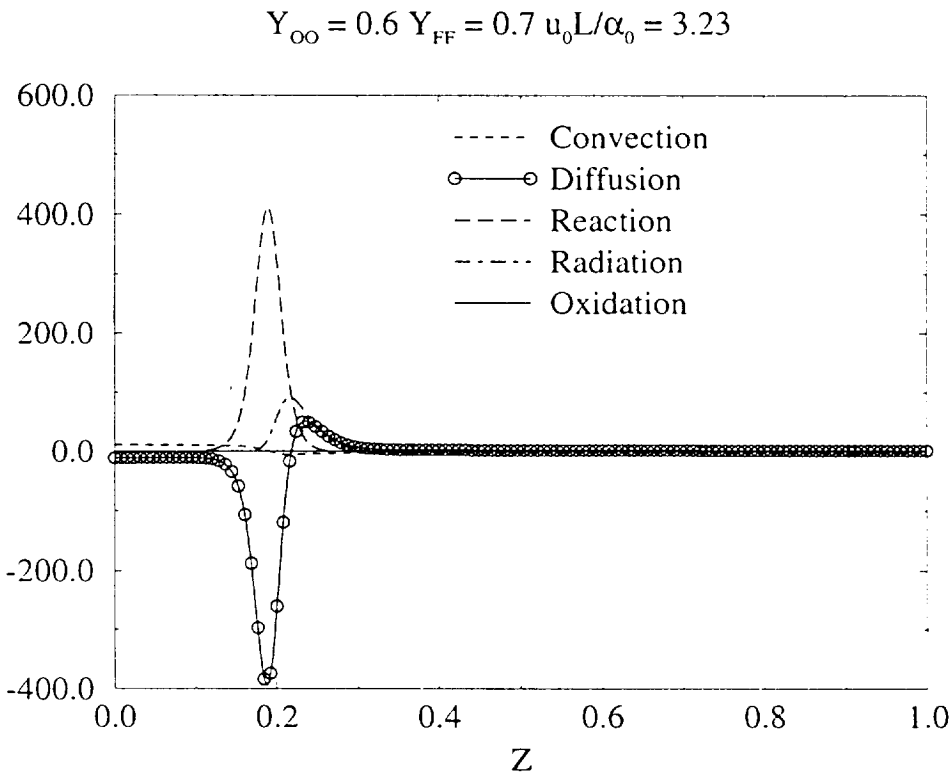

Figure 6.4. The Contribution of various terms in the energy equation.

diffusion term is positive near the right edge of the reaction term profile and it recovers the radiative loss term in that area. Thus the radiative loss term is countered by both the reaction term and the diffusion term. The peak of the temperature profile is at $Z = 0.19$ and the radiative loss term maximum is at $Z = 0.216$. Interestingly, the soot volume fraction maximum occurs at $Z = 0.224$, indicating that the radiation term profile maximum is between the maxima of temperature and soot volume fraction profiles.

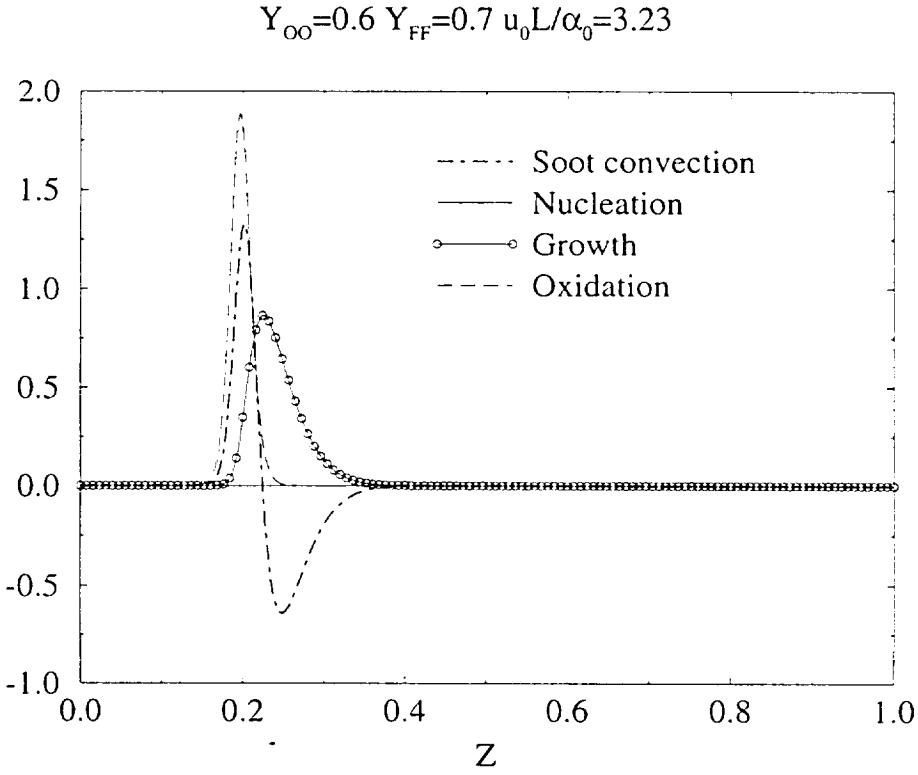

Figure 6.5. The contribution of various terms in the soot volume fraction equation.

Figure 6.5 shows the profiles of the different terms in the soot volume fraction equation. It is seen that the soot growth and oxidation regions do not overlap very significantly. This is expected in a diffusion flame. For most part soot growth ($\bar{B}\bar{r}_g$)

is balanced by soot convection term ($(D_{s0}/u_0 L\bar{s}_0^2)(d^2 f_V/dZ^2)$). However, when oxidation ($\bar{C}r_{ox}$) is present the sum of convection and soot growth terms compete with the oxidation term.

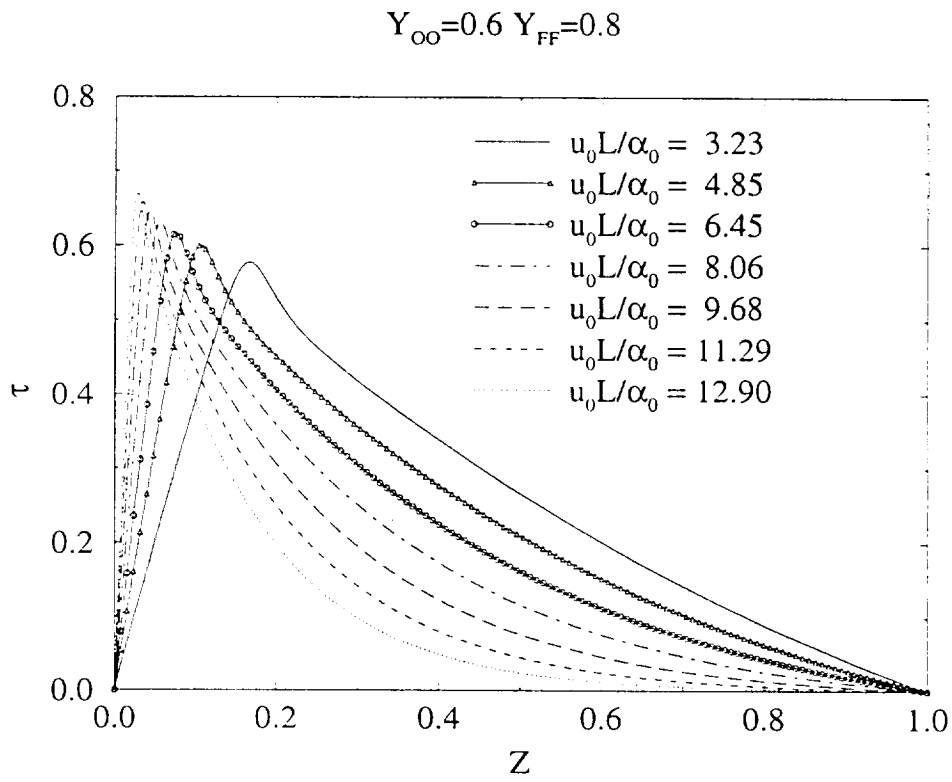

Figure 6.6. The effect of u_0 on temperature profile for a given stoichiometry.

We next focus on the effect of fuel blowing velocity, u_0, on the temperature profile when the fuel and oxidizer mass fractions in the reservoir are assumed to be fixed. For $Y_{OO} = 0.6$ and $Y_{FF} = 0.8$ the temperature profiles for different values of u_0 are plotted in Figure 6.6. As mentioned before, $L = 0.02\ m$ and $\alpha_0 = 1.24\times10^{-4}\ m^2/s$. The fuel flow velocity u_0 is increased from 0.02 m/s to 0.08 m/s with increments of 0.01 m/s. With increasing u_0L/α_0, i.e., with increasing u_0 the maximum flame temperature is found to increase. Also, the increased fuel supply pushes the flame

closer to the oxidizer wall. It is also to be noted that the movement of the flame toward the oxidizer wall with increasing fuel flow rates is quite rapid for lower values of u_0. However, the rate of migration is mitigated for higher values of u_0. The slower rate of movement can presumably be attributed to the proximity of the flame to the oxidizer wall for high values of u_0. It is important to mention here that we have already noted similar flame behavior in the absence of radiative losses ($N_R = 0$) in section 4.7 of chapter 4.

We now focus on the drop in the maximum flame temperature compared to the adiabatic flame temperature. As discussed in chapter 3, the quantity of interest is $\Delta\tau_f$ and is defined as $1 - \tau_f$ where τ_f is the maximum flame temperature. Figure 6.7 is a plot showing the variation of $\Delta\tau_f$ as a function of the nondimensional fuel flow rate at the fuel wall, i.e., $u_0 L/\alpha_0$.

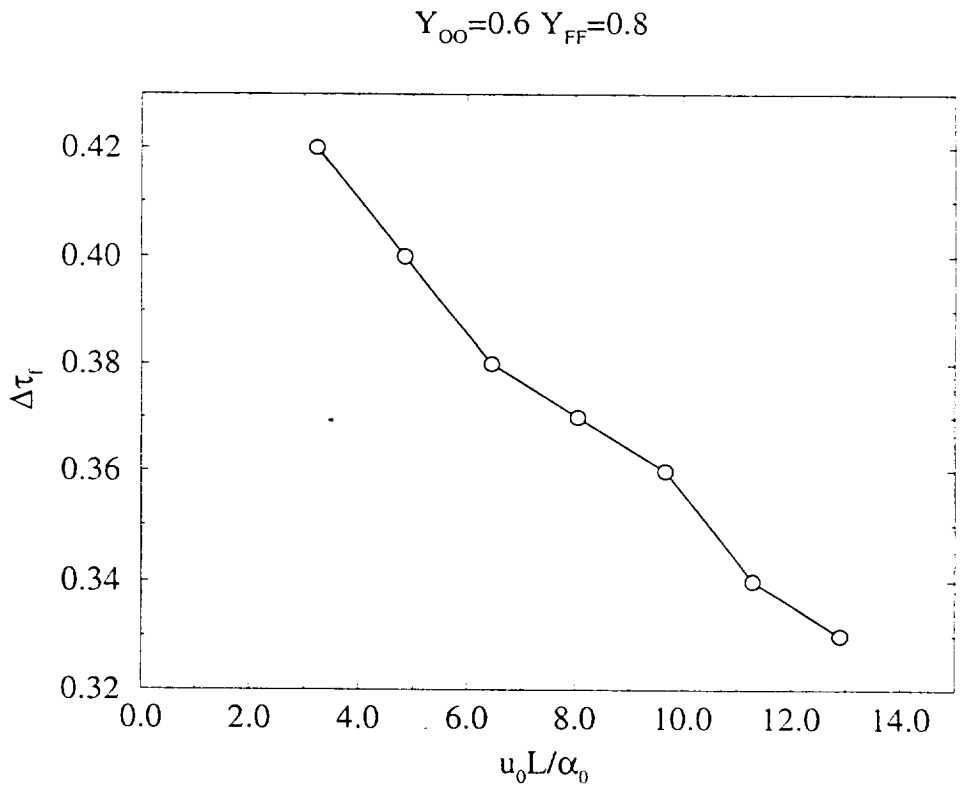

Figure 6.7. The effect of u_0 on the reaction term for a given stoichiometry.

Evidently, Figure 6.7 indicates that there is a drop in the quantity $\Delta\tau_f$, i.e., an increase in τ_f with increasing u_0. This is a direct consequence of the results illustrated in Figure 6.6.

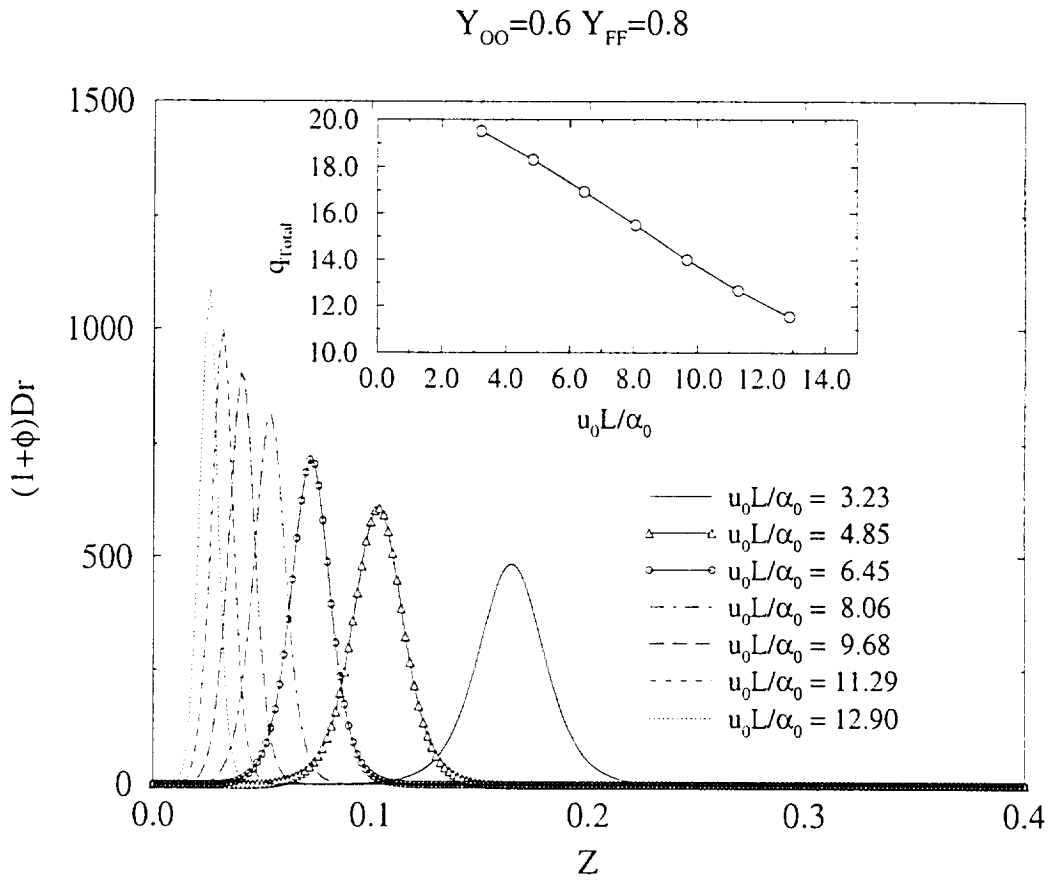

Figure 6.8. The effect of u_0 on reaction term for a given stoichiometry.

The reaction term$((1+\phi)\mathcal{D}r)$ also exhibits interesting behavior for increasing u_0. Figure 6.8 indicates that for low fuel flow rates the reaction term is far away from the oxidizer wall ($Z = 0$) and it is quite broad in Z space. With increased fuel flow rates the reaction rate profile becomes narrower and exhibits higher maximum values. Close to the oxidizer wall a very sharp reaction term profile is observed, e.g., for $u_0L/\alpha_0 = 12.90$. Since the profiles become narrower and taller with increasing

u_0 values. the integrated value of the reaction term, i.e., $q_{Total} = \int_0^1 (1+\phi)\mathcal{D}rdZ$ was also examined. The result is shown as inset to Figure 6.8.

In order to understand the behavior of the reaction rate profile better the species mass fraction profiles were also investigated.

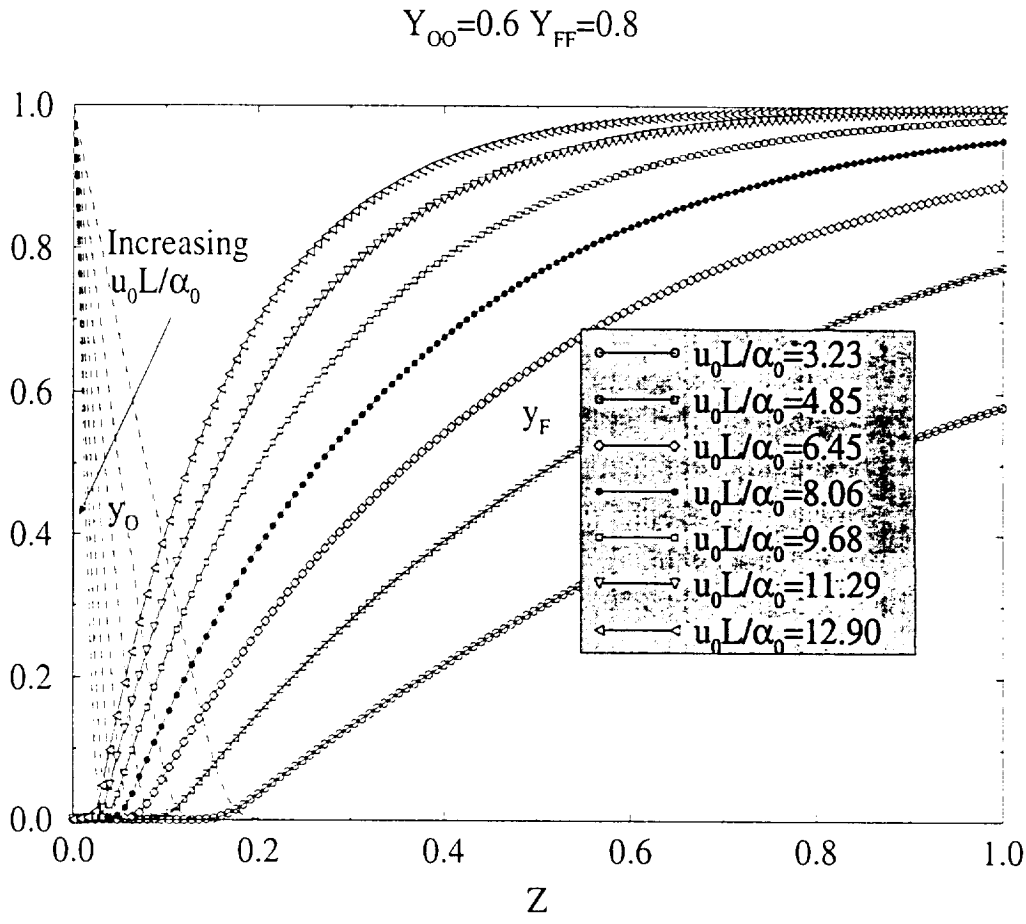

Figure 6.9. The influence of u_0 on the species mass fraction profiles for a given stoichiometry.

It was found that with increased fuel blowing there is a substantial change in the fuel mass fraction profile. The fuel mass fraction at the wall increases considerably with increased fuel blowing and saturates to a value of about unity for $u_0L/\alpha_0 = 12.90$. This tremendous increase in fuel mass fraction on the fuel side of the flame pushes

the reaction zone closer to the wall and compresses the reaction zone. The oxidizer mass fraction for different cases are also shown on the same plot. The direction of movement of the y_O profile with increasing $u_0 L/\alpha_0$ is indicated by an arrow on the plot.

A study of figures 6.6 and 6.9 in conjunction was found to be quite illuminating. From Figure 6.6 we note that for high values of $u_0 L/\alpha_0$ close to the fuel wall the nondimensional temperature is close to zero. Figure 6.9, on the other hand, indicates that the normalized fuel mass fraction values are close to unity near the fuel wall. For example, when $u_0 L/\alpha_0 = 12.90$, $\tau \simeq 0$ and $y_F \simeq 1$ for $Z \geq 0.6$. This clearly suggests that in this case, for $Z \geq 0.6$ the conditions in the domain are approximately the same as in the fuel reservoir, viz., $\tau = 0$, $y_O = 0$ and $y_F = 1$. Hence, the fuel wall has virtually moved in closer to the flame, and has thereby pushed the flame close to the oxidizer wall and compressed the region of heat release. Thus, the intense heat release takes place over a very narrow zone and hence, the peak temperature becomes higher, even though the temperature in most part of the domain decreases, as shown in Figure 6.6.

It is also interesting to scrutinize the soot volume fraction profile for increasing values of u_0. Consistent with the movement of the temperature and reaction rate profiles the soot volume fraction profile also moves toward the oxidizer wall with increased fuel flow, as shown in Figure 6.10. For lower flow rates the soot volume fraction profile is broad but it becomes narrower and taller for increased u_0, similar to the behavior of the reaction zone. Also, the soot volume fraction at the oxidizer wall is zero for low values of u_0 and all the soot produced get oxidized on the oxidizer side of the flame. However the same is not true for enhanced fuel blowing and for $u_0 L/\alpha_0 = 12.90$, for example, the soot volume fraction at the wall is 1.39×10^{-5}, indicating that a significant amount of soot remains on the oxidizer side without being oxidized.

Having analyzed the effect of u_0 on τ and f_v profiles we now focus our attention

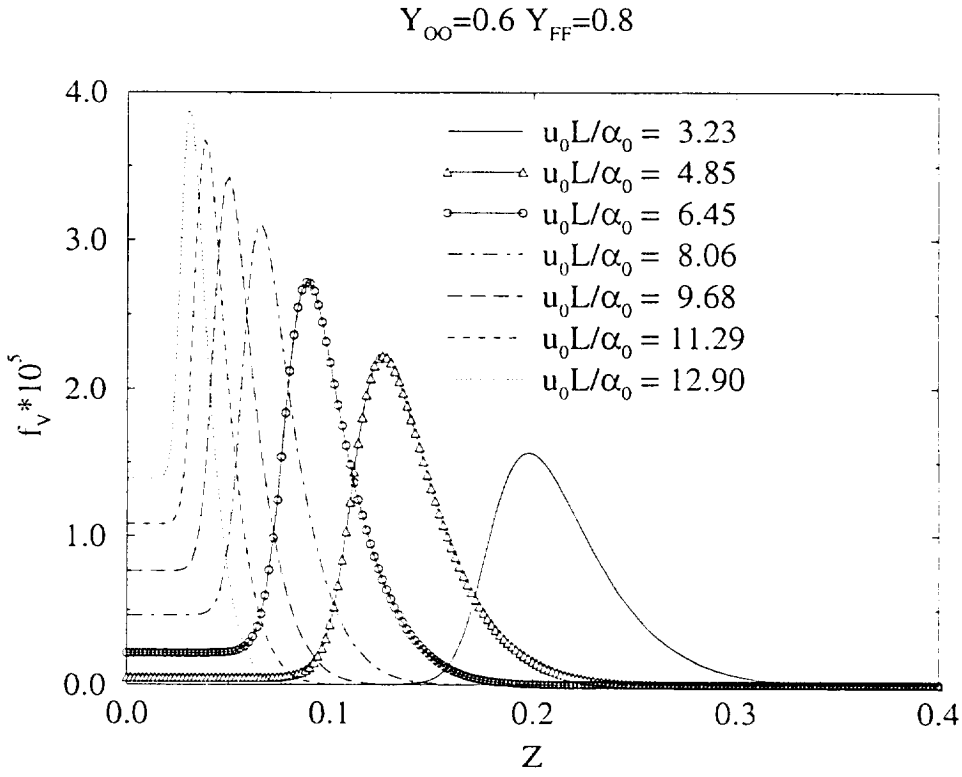

Figure 6.10. The effect of u_0 on the soot volume fraction profile for a given stoichiometry.

on the radiation term, $\Gamma_R \bar{f}_V (1-\alpha(1-\tau))^2((1-\alpha(1-\tau))^4 - (1-\alpha)^2)$. We note that the radiation loss term is explicitly dependent on the temperature and soot volume fraction profiles. We hence expect the radiation loss profile to also migrate toward the oxidizer wall with increasing values of u_0. Figure 6.11 reflects the expected behavior in the radiative loss term profile. The integrated value of the radiative loss term in Z space is also found to decrease with increasing $u_0 L/\alpha_0$.

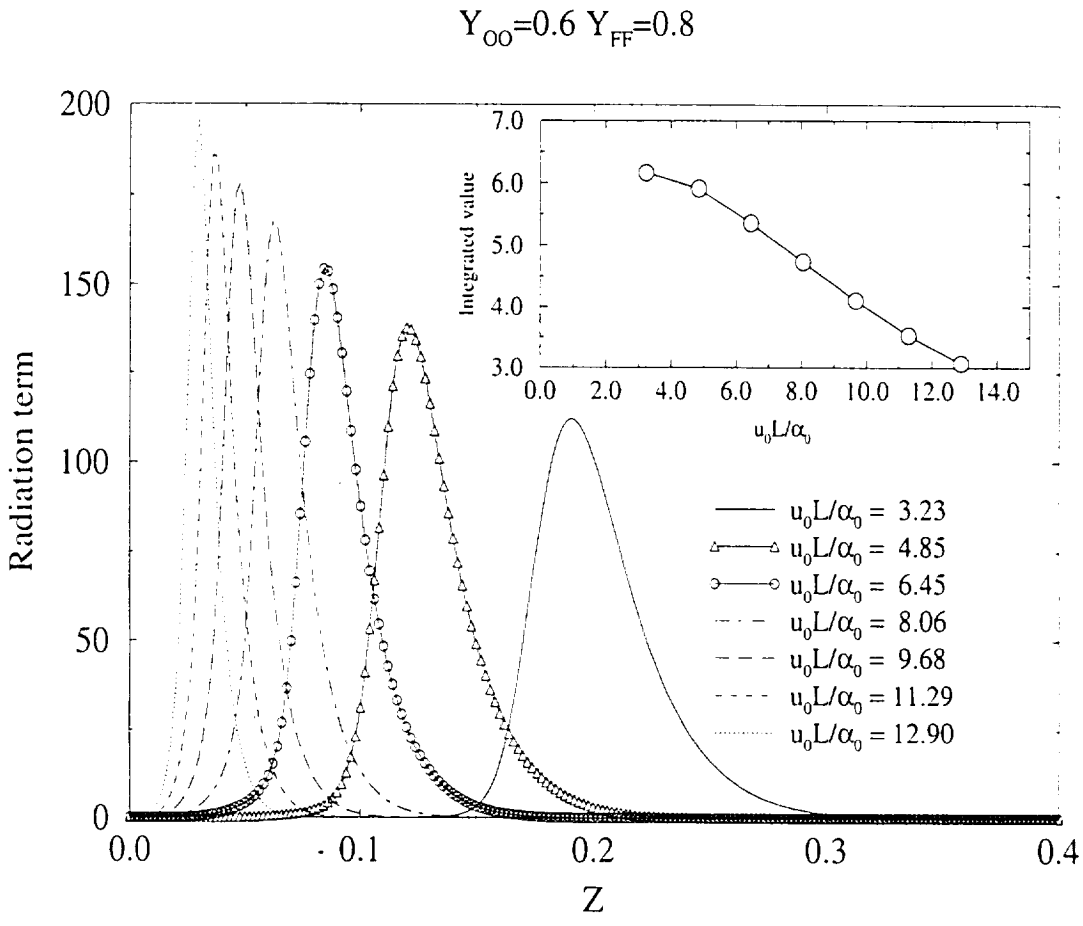

Figure 6.11. The effect of u_0 on the radiative loss term profile for a given stoichiometry.

The maximum of the radiative loss profile was always found to be between the maxima of the τ profile and the f_V profile, i.e., $Z_\tau < Z_{Rad} < Z_{f_V}$, with Z_i denoting the location of the maximum of the quantity i. The maxima of the reaction rate profile

was found to exist always to the left of the of Z_r for the fuel rich (ϕ<1) stoichiometries considered in the present work.

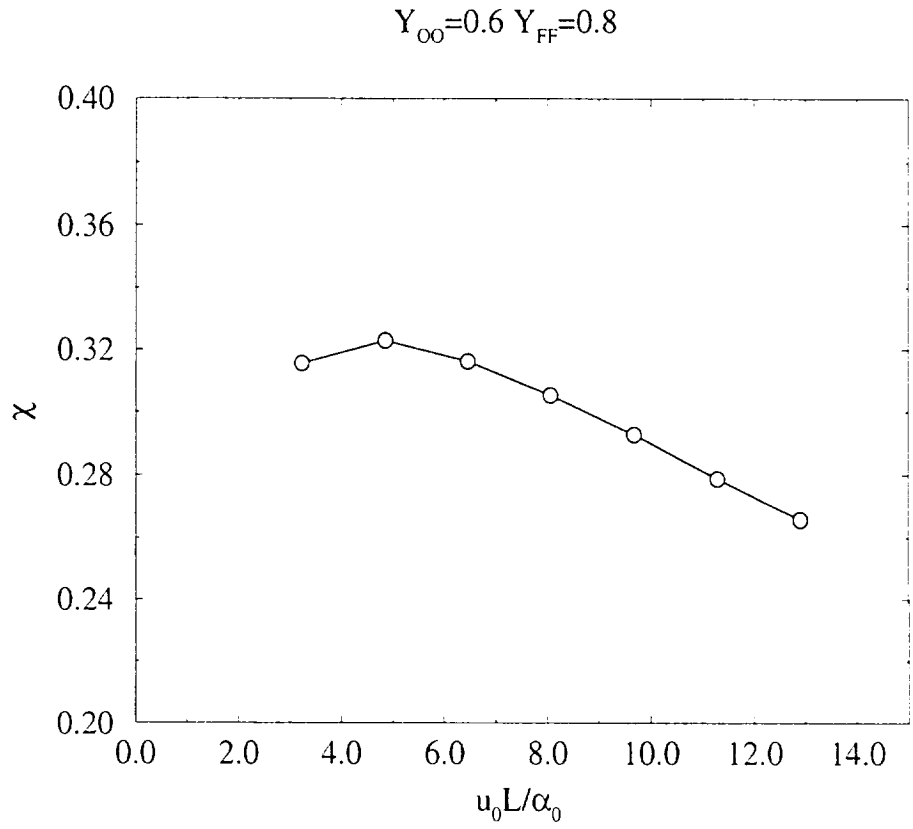

Figure 6.12. The effect of u_0 on the radiative loss term profile for a given stoichiometry.

Next, a radiative heat loss fraction, χ, is calculated. As described in chapter 3, χ is defined as the ratio of the heat lost due to radiation and the heat generated in the combustion process, i.e., $\chi = q_{Rad}/q_{Total}$. Figure 6.12 indicates that the radiative fraction changes very little with increasing value of u_0. The mean value of χ is about 0.3. This agrees quite well with the commonly used value of χ in combustion literature [4].

In order to understand the effect of radiative losses better we studied the temperature and species profiles when no soot is generated and there are no radiative losses.

This necessitates the solution of nondimensional temperature and species equations with the only source terms resulting from the primary combustion reaction. This is the same as the treatment in chapter 4 and we would focus on the solutions when $N_R = 0$.

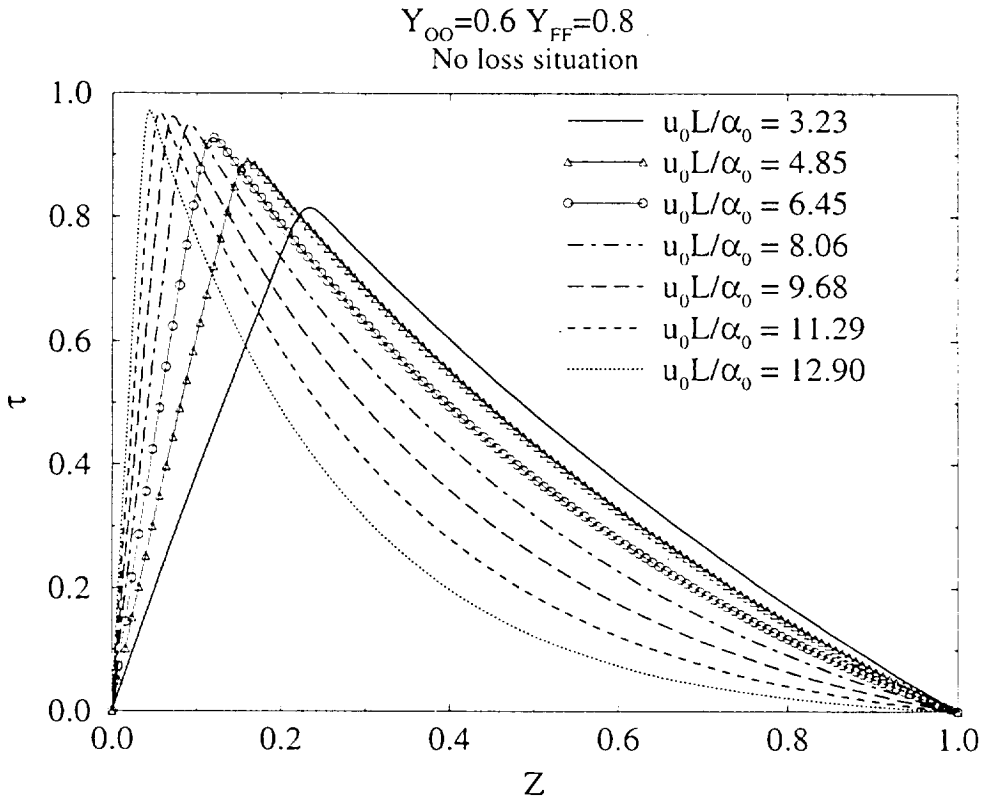

Figure 6.13. The effect of u_0 on the τ profile for a given stoichiometry on the assumption of no radiative losses.

The temperature profile shown in Figure 6.13 indicates that similar to the radiative loss situation the profiles move toward the oxidizer wall on increased fuel blowing. The maximum of the nondimensional temperature profile also increases with increasing u_0. Interestingly the reaction rate profile also indicates a consistent direction of movement (Figure 6.14). The integrated value of the reaction term, q_{Total}, also decreases with

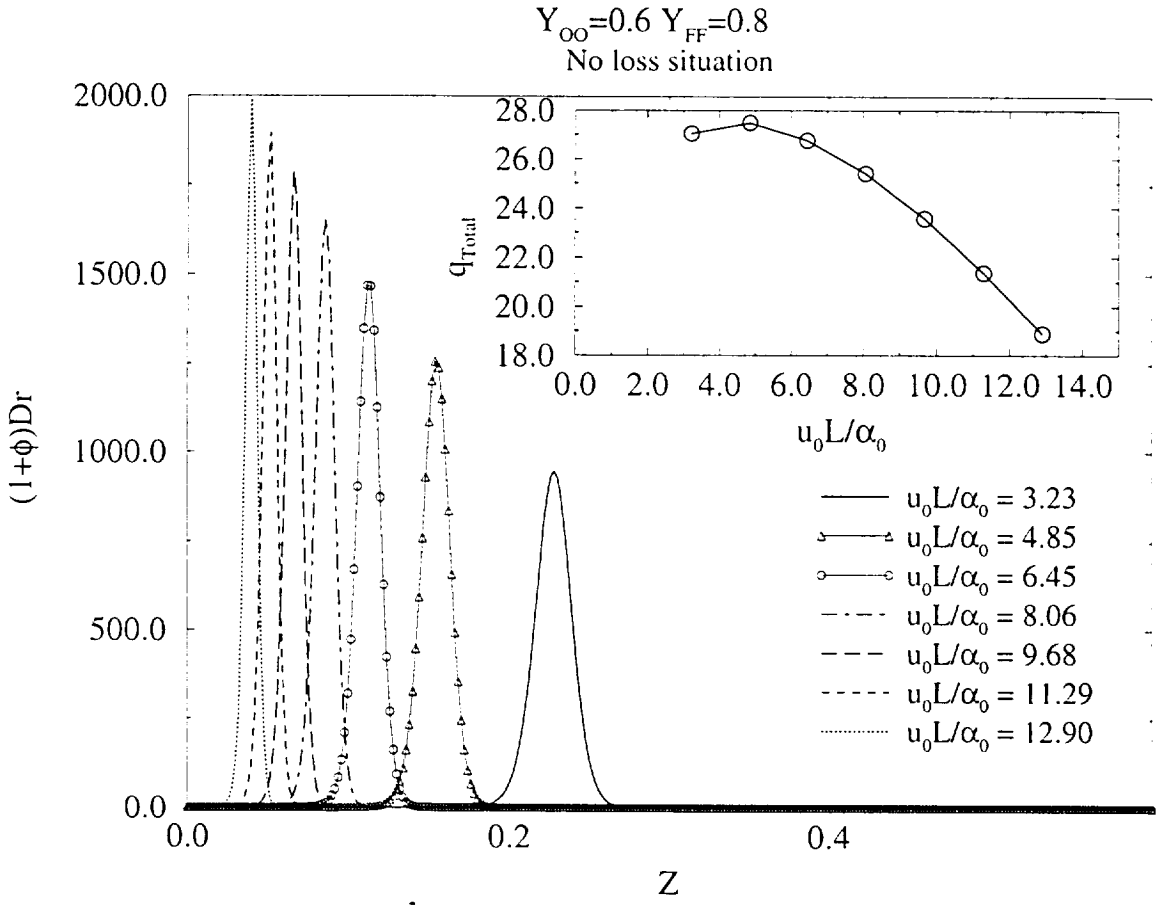

Figure 6.14. The effect of u_0 on the $(1 + \phi)\mathcal{D}r$ profile for a given stoichiometry on the assumption of no radiative losses.

increasing $u_0 L/\alpha_0$, indicating that the radiative losses are not primarily responsible for this attenuation of the value of q_{Total}. The proximity of the oxidizer wall is of crucial importance in this issue. It is also interesting to note that q_{Total} increases as $u_0 L/\alpha_0$ increases from the low value of 3.23 to 4.85. However in the higher range of values of $u_0 L/\alpha_0$ the flame is extremely close to the oxidizer wall and increases in $u_0 L/\alpha_0$ necessarily result in a drop in the value of q_{Total}. Thus our simple analysis indicates that heat losses to the wall and radiative losses are both important to the flame in a significant way.

We also examined the effect of changing the oxidizer mass fraction when both the fuel mass fraction at the wall (Y_{FF}) and the fuel flow rate (u_0) are kept constant.

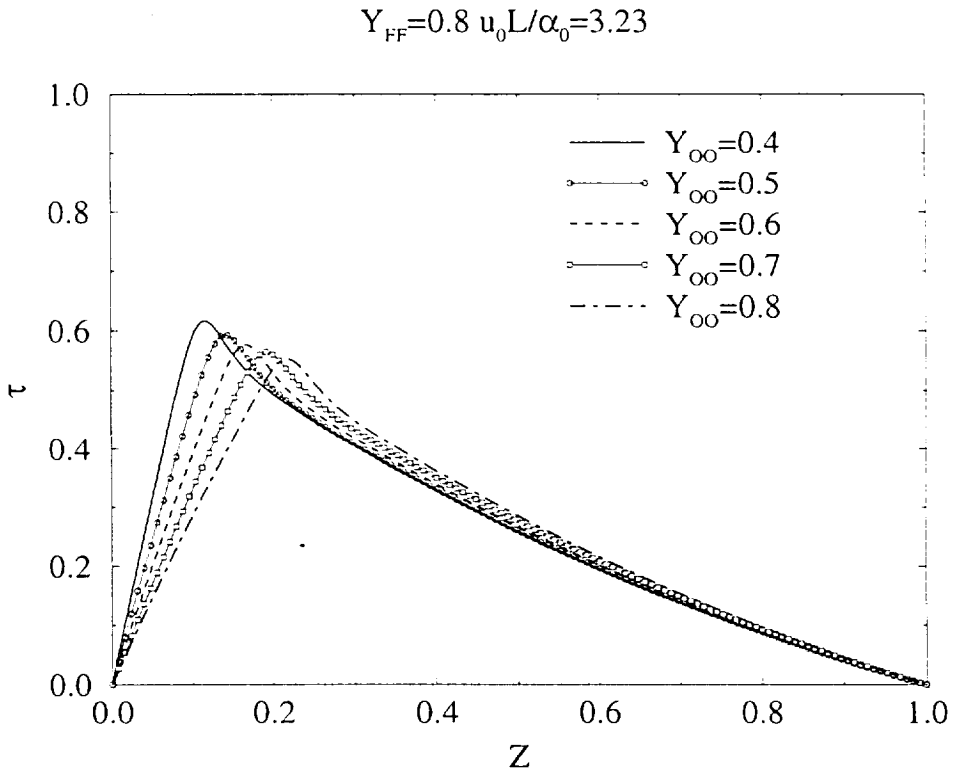

Figure 6.15. The effect of Y_{OO} on the τ profile for a given Y_{FF} and a given $u_0 L/\alpha_0$.

On increasing Y_{OO} the temperature profile maximum moves more toward the fuel wall. However the magnitude of the maximum keeps on decreasing as Y_{OO} is increased. The species profiles are also studied in detail for a better understanding of the flame. Figure 6.16 illustrates the normalized oxidizer and fuel mass fraction profiles. We observe that the oxidizer mass fractions (y_O) are everywhere higher when

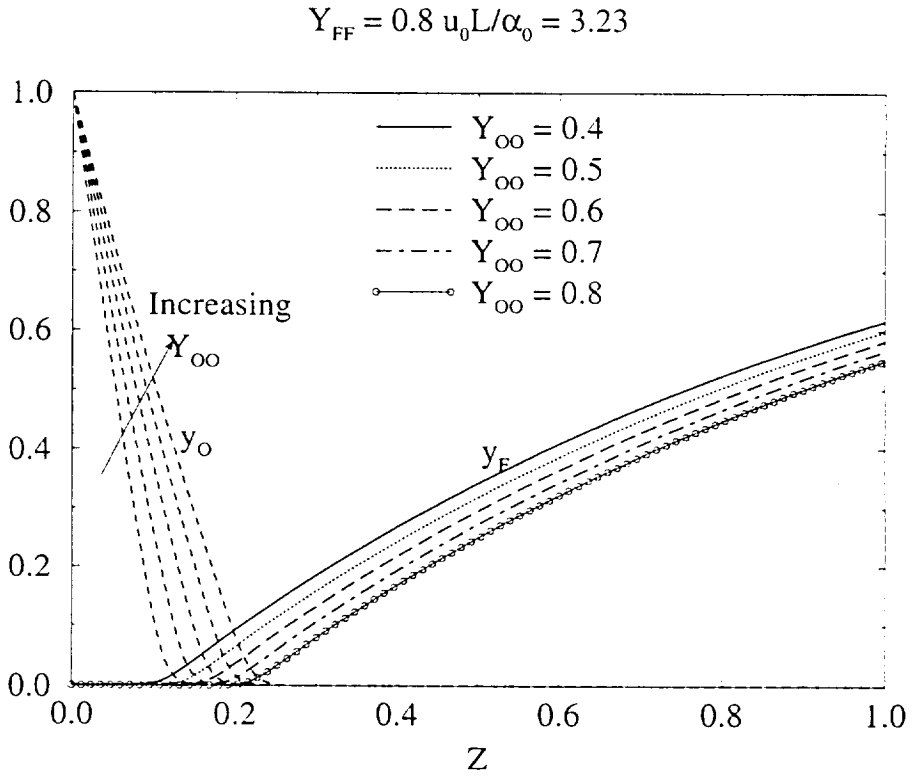

Figure 6.16. The influence of Y_{OO} on the species profiles for a given Y_{FF} and a given $u_0 L/\alpha_0$.

Y_{OO} is increased. In sharp contrast, the normalised fuel mass fraction (y_F) values are lower everywhere for increased Y_{OO} values. Also, the normalised fuel mass fraction values at the wall decrease on increasing Y_{OO} values. The significant decrease in y_F values result in decreased reaction rates, as illustrated in Figure 6.17. The reaction rate profile also moves toward the fuel wall on increasing the value of Y_{OO}. The

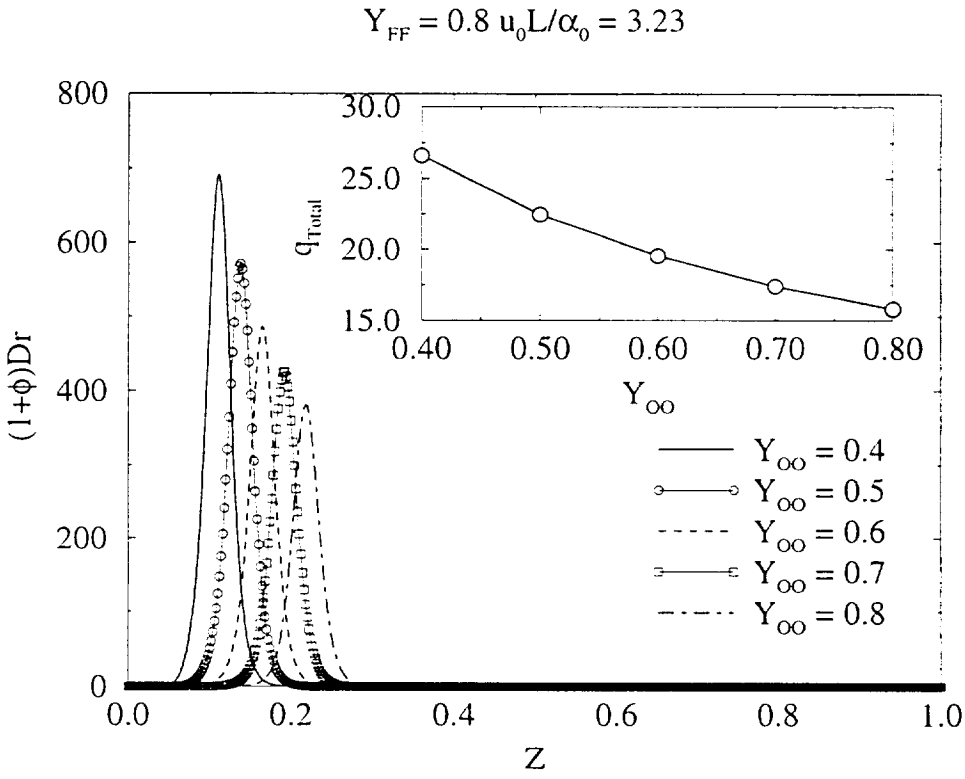

Figure 6.17. The influence of Y_{OO} on the reaction rate for a given Y_{FF} and a given u_0L/α_0.

integrated reaction rate, q_{Total}, decreases with increasing Y_{OO}.

The soot volume fraction profile is investigated next. As anticipated from the movement of the temperature and reactivity profiles, the soot volume fraction profile moves toward the fuel wall. With increasing Y_{OO}, the temperature values decrease and consequently, less soot is produced. It has to be mentioned here that for lower values of Y_{OO} the soot volume fraction profile is located close to the oxidizer wall and there is a residual soot volume fraction near the wall, which is not oxidized. For higher values of Y_{OO} there is no residual soot volume fraction near the wall. The radiation

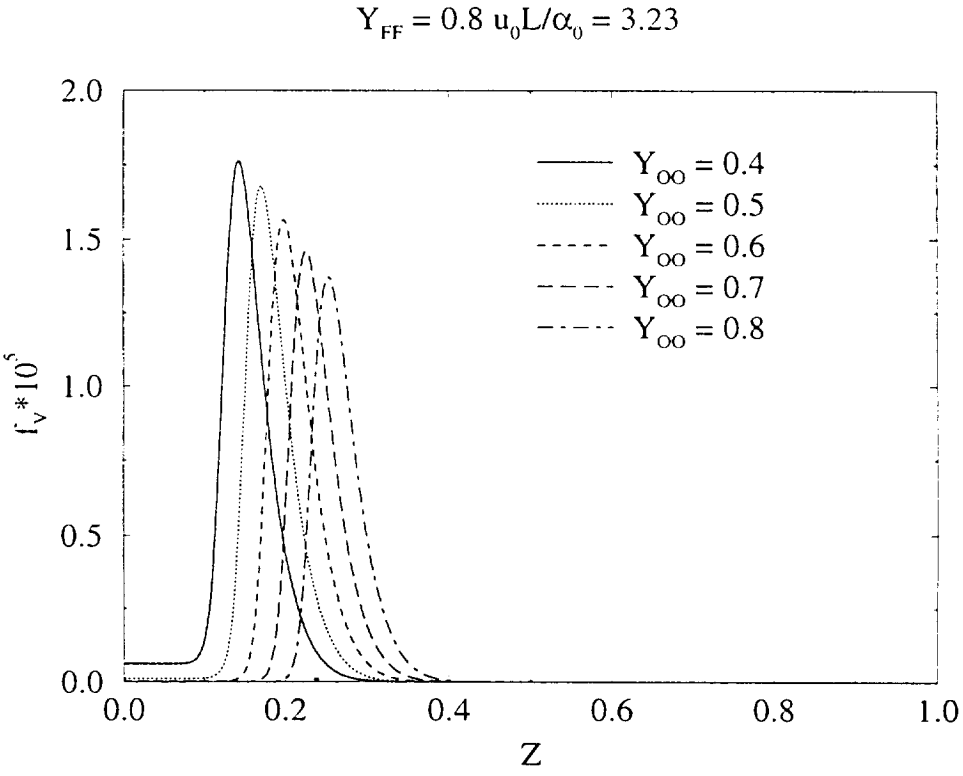

Figure 6.18. The influence of Y_{OO} on the soot volume fraction profile for a given Y_{FF} and a given u_0L/α_0.

term profile (see Figure 6.19) also moves toward the fuel wall and the maximum of the profile also decreases in magnitude as Y_{OO} is increased. Investigation of the integrated

value of the radiation term profile was also carried out and the result is shown as inset to Figure 6.19. The integrated value decreases as a function of increasing Y_{OO}. The

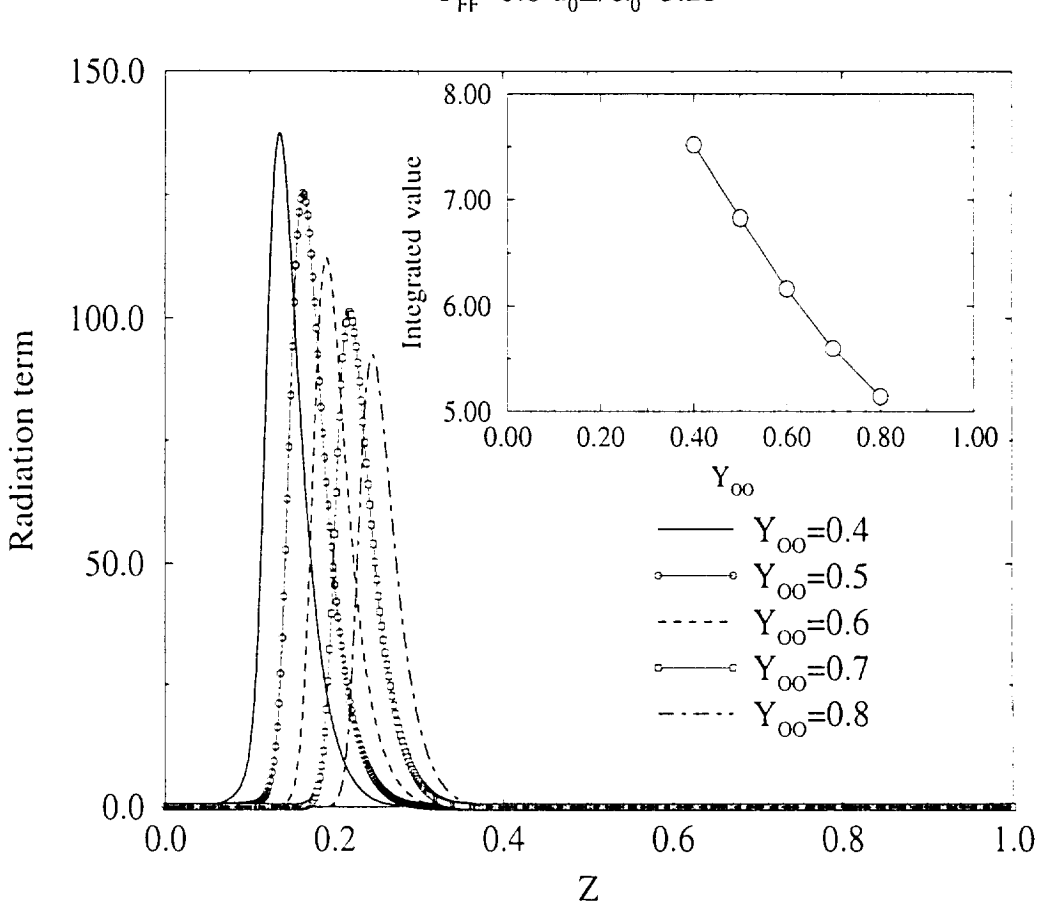

Figure 6.19. The effect of Y_{OO} on the radiation term profile for a given Y_{FF} and a given u_0L/α_0.

radiative fraction values were also investigated and are plotted in Figure 6.20. The χ values increase with increasing Y_{OO} and are in the vicinity of 0.3.

The effect of increasing Y_{FF} for a given u_0 and a given Y_{OO} is investigated next. The temperature profile is observed to move toward the oxidizer wall, as expected (see Figure 6.21). However, there is also a drop in the temperature profile maximum. A plot of the drop in peak flame temperature as a function of the fuel wall mass

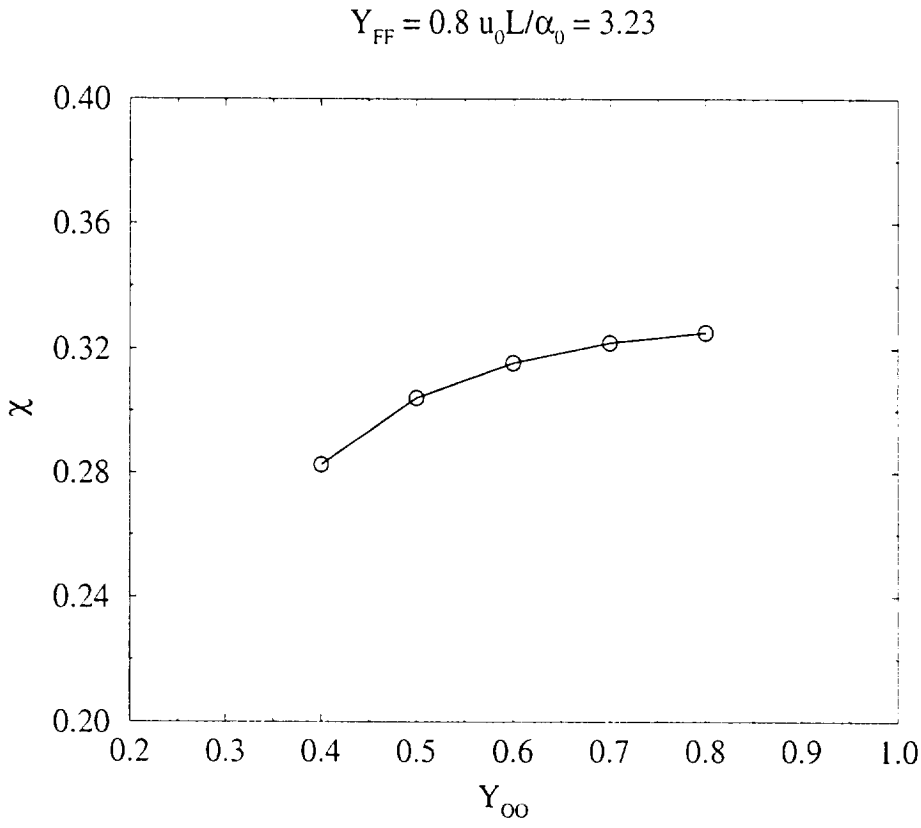

Figure 6.20. The effect of Y_{OO} on the radiative fraction for a given Y_{FF} and a given u_0L/α_0.

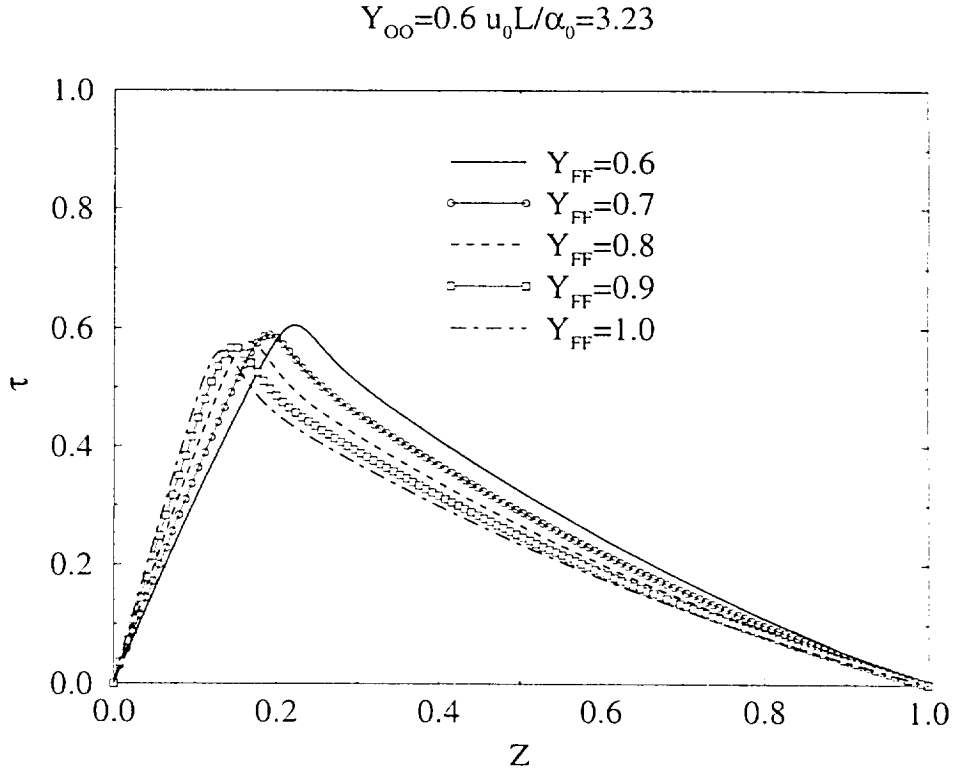

Figure 6.21. The effect of Y_{FF} on the temperature profile for a given Y_{OO} and a given u_0L/α_0.

fraction is shown in Figure 6.22.

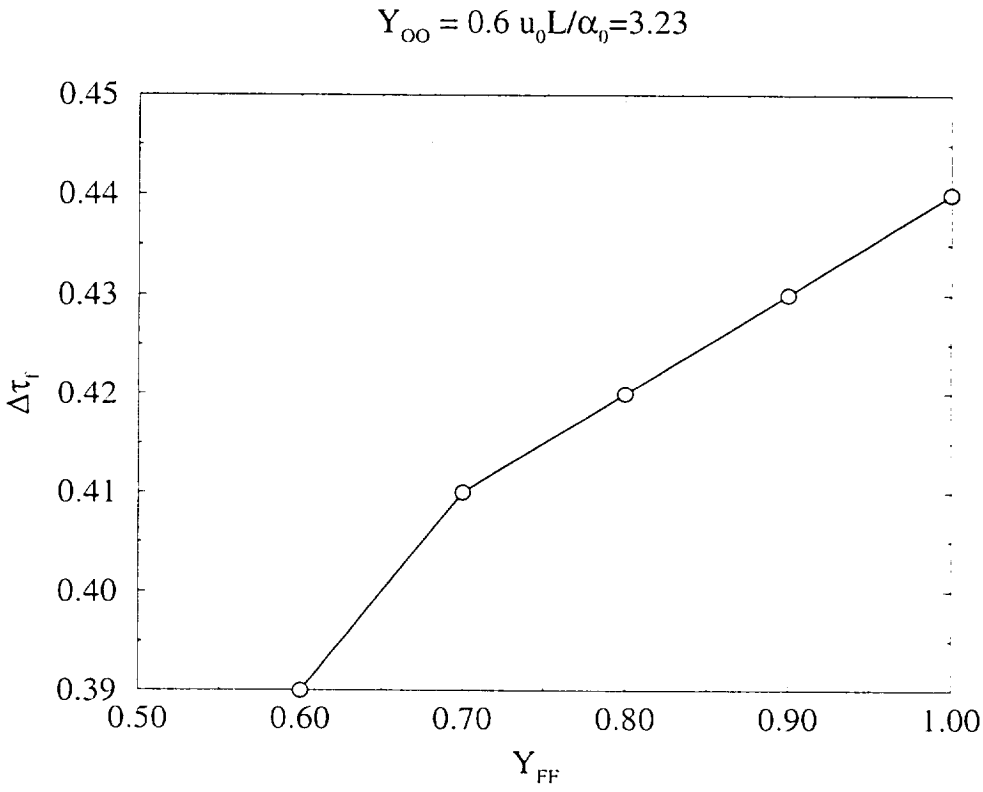

Figure 6.22. The drop in peak flame temperature as a function of Y_{FF}.

The reaction rate profile also moves toward the oxidizer wall on increasing Y_{FF} as shown in Figure 6.23. Interestingly, the reaction rate profile maximum increases with increasing Y_{FF}. The integrated value of the reaction rate, q_{Total}, increases with increasing Y_{FF}, unlike in a previous situation when u_0 was increased for a fixed set of Y_{OO} and Y_{FF}.

The species mass fraction profiles are shown in Figure 6.24.

It is clear from a comparison of Figure 6.9 and Figure 6.24 that increasing fuel blowing rate has a much stronger effect on the fuel mass fraction profile than increasing the fuel mass fraction at the fuel reservoir.

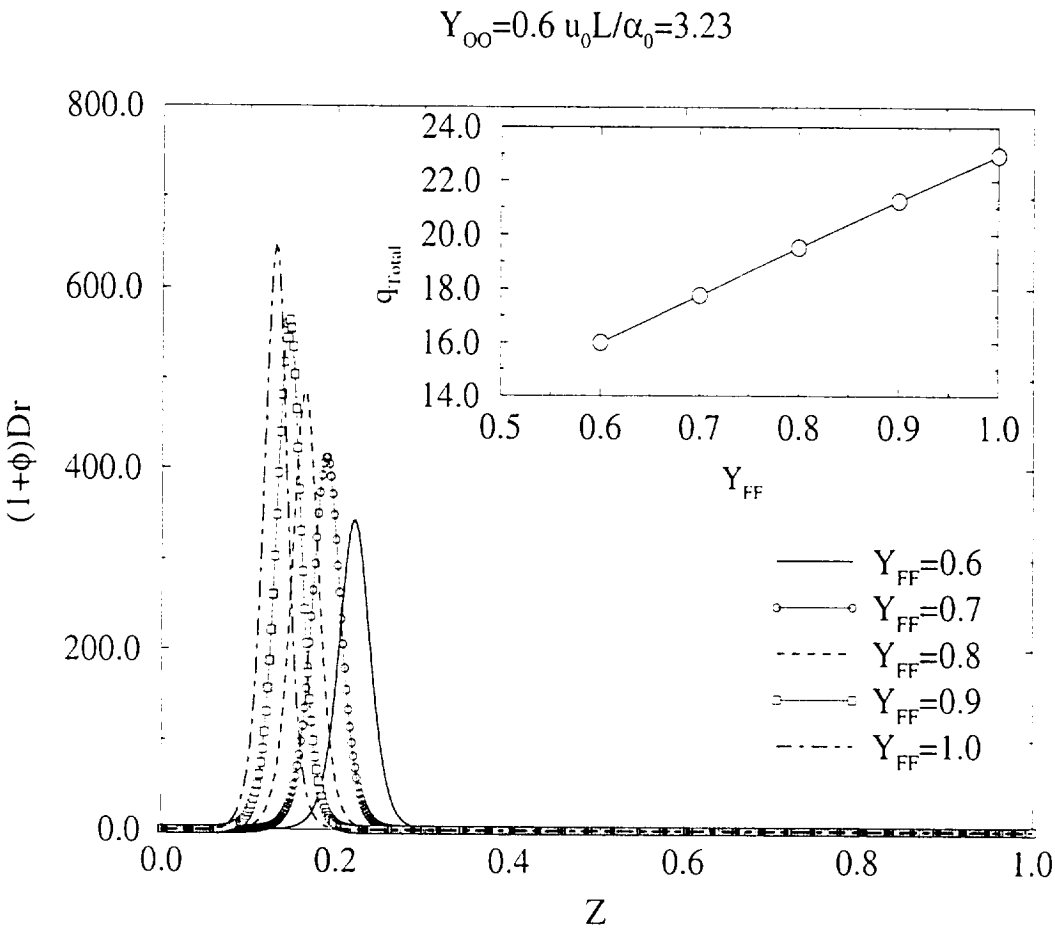

Figure 6.23. The effect of Y_{FF} on the reaction term profile for a given Y_{OO} and a given u_0L/α_0.

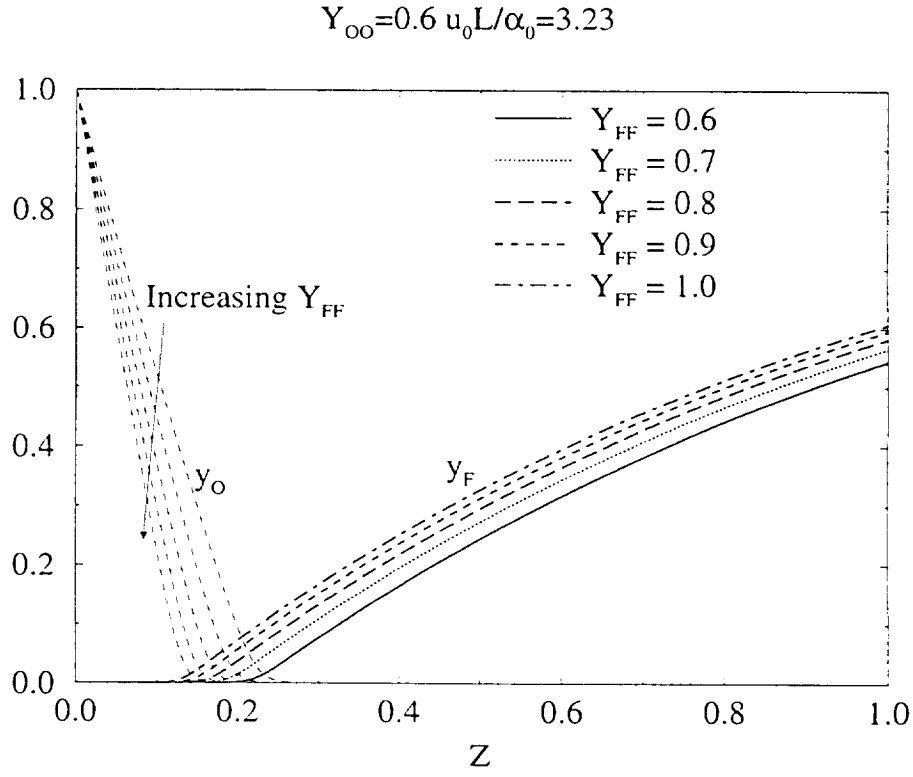

Figure 6.24. The effect of Y_{FF} on the species profiles for a given Y_{OO} and a given u_0L/α_0.

Correspondingly the soot volume fraction profiles are also plotted in Figure 6.25. Soot volume fraction increases as Y_{FF} is increased and the profile moves closer to the

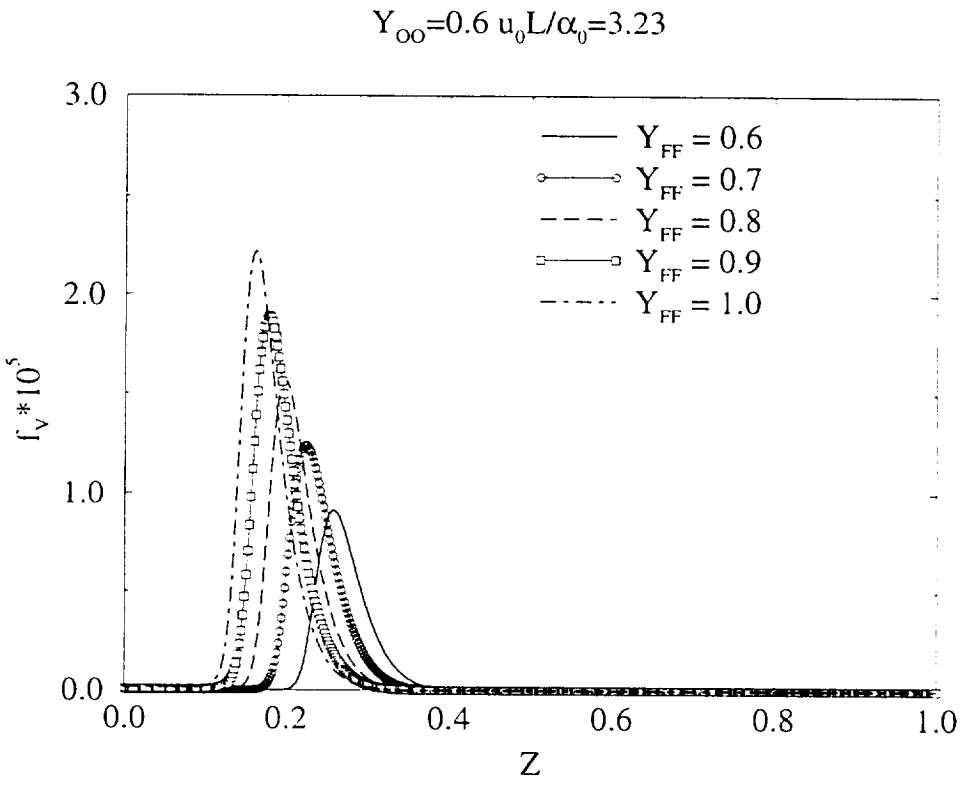

Figure 6.25. The effect of Y_{FF} on the soot volume fraction profile for a given Y_{OO} and a given u_0L/α_0.

oxidizer wall in accordance with the movement of the temperature and reaction rate profiles. Figure 6.26 shows the radiation term profile. The integrated value of the radiative loss profile is found to increase with increasing Y_{FF} values.

The radiative fraction χ indicates an increasing trend with Y_{FF} (See Figure 6.26. It should also be noted that the value of the radiative fraction is close to 0.3 in all cases.

It is also of interest to examine the velocity profile, u, for a typical flame. As discussed before, the velocity u is given by equation 6.2, and hence is dependent

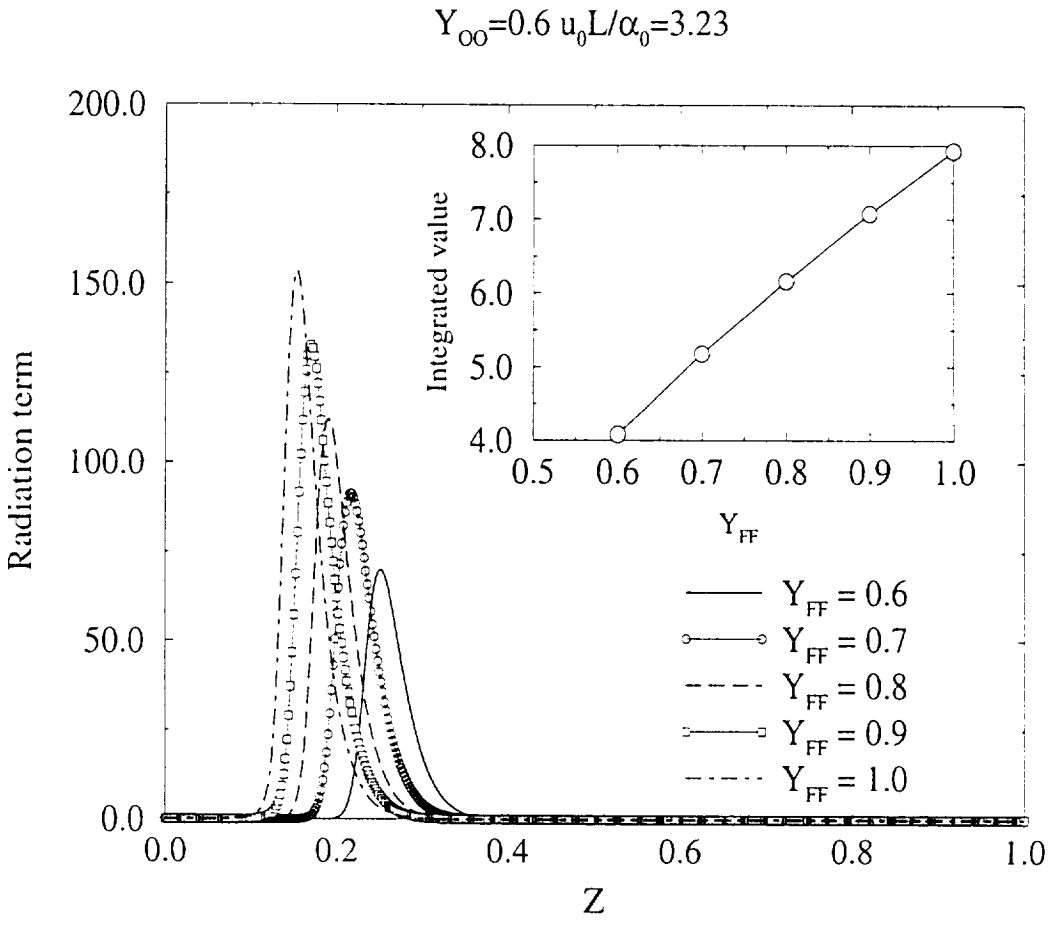

Figure 6.26. The effect of Y_{FF} on the radiation term profile for a given Y_{OO} and a given u_0L/α_0.

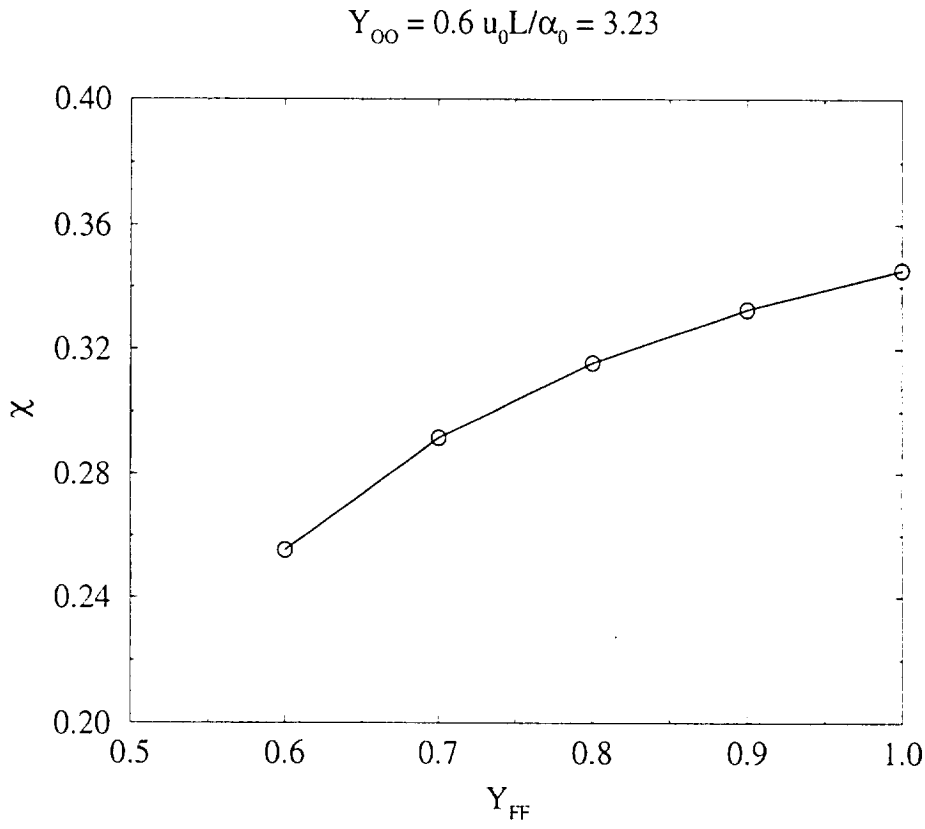

Figure 6.27. The effect of Y_{FF} on the radiative fraction for a given Y_{OO} and a given u_0L/α_0.

on the density distribution $\bar{\rho}$. The $\bar{\rho}$ distribution is obtained using equation 3.16 of chapter 3 and a typical case is plotted in Figure 6.28. The normalised density is the highest at the close to the walls and it attains a minimum at the maximum temperature location.

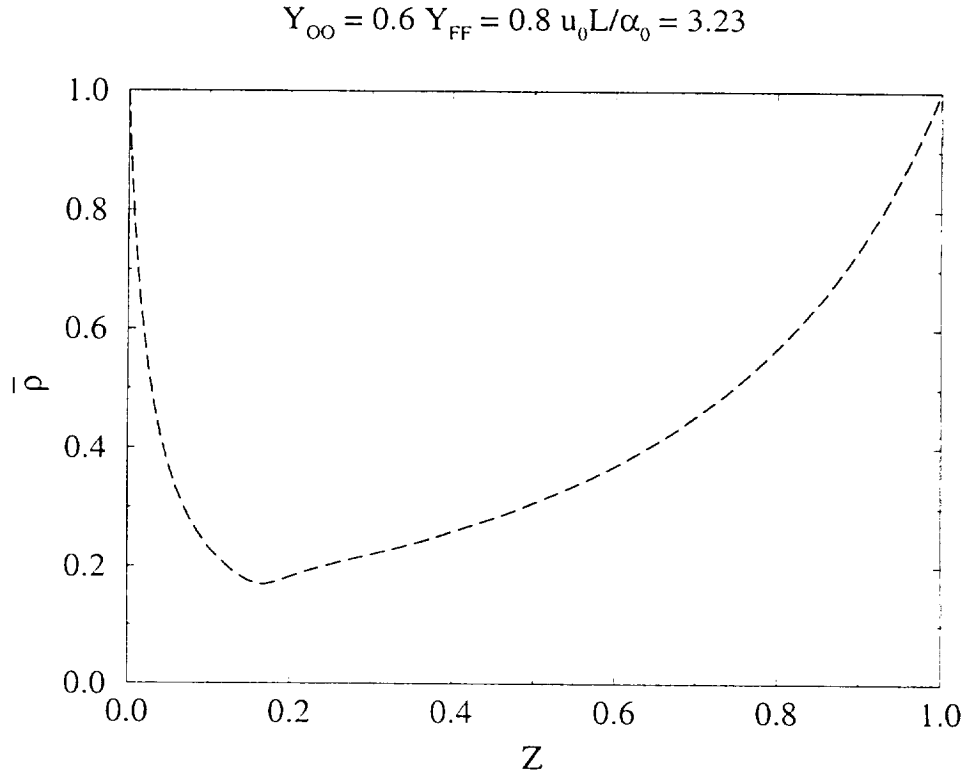

Figure 6.28. The $\bar{\rho}$ distribution plotted in the Z coordinate.

The velocity distribution is plotted for two different mass flow rates in Figure 6.29. Figure 6.29 depicts the profiles for $u_0 L/\alpha_0 = 3.23$ and $u_0 L/\alpha_0 = 12.90$. The velocity u is quite high near the flame location and decreases to its nominal value u_0 at either wall. The magnitude of u is much higher when $u_0 L/\alpha_0 = 12.90$, as expected. The maximum velocity is $\sim 12\ cm/s$ when $u_0 L/\alpha_0 = 3.23$ and it increases to $\sim 12\ cm/s$ when $u_0 L/\alpha_0 = 12.90$.

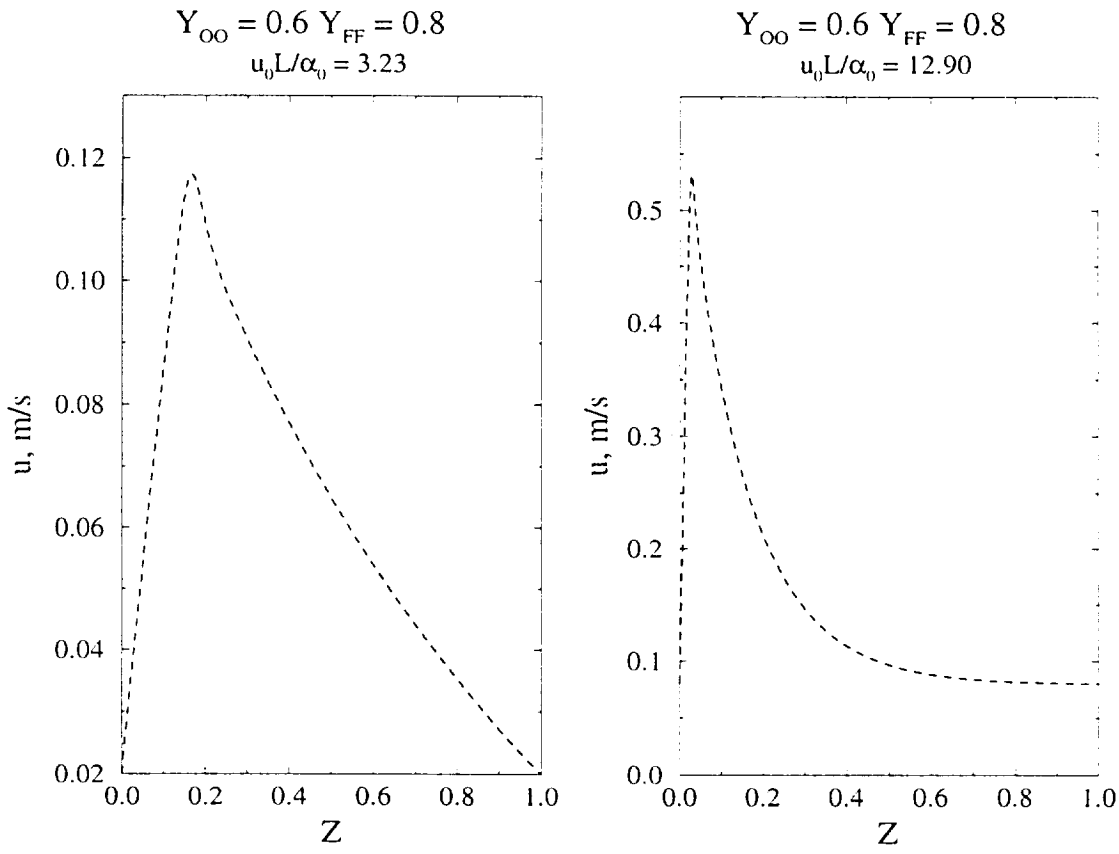

Figure 6.29. The velocity distribution for $u_0L/\alpha_0 = 3.23$ and $u_0L/\alpha_0 = 12.90$.

The influence of thermophoresis was examined by plotting $\bar{m}_T$ as a function of Z. As noted in section 6.1.1 $\bar{m}_T$ is given by equation 6.18. Figure 6.30 shows the variation of $\bar{m}_T$ for a low velocity ($u_0 L/\alpha_0 = 3.23$) and for a higher velocity ($u_0 L/\alpha_0 = 12.90$). It is apparent from the figure that the value of $\bar{m}_T$ is not significant for most part

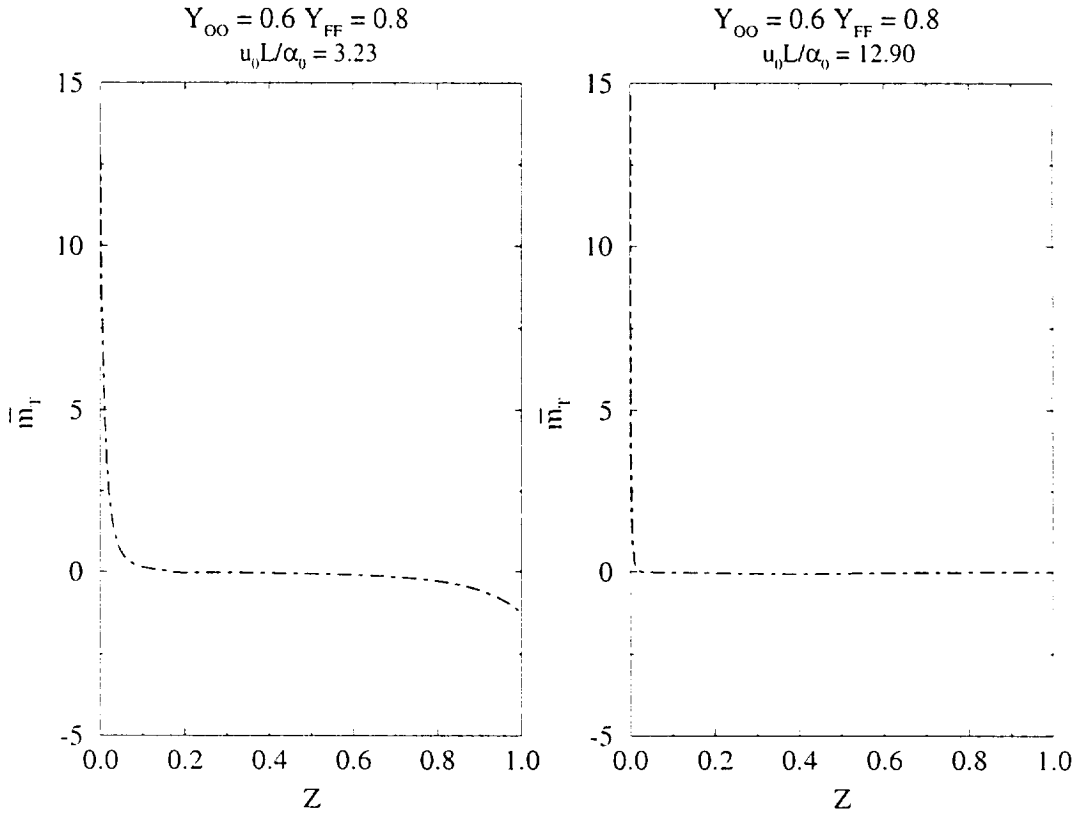

Figure 6.30. The quantity $\bar{m}_T$ plotted as a function of Z.

of the domain and it increases near the cold walls. For $u_0 L/\alpha_0 = 3.23$ the influence of thermophoresis is significantly more important compared to the high velocity case ($u_0 L/\alpha_0 = 12.90$).

Next, the thermophoretic velocity u_T and the ratio of the thermophoretic velocity and the convective flow velocity, i.e., u_T/u are plotted in the physical coordinate x. We recall that the fuel wall is located at $x = 0$ m and the oxidizer wall is located

at $x = 0.02\ m$. Figure 6.31 indicates that u_T is small in both low and high velocity

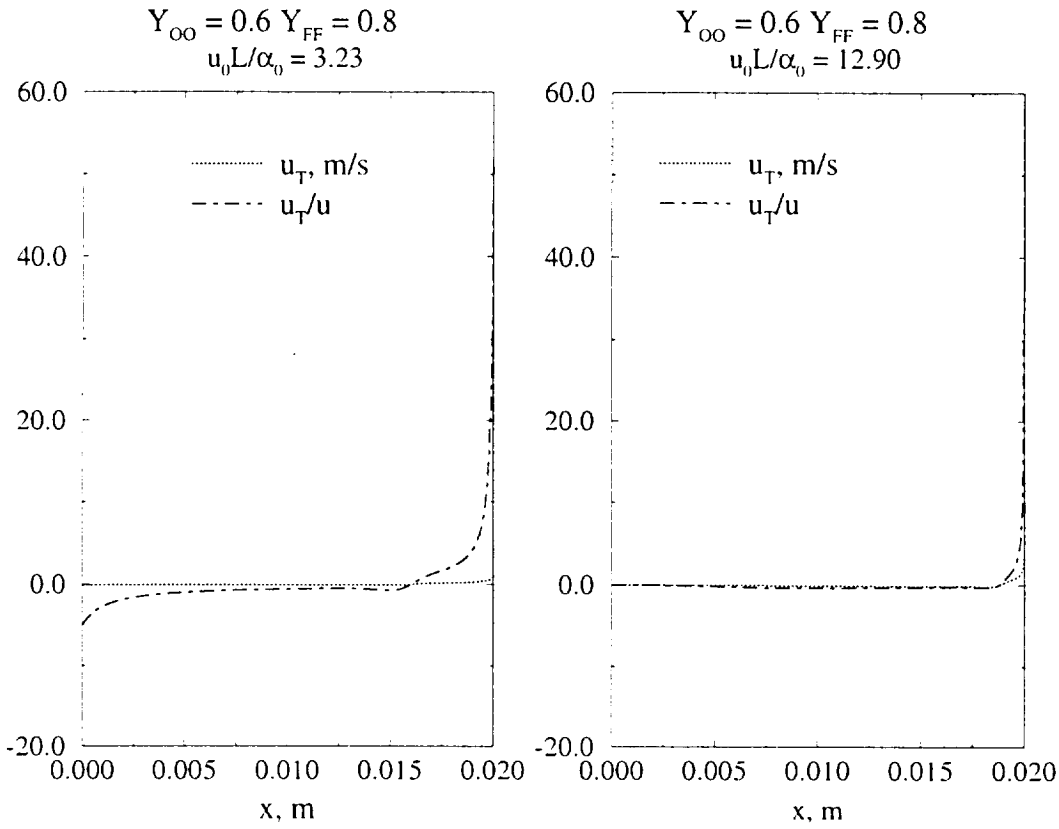

Figure 6.31. The quantities u_T and u_T/u plotted as a function of the physical coordinate x.

cases. However, the ratio u_T/u is quite important over a significant region near either wall. For $u_0L/\alpha_0 = 12.90$, however, u_T/u seems significant only near the oxidizer wall.

6.5 Estimation of the Soot Volume Fraction Profile

In section 5.6 of chapter 5 we estimated the soot volume fraction profile assuming Burke-Schumann, or, IRR profiles for the temperature and species. However,

Burke-Schumann profiles are not accurate enough in a finite chemistry situation with radiative losses. The temperature values are too high for the IRR case and consequently, the soot volume fraction values are unrealistically high in some cases. Hence, the adiabatic flame temperature was arbitrarily chosen to produce a realistic range of soot volume fraction values. A more involved treatment is necessary when the influences of finite chemistry and radiative loss are included. In this section we purport to introduce the effect of radiative losses in a very simple way and derive a modified expression for the temperature, species and soot volume fraction.

Let us first assume that the peak value of the nondimensional temperature, τ, is a fraction ξ. Then, equation 4.13 can be modified to write

$$\tau = \begin{cases} \xi \frac{1-e^{-Z/\epsilon}}{1-e^{-Z_f/\epsilon}} & 0 \leq Z \leq Z_f, \\ \xi \frac{e^{-1/\epsilon}-e^{-Z/\epsilon}}{e^{-1/\epsilon}-e^{-Z_f/\epsilon}} & Z_f \leq Z \leq 1. \end{cases} \tag{6.19}$$

We note that when $\xi = 1$ we get the Burke-Schumann profiles. We will still use equation 5.24, which is an expression for the balance of soot convection and growth terms. Also, similar to the treatment in section 5.6 of chapter 5 we try to express the normalised fuel mass fraction y_F in terms of the fuel side temperature distribution, τ. We obtain $y_F = a(1 - \tau/\xi)$. Also, dZ can be written as $dZ = -a\epsilon/[a\tau - (a-1)\xi]$. Using the expressions for y_F and dZ in equation 5.24 we get

$$\frac{1}{\bar{f}_V^{2/3}} d\bar{f}_V = [\bar{B}\bar{s}_0(1-\alpha)^{4/3}a^{13/6}\epsilon] \frac{(1-\tau/\xi)^{7/6} e^{-(\bar{\beta}_r + \frac{\bar{\beta}_a}{6})(\frac{1-\tau}{1-\alpha(1-\tau)})}}{(1-\alpha(1-\tau))^{5/6}(a\tau-(a-1)\xi)} d\tau. \tag{6.20}$$

Again we note that setting $\xi = 1$ in equation 6.20 recovers equation 5.28 of section 5.6. On integrating equation 6.20 subject to the boundary condition $\bar{f}_V = 0$ at $Z = 1$ we get the soot volume fraction profile. However, integrating equation 6.20 involves

evaluating the integral

$$I_1 = \int_0^{\tau} \frac{(1-\frac{\tau}{\xi})^{7/6} e^{-(\bar{\beta}_{\tilde{\gamma}}+\frac{\bar{\beta}_{\tilde{\alpha}}}{6})(\frac{1-\tau}{1-\alpha(1-\tau)})}}{(1-\alpha(1-\tau))^{5/6}(a\tau-(a-1)\xi)} d\tau \tag{6.21}$$

Substituting $u = 1-\tau$ and writing $\beta_{\gamma\alpha} = \bar{\beta}_{\tilde{\gamma}} + \frac{\bar{\beta}_{\tilde{\alpha}}}{6}$ we arrive at the following expression for I_1:

$$I_1 = \frac{1}{\xi}\int_u^1 \frac{(u-(1-\xi))^{7/6} e^{\frac{-\beta_{\gamma\alpha} u}{(1-\alpha u)}}}{(1-\alpha u)^{5/6}(\xi + a(1-u-\xi))} du \tag{6.22}$$

This integral could not be evaluated by analytical means. To simplify the integrand, the exponents 7/6 on $(u-(1-\xi))$ and 5/6 on $(1-\alpha u)$ were both replaced by unity. The simplified integral, say I_2, was evaluated using the commercial code *MAPLE*. The result was in terms of exponential integrals, similar to equation 5.32 of chapter 5.

We note here that the maximum flame temperature is not known and has to be approximately determined in order to evaluate the soot volume fraction profile using equation 6.20. In the present work, we use the value of ξ directly from the numerically obtained solution of the temperature profile. Figure 6.32 shows the numerical solutions for the temperature, species and soot volume fraction profiles when $Y_{OO} = 0.5$, $Y_{FF} = 0.4$ and $u_0 L/\alpha_0 = 4.85$. Using the value of ξ from the numerical solution in equation 6.19 we determine a nondimensional temperature profile, τ. The normalised species mass fraction profiles are then determined iteratively, similar to the procedure described in section 4.5 of chapter 4. Based on these analytically obtained temperature and species profiles we numerically solve the soot volume fraction equation. The solution is plotted in Figure 6.32. The analytical solution of the soot volume fraction equation involving exponential integrals is also plotted in Figure 6.32. It is clear that the analytical solutions for τ, y_O and y_F are in very close agreement with the numerical solutions. Also, the soot volume fraction profile obtained on the assumption of the analytical τ, y_O and y_F profiles approximates the numerical solution reasonably well.

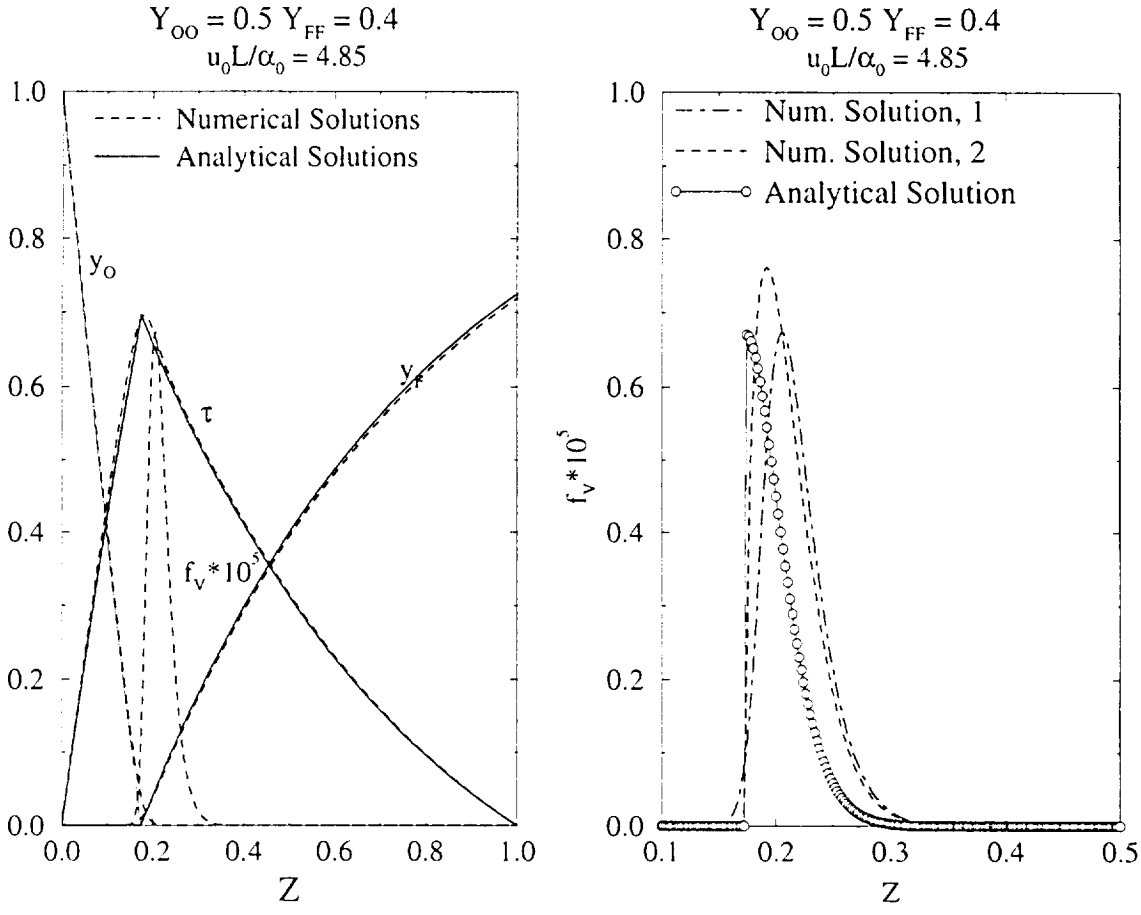

Figure 6.32. Comparison of f_V profiles when $Y_{OO} = 0.5$, $Y_{FF} = 0.4$ and $u_0L/\alpha_0 = 4.85$. *Numerical Solution, 1* refers to the simultaneous solution of coupled equations of τ, y_O, y_F and f_V. *Numerical Solution, 2* refers to the solution of the soot volume fraction equation on the assumption of analytical profiles for τ, y_O and y_F. The analytical solution of the soot volume fraction equation involves the evaluation of the integral I_2 in terms of exponential integrals.

The soot volume fraction values are in good agreement and the numerical solution of the soot volume fraction equation is also capable of predicting the soot zone thickness fairly well.

6.6 Conclusions

The comprehensive soot radiation problem was analyzed in this chapter assuming soot radiation in the optically thin limit. For soot formation, the model of Syed, Stewart and Moss [1] was used. The semi-empirical formula of Nagle and Strickland-Constable [2] was used for soot oxidation. The conservation equations were numerically solved for a range of parameter values and the results were analyzed to study the influences of the various parameters on the flame structure and the flame radiation.

The soot volume fraction profile was always found to exist on the fuel side of the flame with the location of the peak soot volume fraction being $1 - 2\ mm$ to the fuel side of the location of the maximum temperature. This is in accordance with experimental observations [30]. The peak of the radiation term was always located between the peak temperature and peak soot volume fraction locations.

The influence of increasing the fuel blowing velocity, u_0, was investigated first. On increasing u_0 the temperature and reaction rate profiles migrated toward the oxidizer wall. The maximum flame temperature increased as u_0 was increased. The integrated value of the reaction term, i.e., q_{Total}, decreased as u_0 was increased. A higher fuel blowing rate managed to push the flame against the oxidizer wall, and consequently, the heat losses to the wall also increased. This resulted in a reduction in the value of q_{Total}. It was also found that the rate of movement of the flame toward the oxidizer wall decreased with higher values of u_0 and the reaction rate profile became taller and narrower. A similar trend was also observed for the soot volume fraction profile and the radiative loss profile. The integrated value of the radiation term, i.e., q_{Rad},

decreased with increasing u_0. The value of the radiative fraction was around 0.3.

On increasing Y_{OO} for a given Y_{FF} and $u_0 L/\alpha_0$ the flame migrated toward the fuel wall and the temperature, as well as the reaction rate values decreased. The soot volume fractions, as well as the q_{Rad} values decreased in such a situation.

Finally, Y_{OO} and $u_0 L/\alpha_0$ values were kept fixed and Y_{FF} values were increased to study the flame behavior. The flame moved toward the oxidizer wall and the peak flame temperature decreased with increasing Y_{FF}. However, the q_{Total} values increased. The soot volume fraction values also increased. The radiation term profile also moved toward the oxidizer wall and the q_{Rad} values increased with increases of Y_{FF}. The radiative loss fraction was found to be around 0.3.

On including a correction factor for the peak temperature it was possible to modify the analytical expressions for the Burke-Schumann temperature and species profiles to agree with the numerical solution. Such an agreement was possible primarily because there was very little leakage of fuel and oxidizer across the flame. Using the modified expressions for the temperature and species profiles it was possible to develop an analytical expression for the soot volume fraction profile based on the method already described in chapter 5. The analytically obtained soot volume fraction profile agreed very well with the numerical solution.

A radiative extinction was not observed in any of the cases tested. This indicates that a steady state extinction is not quite likely. As mentioned before, the radiative fraction value was about 0.3 in all the cases and a decrease (increase) in the q_{Total} values resulted in a decrease (increase) of q_{Rad}. This phenomenon seems to indicate that the radiative losses from a flame bears a direct relationship with the heat release and an excessive increase of radiative losses is not likely when the heat release decreases.

CHAPTER 7

Conclusions and Recommendations for Future Work

The work presented in this dissertation has revealed interesting features of the structure of a radiating diffusion flame. A qualitative analysis of a diffusion flame with a hypothetical $sech^2$ radiative loss profile indicated that for a loss term fixed in space, the flame can break through the loss zone on increasing the radiative loss term sufficiently. It was also shown that such a "break through" is only possible for thin radiative loss zones placed immediately next to the ideal flame location, Z_f.

For pure diffusion flames the increase in radiative losses always resulted in the flame moving toward the oxidizer side. For a diffusion flame with convective fuel flow from the fuel wall even the opposite was observed. Evidently, the interaction of convection, diffusion, reaction and radiative losses is harder to predict compared to a pure diffusion flame situation, when the effect of convection is not present.

An analytical model of soot profile was determined which accurately predicts the soot zone thickness when Burke-Schumann profiles were assumed for the temperature and the species mass fractions. Such a model was based on the observation that the primary balance for the flames studied in our configuration revealed a balance between the processes of soot growth and soot convection.

Such a balance was also evident from an analysis of the results of the comprehensive soot radiation problem (chapter 6). We also discovered that in accordance with experimental results for sooting diffusion flames the soot growth and oxidation regions do not significantly overlap, as expected in a diffusion flame. The soot volume fraction maximum was found to occur on the fuel side of the flame and was typically at a distance of $1-2\ mm$ from the temperature maximum. The radiation loss profile peak was always situated in between the flame temperature peak and the soot volume fraction peak. We note that the radiative fraction was around 0.3 for the flames studied. The consequence of increasing the fuel flow velocity at the wall, u_0, was to push the flame closer to the oxidizer wall. Correspondingly, the reaction rate profile became narrower and taller, and its integrated value q_{Total} decreased with increasing u_0. The integrated value of the radiative loss term also decreased with increasing u_0.

In another study, the oxidizer reservoir mass fraction, Y_{OO}, was kept fixed along with the fuel blowing velocity u_0. The fuel reservoir mass fraction was increased from 0.6 to 1.0 in steps of 0.1. It was observed that the flame moved closer to the oxidizer wall and the peak flame temperature decreased with increasing Y_{FF} values. The temperature maximum decreased even though the integrated value of the reaction rate, q_{Total}, increased. The integrated value of the radiative loss term, q_{Rad} also increased and the radiative loss fraction value was about 0.3 in all cases. Thus, it was found that the radiative losses depend directly on the amount of heat released and in the cases studied, the radiative losses adjusted to the heat release in such a way that the radiative fraction values were about 0.3.

A radiative extinction was not observed in any of the cases studied, indicating that a steady state extinction is unlikely. Also, since the radiative fraction values were close to 0.3 in all cases, it seemed that the flame tried to limit the heat losses with any decrease of heat release.

The analytical model developed in chapter 5 for the soot volume fraction profile

used the assumption of Burke-Schumann temperature and species mass fraction profiles. However, for a diffusion flame with radiative losses the temperature and species profiles are significantly different from the infinite reaction rate profiles. Hence, a correction factor ξ was used for the peak flame temperature. The analytical expressions for the Burke-Schumann profile were modified to include the factor ξ. The resultant profiles matched very well with the numerical solution of the comprehensive soot radiation problem discussed in chapter 6. Based on the method described in chapter 5 utilizing the balance between soot growth and convection an analytical expression was then developed for the soot volume fraction profile including the effect of ξ. The analytically obtained soot volume fraction profile matched fairly well the numerical solution of the comprehensive problem.

The soot model used in the present work has received significant attention in the literature. However, the physico-chemical processes which lead to the evolution and burn-out of soot particles are still not well understood. It is anticipated that more accurate and versatile soot models will appear as the investigation on soot processes in flames intensifies with the help of better diagnostic and modeling capabilities. Thus, future work has to utilise more accurate descriptions of soot processes.

It will also be important to investigate the effect of soot radiation in the optically thick limit. A more comprehensive radiation-soot interaction model has to be envisaged for that purpose. The soot volume fraction in our flames analyzed in chapter 6 was in the range $10^{-7} - 10^{-5}$. For soot volume fractions in the vicinity of the upper limit, it will be worthwhile to examine the influence of a more comprehensive radiation model.

The radiation from the combustion gases was neglected in our analyses. This effect can also be included for a more accurate description of the flame behavior.

In our problem the heat losses from the flame occurred because of the radiating soot particles and also due to the presence of cold reservoir walls. It will be interesting

to study the effect of other configurations on this flame, specially when conductive losses to cold boundaries are significantly reduced. For example, it will be interesting to study the effect of radiation from a fuel strip burning in an ambient oxidizer field where the boundaries of the domain are far apart. The influence of strain in such a field on the flame structure and the radiative loss profile will be quite worthwhile to study.

Methane was chosen as the fuel in the current work because the important parameter values for one-step methane combustion reaction are available. However, methane is not a heavily sooting fuel and in future, it will be interesting to investigate the problem with more readily sooting fuels, such as ethylene, acetylene, etc.

APPENDICES

APPENDIX A

Asymptotic Calculations for a Simplified Model of the Interaction of a Diffusion Flame with a Heat-Loss Zone

A.1 Abstract

In this Appendix we examine a highly simplified model problem for the interaction of a diffusion flame (DF) with a heat-loss zone (the "soot" layer). Explanations are provided for DF migration (observed in chapter 3) and ultimate quenching when $N_R \Delta Z_R$ is made large enough (chapters 3, 4).

A.2 Introduction

The purpose of this study is to theoretically analyze the influences of a heat loss zone on a diffusion flame (DF).

Although fundamental soot formation chemistry has been examined in detail for

many years, the number of studies exploring its relation to actual physical processes in flames is few. In the sooty region of a DF there are intense heat losses to the surroundings, perhaps strong enough to retard chemical activity or, under proper conditions, to cause extinction. The model considered here examines this question by paring the physics to a minimum and focusing only on the skeletal features of the flame/radiation interaction. Here we eliminate convection (natural and forced), thermophoresis, and particulate oxidation, all of which are important in actual sooty flames. For example, when convection is eliminated (not simply by transformation to a coordinate system in which the convection and diffusion terms are combined into one overall "convective-diffusive" term, but actually and entirely eliminated), the standard formulations of the soot conservation equation become untenable because there is no means for balancing the creation/destruction terms with a convection term; a different interpretation of the soot zone is required.

The approach followed here will be to examine a simple model thoroughly. The emphasis will be placed on making mathematically definite statements that can be turned into physically useful criteria, given the limitations of the model. We note that our goal is to describe - not simulate - the influence on DFs of radiant heat losses from particulates.

Finally, we observe that a study very similar to this one was published in the literature [56] but an error in one of the calculations prevented correct conclusions from being drawn. In this study the error is corrected. Revised results are presented and interpreted.

A.3 Formulation

A.3.1 Physical Discussion

The following simplifications are employed in this study: *geometrically*, we consider the one-dimensional "stagnant film" diffusion flame (DF). The porous fuel wall, at temperature T_0, is located at $x = 0$, parallel to the oxidizer wall which also has $T = T_0$ and is located at $x = L$. The mass fractions of fuel and oxidizer at these walls are Y_{FF} and Y_{OO} respectively (see Figure 3.1).

Dynamically, we limit ourselves to the case of zero mean flow; the movement of species occurs strictly by diffusion. In addition, we neglect the thermophoretic flow that is known to occur with particulates in regions of high thermal gradients, because we wish to examine only the thermal and chemical influences of heat losses. In summary, we have a one-dimensional stagnant-film DF with no mean flow ($u = 0$) and no thermophoretic flow ($u_T = 0$). We also impose the steady-state condition ($\partial(.)/\partial t = 0$). For the combustion *chemistry* we assume that the reaction at the DF occurs through a single irreversible step, $F + \nu O \rightarrow (1 + \nu)P$ (on a mass basis), with high activation energy. The "soot-formation mechanism", which we hypothesize occurs on the fuel side of the DF, is assumed not to consume fuel. That is, only "trace" amounts of fuel are required to make "soot" particulates. Also, since the "soot distribution" will be specified, we do not require a separate soot species equation. Nor is it necessary to consider a number-density equation, since we assume that our "soot" particulates are simply a collection of immobile radiating masses located in a preassigned region on the fuel side of the DF. Strictly speaking, there is no need even to discuss "particulates" like "soot" because none of the explicit features commonly associated with particulates appear in our analysis. The relevant features of our "soot particulate layer" are exclusively thermal: the layer produces only a region of enthalpy loss that may alter the DF structure and cause extinction.

Even if extinction does not occur the heat losses may weaken the DF. The relationship between DF-weakening and heat-loss enhancement is an interesting one that may, within the limits of this analysis, be quantified. We assume that the fuel and oxidizer walls are perfectly transmitting so the heat lost from the "soot" layer is permanently lost. Finally, we observe that the "soot" layer is presumed to remain always on the fuel side of the DF, thereby eliminating discussions of "soot oxidation", etc.

A.3.2 The Mathematical Problem

The boundary-value problems governing the distributions of temperature, fuel mass fraction and oxidizer mass fractions are, respectively,

$$\left.\begin{array}{lll} (i) & \frac{d}{dx}(\lambda\frac{dT}{dx}) = -Q_F w + \frac{dq_R}{dx}, & T(0) = T(L) = T_0, \\ (ii) & \frac{d}{dx}(\rho D_F \frac{dY_F}{dx}) = w, & Y_F(0) = Y_{FF}, Y_F(L) = 0, \\ (iii) & \frac{d}{dx}(\rho D_O \frac{dY_O}{dx}) = \nu w, & Y_O(0) = 0, Y_O(L) = Y_{OO}. \end{array}\right\} \qquad (A.1)$$

where $w = \rho A Y_O Y_F \exp(-E/RT)$ is the chemical reaction term, with units mass/vol-sec, Q_F is the chemical heat release, with units energy/mass, and dq_R/dx is the radiant heat-loss term, with units energy/vol-s. The quantity q_R is the radiant energy flux. We nondimensionalize these equations by defining $\tau = (T - T_0)/(T_f - T_0)$, $y_F = Y_F/Y_{FF}$, $y_O = Y_O/Y_{OO}$, $\xi = s/s_0$, where $s = \int_0^x \rho dx$ is a mass-based coordinate and $s_0 = \int_0^L \rho dx$ is its maximum value. We observe that $0 \leq \xi \leq 1$ and that the "flame temperature" T_f is presently undefined. We consider the case $\rho\lambda$ = constant, $\rho^2 D_i$ = constant and $L\epsilon_O = L\epsilon_F = 1$. We define $\bar{q}_R = q_R/q_{R,ref}$ as the nondimensional radiant flux. We shall return to this quantity after our discussion of the chemical and

heat-transfer features of our problem. Our nondimensional equations are

$$\frac{d^2}{d\xi^2}\begin{pmatrix}\tau\\ y_F\\ y_O\end{pmatrix}=\begin{pmatrix}-\bar{Q}_F\\ 1\\ \phi\end{pmatrix}\mathcal{D}r+\begin{pmatrix}1\\ 0\\ 0\end{pmatrix}N_R\frac{d\bar{q}_R}{d\xi}. \tag{A.2}$$

subject to

$$\begin{pmatrix}\tau(0)\\ y_F(0)\\ y_O(0)\end{pmatrix}=\begin{pmatrix}0\\ 1\\ 0\end{pmatrix},\begin{pmatrix}\tau(1)\\ y_F(1)\\ y_O(1)\end{pmatrix}=\begin{pmatrix}0\\ 0\\ 1\end{pmatrix}. \tag{A.3}$$

Here $\bar{Q}_F = Q_F Y_{FF}/C_p(T_f - T_0)$ is the nondimensional heat release, which equals $(1+\phi)$. $\mathcal{D} = (As_0{}^2C_p/\rho_0\lambda_0)Y_{OO}\exp(-E/RT_f)$ is the Damköhler number, $\phi = \nu Y_{FF}/Y_{OO}$ is the stoichiometric index and $N_R = q_{R,ref}/[\lambda_0(T_f - T_0)/(s_0/\rho_0)]$ is a nondimensional measure of the radiant heat flux. We note that quantities with subscripts "0" are at ambient conditions attained at either wall. The reaction term is given by $r = y_O y_F \exp[-\beta(1-\tau)/[1-\alpha(1-\tau)]]$, where $\beta = E\alpha/RT_f$ and $\alpha = 1 - T_0/T_f$. Let us now form the combination $H \equiv \tau + by_F + cy_O + d$, which satisfies the equation $d^2H/d\xi^2 = (-\bar{Q}_F + b + c\phi)\mathcal{D}r + N_R d\bar{q}_R/d\xi$. We can choose b and c so that $\bar{Q}_F = b + c\phi$ thereby eliminating the reaction term.

In the absence of radiative heat losses we put $N_R = 0$ and denote $H = H_0$, giving $d^2H_0/d\xi^2 = 0$, which integrates to $H_0 = A + B\xi$. At the fuel wall $H_0 = 0$, $\tau = 0$, and $y_O = 0$ whereas at the oxidizer wall $H_0 = 0$ and $\tau = y_F = 0$, giving $H_0 = \tau - d(y_O + y_F - 1) = 0$. At the flame $y_O = y_F = 0$ and $\tau = 1$ giving $d = -1$ and $b = c = 1$. Hence, the quantity $H = \tau + y_O + y_F - 1$ is a convenient measure of the excess (or defect) of local enthalpy.

In our case the heat losses by radiation produce an "enthalpy sink" that is de-

scribed by

$$\frac{d^2H}{d\xi^2} = \mathcal{N}_R \frac{d\bar{q}_R}{d\xi}, \quad H(0) = H(1) = 0. \tag{A.4}$$

where $H = \tau + y_O + y_F - 1$. We observe that this definition of H leads to $\bar{Q}_F = (1 + o)$ (since $b = c = 1$) giving $T_f = T_0 + Q_F Y_{FF}/C_p(1 + o)$ for the adiabatic flame temperature. We also observe that with heat losses the flame temperature will not rise to its theoretical maximum even when $\beta \to \infty$. Hence, we may expect a slight redefinition later of the Damköhler number $\mathcal{D}$ in terms of a flame temperature somewhat lower than T_f.

We note that the derivation of an excess-enthalpy function may be achieved "physically". The conservation equation for the enthalpy takes the form of equation A.4 when convective transport and body force effects and preferential species transport ($Le_i \neq 1$) are neglected. Since $h = \sum_{i=1}^{N} h_i Y_i$ and $h_i = h_i^0 + \bar{C}_p(T - T_0)$, it is easy to recover our nondimensional H.

Finally, we observe that even in the most difficult and general case, such as when the radiation term depends on the spatial coordinate and the temperature and the fuel mass fraction, as long as no fuel-to-soot depletion terms enter the species equations (equations A.1.(ii) and A.1.(iii)) we can still define the mixture fraction variable $Z = (oy_F + 1 - y_O)/(o + 1)$ that satisfies $Z_{\xi\xi} = 0$ with $Z = 0$ at $\xi = 1$ and $Z = 1$ at $\xi = 0$. This provides an important simplification of the governing equations. The solution for Z is $Z = 1 - \xi$, whereby

$$\left.\begin{aligned} &(i) \quad y_O = (1 - Z) - (1 - Z_f)(\tau - H), \\ &(ii) \quad y_F = Z - Z_f(\tau - H), \end{aligned}\right\} \tag{A.5}$$

where $Z_f = (1 + o)^{-1}$ is the DF flame location in the flame coordinate system. Then the equation for τ (the first of equations A.2) and the equation for H (equation A.4)

become

$$\left.\begin{array}{ll} (i) & \tau_{ZZ} = -(1+\phi)\mathcal{D}r(H,\tau,Z) + N_R(-d\bar{q}_R/dZ), \quad \tau(0) = \tau(1) = 0 \\ (ii) & H_{ZZ} = N_R(-d\bar{q}_R/dZ), \qquad\qquad\qquad\qquad\quad H(0) = H(1) = 0. \end{array}\right\} \tag{A.6}$$

Hence, the solution for τ, y_O and y_F is reduced to the solution of two coupled nonlinear equations, equations A.6.(i) and A.6.(ii). Equations A.5 and A.6 suggest defining $S = \tau - H$ giving

$$\left.\begin{array}{ll} (i) & S_{ZZ} = -(1+\phi)\mathcal{D}r, \qquad S(0) = S(1) = 0. \\ (ii) & H_{ZZ} = N_R(-d\bar{q}_R/dZ), \quad H(0) = H(1) = 0. \end{array}\right\} \tag{A.7}$$

where $r(H,S,Z) = [1 - Z - (1 - Z_f)S][Z - Z_f S]\exp[-\beta(1 - S - H)/[1 - \alpha(1 - S - H)]]$. It is clear that some rather interesting behaviors may be expected, especially in the general case when the radiation term is a complicated function of Z, τ, and perhaps other variables. However, we shall examine only the simple case when $\bar{q}_R$ is a prescribed function of Z. We shall see that even for this case many complexities arise.

A.3.3 The Form of $H(Z)$

The enthalpy defect $H(Z)$ is obtained by integrating equation A.4 or equation A.7.(ii) twice. We consider the simple case when the radiant heat transfer term is a known, specified function of position. Then the integrations may be carried out explicitly. Because of the eventual double integration, we do not need to be particular in our choice for the radiant heat flux, $d\bar{q}_R/dZ$. Hence, we let

$$-\frac{d\bar{q}_R}{dZ}(Z) = U_0(Z_{R-}) - U_0(Z_{R+}), \tag{A.8}$$

as shown in Figure A.1. The quantities Z_{R-} and Z_{R+} are the boundaries of the heat

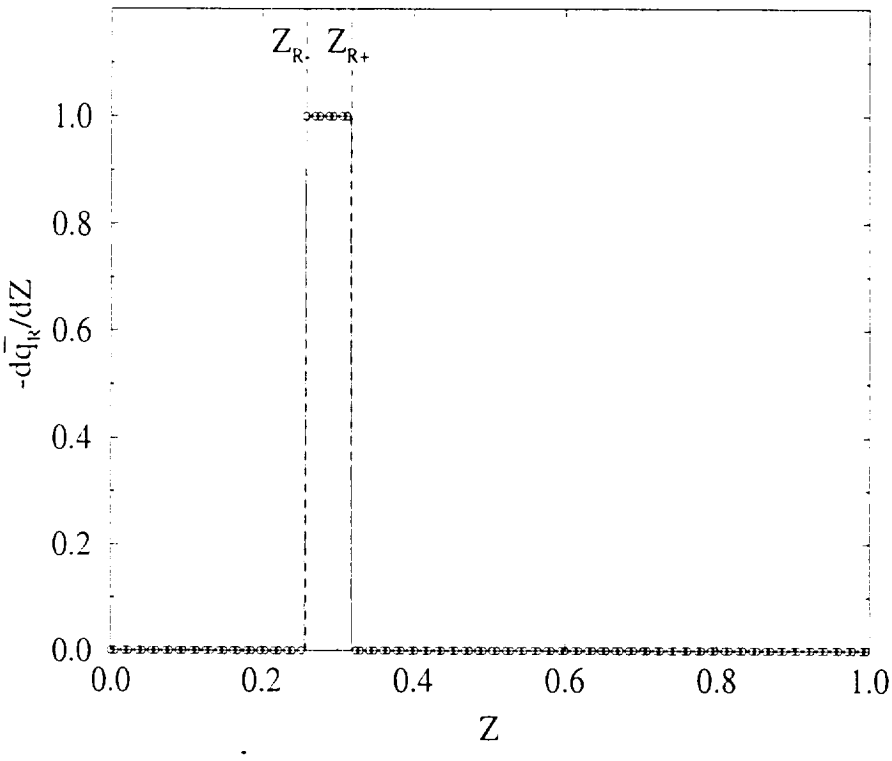

Figure A.1. The "top-hat" profile for $-d\bar{q}_R/dZ$.

loss zone. We note that $Z_{R-} \geq Z_f$ and that there are *no restrictions* on Z_{R+} other than $Z_{R+} < 1$. i.e., Z_{R+} does not have to be "close" to Z_{R-}. From equation A.8 we see that $d\bar{q}_R/dZ$ is a "well" function, and that $-d\bar{q}_R/dZ$ is a "top-hat" profile. The solution for $H(Z)$ (see Figure A.2) is

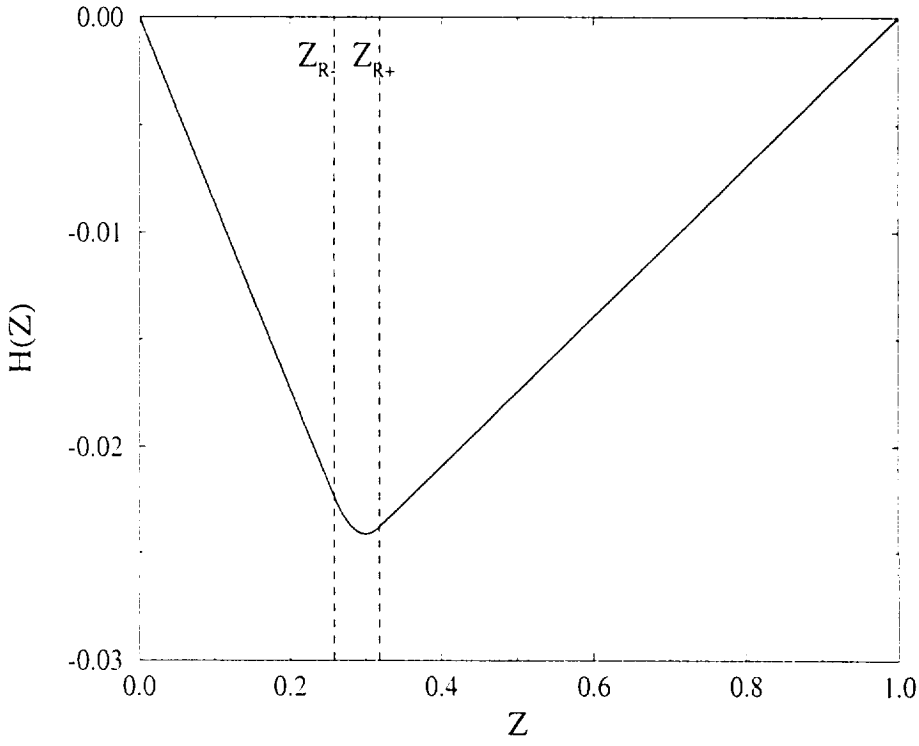

Figure A.2. The function $H(Z)$.

$$
\begin{aligned}
&(i) \quad 0 \leq Z < Z_{R-}: && H = -N_R \Delta Z_R [1 - \theta/2] Z, \\
&(ii) \quad Z_{R-} < Z < Z_{R+}: && H = -N_R \tfrac{\Delta Z_R \theta}{2} \left[1 + \tfrac{\Delta Z_R \theta}{4} - \tfrac{\Delta Z_R + \theta}{2}\right] \\
& && \quad + \tfrac{N_R}{2} \left[Z - \left(\tfrac{\Delta Z_R + \theta}{2} - \tfrac{\Delta Z_R \theta}{2}\right)\right]^2 \\
&(iii) \quad Z_{R+} < Z \leq 1: && H = -N_R \tfrac{\Delta Z_R \theta}{2} (1 - Z)
\end{aligned}
\tag{A.9}
$$

It is not difficult to demonstrate that H is less than or equal to zero on the entire interval. We observe that the values and gradients of $H(Z)$ are continuous across Z_{R-} and Z_{R+}, although the second derivative of $H(Z)$ - see equations A.7.(ii) and A.8 - is obviously discontinuous. We note that at Z_{R-} and Z_{R+} we have

$$\left.\begin{array}{ll} (i) & H(Z_{R-}) = -N_R \Delta Z_R (1 - \theta/2)^{\frac{(\theta - \Delta Z_R)}{2}}, \\ (ii) & H(Z_{R+}) = -N_R \frac{\Delta Z_R \theta}{2} (1 - \frac{\Delta Z_R + \theta}{2}). \end{array}\right\} \tag{A.10}$$

which we now use to evaluate the influence of soot zone width changes on $H(Z)$. We note first that

$$\left.\begin{array}{ll} (i) & \frac{\partial H(Z_{R-})}{\partial Z_{R+}} = -N_R Z_{R-} (1 - Z_{R+}), \\ (ii) & \frac{\partial H(Z_{R-})}{\partial Z_{R-}} = N_R \left[\frac{({Z_{R+}}^2 - {Z_{R-}}^2)}{2} + Z_{R-}(1 - Z_{R-}) - (Z_{R+} - Z_{R-}) \right]. \end{array}\right\} \tag{A.11}$$

The first of equations A.11 indicates that $H(Z_{R-})$ decreases as Z_{R+} increases for fixed Z_{R-}. The right-hand side of equation A.11.(ii) is generally positive so an increasing Z_{R-} (shrinking loss zone) increases $H(Z_{R-})$. We conclude that $H(Z_{R-})$ decreases as Z_{R+} increases and that it increases as Z_{R-} increases. We can also show for $H(Z_{R+})$ that

$$\left.\begin{array}{ll} (i) & \frac{\partial H(Z_{R+})}{\partial Z_{R+}} = -\frac{N_R}{2} [2 Z_{R+}(1 - Z_{R+}) - (Z_{R+}^2 - {Z_{R-}}^2)], \\ (ii) & \frac{\partial H(Z_{R+})}{\partial Z_{R-}} = N_R Z_{R-} (1 - Z_{R+}). \end{array}\right\} \tag{A.12}$$

so that when the RHS of equations A.12.(i) is negative an increase of Z_{R+} decreases $H(Z_{R+})$, and from equation A.12.(ii) that an increase of Z_{R-} increases $H(Z_{R+})$. In general, therefore, a larger or wider heat-loss zone decreases $H(Z)$ everywhere, whereas a smaller loss zone increases $H(Z)$ everywhere on the interval. This is consistent with our physical intuition. We note from equations A.9 that $H(Z)$ is directly proportional to N_R.

We note from equations A.9.(i) and A.10.(i) and A.7.(iii) and A.10.(ii) that we can write

$$\left.\begin{array}{ll} (i) & 0 \leq Z < Z_{R-}: \quad H = \frac{H(Z_{R-})Z}{Z_{R-}}, \\ (ii) & Z_{R+} < Z \leq 1: \quad H = \frac{H(Z_{R+})(1-Z)}{(1-Z_{R+})}. \end{array}\right\} \tag{A.13}$$

We shall use these convenient formulas extensively.

A.3.4 The Radiation Term

We wish to deduce a realistically calculable form of the "radiation number" given presently as $N_R = q_{R,ref}/[\lambda_0(T_f - T_0)/(s_0/\rho_0)]$, in terms of the undefined $q_{R,ref}$. For optically thin media we know that $dq_R/dx = 4a_p\sigma(T^4 - T_0^4)$, by virtue of equation 5.36 of chapter 5, where a_p is the Planck mean absorption coefficient. Now, $a_p = \int_0^\infty \kappa(\lambda, f_V)e_b(\lambda)d\lambda / \int_0^\infty e_b(\lambda)d\lambda$ and, for soot, $\kappa = Cf_V/\lambda$ where f_V is the soot volume fraction and C is a constant, which has the value of 7 for methane-oxygen diffusion flames [31]. Using the above value of κ, a_p can be determined as $a_p = 1864.32 f_V T$, following the treatment in 5.9.2. Using the expression for a_p and transforming to the Z coordinate we obtain

$$-\frac{\bar{\rho}q_{R,ref}}{L\bar{s}_0}\frac{d\bar{q}_R}{dZ} = 4\times 1864.32 f_V T\sigma(T^4 - T_0^4)$$

We now assume the following: (i) The factor $T(T^4 - T_0^4)$ can be replaced by $T_R(T_R^4 - T_0^4)$ where T_R is the characteristic "radiation-zone" temperature. (ii) Correspondingly, the average value of the gas phase density in the "radiation-zone" can be assumed to ρ_R. (iii) The variation in the "soot" volume fraction dictates the variation of $-d\bar{q}_R/dZ$. Since $-d\bar{q}_R/dZ = U_0(Z_{R-}) - U_0(Z_{R+})$ we therefore define $f_V = f_{V,R}(U_0(Z_{R-}) - U_0(Z_{R+}))$. This gives the f_V distribution like that in Figure A.1. Recalling that $N_R = q_{R,ref}(L\bar{s}_0)/\lambda_0(T_f - T_0)$, we can now write the following expres-

sion for N_R:

$$N_R = \frac{7457.28\sigma T_R(T_R{}^4 - T_0{}^4) f_{V,R}(L\bar{s}_0)^2}{\bar{\rho}\lambda_0(T_f - T_0)}$$

The quantity $\bar{\rho}$ is given by ρ_R/ρ_0, where, as mentioned before, the gas phase density was assumed to be ρ_R. Assuming the pressure to be constant, we can write $\rho_0 RT_0 = \rho_R RT_R$, and consequently, $\bar{\rho} = T_0/T_R$.

In order to get an idea of the magnitude of N_R we now assume some practical values for the different quantities on the RHS of A.14. The flame temperature was chosen to be $T_f = 1700$ K, the characteristic radiation zone temperature, $T_R = 1500$ K and the peak value of the soot volume fraction in the radiation zone was assumed to be $f_{V,R} = 1\times10^{-5}$. On using A.14 we get $N_R = \tilde{N}_R\bar{s}_0^2 = 57.0\bar{s}_0^2$. It has to be noted here that the value of $\bar{s}_0^2$ is of the order of $O(10^{-2})$. In the numerical solution different values of $\tilde{N}_R$ were arbitrarily chosen to study the influence on the temperature and species profiles. The values of $\tilde{N}_R$ were of the order of $O(10^2)$.

A.4 Results

A.4.1 Influence of H on Oxidizer, Fuel and Temperature Profiles

The general solutions for y_O and y_F are given by equations A.5. The approach we shall use here will be to impose restrictions on y_O and y_F then to calculate the resultant τ profiles with the intention of quantifying the influences of $H(Z)$.

Before doing this, however, we shall consider a slightly more general case than the ones we shall analyze in detail. This will serve as a constant reminder of the simplistic nature of our formulation and of the restricted validity of our results. We consider first equation A.5.(i), into which we substitute $\tau - H = 1 - \epsilon$ when $y_O = 0$

in order to obtain the modified flame location

$$Z_f' = Z_f + \epsilon(1 - Z_f). \tag{A.14}$$

suggesting a rightward shift of the flame since $\epsilon > 0$. We consider now equation A.5.(ii), into which we also substitute $\tau - H = 1 - \epsilon$ and suppose that $y_F = 0$ to obtain

$$Z_f' = Z_f - \epsilon Z_f, \tag{A.15}$$

suggesting a leftward shift of the flame since $\epsilon > 0$. Since a simultaneous rightward and leftward shift of the flame is not possible, we suspect that equations A.14 and A.15 suggest that $\tau - H = 1 - \epsilon$ produces a broadening of the DF, and that neither y_O nor y_F are zero there due to reactant leakage through both sides of the DF. Another possibility, which should lead to the "premixed-flame stage" of DF burning [57], is obtained by imposing flame shift through either of equations A.14 or A.15 and supposing that the opposite reactant leaks through the DF: in the case of equation A.14 it is the fuel that leaks, in the case of it is oxidizer.

We shall return later to these complicated considerations of DF shift in the presence of heat losses and reactant leakage. Presently we discuss the case of zero leakage, which is much simpler.

The region $0 \leq Z < Z_f$ is the oxidizer side. When there is no fuel leakage to this side we put $\epsilon = 0$ in A.15 to find $Z_f' = Z_f$ so there is no flame shift. When $y_F = 0$ we find from equation A.5.(ii) that $\tau - H = Z/Z_f$ which reduces equation A.5.(i) to $y_O = 1 - Z/Z_f$. These results are of course identical to the zero-heat-loss Burke-Schumann flame results. On the oxidizer side of the flame we combine the result

$\tau = H + Z/Z_f$ with equation A.13.(i) to obtain

$$\left.\begin{array}{lll} (i) & \tau & = \frac{H(Z_{R-})}{Z_{R-}} Z + \frac{Z}{Z_f}. \\ (ii) & \frac{d\tau}{dZ} & = \frac{H(Z_{R-})}{Z_{R-}} + \frac{1}{Z_f} \end{array}\right\} \qquad \text{(A.16)}$$

indicating that $d\tau/dZ$ on the oxidizer side is smaller than its ordinary value without heat losses, $1/Z_f$. Note that we have implicitly assumed Z_f smaller than Z_{R-} (see Figure A.3). We now consider the region $Z_{R+} < Z < 1$ between the rightmost

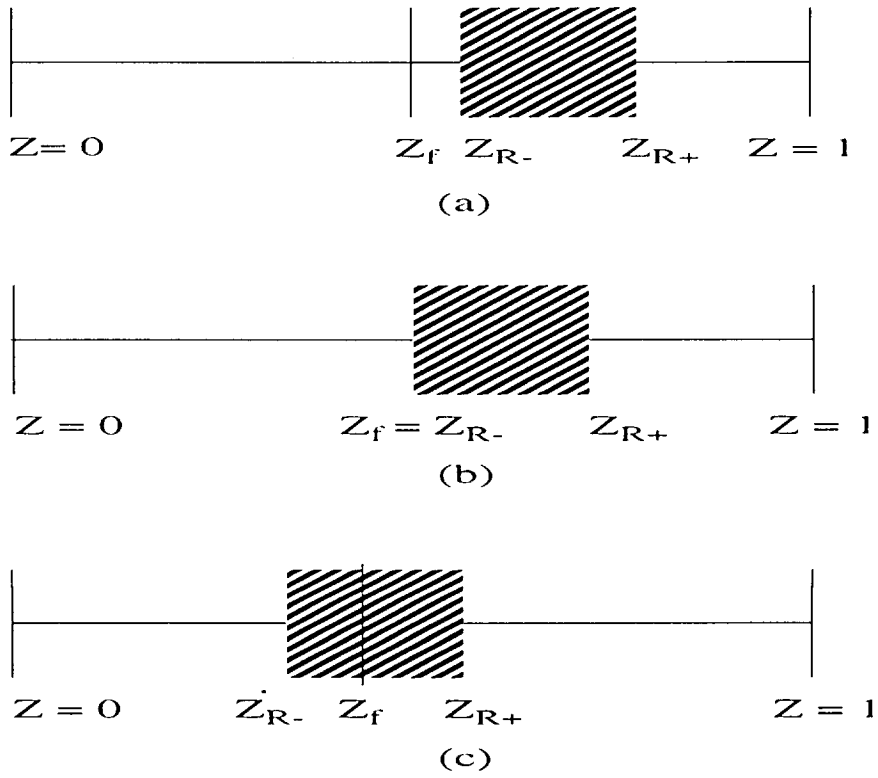

Figure A.3. The location of the soot layer relative to the flame location Z_f. In (a) $Z_f < Z_{R-}$, in (b) $Z_f = Z_{R-}$ and in (c) $Z_f > Z_{R-}$.

edge of the soot zone and the fuel wall. Here we require negligible oxidizer leakage,

so that equation A.5.(i) with $y_O = 0$ gives $\tau - H = (1 - Z)/(1 - Z_f)$ whereby $y_F = (Z - Z_f)/(1 - Z_f)$. The solution for τ , using equation A.13.(ii), is

$$\tau = H(Z_{R+})\left(\frac{1 - Z}{1 - Z_{R+}}\right) + \left(\frac{1 - Z}{1 - Z_f}\right), \tag{A.17}$$

so that we obtain for the fuel-side temperature gradient

$$\frac{d\tau}{dZ} = -\frac{H(Z_{R+})}{1 - Z_{R+}} - \frac{1}{1 - Z_f}. \tag{A.18}$$

Since $H(Z_{R+})$ is negative we see that $d\tau/dZ$ is smaller (in magnitude) than with no heat losses. In other words, $d\tau/dZ$ is less negative than it is without heat losses.

The region between the flame at Z_f and the leftmost edge of the soot zone Z_{R-} must also be examined. When we postulate a zero-leakage flame with $y_O = 0$ we obtain $\tau - H = (1 - Z)/(1 - Z_f)$ and $y_F = (Z - Z_f)/(1 - Z_f)$, the same results as immediately above for the region between $Z = Z_{R+}$ and $Z = 1$. Here, however, we are still situated to the left of the soot zone, where $H(Z)$ is given by equation A.9, whence

$$\begin{aligned} &(i) \quad \tau = \tfrac{H(Z_{R-})Z}{Z_{R-}} + \left(\tfrac{1-Z}{1-Z_f}\right), \\ &(ii) \quad \tfrac{d\tau}{dZ} = \tfrac{H(Z_{R-})}{Z_{R-}} - \tfrac{1}{1-Z_f}. \end{aligned} \tag{A.19}$$

Since $H(Z_{R-})$ is negative, $d\tau/dZ$ is more negative than the zero-loss profile. The slope of $\tau(Z)$ is therefore steeper here.

The only region remaining to be analyzed is the soot layer itself, where $Z_{R-} < Z < Z_{R+}$. Here we use equation A.9.(ii) for $H(Z)$, which we rewrite for convenience as

$$H(Z) = H(Z^*) + \frac{N_R}{2}(Z - Z^*)^2 \tag{A.20}$$

where

$$Z^* = Z_{R+} - (Z_{R+}^2 - Z_{R-}^2)/2 = (\Delta Z_R + \theta)/2 - \Delta Z_R \theta/2,$$

$$\begin{aligned} H(Z^*) &= -N_R \frac{(Z_{R+}^2 - Z_{R-}^2)}{2} \left[1 + \frac{(Z_{R+}^2 - Z_{R-}^2)}{4} - Z_{R+} \right] \\ &= -N_R \frac{\Delta Z_R \theta}{2} \left[1 - \frac{(\Delta Z_{R+} \theta)}{2} + \frac{\Delta Z_R \theta}{4} \right]. \end{aligned}$$

When $y_O = 0$ in the soot layer we obtain, as for equations A.17, A.18 and A.19

$$\begin{aligned} &(i) \quad \tau = H(Z) + \tfrac{1-Z}{1-Z_f}, \\ &(ii) \quad \tfrac{d\tau}{dZ} = N_R(Z - Z^*) - \tfrac{1}{1-Z_f}. \end{aligned} \tag{A.21}$$

Unlike equations A.18 and A.19.(ii) for the gradients on either side of the soot layer we see from equation A.21.(ii) that $d\tau/dZ$ is not constant. It is easily shown that $d\tau/dZ$ given by equation A.21.(ii) matches to equations A.18 and A.19.(ii) on opposite sides of the soot layer. Hence, both the temperature τ and the temperature gradient $d\tau/dZ$ are continuous through and across the soot layer.

We can now use equations A.16.(ii), (16.ii), A.19.(ii) and A.19.(ii) for $d\tau/dZ$ in the four zones considered to plot the characteristic temperature and H profiles in the domain $0 \leq Z \leq 1$. These profiles are drawn in Figure A.4, where we note that $\tau - H = Z/Z_f$ on the oxidizer side, that $\tau - H = (1 - Z)/(1 - Z_f)$ on the fuel side, and that τ is non-analytic only at $Z = Z_f$.

We note briefly that as Z_{R-} approaches Z_f from the right (see Figure A.3) subject to the continued constraint $y_O = 0$ for $Z > Z_f$ we can use either equation A.19 or equation A.21 for $d\tau/dZ$ by letting $Z_{R-} \rightarrow Z_f$ therein, viz.,

$$\frac{d\tau}{dZ} = \frac{H(Z_f)}{Z_f} - \frac{1}{1 - Z_f} = -N_R(Z_{R+} - Z_f) \left[1 - \frac{(Z_{R+} + Z_f)}{2} \right] - \frac{1}{1 - Z_f}.$$

In this case, the heat-loss layer touches the flame on the fuel side.

We examine the changes of slope $d\tau/dZ$ caused by the heat-loss zone. From equation A.19 we see that the slope decrement at $Z = Z_{R-}$ to the undisturbed slope

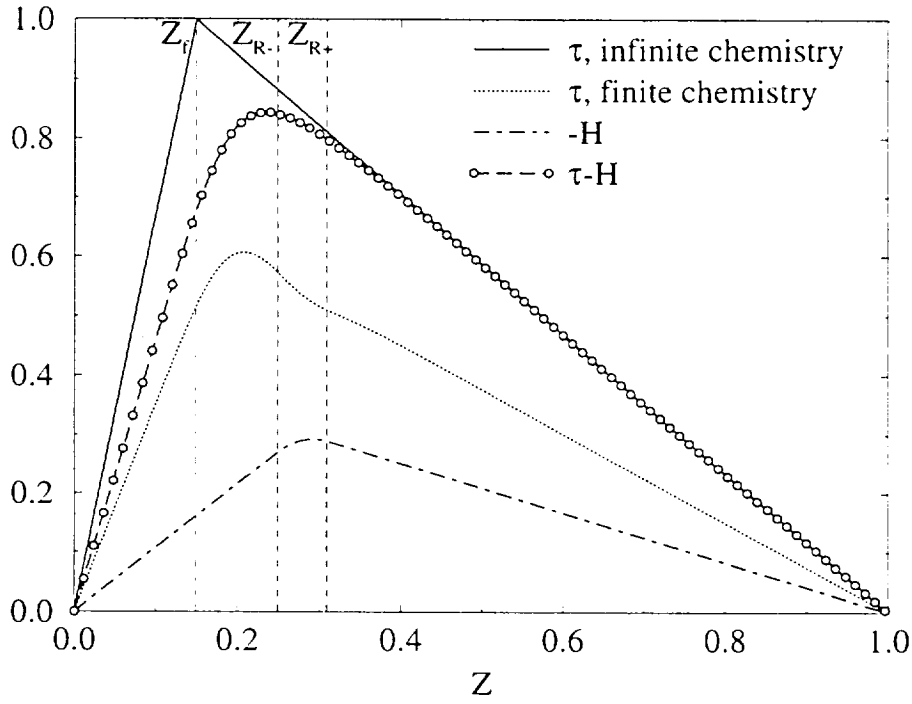

Figure A.4. τ and h profiles.

$-1/(1 - Z_f)$ is $H(Z_{R-})/Z_{R-}$, whereas the slope increment at $Z = Z_{R-}$ given by equation A.18 is $-H(Z_{R+})/(1 - Z_{R+})$. The decrement at Z_{R-} makes an already-negative slope more negative whereas the increment at Z_{R+} makes the final slope between the soot layer and the wall at $Z = 1$ less negative. The ratio of the absolute values of the decrement and increment are

$$\frac{(\text{decrement})}{(\text{increment})} = \frac{-H(Z_{R-})/Z_{R-}}{-H(Z_{R-})/(1 - Z_{R+})} = \frac{2}{\theta} - 1.$$

Consequently, when $\theta > 1$ the ratio is smaller than one and the increment is larger than the decrement. When $\theta < 1$ the opposite is true, see Figure A.5 and Figure A.6.

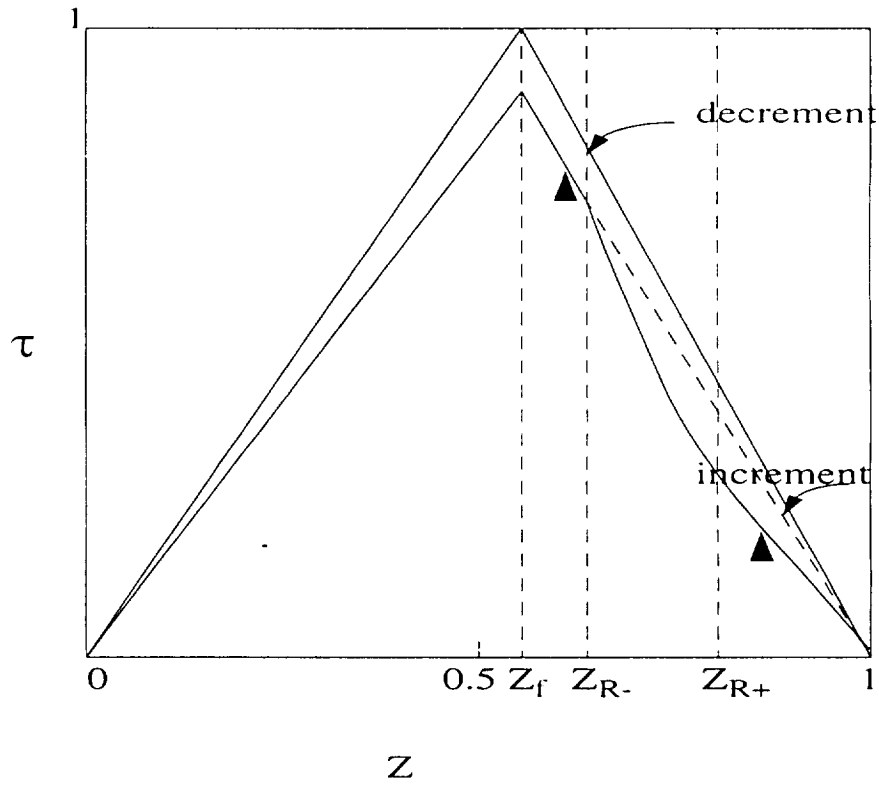

Figure A.5. The case $\theta > 1$.

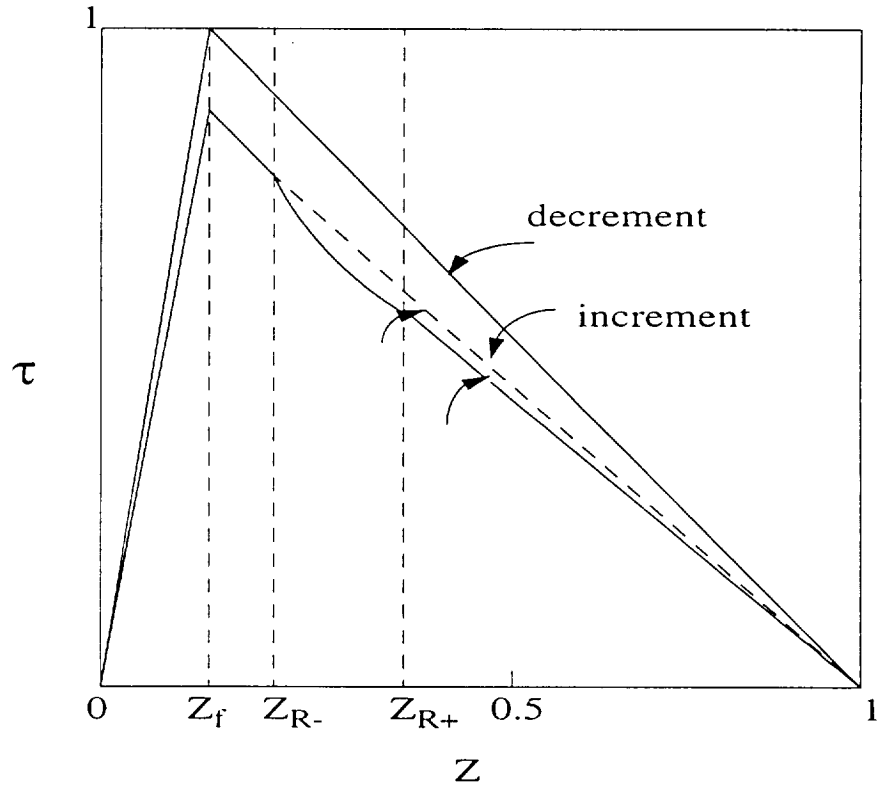

Figure A.6. The case $\theta < 1$.

Finally, we shall examine the influence of the loss zone on the temperature profiles on either side of the DF. It is through these altered temperature gradients that the loss zone changes the rate of flame chemistry, this weakening and perhaps even extinguishing the flame. We shall examine only the "outer" problem, not the detailed inner reaction zone, which is studied in section A.4.3. From equations A.16.(ii) and A.19.(ii) we write

$$0 \le Z < Z_f: \quad \frac{d\tau}{dZ} = -\frac{|H(Z_{R-})|}{Z_{R-}} + \frac{1}{Z_f} \equiv -\Sigma + \frac{1}{Z_f},$$
$$Z_f < Z < Z_{R-}: \quad \frac{d\tau}{dZ} = \frac{|H(Z_{R-})|}{Z_{R-}} - \frac{1}{1-Z_f} \equiv -\Sigma - \frac{1}{1-Z_f},$$

where $\Sigma \equiv |H(Z_{R-})|/Z_{R-} = \mathcal{N}_R \Delta Z_R (1 - \theta/2)$ is the slope change produced by the

radiative loss zone. It is easily shown that $\partial\Sigma/\partial Z_{R+}$ is always greater than or equal to zero, with $\partial\Sigma/\partial Z_{R+} = 0$ at $Z_{R+} = 1$. Hence, for fixed N_R the maximum value of Σ is $\Sigma_{MAX} = N_R(1 - Z_{R-})^2/2$. From above, we see immediately that the maximum possible value of Σ regardless of whether $Z_{R+} \rightarrow 1$ or not is $\Sigma = 1/Z_f$; at this $\Sigma-$ value the temperature gradient on the oxidizer side vanishes. In other words, as $\Sigma \rightarrow 1/Z_f$ the $\tau-$ profile on the oxidizer side crashes. From the definition of Σ we find that $\Sigma = 1/Z_f$ gives, for fixed Z_f, Z_{R+}, Z_{R-}, the constraint

$$(N_R)_{MAX} = \frac{1}{\Delta Z_R}\frac{1}{Z_f}\frac{1}{(1 - \theta/2)}, \tag{A.22}$$

which we shall compare with other estimates of $(N_R)_{MAX}$. We shall see later that when the $(N_R)_{MAX}$ estimate is refined the dependence on ΔZ_R, Z_f and $(1 - \theta/2)$ remains unchanged.

As the oxidizer-side τ profile is crashing, the fuel-side temperature gradient approaches the value $-(1/Z_f + 1/(1 - Z_f))$ from above. Hence, the heat losses from the fuel side approach a maximum as the heat losses from the oxidizer side approach zero. The combined heat losses are given by

$$L \equiv \left|\frac{d\tau}{dZ}\right|_{\text{fuel side}} + \left|\frac{d\tau}{dZ}\right|_{\text{oxidizer side}} = \frac{1}{Z_f(1 - Z_f)}, \tag{A.23}$$

which are fixed when Z_f is fixed. Hence, the decrease of oxidizer-side losses by conduction is exactly balanced by increased fuel-size losses.

We conclude by observing that $\partial\Sigma/\partial Z_{R+} = N_R(1 - Z_{R+})$ is positive while $\partial\Sigma/\partial Z_{R-} = -N_R(1 - Z_{R-})$ is negative, indicating that as Z_{R+} increases (decreases), Σ increases (decreases) because the loss-zone is thicker (thinner); also as Z_{R-} increases (decreases), Σ decreases (increases) because the loss zone is thinner (thicker). Consequently, the two most immediate means for independently changing the magnitude of

the heat loss term are to change N_R or ΔZ_R. This suggests rewriting equation A.22 as

$$(N_R \Delta Z_R)_{max} = \frac{1}{Z_f} \frac{1}{(1-\theta/2)}, \tag{A.24}$$

because the LHS is now a combined heat-loss amplitude. The quantity $\theta/2 = (Z_{R+} + Z_{R-})/2$ contains the loss-zone thickness implicitly, since we can write $\theta = \Delta Z_R + 2Z_{R-}$, but it is clear that ΔZ_R can be changed without changing θ; hence we expect the heat-loss amplitude to be relatively insensitive to changes in θ except in the extreme (and unrealistic) case $\theta \rightarrow 2$.

A.4.2 Influence of Negative H on Flame Shift

We have determined from our numerical work, see especially chapters 3, 4, that for certain initially-specified parameters of combustion and heat loss, including stoichiometric parameters ϕ or Z_f, loss-zone width (Z_{R-}, Z_{R+}) and loss-zone intensity (N_R), the reaction zone can shift from its original location near Z_f to values quite different from Z_f. Interestingly, the shift is usually toward the loss zone rather than away from it.

In this subsection we shall attempt to explain this preferential flame shift by examining two model problems. In the first model, we examine a Burke-Schumann infinite reaction rate (IRR) flame for three distinct cases,

i) finite separation between Z_f and Z_{R-} with $Z_{R-} > Z_f$.

ii) zero separation between Z_f and Z_{R-}, i.e., $Z_{R-} = Z_f$.

iii) finite separation between Z_f and Z_{R-} with $Z_{R-} < Z_f$.

These cases are illustrated in figure A.3.(a), (b), (c). One might say from these figures that it is not the flame that has shifted but the loss zone. For our simple analysis, which is steady, this is not important because it is the relative influence that we are

interested in. In the second model, various extensions are made of the discussion at the beginning of section A.4.1 on partially premixed DFs.

We proceed with our examination of the first model: case (i): $0 < Z_f < Z_{R-} < Z_{R+} < 1$ (see Figure A.3.(a)). We see from equations A.16.(i) and A.19.(ii) that the τ values are identical at $Z = Z_f$, that is, the heat-loss zone has not produced an explicit flame shift. Consequently, in order to make deductions about flame shift we must examine other quantities. We observe first that as $H(Z_{R-})$ becomes more negative, through increased N_R, say, the temperature τ monotonically decreases on the entire interval. This decrease, however, is subject to the constraint that the minimum $\tau-$value is zero. On the oxidizer side, where τ is given by equation A.16, the minimum possible value of the loss term occurs when $Z = Z_f$, i.e., $[H(Z_{R-})Z_f/Z_{R-}]_{min} = -1$. Substitution for $H(Z_{R-})$ from equation A.10 leads to

$$N_R \Delta Z_R \leq \frac{1}{Z_f(1 - \theta/2)}, \tag{A.25}$$

which is identical to equation A.24. On the fuel side we can develop two conditions, one at Z_{R-} and one at Z_{R+}, both involving the constraint $\tau \geq 0$. At $Z = Z_{R-}$, equation A.19 subjected to the constraint $\tau \geq 0$ yields

$$N_R \Delta Z_R \leq \frac{1}{Z_f(1 - \theta/2)} \left[\frac{Z_f}{Z_{R-}} \frac{1 - Z_{R-}}{1 - Z_f} \right].$$

Since $Z_f/Z_{R-} < 1$ and $(1 - Z_{R-})/(1 - Z_f) < 1$ the factor in square brackets is smaller than unity so that the upper bound for $N_R \Delta Z_R$ is smaller than for the previous result. Consequently, the upper bound for $N_R \Delta Z_R$ is smaller at $Z = Z_{R-}$ than it is at $Z = Z_f$. Finally, at $Z = Z_{R+}$, equation A.17 subjected to $\tau \geq 0$ with equation A.10.(ii)

used for $H(Z_{R+})$ leads directly to

$$N_R \Delta Z_R \leq \frac{1}{Z_f(1-\theta/2)} \left[\frac{Z_f}{\theta/2} \frac{1-\theta/2}{1-Z_f} \right]. \tag{A.26}$$

Since $Z_f/(\theta/2)$ and $(1-\theta/2)/(1-Z_f)$ are both smaller than unity, this restriction on $N_R \Delta Z_R$ is also tighter than equation A.24. Between the latter two inequalities for $N_R \Delta Z_R$ it is relatively easily shown that

$$\frac{Z_f}{\theta/2} \frac{1-\theta/2}{1-Z_f} < \frac{Z_f}{Z_{R-}} \frac{1-Z_{R-}}{1-Z_f}. \tag{A.27}$$

Hence, for our case (i) we have determined that the most stringent upper bound on $N_R \Delta Z_R$ is given by equation A.26 since it produces the smallest allowed $N_R \Delta Z_R$ value. For values larger than the upper bound of equation A.26 this case (i) flame will extinguish.

What we shall do in the following analysis is to similarly derive the most stringent restrictions on $N_R \Delta Z_R$ from cases (ii) and (iii), then to compare them to equation A.26. Then elementary deductions for the DF and heat-loss-zone interaction are made. Case (ii): $0 < Z_f = Z_{R-} < Z_{R+} < 1$ (see Figure A.3.(b)). We impose the constraint $\tau \geq 0$ at $Z = Z_f = Z_{R-}$ and at $Z = Z_{R+}$. At $Z_f = Z_{R-}$ we use equation A.16.(i) to find $H(Z_{R-}) + 1 \geq 0$ whereby we obtain equation A.24 with $\theta = Z_f + Z_{R+}$. This, except for the fact that $Z_{R-} = Z_f$, is identical to the first constraint of case (i). At $Z = Z_{R+}$, we use equation A.17 which once again leads to equation A.26, although we must recall that $Z_{R-} = Z_f$ in θ. This constraint on $N_R \Delta Z_R$, as in case (i), is more severe than the one evaluated at $Z_f = Z_{R-}$.

We now ask whether the most rigorous constraint derived here in case (ii) is more or less severe than the most rigorous constraint derived in case (i). We suppose that Z_{R+} and Z_{R-} are unchanged between cases (i) and (ii), so that only Z_f has changed,

see Figures A.3.(a), (b). In other words, ΔZ_R and θ are unchanged, so the ratio

$$\frac{(N_R \Delta Z_R)_{\text{case (ii)}}}{(N_R \Delta Z_R)_{\text{case (i)}}} = \frac{\left\{\frac{1}{Z_f(1-\theta/2)}\left[\frac{Z_f}{\theta/2}\frac{1-\theta/2}{1-Z_f}\right]\right\}_{\text{case (ii)}}}{\left\{\frac{1}{Z_f(1-\theta/2)}\left[\frac{Z_f}{\theta/2}\frac{1-\theta/2}{1-Z_f}\right]\right\}_{\text{case (i)}}} = \frac{(1-Z_f)_{\text{case (i)}}}{(1-Z_f)_{\text{case (i)}}} > 1 \quad \text{(A.28)}$$

Therefore, the tightest constraint for case (ii) is larger than the tightest constraint for case (i). In other words, larger values of $N_R \Delta Z_R$ can be attained before extinction when the flame moves as shown from its position in Figure A.3.(a) to that of Figure A.3.(b) at the leftmost edge of the loss zone.

Strictly speaking, the IRR flame in this simple model cannot relocate itself in response to heat losses the way it can in finite-rate chemistry numerical simulations. In order to move this flame we must alter the stoichiometry o, thereby changing Z_f. In the IRR limit, however, this change of Z_f has no influence on the flame vigor because the reaction still occurs with infinite rapidity. The constancy of flame vigor allows us to make the following statement: all other things being equal, the constraints or upper bounds on $N_R \Delta Z_R$ become less severe as the flame approaches the loss zone. These results suggest that as $N_R \Delta Z_R$ increases, it becomes easier to extinguish the flame for which there is separation between the flame and soot zones, and that as this separation decreases the $N_R \Delta Z_R$ value can be pushed to higher values before extinction occurs. For a transient flame we are led to expect that as $N_R \Delta Z_R$ increases the flame should move toward the loss zone to prolong its survival.

Case (iii): $0 < Z_{R-} < Z_f < Z_{R+} < 1$. Here the DF is fully within the loss zone. We impose the requirement $\tau \geq 0$ at $Z = Z_{R-}$ and $Z = Z_{R+}$ to once again obtain equation A.24 at Z_{R-} and equation A.26 at Z_{R+}. The latter constraint is the more severe, as in cases (i) and (ii). We now observe that there are two subcases depending on whether the flame at Z_f lies between the left end and the midpoint ($Z = \theta/2$) or whether it lies between the midpoint and the right end (Z_{R+}). For these cases we

obtain

$$(\mathcal{N}_R\Delta Z_R)_i < \frac{1}{Z_f(1-\theta/2)}\left[a_i\frac{1-\theta/2}{1-a_i\theta/2}\right], i = 1,2$$

where

$$i = 1: \quad Z_{R-} < Z_f < \theta/2: \quad Z_f/(\theta/2) = a_1 < 1$$
$$i = 2: \quad \theta/2 < Z_f < Z_{R+}: \quad Z_f/(\theta/2) = a_2 < 1$$

It is easily demonstrated that $(\mathcal{N}_R\Delta Z_R)_1 < (\mathcal{N}_R\Delta Z_R)_2$, so that by moving from Z_{R-} toward Z_{R+} the extinction constraint is loosened. Once again, the DF may move rightward through the loss zone in order to prolong its existence.

We conclude from our analysis of cases (i), (ii), (iii) that as the numerical value of $\mathcal{N}_R\Delta Z_R$ increases, the DF can survive by moving first toward the loss zone and then through toward the fuel side. At each increased Z_f value in its rightward migration in mixture-fraction space, the extinction value of $\mathcal{N}_R\Delta Z_R$ becomes still larger, suggesting that the DF is now slightly more difficult to extinguish, see Figure A.7.

We ask, why this should be so? Why should the $\mathcal{N}_R\Delta Z_R$ value for extinction increase as the DF moves toward and through the loss zone? The logical explanation in this IRR formulation is that when the DF is in or very near the loss zone its temperature on average is higher. Hence, larger $\mathcal{N}_R\Delta Z_R$ values are required to extinguish it. We now examine the second model, which amounts to an extension of the discussion at the beginning of section A.4.1. In our numerical results we nearly always observe a rightward shift of the flame location. Since $y_O = 0$ is imposed at the DF there must be leakage of fuel; as the radiative losses are increased through increased $\mathcal{N}_R\Delta Z_R$, we anticipate that the value of $\tau - H = 1 - \epsilon$ will further decrease (i.e., ϵ will continue to increase), so that from equation A.14 the flame will continue to shift rightward. Without a more detailed analysis, however, of the type outlined in

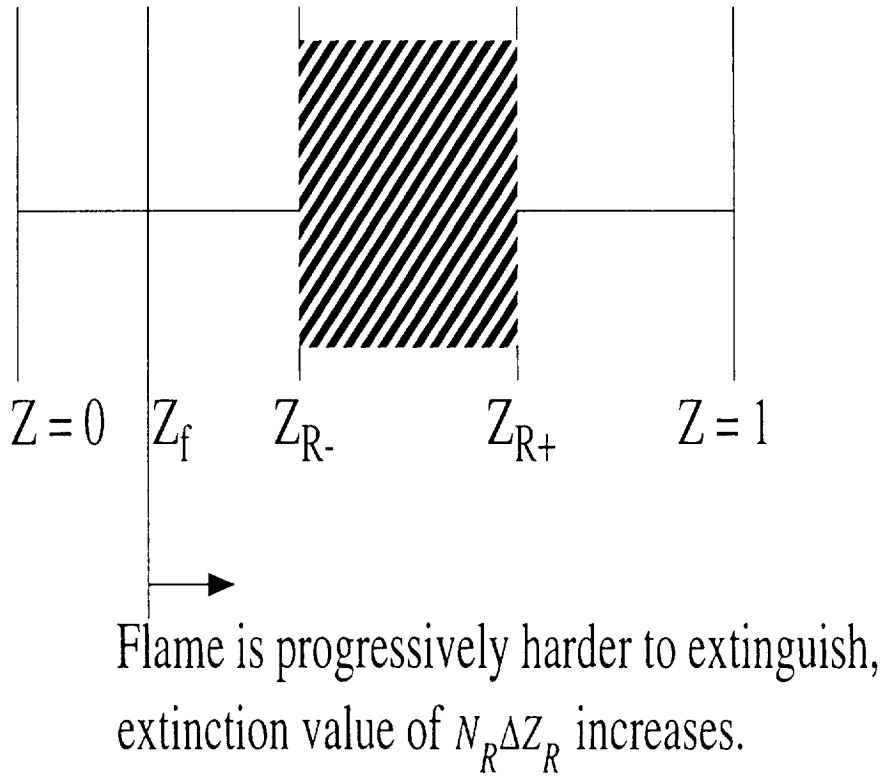

Figure A.7. The direction of increase of $N_R \Delta Z_R$ with flame movement.

Liñán [57], and a rational explanation for why it should be y_O that vanishes at the DF and not y_F, this explanation is little more than a plausibility argument. Support for the condition $y_O = 0$ at the DF is produced in chapter 6. The fuel, not the oxidizer, leaks through the DF probably because all of the cases we have studied are overall fuel rich ($\phi > 1$).

A.4.3 Reaction-Zone Analysis using Activation-Energy Asymptotics

Here we shall solve equations A.7.(i) and A.7.(ii) across the reaction zone in order to deduce an extinction criterion that is more realistic than those produced in section A.4.2. Before proceeding we note that the mass coordinate s_0 may be rewritten as

$$s_0 = \int_0^L \rho dx = \rho_0 L \int_0^1 \bar{\rho} d\bar{x} \equiv \rho_0 L \bar{s}_0,$$

where

$$\bar{s}_0 = \int_0^1 \bar{\rho} d\bar{x}. \tag{A.29}$$

and that the Damköhler number may be rewritten as

$$\mathcal{D} \doteq \left[\frac{AL^2}{\alpha_0} Y_{OO} e^{-E/RT_f} \right] \bar{s}_0^2 \equiv \tilde{\mathcal{D}} \bar{s}_0^2. \tag{A.30}$$

in order to illustrate the dependence of $\mathcal{D}$ on $\bar{s}_0$, which can change depending on the integrated value of $\bar{\rho}$ on the interval. We note that in equation A.30 the quantity $\mathcal{D}$ is a fixed numerical value, and that $\alpha_0 = \lambda_0 / \rho_0 C_p$.

We require only one hypothesis to carry through our analysis, namely the reaction zone (flame) and loss zone (soot layer) are physically separated each from the other. When this is true, the enthalpy defect in the entire region $0 < Z < Z_{R-}$ bounding

the flame near Z_f is given by equation A.9.(i) or equivalently equation A.13.(i). The temperature gradients on either side of the DF are given by equation A.16.(ii) for $0 \leq Z < Z_f$ and equation A.19.(ii) for $Z_f < Z < Z_{R-}$. The corresponding conditions on the variable S in equation A.7 become, respectively,

$$\begin{aligned} &(i) \quad \tfrac{dS}{dZ} = \tfrac{1}{Z_f}, \qquad 0 \leq Z < Z_f \\ &(ii) \quad \tfrac{dS}{dZ} = \tfrac{1}{1-Z_f}, \quad Z_f \leq Z < Z_{R-}. \end{aligned} \tag{A.31}$$

We observe that the S gradients on either side of the DF are identical to the $\tau-$ gradients when there are no heat losses, i.e., when $H = 0$. The only difference in the boundary value problem of equations A.7.(i) with gradient conditions A.31 on the flame-zone part of the solution is the presence of H in the Arrhenius exponent.

We now perform an activation-energy-asymptotic (AEA) analysis of the reaction zone by defining

$$S = 1 - (o + a\eta)/b\beta, \eta = (Z - Z_f)\beta c,$$

along with

$$\beta H = \frac{\beta H(Z_{R-})Z}{Z_{R-}} = \frac{\beta H(Z_{R-})Z_f}{Z_{R-}} + (\frac{H(Z_{R-})}{cZ_{R-}})\eta.$$

which when substituted into the Arrhenius exponent give

$$\frac{-\beta(1-(S+H))}{1-\alpha(1-(S+H))} = \frac{-(\Phi + a\eta)/b + \beta H(Z_{R-})Z_f/Z_{R-} + H(Z_{R-})\eta/cZ_{R-}}{(1+\alpha H(Z_{R-})Z_f/Z_{R-}) - (\alpha/\beta)[(\Phi + a\eta)/b - H(Z_{R-})\eta/cZ_{R-}]}. \tag{A.32}$$

This obviously reduces to the standard zero-heat-loss result when we put $H = 0$. From equation A.33 we have two cases to consider:

Case (i): $H(Z_{R-}) \simeq O(1)$. This reduces equation A.33 to

$$-\frac{\beta(1-S+H)}{1-\alpha(1-(S+H))} = \frac{\beta H(Z_{R-})Z_f/Z_{R-}}{1+\alpha H(Z_{R-})Z_f/Z_{R-}} \tag{A.33}$$

in the first approximation. The temperature residue Φ has been entirely eliminated and the Arrhenius exponent is entirely controlled by the heat-loss term. As $\beta \to \infty$ the DF is extinguished subject to the constraint that the denominator be positive, viz., $1 + \alpha H(Z_{R-})Z_f/Z_{R-} > 0$, which gives $H(Z_{R-})| < Z_{R-}/\alpha Z_f$ or

$$N_R \Delta Z_R < \frac{1}{\alpha Z_f(1-\theta/2)}$$

This estimate for $(N_R \Delta Z_R)_{MAX}$ compares well with the previous estimates of section A.4.2 since it is of the same order of magnitude. However, this case (i) is unrealistic because the DF should long ago have been extinguished. The following case is much more realistic.

Case (ii): $|H(Z_{R-})| \equiv h/\beta$, i.e., $|H(Z_{R-})| \sim O(\beta^{-1})$. The substitution of this expression along with $\Phi = \Phi_0 + \beta^{-1}\Phi_1 + \ldots$, $h = h_0 + \beta^{-1}h_1 + \ldots$ into equation A.33 gives

$$\frac{-\beta(1-(S+H))}{1-\alpha(1-(S+H))} = \frac{-(\Phi+a\eta)}{b} + \frac{h_0 Z_f}{Z_{R-}} + O(\beta^{-1}) \tag{A.34}$$

With this expression along with the choices

$$\left.\begin{aligned} &(i) \quad a = 2Z_f - 1, \\ &(ii) \quad b/c = 2Z_f(1-Z_f) \\ &(iii) \quad b^3 = \tfrac{4\mathcal{D}_0 Z_f{}^2(1-Z_f)^3}{\beta^3}\exp[h_0 Z_f/Z_{R-}]. \end{aligned}\right\} \tag{A.35}$$

and the expansion $\mathcal{D} = \mathcal{D}_0 + \beta^{-1}\mathcal{D}_1 + \ldots$, we obtain the following boundary-value

problem for the reaction zone.

$$\Phi_{\eta\eta} = (\Phi^2 - \eta^2)\exp[-(\Phi + a\eta)/b], \tag{A.36}$$

$$\Phi_\eta \rightarrow \neq 1 \text{ as } \eta \rightarrow \pm\infty \tag{A.37}$$

The only difference between our result and previous studies [57] of the zero-heat-loss DF lies in the factor $\exp[h_0 Z_f/Z_{R-}]$ which appears in the reduced Damköhler number. We note that $h_0 Z_f/Z_{R-}$ means that $h \sim O(1)$ since $Z_f/Z_{R-} \sim O(1)$. And $h \sim O(1)$ means $|H(Z_{R-})| \sim O(\beta^{-1})$: small heat losses can produce DF quenching.

We now make a comparison of the zero and finite-heat-loss cases. Without heat losses ($h = 0$) equation A.33.(iii) becomes

$$b^* = \left[\frac{4\mathcal{D}_0 Z_f^2 (1 - Z_f)^3}{R^3}\right]^{1/3},$$

which differs from the value of b in equation A.33.(iii) only by the absence of the exponential term. At extinction the approximate correlation [57] $b_E = [\epsilon(1 - |a|) - (1 - |a|)^2 + 0.26(1 - |a|)^3 + 0.055(1 - |a|)^4]^{1/3}$ renders b and b^* identical. Hence, for the same Z_f and β we must have

$$\mathcal{D}^*_{OE} = \mathcal{D}_{OE} e^{h_0 Z_f/Z_{R-}}, \tag{A.38}$$

where $\mathcal{D}^*_{OE}$ is the value of $\mathcal{D}_0$ at extinction with no heat losses ($h = 0$) and $\mathcal{D}_{OE}$ is the value of $\mathcal{D}_0$ at extinction with heat losses From equation A.38 we see that the value of the Damköhler number is higher at extinction when there are heat losses. That is, with $\mathcal{D} = t_{flow}/t_{chem}$ and t_{flow} fixed, the characteristic reaction time must be smaller - a faster reaction. Or conversely, without heat losses the chemical reaction can afford to be slower.

From equation A.38 we can write, since h is negative,

$$\mathcal{D}_{OE} = \mathcal{D}_{OE}^{*}[\exp|h_0|]^n, \; n = Z_f/Z_{R-} < 1. \tag{A.39}$$

As Z_{R-} decreases toward Z_f or as Z_f increases toward Z_{R-} the exponent n increases toward unity. For a fixed $\mathcal{D}_{OE}^{*}$, we see that the flame with heat losses is relatively easier to extinguish because its extinction Damköhler number is larger. The largest value of $\mathcal{D}_{OE}$ occurs when $n = 1$, i.e., when the loss zone touches the DF on the fuel side.

We note particularly that $|h_0 Z_f/Z_{R-}| = \beta N_R \Delta Z_R Z_f(1 - \theta/2)$ so that for fixed Z_{R+}, Z_{R-} the quantity $\partial|h_0 Z_f/Z_{R-}|/\partial Z_f$ is positive. As Z_f increases the Damköhler number of extinction increases and the DF is easier to extinguish. This deduction in all respects appears to contradict the deductions of section A.4.2 and the numerical results. We shall discuss it later in section A.5.

We proceed presently to derive an upper bound for the quantity This, of course, is the extinction limit. We rearrange equation A.33, after recalling that $|h_0|Z_f/Z_{R-} = \beta N_R \Delta Z_R(1 - \theta/2)Z_f$ to obtain the extinction criterion

$$N_R \Delta Z_R = \frac{1}{Z_f(1 - \theta/2)} \frac{1}{\beta} \ln\left[\frac{4\mathcal{D}_0 {Z_f}^2 (1 - Z_f)^3}{{b_E}^3 \beta^3}\right], \tag{A.40}$$

where

$$\begin{aligned} b_E &= \epsilon[(1 - |a|) - (1 - |a|)^2 + 0.26(1 - |a|)^3 + 0.055(1 - |a|)^4]^{1/3} \\ a &= 2Z_f - 1 \\ \mathcal{D}_0 &= \tilde{\mathcal{D}}\bar{s}_0^2; \tilde{\mathcal{D}} = (AL^2/\alpha_0) Y_{OO} \exp(-E/RT_f). \end{aligned} \tag{A.41}$$

Comparison of equation A.40 to the $N_R \Delta Z_R$ upper bounds obtained in section A.4.2 shows that the basic dependencies on Z_f and $1 - \theta/2$ are the same, but the maximum

value is reduced by the factor β^{-1}. The dependence on $\mathcal{D}_0$ is logarithmic and therefore fairly weak.

Comparisons with numerically-calculated extinction results were made for some cases. These are shown in Figure A.8. We observe that the extinction radiation

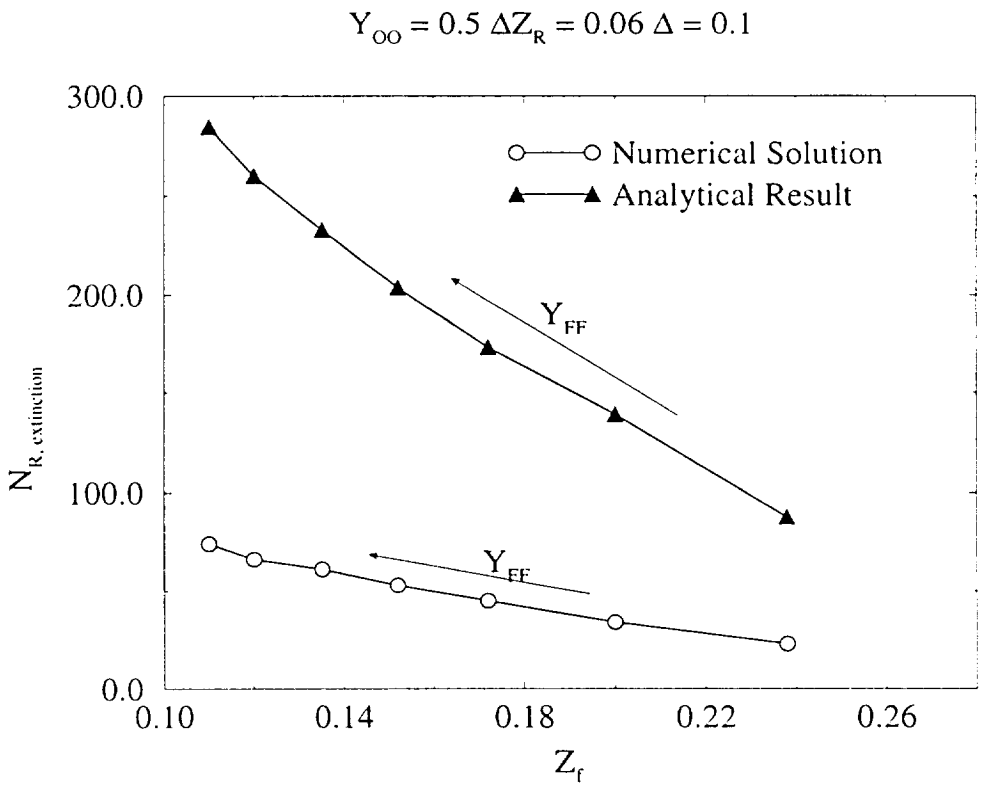

Figure A.8. Comparison of numerical and analytical solutions for the extinction radiation number.

number value increases as Z_f decreases for a given Y_{OO}, i.e., for increasing values of Y_{FF}. The direction of increasing Y_{FF} has been indicated in Figure A.8 by an arrow. The difference between the analytical and numerical solutions is quite prominent and indicates poor agreement between the two. However, a closer scrutiny of the curves indicates that the analytically obtained extinction values are roughly 4 times

those obtained from the numerical solution. Hence, the results indicate that we may introduce a correction factor in A.40 to correlate the analytical results with the numerical solution.

A.4.4 Influence of Heat-Loss Zone on Flame Displacement

Where there is a temperature decrement, as shown in Figure A.5 and Figure A.6, the density increases. This produces a displacement of the flame toward the fuel side. We demonstrate this by writing the flame location as

$$Z_f = \frac{1}{(1+o)} = 1 - \frac{s_f}{s_0} = 1 - \frac{\int_0^{x_f} \rho dx}{\int_0^L \rho dx} \tag{A.42}$$

This can be rearranged to yield

$$\int_0^{x_f} \rho dx = o \int_0^L \rho dx. \tag{A.43}$$

which we examine for the cases with and without heat losses. If the flame zone is negligibly thin we can write $\rho = \rho_0 - (\rho_0 - \rho_f)(L-x)/(L-x_f)$ on the oxidizer side between x_f and L, giving $\rho(x_f) = \rho_f$ and $\rho(L) = \rho_0$ and yielding $o(L-x_f)(\rho_0+\rho_f)/2$ for the RHS of equation A.43. For the LHS (the fuel side) we shall for demonstration purposes can use two different ρ distributions, the linear profile without heat losses, $\rho^{(1)} = \rho_0 - (\rho_0 - \rho_f)(x/x_f)$, and a nonlinear profile with losses, $\rho^{(2)} = \rho_0 - (\rho_0 - \rho_f)(x/x_f)^2$: we see that $\rho^{(2)}$ is always larger than $\rho^{(1)}$. Substitution into the LHS above yields $x_f(\rho_0+\rho_f)/2$ and $x_f(\rho_0+2(\rho_0+\rho_f)/2)/3$, respectively, from which we find, after equating to the RHS, $(x_f/L)^{(1)} = o/(1+o)$ and $(x_f/L)^{(2)} = \bar{\rho}o/(\rho_0/3 + \bar{\rho}(o+2/3))$, where $\bar{\rho} = (\rho_0+\rho_f)/2$.

We then form the difference

$$\begin{aligned} \left(\frac{x_f}{L}\right)^{(1)} - \left(\frac{x_f}{L}\right)^{(2)} &= \frac{\phi M}{(1+\phi)(1+\phi+M)}; \\ M &= \frac{1}{3}\left(\frac{\rho_0-\rho_f}{\rho_0+\rho_f}\right) > 0 \end{aligned}$$

Hence, case 2 with heat losses has a smaller value of x_f/L indicating that the flame is displaced to the fuel side.

Although our demonstration has employed simple ρ distributions, it is generally valid whenever ρ on the oxidizer side is unchanged by the heat losses and when the nondimensional reaction layer thickness, $\Delta x_f/L$, is small.

Because our analysis in the sections preceding this one is performed in terms of the mixture-fraction Z,the influences of heat losses on Z_f must be examined before making definite conclusions. In any case, the flame movement caused by density changes does not alter the flame location in the Z coordinate, since $Z_f = (1+\phi)^{-1}$ is unchanged.

A.5 Discussion and Conclusions

In this study we have constructed a simplified model of the heat-loss zone interaction with a DF. The model involves the solution of two coupled equations for the temperature and the heat-loss distribution. The fuel and oxidizer mass fractions do not enter the calculations since the "soot" is formed from trace amounts of the fuel. We demonstrated that a feasibility argument could be made to describe the movement of the flame toward and even through the heat-loss zone, which behavior is observed for the numerical simulation, see chapters 3,blotex of this thesis. The essence of the argument is that the upper bound for the extinction value of $N_R\Delta Z_R$ is increased as the flame moves toward (and through) the loss zone. We demonstrated later that the $N_R\Delta Z_R$ values calculated in section A.4.2 were unrealistically large: that, coupled

with the complete absence of finite-rate chemistry, rendered the analysis suggestive only. Nevertheless, it does square with the available evidence, which indicates that the DF response to increased heat losses is to burrow through the loss zone, if possible. In some cases it emerges from the other side weakened (and ready to be extinguished with further increases of N_R) but nevertheless existing. Hence, the plausibility arguments advanced in section A.4.2 are consistent with the actual sequences of events as obtained from numerical simulations.

The finite-chemistry calculations, however, seem to contradict the section A.4.2 calculations because they say that as the DF moves closer to the loss zone the extinction Damköler number becomes larger, making the flames easier to extinguish.

This apparent contradiction between the two results, however, is resolved when one analyzes the problem in terms of competing mechanisms. One mechanism is the section A.4.2 impulse for DF translation through the loss zone, the second mechanism is the section A.4.3 tendency of the extinction $\mathcal{D}$ to rise making actual extinction easier. The two mechanisms are made compatible and complementary by considering the following two cases. In the first case the value of $\mathcal{D}$ is so large that traversal of the loss zone doesn't allow $\mathcal{D}_E$ to exceed $\mathcal{D}$; this DF therefore survives the full traversal event and is ultimately extinguished only when $N_R \Delta Z_R$ becomes much larger. In the second case, $\mathcal{D}$ is of borderline magnitude; as the DF approaches the loss zone the condition $\mathcal{D} \leq \mathcal{D}_E$ ensues somewhat later. Here the DF can therefore be extinguished before it traverses the loss zone. The deciding quantity for both of these scenarios is the initial $\mathcal{D}$ value. When it is "large", complete loss-zone traversal is possible, when it is "small", only partial traversal is possible before extinction.

The prospect of a DF traversing the soot zone raises the interesting possibility of a soot- zone-induced flame flicker. The soot zone weakens the DF which then collapses toward the soot layer. At a certain limiting value, soot begins to leak through the DF where it is immediately oxidized. The added heat release of soot oxidation then

strengthens the DF which retreats to its previous position. The sequence starts from the beginning when the soot zone weakens the DF which then collapses toward the soot layer, etc.

Perhaps the most important result of our analysis is the loss-zone extinction formula, equation A.40. This formula was found to produce good qualitative agreement with numerically-calculated values of the extinction ($N_R \Delta Z_R$), although a multiplicative correction factor was needed to bring the theoretical and numerical results to agreement. A principal ingredient in obtaining the agreement was the retention of the factor $\bar{s}_0^2$ which may be as small as $O(10^{-2})$ and therefore may alter calculated $N_R \Delta Z_R$ values by up to 30%. As shown in chapter 4, we can generalize equation A.40 to account for non-top-hat loss-zone profiles by properly redefining ΔZ_R.

We note finally that many of the physical subtleties of our simplified model problem are discussed in detail in [56]. Despite the error in the calculation of $H(Z)$ and the faulty deductions obtained therefrom, the discussions about the thermophoretic effect, the limits of this model, etc. are correct.

BIBLIOGRAPHY

BIBLIOGRAPHY

[1] K. J. Syed, C. D. Stewart, and J. B. Moss. In *Twenty-Third Symposium (International) on Combustion*, page 1533. The Combustion Institute, Pittsburgh, 1990.

[2] J. Nagle and R. F. Strickland-Constable. In *Proceedings of the Fifth Carbon Conference*, page 154, Pergamon Press, London, 1962.

[3] J. D. Felske and C. L. Tien. *Combustion Science and Technology*, 7:25, 1973.

[4] G. H. Markstein. In *Sixteenth Symposium (International) on Combustion*, page 1407, The Combustion Institute, Pittsburgh, 1976.

[5] C. L. Tien and S. C. Lee. *Progress in Energy and Combustion Science*, 8:41, 1982.

[6] W. L. Grosshandler and J. P. Vantelon. *Combustion Science and Technology*, 44:125, 1985.

[7] S. H. Chan, X. C. Pan, and M. M. M. Abou-Ellail. *Combustion and Flame*, 102:438, 1995.

[8] J. P. Gore and J. H. Jang. *Journal of Heat Transfer*, 114:234, 1992.

[9] Y. R. Sivathanu and J. P. Gore. *Combustion and Flame*, 97:161, 1994.

[10] A. Atreya and I. S. Wichman, 1991. Research proposal submitted to NASA.

[11] W. L. Grosshandler and A. T. Modak. In *Eighteenth Symposium (International) on Combustion*, page 601, The Combustion Institute, Pittsburgh, 1981.

[12] I. M. Kennedy, W. Kollmann, and J. Y. Chen. *Combustion and Flame*, 81:73, 1990.

[13] Hennig Bockhorn. *Soot Formation in Combustion*, chapter A Short Introduction to the Problem - Structure of the Following Parts, page 3. Springer Series in Chemical Physics. Springer-Verlag, 1994.

[14] B.S. Haynes and H. GG. Wagner. Soot formation. *Progress in Energy and Combustion Science*, 7:229, 1981.

[15] Anthony Hamins. *Environmental implications of combustion processes.* CRC Press. Boca Raton. Florida, 1993.

[16] H. B. Palmer and H. F. Cullis. *The Chemistry and Physics of Carbon*, volume 1. Marcel Dekker, New York, 1965.

[17] S. H. Bauer. In *Tenth Symposium (International) on Combustion*, page 511, The Combustion Institute, Pittsburgh, 1965.

[18] K.P. Schug, Y. Manheimer-Timnat, P. Yaccarino, and I. Glassman. *Combustion Science and Technology*, 22:235, 1980.

[19] I. Glassman and P. Yaccarino. In *Eighteenth Symposium (International) on Combustion*, page 1175, The Combustion Institute, Pittsburgh, 1981.

[20] A. Gomez, G. Sidebotham, and I. Glassman. *Combustion and Flame*, 58:45, 1984.

[21] I. Glassman. In *Twenty-Second Symposium (International) on Combustion*, page 295. The Combustion Institute, Pittsburgh, 1988.

[22] S. J. Harris and A. M. Weiner. *Combustion Science and Technology*, 32:267, 1983.

[23] S. J. Harris and A. M. Weiner. *Combustion Science and Technology*, 38:75, 1984.

[24] R. Puri and R. J. Santoro. In *Proceedings of the Third International Symposium on Fire Safety Science*, page 595, 1991.

[25] I. S. Mclintock. *Combustion and Flame*, 12:217, 1968.

[26] J. R. Arthur and D. H. Napier. In *Fifth Symposium (International) on Combustion*, page 303. The Combustion Institute, Pittsburgh, 1955.

[27] S. K. Ray and R. Long. *Combustion and Flame*, 8:139, 1964.

[28] B. B. Chakraborty and R. Long. *Combustion and Flame*, 12:226, 1968.

[29] J. M. Jones and J. L. J. Rosenfeld. *Combustion and Flame*, 19:427, 1972.

[30] R. J. Santoro, T. T. Yeh, J. J. Horvath, and H. G. Semerjian. *Combustion Science and Technology*, 53:89, 1987.

[31] I. M. Kennedy, W. Kollmann, and J. Y. Chen. *AIAA Journal*, 29:1452, 1990.

[32] J. H. Kent and H. GG. Wagner. In *Eighteenth Symposium (International) on Combustion*, page 1117, The Combustion Institute, Pittsburgh, 1981.

[33] J. B. Moss, C. D. Stewart, and K. J. Syed. In *70th PEP AGARD Symposium*, Crete, 1987.

[34] K. M. Leung, R. P. Lindstedt, and W. P. Jones. *Combustion and Flame*, 87:289, 1991.

[35] U. Vandsburger, I. M. kennedy, and I. Glassman. *Combustion Science and Technology*, 39:263, 1984.

[36] R. Siegel and J. R. Howell. *Thermal Radiation Heat Transfer*. Hemisphere Publishing Corporation, 1981.

[37] M. F. Modest. *Radiative Heat Transfer*. McGraw-Hill, Inc., 1993.

[38] J. P. Gore, U.-S. Ip, and Y. R. Sivathanu. *Journal of Heat Transfer*, 114:487, 1992.

[39] Y. R. Sivathanu, J. P. Gore, J. M. Janssen, and D. W. Senser. *Journal of Heat Transfer*, 115:653, 1993.

[40] M. Fairweather, W. P. Jones, and R. P. Lindstedt. *Combustion and Flame*, 89:45, 1992.

[41] H. D. Ross, R. G. Sotos, and J. S. Tien. *Combustion Science and Technology*, 75:155, 1991.

[42] *Microgravity Combustion Science: Progress, Plans, and opportunities*. The NASA Lewis Research Center, USA, 1992.

[43] C. K. Law and G. M. Faeth. *Progress in Energy and Combustion Science*, 20:65, 1994.

[44] H. Ito, O. Fujita, and K. Ito. *Combustion and Flame*, 20:65, 1994.

[45] A. Atreya, S. Agrawal, K. R. Sacksteder, and H. R. Baum. In *32nd Aerospace Sciences Meeting*, page 1, Reno, Nevada, 1994.

[46] K. Pickett, A. Atreya, S. Agrawal, and K. R. Sacksteder. In *33rd Aerospace Sciences Meeting*, 1995. AIAA paper 95-148.

[47] I. S. Wichman. *An Introduction to Combustion Modeling Using High-Activation-Energy Asymptotic (AEA) Methods*. CRC Press, 1993.

[48] F. A. Williams. *Combustion Theory*. The Benjamin/Cummings Publishing Company, Inc., 1985.

[49] I. S. Wichman. PhD thesis, Princeton University, 1983.

[50] L. S. Tzeng, A. Atreya, and I. S. Wichman. *Combustion and Flame*, 80:94, 1990.

[51] J. C. Ku, L. Tong, and P. S. Greenberg. In *Third International Microgravity Combustion Workshop, NASA conference publication 10174*, page 375, NASA Lewis Research Center, 1995.

[52] C. Park and J. P. Appleton. *Combustion and Flame*, 20:369, 1973.

[53] A. Murty Kanury. *Introduction to Combustion Phenomena*. Gordon and Breach Science Publishers, 1984.

[54] L. Talbot, R. K. Cheng, R. W. Schefer, and D. R. Willis. *Journal of Fluid Mechanics*, 101:737, 1980.

[55] J. H. Chen, J. M. Card, M. Day, and S. Mahalingam. In *Eighth International Symposium on Transport Phenomena in Combustion*, 1995.

[56] I. S. Wichman. *Combustion and Flame*, 97:393, 1994.

[57] A. Liñán. *Acta Astronautica*, 1:1007, 1974.